



**HAL**  
open science

# Quantitative analysis of the mechanical properties of healthy and cancer lung tissue for the design of mechano-mimetic culture substrates

Fabien Delebosse

► **To cite this version:**

Fabien Delebosse. Quantitative analysis of the mechanical properties of healthy and cancer lung tissue for the design of mechano-mimetic culture substrates. Physics [physics]. Université Grenoble Alpes [2020-..], 2023. English. NNT: 2023GRALY048 . tel-04405589

**HAL Id: tel-04405589**

**<https://theses.hal.science/tel-04405589>**

Submitted on 19 Jan 2024

**HAL** is a multi-disciplinary open access archive for the deposit and dissemination of scientific research documents, whether they are published or not. The documents may come from teaching and research institutions in France or abroad, or from public or private research centers.

L'archive ouverte pluridisciplinaire **HAL**, est destinée au dépôt et à la diffusion de documents scientifiques de niveau recherche, publiés ou non, émanant des établissements d'enseignement et de recherche français ou étrangers, des laboratoires publics ou privés.

# THÈSE

Pour obtenir le grade de

## DOCTEUR DE L'UNIVERSITÉ GRENOBLE ALPES

École doctorale : PHYS - Physique

Spécialité : Physique pour les Sciences du Vivant

Unité de recherche : Laboratoire des Technologies de la Microélectronique

### **Analyse quantitative des propriétés mécaniques des tissus pulmonaires sains et cancéreux pour la conception de substrats de culture mécano-mimétiques**

### **Quantitative analysis of the mechanical properties of healthy and cancer lung tissue for the design of mechano-mimetic culture substrates**

Présentée par :

**Fabien DELEBOSSE**

#### Direction de thèse :

**Alice NICOLAS**

DIRECTRICE DE RECHERCHE, Université Grenoble Alpes

Directrice de thèse

**Camille MIGDAL**

Cell & Soft

Co-encadrante de thèse

#### Rapporteurs :

**Laurent Malaquin**

DIRECTEUR DE RECHERCHE, LAAS-CNRS

**Allessandro Furlan**

MAITRE DE CONFERENCES HDR, Centre Oscar Lambret / UMR Canther

#### Thèse soutenue publiquement le **2 octobre 2023**, devant le jury composé de :

**Alice NICOLAS**

DIRECTRICE DE RECHERCHE, Université Grenoble Alpes - CNRS  
-LTM

Directrice de thèse

**Laurent Malaquin**

DIRECTEUR DE RECHERCHE, LAAS-CNRS

Rapporteur

**Allessandro Furlan**

MAITRE DE CONFERENCES HDR, Centre Oscar Lambret / UMR  
Canther

Rapporteur

**Charlotte Rivière**

MAÎTRESSE DE CONFERENCES HDR, Institut Lumière Matière  
(ILM), équipe biophysique

Examinatrice

**Grégory Chagnon**

PROFESSEUR, Laboratoire TIMC - Bioméca Team

Président du Jury

**Claude Verdier**

DIRECTEUR DE RECHERCHE, Groupe MC<sup>2</sup> - Laboratoire  
Interdisciplinaire de Physique (LIPhy)

Examineur

#### Invitées :

**Camille Migdal**

Cell & Soft





---

## Analyse quantitative des propriétés mécaniques des tissus pulmonaires sains et cancéreux pour la conception de substrats de culture mécano-mimétiques

---

**RESUME :** Les propriétés mécaniques des tissus (animaux et humains) sont de plus en plus reconnues comme des facteurs déterminants dans la progression de nombreuses maladies, y compris le cancer. Par conséquent, les tests *in vitro* réalisés sur des substrats qui imitent les propriétés mécaniques du tissu d'intérêt devraient gagner en pertinence par rapport à ceux effectués sur des plaques de culture en plastique rigide. Cette thèse explore les propriétés mécaniques des tissus pulmonaires normaux et d'adénocarcinomes de 18 patients et conçoit des substrats de culture mécano-mimétiques pour étudier les réponses cellulaires. La microscopie à force atomique est utilisée en indentation pour caractériser la rigidité des tissus à l'échelle microscopique. Une nouvelle méthodologie est développée pour extraire des descripteurs statistiques de la texture de rigidité des tissus. Ces paramètres sont ensuite utilisés pour créer des substrats souples adaptés à la culture cellulaire exhibant une texture de rigidité mimétique des tissus étudiés. De plus, une analyse est menée pour évaluer la corrélation entre la rigidité et la composition tissulaire. Des hydrogels de polyacrylamide à texture de rigidité ont ensuite été fabriqués par photolithographie à niveau de gris, à l'aide de masques qui intègrent les paramètres géométriques de la texture mécanique des tissus et la réponse de la solution photosensible aqueuse de monomères. En outre, la culture de cellules A549 sur des hydrogels mécano-mimétiques fonctionnalisés a révélé l'influence de la texture de rigidité du substrat sur la prolifération et la migration cellulaire. En développant une plateforme mécano-mimétique polyvalente qui imite les microenvironnements mécaniques physiologiques ou pathologiques, cette thèse fournit les bases de nouvelles avancées dans le développement de supports *in vitro* pour la culture cellulaire avec une physiologie améliorée, avec un bénéfice attendu pour l'accélération de la découverte de médicaments pour un large éventail de maladies.

Mot-clés : mechanotransduction, AFM, oncologie, élasticité, pulmonaire, biophysique

---

---

## Quantitative analysis of the mechanical properties of healthy and cancer lung tissue for the design of mechano-mimetic culture substrates

---

**ABSTRACT :** The mechanical properties of (animal and human) tissues are increasingly recognized as driving factors in the progression of many diseases, including cancer. Therefore *in vitro* tests performed on substrates that mimic the mechanical properties of the tissue of interest are expected to gain in relevance over those performed on stiff, plastic culture plates. This thesis investigates the mechanical properties of lung normal and adenocarcinoma tissues from 18 patients and designs mechano-mimetic culture substrates for studying cellular responses. Indentation-type AFM is used to characterize tissue stiffness at the microscale. A novel methodology is developed to extract statistical descriptors of the stiffness texture of the tissues. These parameters are then used to engineer soft substrates suitable for cell culture with mimetic stiffness texture. In addition, an analysis is carried out to assess the correlation between stiffness and tissue composition. Stiffness-textured polyacrylamide hydrogels were then fabricated by gray-level photolithography, using designed masks that either integrate the geometrical parameters of the mechanical texture from the tissues and the response of the aqueous photosensitive solution of monomers. Furthermore, culturing A549 cells on these functionalized mechano-mimetic hydrogels revealed the influence of substrate textured rigidity on cell proliferation and migration. By developing a versatile mechano-mimetic platform that emulates physiological or pathological mechanical microenvironments, this thesis lays the groundwork for new advances in the development of *in vitro* supports for cell culture with enhanced physiology, with an expected benefit for accelerating drug discovery for a wide range of diseases.

**Keywords:** mechanotransduction, AFM, elasticity, pulmonary, oncology, biophysics

---

## ACKNOWLEDGEMENTS

Embarking on this PhD journey has been an extraordinary experience, filled with challenges, discoveries, and moments of profound growth. It is a path that I could not have traversed alone, and this page is dedicated to acknowledging the many individuals and institutions that have contributed to my academic pursuit.

First and foremost, I want to offer my deepest thanks to God, the guiding force behind all of life's endeavors and challenges. His resolute presence has been a source of strength and inspiration throughout this journey. To my beloved wife, Talita Delebosse, I extend my heartfelt gratitude and love. Your sacrifice, support, and enduring faith in me have been the bedrock of this pursuit. You have stood by me, even as we were separated by continents, and your love has been my constant encouragement. To my dear son, Henry, you are a beacon of joy and motivation. Your innocence and happiness have been a constant reminder of what truly matters, especially in the midst of the most rigorous periods of this journey.

To my father, Christian Delebosse, whose unwavering belief in me has been the basis of my quest of knowledge, I express my profound gratitude. And to my mother, Celice Delebosse, and my sisters, Vanessa and Emanuelle, whose constant love and backing have sustained me, I offer my loving thanks.

I extend my sincere gratitude to my thesis Director, Dr. Alice Nicolas, whose wisdom, guidance, and firm support have been instrumental in shaping this research. Your belief in my competences and your passion for exploring the unknown have inspired me to strive for excellence. Special thanks are extended to Dr. Camille Migdal, CEO of Cell&Soft, for the incredible career opportunity, friendship at all times and generous financial support that allowed the completion of this work. Your trust and investment in this project have made this achievement possible. I am also grateful to the members of the jury, Dr. Laurent Malaquin, Dr. Alessandro Furlan, Dr. Charlotte Rivière, Dr. Claude Verdier and Dr. Grégory Chagnon, for promptly accepting to compose my defense jury and their valuable feedback and encouragement.

To David Fuard, whose readiness and desire to help have consistently provided a valuable resource throughout my research. His insights and suggestions to engage intellectually have enriched my understanding when faced with challenging tasks.

To Dr. Cédric Chaveroux, for the guidance and assertiveness during my PhD yearly evaluations.

To Dr. Lara Chalabreysse for the teachings about lung adenocarcinomas, histology and anatomopathology and her sympathy in receiving me at the HCL.

To Rudolf Dreyer and Andrea Visona, who have been more than just colleagues but friends, supporting me both scientifically and personally. Our many enriching conversations have stimulated my thinking, while their camaraderie has added warmth to my experience.

To Celine Hadji, former Cell&Soft R&D Engineer, for our numerous exchanges about the practical aspects of my thesis. Her insights into the hands-on execution of our shared ideas have been precious in shaping my work.

To Michael Betton from LiPhy, for his diligent attention in making sure the AFM was ready and available. His technical expertise and support have ensured that I had the resources I needed when I needed them, allowing my work to progress smoothly.

To the LTM Direction (Laboratoire des Technologies de la Microélectronique) and staff, who spared no effort to guarantee the availability of equipment and facilities. Their commitment and resourcefulness have played a vital role in the successful realization of my experiments. To Clinec Direction (CEA/Léti), for making their facilities available for tissue preparation, histological staining and cell culture experiments.

My heartfelt appreciation goes to my family and friends in Europe and particularly in Brazil, who, though physically distant, have been emotionally close and supportive every step of the way. Your prayers, encouragement, and belief in me have transcended the distance that separate us for all those years. Finally, thank you to all the people who have been involved in this path whose names might have fallen short from my comments. Their interest in my work, insightful critiques, day-to-day encouragement, culinary delights, and invigorating happy hours have not only fueled my enthusiasm but have also made this challenging process a joyful and rewarding experience.

Ultimately, I hope this work becomes a relevant contribution to society, fulfilling my personal dream of advancing science toward a positive direction for the benefit of humanity. May the knowledge and insights garnered here inspire further exploration and innovation, always aiming to enhance the well-being of our global community.

# TABLE OF CONTENTS

1	INTRODUCTION .....	1
1.1	RIGIDITY SENSING AND MECHANOTRANSDUCTION: EXPLORING THE CELLULAR RESPONSE .....	1
1.2	TISSUE MECHANICS .....	3
1.2.1	Mechanics of the ECM proteins .....	4
1.2.2	Cell mechanics.....	8
1.2.3	Cell and ECM mechanics are linked.....	9
1.2.4	Tissue mechanics is multiscaled.....	10
1.3	THESIS CONTEXT.....	12
1.3.1	Lung cancers.....	13
1.3.2	Implication of KRAS mutation.....	15
1.3.3	The expected benefit of using 2D mechano-mimetic culture plates .....	16
1.4	THESIS OBJECTIVES .....	18
1.4.1	Characterization of mechanical properties of healthy and tumor human lung tissues .....	18
1.4.2	Fabrication of a two-dimensional soft culture substrate presenting rigidity textures .....	18
1.4.3	Behavior analysis of tumor cell models on soft culture substrates .....	19
1.5	THESIS ENVIRONMENT .....	19
1.6	OUTLINE OF THE THESIS.....	20
2	CHARACTERIZATION OF MECHANICAL PROPERTIES OF HEALTHY AND TUMOR HUMAN LUNG TISSUE .....	23
2.1	FUNDAMENTAL CONCEPTS .....	24
2.1.1	Atomic Force Microscopy (AFM).....	24
2.1.2	Indentation-Type Atomic Force Microscopy (IT-AFM) .....	25
2.1.3	Contact mechanics on soft biological samples .....	26
2.2	MATERIALS AND METHODS .....	33
2.2.1	Preparation of the tissue sections.....	33
2.2.2	Biomechanical measurements of lung tissues using AFM .....	34
2.2.3	Data processing and analysis .....	34
2.2.4	Data selection for analysis optimization .....	36
2.2.5	Statistical analysis.....	36
2.3	RESULTS .....	37
2.3.1	Histological comparison between healthy and tumor human lung tissues.....	37
2.3.2	Human tumor lung tissue is stiffer than healthy lung tissue .....	38
2.3.3	Both healthy and tumor lung tissues show a predominant linear elastic behavior at the microscale 42	
2.3.4	Importance of considering the adhesive interaction of the tip with the tissue .....	42



2.3.5	Correlation of tissue stiffness with the clinical characteristics of the patients.....	44
2.4	DISCUSSION .....	46
3	STUDY OF STIFFNESS TEXTURES IN TISSUES .....	53
3.1	FUNDAMENTAL CONCEPTS .....	54
3.1.1	Stiffness heterogeneity in biological samples.....	54
3.1.2	Shape descriptors.....	57
3.2	MATERIALS AND METHODS .....	59
3.2.1	Mechanical characterization using AFM with CellHesion Module.....	59
3.2.2	Image processing of rigidity maps.....	60
3.2.3	Statistical Analysis .....	60
3.3	RESULTS .....	61
3.3.1	Comparison of stiffness measurement using the standard piezo scanner and CellHesion.....	61
3.3.3	Analysis of tissue stiffness texture for stiffness heterogeneity pattern design.....	63
3.3.4	Extraction of mask design parameters .....	66
3.4	DISCUSSION .....	68
4	CORRELATION BETWEEN STIFFNESS AND LUNG TISSUE COMPOSITION ...	74
4.1	FUNDAMENTAL CONCEPTS .....	75
4.1.1	Healthy and adenocarcinoma lung tissue composition .....	75
4.1.2	The role of collagen in cell and tissue stiffness .....	76
4.1.3	The role of $\alpha$ -SMA in cell and tissue stiffness.....	78
4.1.4	The role of vimentin in cell and tissue stiffness .....	78
4.2	MATERIALS AND METHODS .....	81
4.2.1	Tissue preparation.....	81
4.2.2	Trichrome Goldner staining.....	81
4.2.3	Immunofluorescence .....	82
4.2.4	AFM measurements.....	83
4.2.5	Image acquisition.....	83
4.2.6	Data and statistical analysis .....	83
4.3	RESULTS .....	84
4.3.1	Correlation between collagen content and tissue stiffness.....	84
4.3.2	Analysis of correlation between stiffness and vimentin .....	85
4.3.3	Analysis of correlation between stiffness and alpha-smooth muscle actin ( $\alpha$ -SMA) .....	86
4.3.4	Correlation between collagen, vimentin, and $\alpha$ -SMA .....	87
4.3.5	Vimentin distribution in A549 cells appears to be similar to that observed in cells present within lung adenocarcinoma tissue .....	88
4.4	DISCUSSION .....	89

5	MIMICKING TISSUE STIFFNESS TEXTURE ON HYDROGEL .....	94
5.1	FUNDAMENTAL CONCEPTS .....	95
5.1.1	Microfabrication techniques .....	95
5.1.2	Hydrogel cross-linking strategies .....	97
5.1.3	Polyacrylamide (PA) hydrogel .....	98
5.1.4	Stiffness pattern hydrogel fabrication techniques .....	101
5.1.5	Hydrogel surface functionalization.....	103
5.1.6	From rigidity maps to mechano-mimetic hydrogels .....	104
5.2	MATERIALS AND METHODS .....	105
5.2.1	Pattern mask design .....	105
5.2.2	Gray-level Mask Fabrication .....	106
5.2.3	Fabrication of stiffness-patterned polyacrylamide hydrogel .....	108
5.2.4	Mechanical characterization of the hydrogel and stiffness patterns .....	109
5.2.5	Surface functionalization of stiffness-patterned hydrogels.....	110
5.3	RESULTS .....	113
5.3.1	Random circle pattern design generation.....	113
5.3.2	Random circle pattern mask fabrication .....	114
5.3.3	Optimization of mask design and hydrogel fabrication parameters.....	116
5.3.4	Micron-scaled random circle patterns geometry and rigidity on polyacrylamide hydrogels .....	120
5.3.5	Stiffness distribution of polyacrylamide hydrogel and compared to tumor stiffness distribution	122
5.3.6	Fine-tuned surface functionalization .....	125
5.4	DISCUSSION .....	128
6	CELL CULTURE ON MECHANO-MIMETIC HYDROGELS .....	134
6.1	FUNDAMENTAL CONCEPTS .....	135
6.1.1	Cells respond to rigidity .....	135
6.1.2	Chemical patterning of the substrate influences cell behavior.....	135
6.1.3	Stiffness patterning also impacts cell behavior.....	137
6.1.4	Characterization of cell motility by Mean Square Displacement and Velocity autocorrelation function	138
6.2	MATERIALS AND METHODS .....	141
6.2.1	Fabrication of stiffness-patterned polyacrylamide hydrogel .....	141
6.2.2	Calibration of the surface density of the protein coatings .....	141
6.2.3	Surface functionalization of the hydrogels .....	142
6.2.4	Cell culture and seeding .....	143
6.2.5	Image acquisition.....	143
6.2.6	Image analysis .....	144
6.2.7	Particle Image Velocimetry and Correlation length .....	144
6.3	RESULTS .....	146

6.3.1	Initial cells spreading is higher on uniform hydrogel than on patterned hydrogel.....	146
6.3.2	Subconfluent cells move with a lower velocity on patterned hydrogel .....	147
6.3.3	Analysis of the diffusive behavior of cells on both hydrogels.....	149
6.3.4	Measure of the dynamics of cell growth at subconfluency.....	149
6.3.5	Cell density at confluency is higher in RCP hydrogel resulting in lower mean cell size.....	151
6.3.6	Analysis of cell movement at confluency.....	151
6.4	DISCUSSION .....	154
7	CONCLUSIONS .....	160
8	PERSPECTIVES .....	164
	BIBLIOGRAPHY .....	169
	APPENDIX A .....	187

## LIST OF ACRONYMS

ACTA2 – Actin, Alpha 2, Smooth Muscle, Aorta	HCL – Hydrochloric Acid
AFM – Atomic Force Microscopy	HDAC – Histone Deacetylase
AKT – Protein Kinase B	HPV – Human Papillomavirus
AMP – Adenosine Monophosphate	HUVE – Human Umbilical Vein Endothelial (cells)
AMPK – AMP-Activated Protein Kinase	IF – Immunofluorescence
ANOVA – Analysis of Variance	IT – Information Technology
$\alpha$ -SMA – Alpha Smooth Muscle Actin	JKR – Johnson-Kendall-Roberts
BSA – Bovine Serum Albumin	KRAS – A gene that may mutate in various cancers
CEA – Commissariat à l'Énergie Atomique et aux Énergies Alternatives	LOX – Lysyl Oxidase
CI – Confidence Interval	LTM – Laboratoire des Technologies de la Microélectronique
CLARA – Cancéropôle Lyon Auvergne Rhône-Alpes	MAPK – Mitogen-Activated Protein Kinase
CMOS – Complementary Metal-Oxide-Semiconductor	MBE – Molecular Beam Epitaxy
COPD – Chronic Obstructive Pulmonary Disease	MD – Maugis-Dugdale
COS – Carpick-Ogletree-Salmeron	MDA-MB – A classification for human breast cancer cell lines
CRCL – Cancer Research Center of Lyon	MDPI – Multidisciplinary Digital Publishing Institute
DAPI – 4',6-Diamidino-2-Phenylindole	MEMS – Microelectromechanical Systems
DI – Deionized (water)	MSC – Mesenchymal Stem Cells
DMEM – Dulbecco's Modified Eagle Medium	MSD – Mean Squared Displacement
DMT – Derjaguin-Muller-Toporov	MT - Microtubules
DNA – Deoxyribonucleic Acid	MWU – Mann-Whitney U Test
ECM – Extracellular Matrix	NA – Numerical Aperture or Not Applicable
EDTA – Ethylenediaminetetraacetic Acid	NHS – N-Hydroxysuccinimide
EGF – Epidermal Growth Factor	NIL – Nanoimprint Lithography
EGFR – Epidermal Growth Factor Receptor	NSCLC – Non-Small Cell Lung Cancer
EUVL – Extreme Ultraviolet Lithography	OCT – Optimal cutting temperature compound
FAK – Focal Adhesion Kinase	PA – Polyacrylamide
FBS – Fetal Bovine Serum	PBS – Phosphate-Buffered Saline
FD – Force-Distance	PDZ – Post-Synaptic Density Protein (PSD95), Drosophila Disc Large Tumor Suppressor (Dlg1), Zonula Occludens-1 Protein (zo-1)
FFT – Fast Fourier Transform	PEG – Polyethylene Glycol
FN – Fibronectin	PFA – Paraformaldehyde
GFP – Green Fluorescent Protein	PI – Propidium Iodide or Principal Investigator
GSD – Geometric Standard Deviation	PIFOC – Piezo Focus Device
GTP – Guanosine Triphosphate	
HA – Hyaluronic Acid	

PIV – Particle Image Velocimetry  
PT – Pietrement-Troyon  
PTEN – Phosphatase and Tensin Homolog  
PVD – Physical Vapor Deposition  
PZT – Lead Zirconate Titanate  
RAS – Rat Sarcoma (a family of related proteins)  
RCP – Random Circle Pattern  
RGB – Red, Green, Blue  
ROCK – Rho-Associated Protein Kinase  
ROI – Region of Interest  
SANPAH – N-Succinimidyl-6-(4'-Azido-2'-Nitrophenylamino)Hexanoate  
SCLC – Small Cell Lung Cancer  
SD – Standard Deviation  
SDA – Sodium Dodecyl Sulfate  
SE – Standard Error  
SORT – Surface Over the Rigidity Threshold  
STAT – Signal Transducer and Activator of Transcription  
TAZ – Transcriptional Coactivator with PDZ-Binding Motif  
TGF – Transforming Growth Factor  
UGA – Université Grenoble Alpes  
UV – Ultraviolet  
VEGF – Vascular Endothelial Growth Factor  
 $V_{RCP}$  – Cell velocity in random circle pattern hydrogel  
 $V_u$  – Cell velocity in uniform hydrogel  
VWC – von Willebrand Factor C  
YAP – Yes-Associated Protein  
ZL – z-length (specific length measurement)

## LIST OF FIGURES

Figure 1.1 – Fibroblast cell deforming a thin-silicone sheet [3].	1
Figure 1.2 – Schematic illustration from [5] representing the sequential link between the extracellular matrix, integrins, mechanosensitive adaptor proteins, and actin. The application of force by myosin on actin filaments initiates a domino effect of force transmission across various elements. This results in the alteration of conformations in adaptor proteins and influences the unbinding events.	2
Figure 1.3 – Human mesenchymal stem cells (MSCs) cultured on increasingly stiff 2D substrates display increasing spread area [10]. Scale bar, 50 $\mu\text{m}$ .	2
Figure 1.4 – Human MSCs exhibit enhanced spreading on stiffer substrates, yet on laminin-coated hydrogels, they appear smaller than on other ECM protein coatings [10]. Bar, 50 $\mu\text{m}$ .	3
Figure 1.5 – The complex domain structures of representative ECM proteins. (a) Fibronectin, encoded by a single gene, undergoes alternative splicing to produce different proteins, and it interacts with integrins and proangiogenic growth factors. (b) Fibrillin-1, carrying EGF-like domains along with unique TB (TGF $\beta$ -binding) and hybrid domains, shows interaction with other matrix proteins and growth factors. (c) LTBP-1, a member of a four-gene family structurally related to fibrillins, exhibits binding sites for TGF- $\beta$ /LAP latent complex, fibrillin, and Fibronectin. (d) Thrombospondin-1 (TSP-1) stands out with its unique structure and antiangiogenic activity. These detailed domain structures illustrate the intricate roles of ECM proteins in cellular activities and tissue dynamics [16].	4
Figure 1.6 – Fibronectin (FN) interacts with cells through multiple domains. FN binds to integrins, other ECM proteins, and growth factors, localizing these signals at the cellular level. The close arrangement of the domains in FN brings different receptors together, enabling complex, integrated signaling to the cell. This model suggests that FN and its associated ECM proteins orchestrate these signals, playing a crucial role in processes like angiogenesis. The presence of alternatively spliced domains in FN introduces additional complexity to these interactions [16].	5
Figure 1.7 – Measurement of dynamic shear storage moduli ( $G'/G''$ ) at varying strain amplitudes ( $\gamma$ ) for a range of crosslinked biopolymer networks.	7
Figure 1.8 – Schematic diagram highlighting the three key cytoskeletal filaments - actin filaments, intermediate filaments, and microtubules, which, along with molecular motors, constitute the mechanical framework of the cell [40].	8
Figure 1.9 – Diagram illustrating how disease alters the ECM and thus tissue mechanics [69].	11
Figure 1.10 – Incidences of non-small cell lung cancers as compared to small cell lung cancer. Compiled from [95].	14
Figure 1.11 – Schematic representation of the KRAS pathways with various target inhibitors. The top section of the figure depicts the activation process of KRAS. KRAS gets activated upon interaction with GEF, binding to GTP, which represents its active state. The role of GAP in this sequence, which includes the release of a phosphate group, consequently, leads to the inactivation of KRAS. The right segment of the figure showcases a condition resultant from tumorigenesis where GAP is inhibited, causing a continuous activation state of KRAS. As a consequence of this persistent KRAS activation, a series of intracellular pathways are stimulated, culminating in cellular proliferation, differentiation, and survival mechanisms [112].	15

Figure 1.12 – (a) AFM measurements on human healthy and tumor lung tissue using a spherical tip to probe the rigidity at the micron scale. (b) Treated data translated to hundreds of 2D rigidity maps. (c) Statistical representation of the rigidity distribution of healthy or tumor lung tissue. ....	18
Figure 1.13 – (a) Fabrication of engineered hydrophobic gray level mask using contact optical lithography processes. (b) UV A illumination at a specific time to print a heterogeneous rigidity pattern onto the polyacrylamide hydrogel. (c) Polyacrylamide hydrogel with representative rigidity pattern at the $\mu\text{m}$ scale of healthy and tumor human lung tissue. ....	18
Figure 2.1 – A schematic illustration of the AFM working principle illustrates the key components and the fundamental mechanism of an atomic force microscope (Adapted from Müller et al. [138]). The interaction between the sharp tip and the sample surface results in cantilever deflection, which is monitored by the position-sensitive photodiode. The feedback mechanism and piezo scanner work together to maintain optimal tip-sample interaction, enabling high-resolution imaging and force measurements at the piconewton range. ....	24
Figure 2.2 – In IT-AFM, a tip (e.g., colloidal probe) is used to indent and retract from a sample, enabling the measurement of local interactions and properties of the material (Left). The typical force-indentation curve (Right), also known as force-distance (FD) curve in literature, is characterized by the approach (blue) and retraction (red) curve, which describes the relationship between the force exerted by the cantilever and the indentation depth on the sample surface during measurement. (Adapted from [142]). ....	26
Figure 2.3 – Diagram of force-distance curves according to the Hertzian, DMT, JKR, and MD theories. Force-distance curves are displayed for the approach segment of the cycle. (Adapted from [146]) ....	28
Figure 2.4 – On the left, the plot of the raw force-distance curve; on the middle, the linearization of the FD curve to select and fit the linear region; on the right, the original force-distance curve fitted for Hertz, DMT and JKR. In this example, using the Hertz model yielded a stiffness of 1.90 kPa, whereas DMT/JKR 1.52 kPa. ....	30
Figure 2.5 – Adhesion map for a spherical probe. The dimensionless load and the Tabor parameter $\mu$ indicate the most appropriate model. $F$ represents the normal indentation force. Adapted from [157]. ....	32
Figure 2.6 – Example of the original curve, linear region fit on $F^{2/3}$ , model fit of rejected (a) and selected curve (b) with determination of contact point <sup>[77]</sup> and indentation values of the linear region. ....	35
Figure 2.7 – Toluidine blue-stained tissue sections of paired biopsies. (a-b) Healthy and acinar adenocarcinoma tissues from patient 14EX00110. (c-d) Healthy and solid adenocarcinoma tissues from patient 13EX00166. Bars, 100 $\mu\text{m}$ . ....	37
Figure 2.8 – Healthy and adenocarcinoma lung tissue stiffness distributions of 15EH04592 (acinar) and 13EX00166 (solid). Histograms are fitted for a lognormal distribution. The blue dotted lines represent the median and the red dashed lines the geometric mean of the distribution. Values are reported in Table 2.2. ....	40
Figure 2.9 – (a) Healthy and tumor lung tissue stiffness distributions of the cohort; **** $p < 0.0001$ ; (b) Box scatter plot of healthy and tumor tissue median stiffnesses. ....	41
Figure 2.10 – Acinar (Left) and solid (Right) x healthy lung tissue stiffness distributions; ** $p \leq 0.01$ . ....	41
Figure 2.11– Comparative box plots illustrating the distribution of stiffness values. (a) Stiffness values are grouped by gender, with female (F) and male (M) samples shown side by side, highlighting the similarities in stiffness distributions between the two groups. (b) Stiffness values are categorized by cancer stage (1, 2, and 3), illustrating the distribution of stiffness within each stage and enabling a visual comparison of the medians and interquartile ranges across stages. (c) Scatter plots and linear regression lines for healthy and tumor tissue stiffness as a function	

of age. (Left) Healthy tissue stiffness (blue circles) plotted against age and (Right) tumor tissue stiffness (red circles) plotted against age with their respective mean stiffness values (black dashed line). .....	45
Figure 3.1 – Different modes of AFM force map acquisition <b>(a)</b> Single-frequency <b>(b)</b> Position-dependent ..... <b>(c)</b> Frequency sweep <b>(d)</b> Time-dependent. Adapted from Krieg et al. [142].....	54
Figure 3.2 – <b>(a)</b> REF-52 myofibroblasts focal adhesions stained for vinculin (green), $\alpha$ -SMA (blue), and F-actin (phalloidin; red) after standard fixation [200] Bar: 20 $\mu$ m). <b>(b)</b> Schematic representation of the main mechanosensing players involved in cell-ECM interaction at the focal adhesion (FA) site. Alterations in tension, stiffness, or other mechanical stimuli in the extracellular environment are detected by clusters of integrins, which respond by changing their morphology or distribution, and this in turn recruits focal adhesion kinases (FAK) [199]. <b>(c)</b> Focal adhesion size as a function of substrate stiffness [200]. .....	55
Figure 3.3 – Example of AFM rigidity maps of cervix healthy tissues (left) and tumor tissue (right) showing more heterogeneity in tumor tissue. Adapted from Fuhs et al. [205]. .....	56
Figure 3.4 – Example of rigidity map (left) and binarized map after applying an arbitrary rigidity threshold. ....	58
Figure 3.5 – <b>(a)</b> Hydrogel stiffness as a function of indenter type and piezo size at different UV illumination times with fixed set-point force at 4 nN, retract speed at 2 $\mu$ m/s and z-length at 4 $\mu$ m. <b>(b)</b> Comparison between measurements made with 4 and 30 $\mu$ m retract z-length. Values are represented as mean $\pm$ SEM. ....	61
Figure 3.6 – Example of rigidity map from acinar adenocarcinoma and healthy lung of patient 16EH07456. <b>(a,d)</b> Reference Toluidine-blue stained sections (Bars: 500 $\mu$ m). <b>(b,e)</b> Bright field optical images zoomed at the tumor region and healthy region, respectively (Bars: 50 $\mu$ m). <b>(c,f)</b> Rigidity maps (100x100 $\mu$ m <sup>2</sup> , 10x10 pixels) with 85% and 75% of the curves exploitable, respectively.....	62
Figure 3.7 – Example of rigidity map from solid adenocarcinoma and healthy lung and of patient 13EX00166. <b>(a,d)</b> Reference Toluidine-blue stained sections (bars: 500 $\mu$ m). <b>(b,e)</b> Bright field optical images zoomed at the tumor region and healthy region, respectively (bars: 50 $\mu$ m). <b>(c,f)</b> Rigidity maps (100x100 $\mu$ m <sup>2</sup> , 10x10 pixels) with 89% and 90% of the curves exploitable, respectively. ....	63
Figure 3.8 – Conversion of a rigidity map <b>(a)</b> into a binary mask <b>(b)</b> applying a 2.9 kPa rigidity threshold.....	64
Figure 3.9 – Distribution of pattern areas above the rigidity threshold for healthy and tumor tissues. ....	64
Figure 3.10 – % of surface over the rigidity threshold (% SORT) per patient. ....	65
Figure 3.11 – Average shape considering the shape descriptors for healthy and tumor tissues with Aspect Ratio = 1.73, Circularity = 0.58 and Solidity = 0.90, 1 pixel = 1.0851 $\mu$ m.....	66
Figure 4.1 – Pathological transformations within the lung's interstitial extracellular matrix (ECM) in healthy and cancerous conditions. <b>(a)</b> General view of the lung, highlighting the parenchyma on healthy and cancer locations. <b>(b)</b> The integrity of a healthy interstitial ECM, which is a flexible network of collagens, elastin, and fibronectin, tethered to the basal membrane of the epithelial cell layer, is upheld by the activity of resident fibroblasts. <b>(c)</b> In the context of cancer, primary and metastatic tumors are encapsulated by a dense, rigid stroma, rich in highly crosslinked collagens, along with amplified levels of fibronectin, tenascin C, and hyaluronan. <b>(d)</b> Legend with components present on both conditions. Adapted from [34]. .....	75
Figure 4.2 – Impact of matrix rigidity on the Young's modulus of cells. <b>(a)</b> FBs and CAFs using optical microscopy, grown on collagen substrates of varying concentrations, <b>(b)</b> Relative Young's modulus of the substrate, and <b>(c)</b> AFM-measured Young's modulus of live cells [235]. .....	77



Figure 4.3 – SV40T induces increased cell stiffness via HDAC6. <b>(a)</b> Force curves acquired on BJhTERT cells (black), BJhTERT+SV40T cells (light gray), and BJhTERT+SV40T cells treated with tubacin (dark gray). <b>(b)</b> Quantification of cells stiffnesses at 30 nN load. <b>(c)</b> Representative BJhTERT+SV40T cells treated with DMSO and tubacin analyzed for organization of vimentin intermediate filaments. Black and white images show vimentin and merged images show vimentin (green) and F-actin (red). <b>(d)</b> Quantification of the collapse of the vimentin IF network in cells [253].	79
Figure 4.4 – Schematic of the cellular orientation of tubulin (green), actin (red), and focal adhesion (light orange) in cells positive and negative for vimentin (dark orange). In vimentin-positive cells, microtubules are located near the cell nucleus, with actin forming stress fibers at the cell base, indicating EMT-related protein expression. When vimentin is depleted, microtubules disperse, and actin forms spike-like structures at the cell edges, along with cell membrane extension. This also reduces focal adhesion. These changes weaken the cells and affect their directional movement, showing the role of vimentin in EMT-related mechanoregulation and cancer progression. From [254].	80
Figure 4.5 – Schematic depicting the positions of the sections in the biopsy and the varying section cut thicknesses utilized for different procedures such as toluidine blue staining, trichrome Goldner, immunohistofluorescence, and AFM, from the left to right. The table shows the number of maps analyzed with AFM. T1 and T2 denote 2 ensembles of sections performed at 2 different altitudes in the biopsies.	81
Figure 4.6 – Collagen intensity as a function of stiffness for both tumor subtypes.	84
Figure 4.7 – Vimentin intensity as function of stiffness for both tumor subtypes.	86
Figure 4.8 – $\alpha$ -SMA intensity as function of stiffness for both tumor subtypes.	87
Figure 4.9 – Correlation analysis of vimentin, $\alpha$ -SMA, and collagen contents. <b>(a)</b> Scatterplot showing the correlation between vimentin and $\alpha$ -SMA ( $\rho = 0.66$ ; $p = 0.038$ ). <b>(b)</b> Scatterplot showing the correlation between vimentin and collagen ( $\rho = 0.32$ ; $p = 0.37$ ). <b>(c)</b> Scatterplot showing the correlation between $\alpha$ -SMA and collagen. ( $\rho = 0.64$ ; $p = 0.048$ ).	88
Figure 4.10 – Comparative analysis of vimentin in A549 cells and lung adenocarcinoma tissue: The figure depicts the relative expression of vimentin, a type III intermediate filament protein, in A549 lung carcinoma cells and tissue samples from patients with lung adenocarcinoma. <b>(a)</b> shows immunofluorescence staining of vimentin (red) in A549 cells, while <b>(b)</b> presents similar staining in lung adenocarcinoma tissue, potentially presenting a mesenchymal state. Bars in 50 $\mu\text{m}$ .	89
Figure 5.1 – Schematic of substrate exposure using a mask.	96
Figure 5.2 – Graphic representation from [299] of the combination of an elastic polyacrylamide network with a viscous solution of linear polyacrylamide, resulting in the formation of a viscoelastic gel. The entrapment of linear chains within the network is responsible for generating the viscoelastic properties of the hydrogel, highlighting the non-viscous nature of polyacrylamide.	100
Figure 5.3 – Different fabrication techniques to engineer hydrogels with stiffness patterns and structures. <b>(a)</b> Microfluidics, <b>(b)</b> Stereolithography, <b>(c)</b> Micropillars, <b>(d)</b> Photodegradation and <b>(e)</b> Photopolymerization.	102
Figure 5.4 – Roadmap for developing mechano-mimetic hydrogels, going AFM characterization of lung tissue to mechano-mimetic hydrogel.	104
Figure 5.5– <b>(a)</b> Generated random circle radii gaussian distribution with 10000 values center at $M = 2.27$ and $\sigma = 0.61$ , corresponding to natural logarithm of the geometric mean of the rigidity pattern radii distribution. <b>(b)</b>	

Exponential of the gaussian distribution with geometric mean = 9.7 $\mu\text{m}$ , hence the radii log-normal distribution from where random radii will be selected. ....	105
Figure 5.6 – Mask fabrication processing steps. From left to right: Ti+Cr layer is deposited, positive resin is spin-coated, soft-baked for 50 s at 100 °C , then pattern is transferred using SmartPrint UV, next development using AZ400K for 18 to 20 s, finally removing resin with acetone. ....	108
Figure 5.7 – (a) Structure of the heterobifunctional sulfo-LC-SDA. (b) NHS-ester diazirine crosslinking mechanism involves NHS esters reacting with primary amine groups (-NH <sub>2</sub> ) within pH 7-9 buffers, forming stable amide bonds and releasing NHS. Photoactivation of diazirines with long-wave UV light (330-370 nm) results in reactive carbene intermediates [313]. ....	110
Figure 5.8 – Schematic representation of the different protocols employed for surface functionalization of the hydrogel. Each protocol is characterized by a unique sequence of steps, including immersion in sulfo-LC-SDA, UV exposure, and dehydration steps. ....	111
Figure 5.9 – Random circle pattern generated using a custom-made algorithm implemented in MATLAB. ....	114
Figure 5.10 – (Left) Random circle pattern design template. (Right) Example of a fabricated gray-level mask with random circle patterns after chromium etching. ....	115
Figure 5.11 – Stiffness distribution of 12s60% hydrogels fabricated with (a) 15 nm and (b) 18 nm of chromium gray-level mask. ....	116
Figure 5.12 – Comparison between (a) the optimized gray-level mask and (b) the hydrogel obtained with 18s UV exposure at 4.8 mW/cm <sup>2</sup> (18s30%). Bars: 100 $\mu\text{m}$ . ....	118
Figure 5.13 – Comparative analysis of circle size distributions across the optimized design, gray-level mask, and the fabricated hydrogel for 18s30%. A slight shift in the distribution is noted between stages, underscoring the variations that occur throughout the fabrication process. ....	118
Figure 5.14 – Optimization of hydrogel fabrication parameters. Median stiffness of the gel as a function of the surface energy transmitted for reticulation. The optimal combination of illumination time 18s and 30% of maximal lamp intensity (4.8 mW/cm <sup>2</sup> ) represented by the blue triangle marker was determined based on the closest match to the median stiffness of the tumor distribution. ....	119
Figure 5.15 – (a) Stiffness x Radius of 18s 30% hydrogel n=60 circles , (b) Stiffness x Radius 22s 30% hydrogel n=72 circles. ....	120
Figure 5.16 – AFM acquired rigidity maps showing the stiffness variation within the 18s30% polyacrylamide hydrogel. (a) It clearly indicates that the smaller circles present a lower stiffness as compared to their larger counterparts, illustrating the relationship between pattern size and mechanical properties within the hydrogel structure. (b) Stiffness variation across a large circle pattern. ....	121
Figure 5.17 – Boxplots with detailed mechanical characterization of a hydrogel 18s30%. Each boxplot represents the distribution of datapoints for soft background (n=203), rigid circles (n=100), and overall random regions (n=2652) within the hydrogel. Overall datapoints obtained from rigidity maps with dimensions of 100x100 $\mu\text{m}$ , in resolutions of 20x20 and 25x25 pixels. The comparison is made with a similar dataset from tumor tissue consisting of 2151 datapoints. ....	121
Figure 5.18 – Comparative AFM characterization of hydrogels polymerized under different conditions. (a) Phase image captured at 20x magnification of a hydrogel exposed at 9s 100% intensity, illustrating the random pattern across the hydrogel. (b) Corresponding stiffness distribution derived from the hydrogel in (a), demonstrating the	

unsought range of mechanical properties. (c) Phase image captured at 20x magnification of a hydrogel exposed at 18s30% intensity. (d) Corresponding stiffness distribution, demonstrating the achieved replication of tumor-like mechanical heterogeneity in the hydrogel, as a result of fine-tuning the fabrication parameters. ....	123
Figure 5.19 – (a) Post sulfo-LC-SDA grafting, the hydrogel illuminated for 30s at 30% UV showed no fractures. (b) Following collagen, I deposition, fractures were observed on the same sample. (c) Fractures were evident with GFP-labeled fibrinogen functionalization at 1 $\mu\text{g}/\text{cm}^2$ . (d) A549 cells seeded on the hydrogel (b) adhered and aligned along the fractures, where collagen I was abundant. Magnification: at 20x, Bars: 100 $\mu\text{m}$ . ....	126
Figure 5.20 – Different surface functionalization protocols on 22s30% hydrogels with GFP labeled fibrinogen. (a) Uniformly functionalized hydrogel achieved via sulfo-LC-SDA dehydration, immediate UV exposure, and protein deposition. (b) Overfunctionalization of the hydrogel background. (c) Overfunctionalization of the stiff patterns with fractures due to prolonged sulfo-LC-SDA dehydration and protein drying. (d) Optimized protocol outcome showcasing successful overfunctionalization with 200 $\mu\text{g}/\text{ml}$ fibrinogen and fracture prevention. The bright dots are aggregates of fibrinogen coming from inappropriate storage conditions. ....	127
Figure 6.1 – The diffusional behavior can be classified based on the time-dependent properties of the Mean Squared Displacement (MSD). Adapted from de Bruin et al. [336].....	139
Figure 6.2 – Stiffness distribution of 22s30% polyacrylamide hydrogel. ....	141
Figure 6.3 – Mean intensity of fibrinogen at varying concentrations. 200 $\mu\text{g}/\text{ml}$ fibrinogen concentration present similar fluorescence compared to 1 $\mu\text{g}/\text{cm}^2$ fibrinogen. ....	142
Figure 6.4 – Comparative analysis of cell morphology and distribution on unpatterned (left) and patterned (right) hydrogels. Both images were captured 4 hours post-seeding, at the same magnification (20x), and are representative of the typical cell morphology and distribution observed in each condition. Bars: 100 $\mu\text{m}$ . Differences in cell distribution, size, and shape between the two conditions can be visually noted, underscoring the effect of micrometer-sized stiffness texture on cellular behavior. ....	146
Figure 6.5 – Superimposed cell trajectories on microscopy images of unpatterned (left) and patterned (right) hydrogels. Images are shown at the final time. Each trajectory is depicted as a blue line showing the path taken by a single cell during a 10-hour period . The starting point of each trajectory is marked in green, and the ending point is marked in red. Yellow arrows indicate the direction of movement along each trajectory and yellow circles shows the circle patterns. Bars: 100 $\mu\text{m}$ . ....	148
Figure 6.6 – (a) Mean cell step and (b) mean cell velocities with their respective standard deviations on uniform and patterned (RCP) hydrogels after 10-hours of culture. ....	148
Figure 6.7 – Comparative analysis of cell mean square displacement (MSD) on unpatterned (a) and patterned (b) hydrogels. Each point on the graph represents the average MSD for 5 cells.....	149
Figure 6.8 – Temporal progression of cell confluency on uniform (a) and patterned (RCP) (b) hydrogels. Red and blue curves show the confluency index of two positions in the culture plate.....	149
Figure 6.9 – Cell density and mean size at confluency on uniform and patterned (RCP) hydrogels: (a) Comparison of cell density, (b) Comparison of average cell size. Mean values are derived from three distinct positions for each hydrogel type, with error bars indicating standard deviation. ....	151
Figure 6.10 – Velocity autocorrelation function (VACF) and fits for cells on uniform and patterned (RCP) hydrogels. VACF for three different positions, represented by bright blue, blue and red, respectively are shown. (a) The VACF are fitted by an exponential decay $e - x\xi$ (dashed lines). The inset on the right shows a zoomed-in	

view of the initial region, which illustrates the divergence of the experimental data from the expected exponential decay. (b) Fit by a faster decaying function  $1 + x\xi - a$  (dashed lines). The dotted lines represent the fitted function, which provides a better representation of the observed decay in the correlation function compared to the exponential fit. The inset shows a close-up view of the initial region, which emphasizes the characteristic length ( $\xi$ ) and its differences between cells cultured on uniform and RCP hydrogels. .... 152

Figure 6.11 – Computed (a) Mean decay exponent  $a$  and (b) Mean characteristic lengths  $\xi$  obtained from the average autocorrelation function fits of the three positions for cells cultured uniform and patterned (RCP) hydrogels with their respective standard errors. .... 152

Figure 6.12 – Mean velocity magnitudes of cells cultured on uniform and patterned (RCP) hydrogels. (a) The plot displays the computed velocity magnitudes at 3 positions for both types of hydrogels. (b) Mean velocity magnitudes of cells cultured on uniform and RCP hydrogels, with their respective standard error. (c) Comparison of velocity magnitude presenting statistically significant difference with  $p < 0.001$ . .... 153

Figure 8.1 – (a) HBECs grown on uniformly soft substrates accumulate in S phase, meaning that the translational program is partly halted. (b) Cell passages limit the differentiation capabilities of HBECs in an alveolar tissue when they are grown on plastic but not on a uniformly soft substrate. Hematoxylin & Eosin staining. .... 165

Figure 8.2 – (a) Phase contrast micrograph of a REF52 cell on a rigidity-patterned matrix. (b) Paxillin, a protein involved in focal adhesion and cell signaling, shows primary accumulation on the stiffer 'dots' of the matrix. (c) Mapping of the traction stresses generated by the cell. The periodic distribution of stress magnitudes, indicated by the autocorrelation function, aligns with the patterned rigidity of the matrix. (d) Overlay of stress magnitude (white) and paxillin staining (green), revealing a colocalization at regions of high stress and paxillin concentration. (e) A graphical representation of the stress amplitude across the cell. The stress is significantly larger on the stiffer dots as compared to the softer background, indicating an adaptive cellular response to substrate rigidity. (f) Scatter plot showing a linear correlation between average cell-generated traction stresses and the local Young's modulus of the hydrogel, indicating the mechanosensitive nature of cell-substrate interactions. Different pairs of rigidity are marked with unique symbols. Error bars represent the standard error of the mean. Image from [220]. .... 166

Figure 8.3 – (a) Quantification of intracellular YAP activation in hMSCs on regular and randomly patterned hydrogels. A sigmoidal increase in YAP activation occurs in regular patterns with a significant jump between 25% and 50% stiffness. This effect is absent on random patterns. (b) Cell spreading area on regularly and randomly patterned hydrogels. Consistent with YAP activation, spreading increases with stiffness on regular patterns, but is insensitive to stiffness changes on random patterns. (c) Cellular circularity decreases relative to stiffness on regular patterns, with no significant change observed on random patterns. Adapted from [227]. .... 167

Figure 8.4 – Perspectives inputs and outputs scheme. Outputs inside the box. Genetic profile and phenotype stability will be performed by CRCL and will serve as input to for data correlations. .... 167

## LIST OF TABLES

Table 2.1 – Summary of pre- and post-processing of force-distance curves.....	38
Table 2.2 – Median Young’s moduli, dispersion, multiplicative standard deviation (SD), and number of curves (n) processed using JKR model.....	39
Table 2.3 – Young’s moduli, characteristic length and interfacial energies of healthy and tumor lung tissues obtained from the fits by Hertz, JKR and DMT models, and the intervals that account for 68.3% of the measurements. ....	42
Table 2.4 – Tabor parameter $\mu$ for DMT and JKR analysis, for $z_0$ ranging from 100 to 400 nm. ....	43
Table 2.5 – Young’s moduli, characteristic length and interfacial energies for acinar and solid adenocarcinomas obtained from the fits by Hertz, JKR and DMT models, and the intervals that account for 68.3% of the measurements. ....	44
Table 2.6 – Clinical characteristics of a cohort of 18 patients. ....	44
Table 3.1 – Basic shape descriptors definitions and their corresponding formula. ....	58
Table 3.2 – Summary statistics of analyzed rigidity maps with surface coverage or % of surface over the rigidity threshold (%SORT), geometric means of rigidity pattern areas, and basic shape descriptors. ....	65
Table 3.3 – Circular pattern design parameters obeying the lognormal distribution as the patterns measured on patient tissues. ....	67
Table 5.1 – Advantages and disadvantages of polymer precursors used for hydrogel synthesis. Adapted from Tenje et al. [296] .....	99
Table 5.2 – Input parameters from rigidity patterns and resulting design parameters. ....	113
Table 5.3 – Circle size analysis of Figure 5.9 representing the random circle pattern design and the fabricated mask without optimization. Values are in micrometers. ....	115
Table 5.4 – Comparison of parameters across different stages of pattern mask design and hydrogel fabrication. ....	117
Table 6.1– Comparison of cell count, total area, mean area, and percentage surface coverage between unpatterned (uniform) and patterned (RCP) hydrogels. Mean value presented is accompanied by the corresponding standard deviation.....	147
Table 6.2 – Quantitative analysis of cell growth dynamics at subconfluency on different hydrogel positions and hours. ....	150
Table 6.3 – Mean fitting parameters for the velocity autocorrelation function for cells cultured on uniform and RCP hydrogels.....	153

# CHAPTER 1

---

## INTRODUCTION

# 1 INTRODUCTION

## 1.1 RIGIDITY SENSING AND MECHANOTRANSDUCTION: EXPLORING THE CELLULAR RESPONSE

The ability of cells to sense and respond to mechanical cues, such as substrate rigidity, is an essential aspect of cell function. This process, referred to as mechanotransduction, involves a complex array of cellular components and has been the focus of extensive research over the past decade [1],[2]. From the historical work conducted by Harris et al. [3] in 1981, it was demonstrated that cells are not only responsive to chemical signals but also to physical forces in their environment. In this experiment, fibroblastic cells were seeded on thin cross-linked silicone sheets floating on uncross-linked silicone. Small wave-like patterns observed on the silicone surface demonstrated the cell's ability to deform its substrate (Figure 1.1). This pioneering work introduced the concept that substrate rigidity could influence cellular behavior, a hypothesis that has been extensively validated and elaborated upon in subsequent studies.

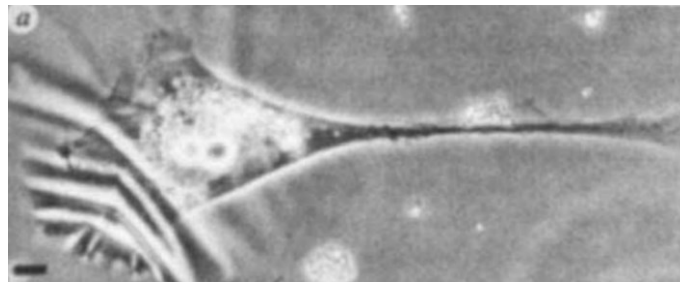


Figure 1.1 – Fibroblast cell deforming a thin-silicone sheet [3].

At the molecular level, rigidity sensing is primarily mediated by integrins, a type of cell surface receptor that forms connections between the extracellular matrix (ECM) and the cell's internal cytoskeleton. Upon binding to ECM proteins, the transmembrane protein integrin triggers a cascade of intracellular events that culminate in changes in cell behavior. More specifically, this molecular mechanism of cell-matrix adhesion mechanosensitivity first involves the activation of integrins (Figure 1.2). Integrins can exist in different conformations, and mechanical force can induce changes in their conformation, leading to their activation and the recruitment of adaptor proteins such as talin and vinculin. These adaptor proteins can then interact with actin filaments and other cytoskeletal components to transmit the mechanical force into the cell, leading to downstream signaling events that can affect cell behavior and function [4], [5]. For instance, molecular mechanisms such as the regulation of protein phosphorylation and gene expression adapt to the stiffness of the support or the presence of external forces [6].

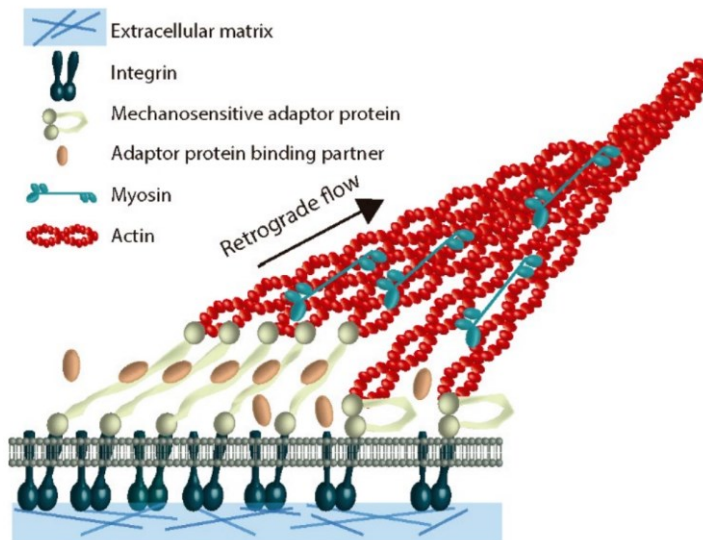


Figure 1.2 – Schematic illustration from [5] representing the sequential link between the extracellular matrix, integrins, mechanosensitive adaptor proteins, and actin. The application of force by myosin on actin filaments initiates a domino effect of force transmission across various elements. This results in the alteration of conformations in adaptor proteins and influences the unbinding events.

Recent reviews provide detailed descriptions of the molecular mechanisms involved in rigidity sensing, including the role of specific signaling pathways and effector proteins [4], [5]. Interestingly, it has been observed that each cell type exhibits optimal spreading and migration on substrates of specific rigidity, with variations in this parameter leading to significant alterations in cell behavior [7], [8]. This phenomenon, known as durotaxis, refers to the preferential migration of cells toward regions of higher rigidity [9]. It has important implications for various biological processes, including tissue development, wound healing, and disease progression. For instance, numerous cell types, including human mesenchymal stem cells (MSCs), exhibit increased spreading and proliferation as stiffness increases [10] (Figure 1.3).

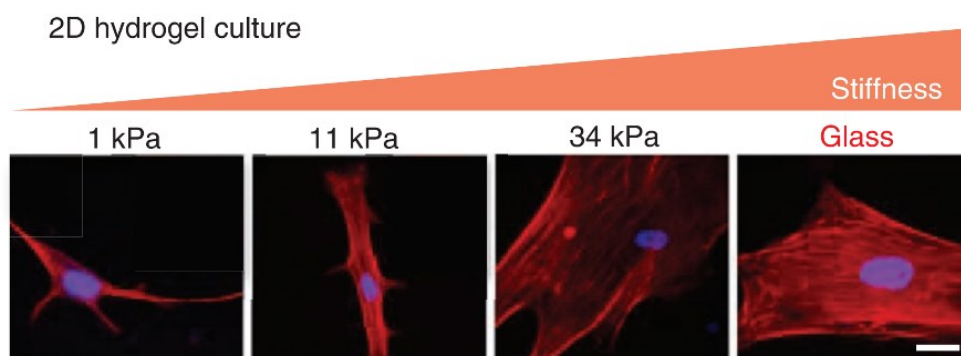


Figure 1.3 – Human mesenchymal stem cells (MSCs) cultured on increasingly stiff 2D substrates display increasing spread area [10]. Scale bar, 50  $\mu\text{m}$ .



However, on laminin-coated hydrogels MSCs showed reduced spreading compared to those on other extracellular matrix protein coatings (Figure 1.4), highlighting the potential for engineering the combination of substrate stiffness and adhesive ligand presentation to manipulate cellular responses [10].

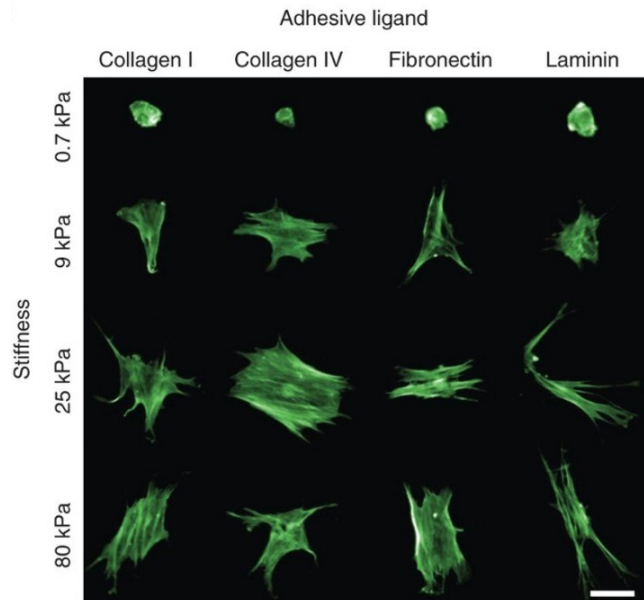


Figure 1.4 – Human MSCs exhibit enhanced spreading on stiffer substrates, yet on laminin-coated hydrogels, they appear smaller than on other ECM protein coatings [10]. Bar, 50  $\mu$ m.

These observations indicate that the effects of substrate rigidity on cell behavior are not only determined by the stiffness of the substrate but depend on the cell type and the precise nature of the ligands involved in cell adhesion. More specifically, it has been shown that U-251MG human glioblastoma cells preferentially migrate towards softer regions on fibronectin coating [11], while primary glial cells from mouse embryos shift from a preferential proliferation on stiff substrates to soft substrates by changing the surface coating from fibronectin to laminin [12]. Thus, this underscores the complexity of mechanotransduction and the need for a nuanced understanding of the underlying factors that can influence cell behavior in response to mechanical cues.

## 1.2 TISSUE MECHANICS

Tissue mechanics provides a fundamental perspective on the behavior and function of biological tissues, anchoring its understanding in the physical properties of its smallest constituents and their interplay at the macroscale. At the core of this complex network are two primary constituents: the extracellular matrix (ECM) and cells. Both contribute synergistically to the overall mechanical properties and functional integrity of the tissue [13], [14].

### 1.2.1 Mechanics of the ECM proteins

The ECM, a three-dimensional network of macromolecules, provides a structural framework for tissue organization. It is made up of hundreds of ECM proteins that include multiple, independently folded domains whose sequences and arrangement are highly conserved. Beyond the structural support, these proteins play vital roles in the differentiation, proliferation, survival, polarity, and migration of cells. As organized solid-phase ligands, ECM proteins can integrate complex multivalent signals to cells in a spatially patterned and regulated fashion [15]. Comprising a variety of proteins, proteoglycans, and polysaccharides, this matrix confers stability, elasticity, and resilience to the tissue. For instance, Hynes highlighted the multifaceted role of the ECM beyond providing structural support, emphasizing its importance in binding, integrating, and presenting growth factor signals to cells, which influences diverse phenomena such as developmental patterning, stem cell niches, cancer, and genetic diseases [16]. The large scale, intricate structure, and conservation of ECM proteins, offering multiple distinct domains, is a common characteristic seen across different species (Figure 1.5).

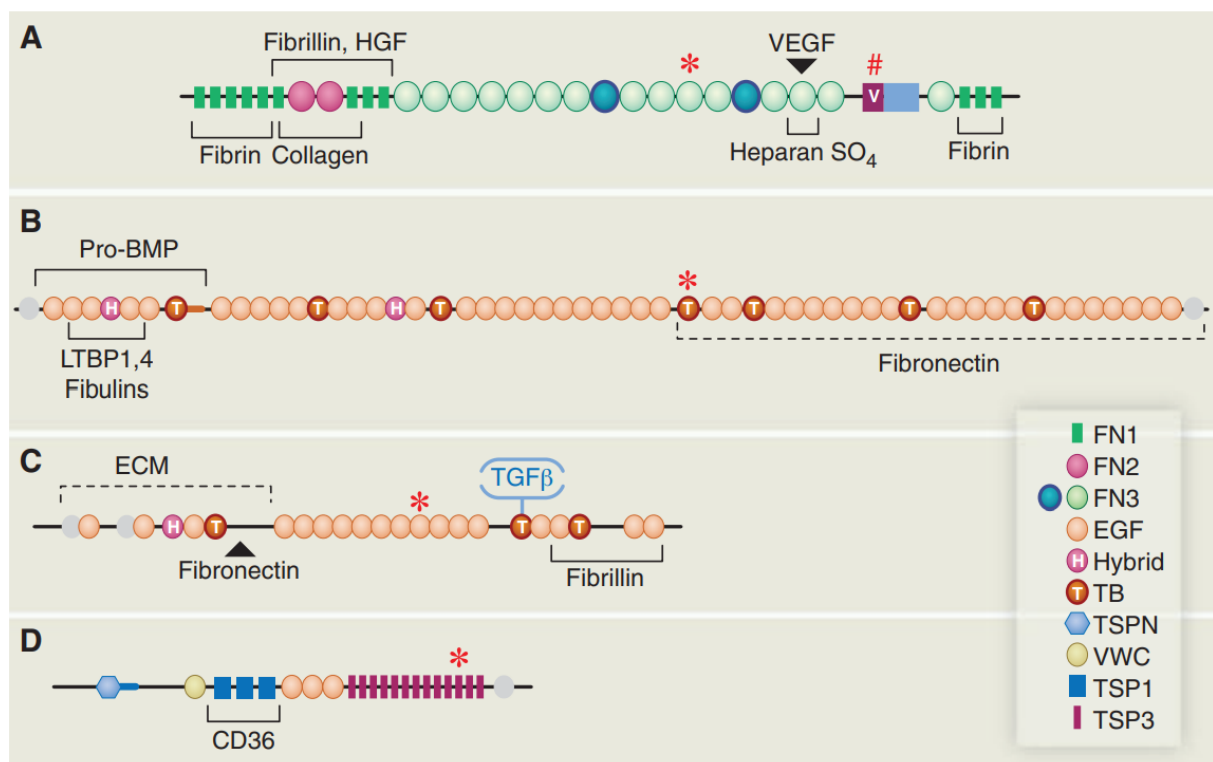


Figure 1.5 – The complex domain structures of representative ECM proteins. (a) Fibronectin, encoded by a single gene, undergoes alternative splicing to produce different proteins, and it interacts with integrins and proangiogenic growth factors. (b) Fibrillin-1, carrying EGF-like domains along with unique TB (TGF $\beta$ -binding) and hybrid domains, shows interaction with other matrix proteins and growth factors. (c) LTBP-1, a member of a four-gene family structurally related to fibrillins, exhibits binding sites for TGF- $\beta$ /LAP latent complex, fibrillin, and Fibronectin. (d) Thrombospondin-1 (TSP-1) stands out with its unique structure and antiangiogenic activity. These detailed domain structures illustrate the intricate roles of ECM proteins in cellular activities and tissue dynamics [16].

ECM proteins predominantly display complex structure, with many individually folded domains whose function of many still remain unexplored (Figure 1.5a). The conservation of these domains in specific arrangements, often orchestrated by tightly regulated alternative splicing, strongly suggests that these specific domains and the architectural blueprints of ECM proteins encapsulate information that is biologically meaningful and of evolutionary significance.

ECM proteins are unique in their ability to bind and control the functions of standard growth factors [17]. These binding domains are found in a wide array of ECM proteins, arranged in various combinations, suggesting that there are still undiscovered interactions between ECM and growth factors. Some of these ECM proteins can even directly interact with cell surface-adhesion receptors like integrins. This co-localization of cell adhesion sites and growth factor binding sites in ECM proteins can bring the growth factors closer to their cell surface receptors, enhancing their signaling and possibly contributing to the formation of stable gradients [18], [19]. Another property of ECM proteins is that they are known for their high conservation, not just in the sequences of specific domains but also in their arrangements. The presence of specific domains can be regulated by alternative splicing, which can modify the domain composition and potentially change the binding of specific growth factors or interactions with cell surface receptors, as seen in the case of the VWC domain in type II collagen [20]. ECM proteins can also work in tandem with growth factors to influence cell proliferation and migration [17]. Experiments on VEGF (Vascular Endothelial Growth Factor) binding by fibronectin (FN) have shown that for such synergy to occur, the binding sites for integrins and VEGF need to be linked in the same molecule [21]. If proximity is crucial, ECM molecules, due to their organized-domain structure, could help organize receptor complexes in the membrane plane, enhancing regulation among the receptors and promoting signal integration (Figure 1.6).

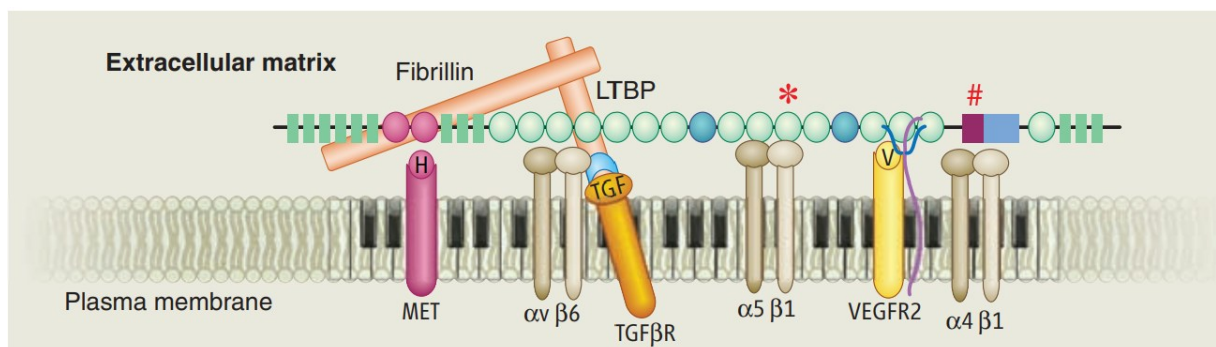


Figure 1.6 – Fibronectin (FN) interacts with cells through multiple domains. FN binds to integrins, other ECM proteins, and growth factors, localizing these signals at the cellular level. The close arrangement of the domains in FN brings different receptors together, enabling complex, integrated signaling to the cell. This model suggests that FN and its associated ECM proteins orchestrate these signals, playing a crucial role in processes like angiogenesis. The presence of alternatively spliced domains in FN introduces additional complexity to these interactions [16].

Moreover, ECM is a dynamic entity that undergoes significant remodeling, especially during development and in response to various diseases. This remodeling process involves the synthesis, deposition, and degradation of ECM components, which include a variety of proteins and polysaccharides [16]. During development, the ECM plays a central role in tissue and organ formation. It provides a scaffold for cell migration and organogenesis, and its composition and structure change to meet the needs of developing tissues [22]. For instance, the ECM in the developing brain is rich in hyaluronic acid and chondroitin sulfate proteoglycans, which provide a permissive environment for neuronal migration and axon growth [23]. As the brain matures, the ECM becomes more restrictive, helping to stabilize neuronal connections [24].

In the context of disease, the ECM also undergoes significant changes. For example, in cancer, the ECM becomes highly disorganized, and its composition changes dramatically [25]. These alterations can promote tumor growth and metastasis by facilitating cell migration, providing survival signals to cancer cells, and contributing to immune evasion [26]. In fibrotic diseases, there is an overproduction of ECM components, leading to the formation of a dense, rigid matrix that impairs organ function [27]. Moreover, Lim et al. discussed the role of ECM-associated components in predicting metastasis, recurrence risk, and survival in early-stage non-small cell lung cancer (NSCLC) patients [28], highlighting potential markers for better diagnosis and prognosis due to their differential expression in primary NSCLC tumors as compared to normal lung tissues.

The ECM is composed of a variety of different types of matrices, each with its own unique rheological properties, playing a decisive role in determining the physical characteristics of the ECM and influencing cellular behavior. Rheology refers to the study of how a material deforms and flows when subjected to applied stresses and shear speeds, and in the context of the ECM, it relates to the mechanical properties of the matrix, such as its stiffness and elasticity. In this context, Storm et al. [29] presented the different rheological measurements for a series of biopolymer networks (Figure 1.7).

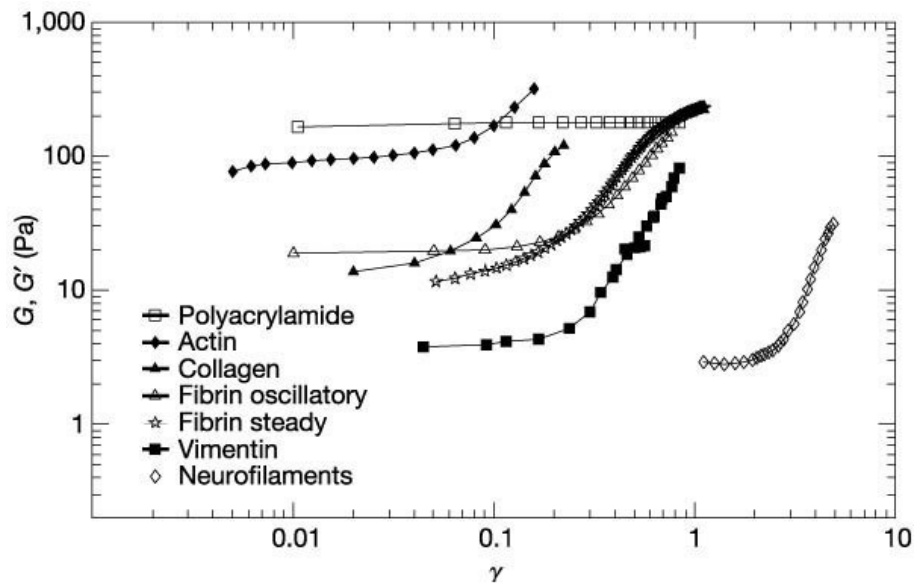


Figure 1.7 – Measurement of dynamic shear storage moduli ( $G/G'$ ) at varying strain amplitudes ( $\gamma$ ) for a range of crosslinked biopolymer networks.

The ratio  $G/G'$  in rheology represents the relationship between the shear modulus ( $G$ ) and the storage modulus ( $G'$ ), key parameters describing the mechanical behavior of a material.  $G$  measures the resistance to shear forces, while  $G'$  indicates the elastic portion of a viscoelastic material. This ratio provides insights into the viscoelastic nature of a material, with higher values indicating more elastic behavior and lower values indicating more viscous behavior.

Predominant ECM components such as collagen, elastin, and fibronectin each have unique mechanical properties [30]. For instance, collagen offers tensile strength to resist deformation, elastin provides elasticity to allow tissues to recoil after stretching, and fibronectin, which principal function is forming fibrin fibers, provide a mechanical and structural scaffold for blood clots at the site of an injury to a blood vessel [31]. For example, type I collagen (Coll I) and fibrin have distinct mechanical properties. The mechanical properties of Coll I matrices are largely determined by the degree of cross-linking between collagen fibrils, which can be modulated by various factors such as pH and temperature [32]. Fibrin, on the other hand, forms a soft, flexible matrix that supports cell adhesion and migration during wound healing and tissue repair. The mechanical properties of fibrin matrices can be modulated by factors such as fibrinogen concentration and the activity of cross-linking enzymes [33].

In conclusion, ECM has a direct role in cellular signaling by presenting biochemical cues and mechanotransduction events that modulate cell function and behavior [15]. The determination of its composition has thus become an important topic in the last few years, either in normal or pathological tissues. Such evaluations are predominantly conducted via mass spectrometry [34],[35]. The implications of these constituents in both healthy and tumorous lung conditions will be further elaborated in Chapter 4.

## 1.2.2 Cell mechanics

The mechanical properties of cells also play a significant role in tissue mechanics. Residing at the heart of life, cells operate as lively mechanical systems with an inherent capacity for force production. This active generation of forces is an energetic process that demands a continual supply of energy, fueling non-equilibrium activities [36]. Such actions are indispensable, orchestrating essential organization and transportation operations vital for cellular functionality. As dynamic entities, cells are capable of sensing and responding to their mechanical environment through mechanotransduction, as described previously [37]. The architecture and shape of these cells mainly originate from the organization of biopolymer filaments and molecular motors, elements that constitute the cytoskeleton. Moreover, cellular mechanics encompass several features, including cell shape, deformability, and contractility, all governed by the cytoskeleton. The three primary types of cytoskeletal filaments – actin filaments, intermediate filaments (e.g., vimentin), and microtubules (MT) – all contribute to the mechanical properties of the cell [38] (Figure 1.8). The balance and interplay between these filaments and their continuous remodeling, driven by motor proteins and influenced by interactions with the ECM, are essential for maintaining cellular integrity and function [39].

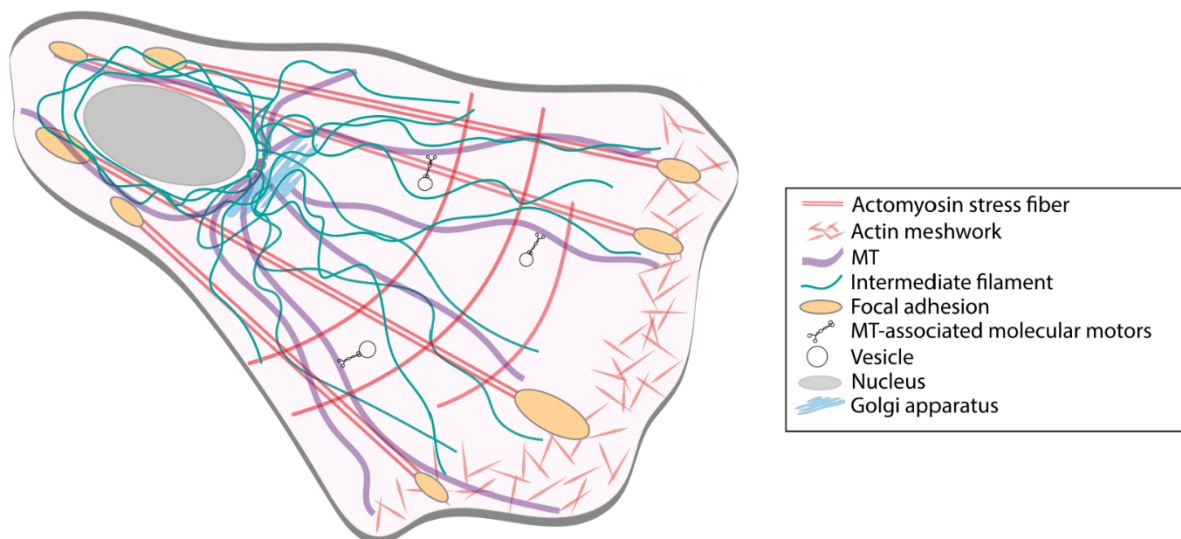


Figure 1.8 – Schematic diagram highlighting the three key cytoskeletal filaments - actin filaments, intermediate filaments, and microtubules, which, along with molecular motors, constitute the mechanical framework of the cell [40].

Quantifying the mechanical properties of cells can help understand how these functions are regulated, which could ultimately be used to develop new therapies for diseases that involve cell dysfunction. Various techniques have been employed to characterize these mechanical properties. These include Atomic Force Microscopy (AFM), which measures forces between

the cell and a probe [41], [42]; Brillouin microscopy, a non-contact method used to assess mechanical properties through interactions of light with acoustic phonons [43]; optical tweezers, which use light to apply forces to cells [44]; and magnetic tweezers, which manipulate magnetic particles inside the cell to measure cellular responses [45]. However, it should be noted that these methods do not always yield consistent results, as cells are highly heterogeneous and dynamic. The chosen measurement method can significantly impact the outcome, underscoring the need for careful interpretation of cellular mechanical properties.

### 1.2.3 Cell and ECM mechanics are linked

Tissue mechanics cannot be exclusively reduced to the mechanics of individual cells and the ECM. Instead, the mechanical properties of the tissue as a whole are an emergent property arising from the collective and coordinated behavior of these constituents. The overall tissue stiffness, for instance, depends not just on the stiffness of the ECM and cells but also on how cells interact with each other and with the ECM, the organization and crosslinking of ECM proteins, and the spatial arrangement of cells within the ECM [46], [47].

Recently, Janmey and colleagues published a review shedding light on the progress made in cell stiffness sensing [48]. Their work extensively described a variety of mechanobiology studies that delve into the influence of substrate stiffness on cellular biology. Other studies have shown that cells, especially cancerous ones, not only perceive but also adapt to their mechanical environment [49]–[51]. When cells encounter a substrate with specific physicochemical properties, they initiate a series of morphological reorganizations. This includes changes in processes such as matrix deposition and the activation of matrix remodeling enzymes, which in turn can alter the chemical and physical properties of the substrate itself. This means that cells possess the ability to alter the rheology of the ECM without necessarily changing its composition. They can do this by cleaving ECM molecules or reorganizing them [52]. Cleavage of ECM molecules, often mediated by enzymes such as matrix metalloproteinases (MMPs), can modify the mechanical properties of the ECM. For example, MMPs can degrade various components of the ECM, leading to a decrease in matrix stiffness and remodeling, potentially influencing cell behavior [53],[54]. Moreover, cells can exert forces on the ECM through their cytoskeleton, leading to the reorganization of ECM fibers. This can result in changes in the mechanical properties of the ECM, such as its stiffness, also without altering its composition [55].

Furthermore, the interplay between cells and ECM also has significant metabolic implications. AMP-activated protein kinase (AMPK), often referred to as the metabolic housekeeper in most cells, plays a central role in this context. Evidence suggests the existence of a feedback loop between AMPK, integrin activation, ECM remodeling, and intracellular stiffness [56]. More specifically, the knockout of AMPK has been observed to result in increased assembly of fibronectin, a high-molecular-weight glycoprotein of the ECM, and an increase in intracellular stiffness in fibroblasts [56].

The concept of targeting both the ECM and cellular stiffness has emerged for cancer therapy and is rooted in the understanding of the dynamic interplay between cancer cells and their microenvironment [51],[57]. This environment comprises both stromal cells and ECM components, which together contribute to cancer cell heterogeneity, clonal evolution, and increased multidrug resistance, eventually leading to cancer progression and metastasis. One potential therapeutic approach could involve targeting enzymes responsible for the increased ECM rigidity often seen in tumors. For instance, lysyl oxidase (LOX) is an enzyme that cross-links collagen and elastin in the ECM, thereby increasing tissue stiffness. Inhibiting LOX activity has been shown to reduce ECM stiffness and hinder tumors [58]. Another potential mechanism could be inhibiting mechanotransduction pathways that respond to the stiffened ECM. Focal adhesion kinase (FAK) is a key player in these pathways, and its inhibition has shown promise in preclinical models of various cancer types [59]. Moreover, modulating the activity of ion channels, such as Piezo1, which respond to mechanical forces and contribute to cellular and tissue stiffness, might be another promising approach [60].

Lastly, considering the interactions between cancer cells and the ECM, therapeutic strategies could be devised to alter the biochemical and biophysical characteristics of the ECM. These changes could disrupt the reciprocal signaling between the cancer cell and its microenvironment, thereby hindering cancer progression and metastasis [57], [61].

#### 1.2.4 Tissue mechanics is multiscaled

Biological tissues present a hierarchical structure spanning multiple length scales, from the molecular to the organ scale, each contributing uniquely to the overall mechanical properties of the tissue. As we ascend from the molecular scale, incorporating individual ECM proteins and cellular components, to higher orders of organization like cells, tissue microarchitecture, and organ structure, distinct mechanical properties emerge [62]. At the smallest scale, individual ECM molecules such as collagen and elastin bear inherent mechanical properties. For instance, collagen fibers, offering tensile strength, have a stiffness in the GPa range, while elastin, conferring elasticity, is considerably less stiff [63]. The stiffness of individual cells, determined



by the cytoskeleton, falls in the kPa range, several orders of magnitude lower than ECM proteins [64]. On an elevated level, cells are organized into tissues, with the ECM being the main responsible for tissue structure. The alignment, density, and crosslinking of collagen fibers, for example, can significantly influence ECM stiffness [65], [66]. Furthermore, the spatial organization and interaction of cells with the ECM add another layer of complexity to tissue mechanics. At the organ level, the overall stiffness is governed not only by the properties of the individual constituents but also by the large-scale architecture of the organ. For instance, in organs such as the heart, this interplay of elements becomes evident. The heart comprises an intricate arrangement of muscle fibers known as the myocardium, which is both highly aligned and anisotropic. The layered orientation of these fibers directly impacts the mechanical properties of the heart, facilitating its capacity to bear the substantial mechanical pressures associated with incessant, rhythmic contractions [67].

The multiscale nature of tissue mechanics is a determining factor in comprehend the significant disparities in stiffness measurements taken at different scales. Measurements at the microscale or nanoscale, sensitive to the properties of individual ECM components and cells, may yield different values compared to macroscale measurements reflecting the properties of the bulk tissue [68]. Understanding the role of each scale in the mechanical properties of biological tissues is fundamental, as changes at any level could potentially alter the overall tissue mechanics, with implications for disease development and progression. On this note, to better understand the implications of ECM change in tissue stiffness during disease, Guimaraes et al. [69] elaborated an educative diagram presented in Figure 1.9.

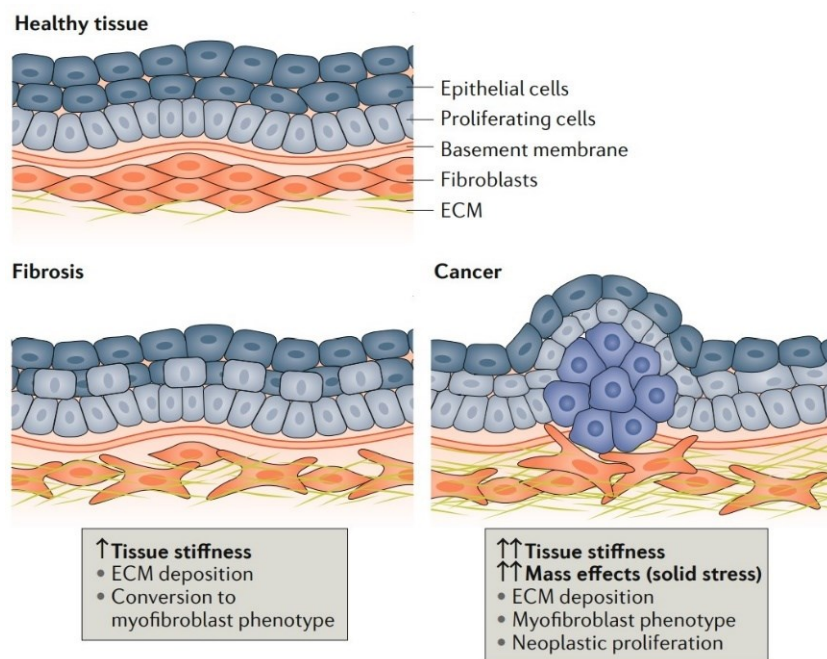


Figure 1.9 – Diagram illustrating how disease alters the ECM and thus tissue mechanics [69].

The mechanical properties of tissues can undergo notable alterations in various pathological conditions, including fibrosis and cancer. These conditions are characterized by an escalated deposition and crosslinking of extracellular matrix fibers. This process, along with the proliferation of fibroblasts and their subsequent differentiation into myofibroblasts, contributes to an elevation in tissue stiffness. Such changes often proceed as a reaction to extended healing periods, tissue injury (in the case of fibrosis), or the presence of neoplastic lesions (as seen in cancer) [69]. In cancerous conditions, the abnormal proliferation of cells can exert pressure on adjacent healthy tissue compartments, causing a phenomenon known as mass effects. This includes complications such as the compression of nerves and blood vessels, and an increase in solid stress, further contributing to the stiffening of local tissue. Furthermore, the capacity of malignant cells to influence the tumor microenvironment, particularly the stromal components, is enhanced in the context of cancer. This promotes a shift towards a profibrotic state [47], exacerbating local fibrosis and thus reinforcing the stiffening of the affected tissue.

Living tissues span a broad range of stiffnesses, reflecting their specialized physiological roles and distinct mechanical environments. At one end of the spectrum, soft tissues like fat tissues exhibit low stiffness, with Young's modulus of less than 1 kilopascal (kPa) [70], [71], [72]. On the other end, calcified tissues like teeth and bone present much higher stiffness, with Young's modulus in the gigapascal (GPa) range [73]. Intermediate stiffness values are observed in tissues such as liver, muscle, and skin, with Young's modulus values typically ranging from hundreds of kPa to several megapascals (MPa) [74], [75], [76].

Thus, the mechanical properties of biological tissues, including their stiffness, are not uniform and exhibit heterogeneity. This variability arises from the complex, often anisotropic architecture of the ECM and the cellular organization, both of which vary between tissues [77]. Measurements at the microscale or nanoscale, which are sensitive to the properties of individual ECM components and cells, may yield different values compared to macroscale measurements that reflect the properties of the bulk organ. Hence, both the inherent range in stiffness across different tissues and the scale- and direction-dependent variability within individual tissues contribute to the complexity of tissue mechanics.

### 1.3 THESIS CONTEXT

It is part of a larger study whose aim to goal is to elaborate soft culture supports that mimic the mechanical properties of tissues. Lung tissues, especially lung adenocarcinoma, were chosen to establish this proof of concept for reasons that are detailed in the next sections.

### 1.3.1 Lung cancers

According to the Global Cancer Observatory, lung cancer is currently the malignant tumor with the highest worldwide incidence in men and second in women, after breast cancer [78]. More specifically, it accounted for 1.8 million deaths in 2020, corresponding to 18,4% of the total [78], [79]. Although the high mortality in most developed western countries, where tobacco consumption was established, and peaked in the middle of the last century, incidence rates from lung cancer continue to decline for men and virtually stabilized for women [80], [81]. On the other hand, in several African countries, South Korea and China, where consumption was more recently established and smoking rates have just peaked or continue to increase, lung cancer rates are growing and are expected to remain rising for at least the next few decades, despite the efforts to reduce smoking habits in these countries [80], [82], [83]. Furthermore, early-stage detection is uncommon and usually serendipitous [84], and most of the time, diagnosis is late, when the disease is already in advanced stages, which prevents effective therapy and contributes to the statistics of this growing global burden.

This malignant neoplasm originates from epithelial cells with altered DNA caused by the action of carcinogens in the tracheobronchial airways [85]. The main carcinogen that acts in the formation of primary lung cancer is cigarette smoke. Although tobacco consumption accounts for around 35% of all cancer deaths and 80% of lung-related cancer [86]–[88], growth of lung cancer cases has been observed in people who have never smoked, representing about 10% to 15% among all cases [89]. There are several factors associated with pulmonary oncogenesis. Among them, an important factor associated with smoking is a pathology called Chronic Obstructive Pulmonary Disease (COPD), an inflammation that occurs in the lower airways and increases the risk of lung cancer by up to 4.5-fold among smokers possessing this condition and is found in 50-90% of lung cancer patients [90], [91]. Other factors that are not associated with tobacco, such as repeated lung infections, history of tuberculosis, vitamin A deficiency or excess, hepatitis B, and HPV, may also contribute to the development of this type of cancer [85], [90]. The World Health Organization classifies lung cancer based on histological characteristics and divides them into two broad categories: small cell lung cancer (SCLC), which affects approximately 15% of patients, and non-small cell lung cancer (NSCLC), occurring in about 85% of lung cancer patients [92]–[95]. NSCLC is further categorized into three main histological subtypes: adenocarcinoma, squamous cell carcinoma, and large cell carcinoma [96], [97]. These categories can develop and proliferate in different ways and are, therefore, unique [97]. Figure 1.10 shows the incidences of NSCLC as compared to SCLC obtained from United States SEER Cancer Statistics Review 1975–2008 study comparing the four histologic types of lung cancer [95].

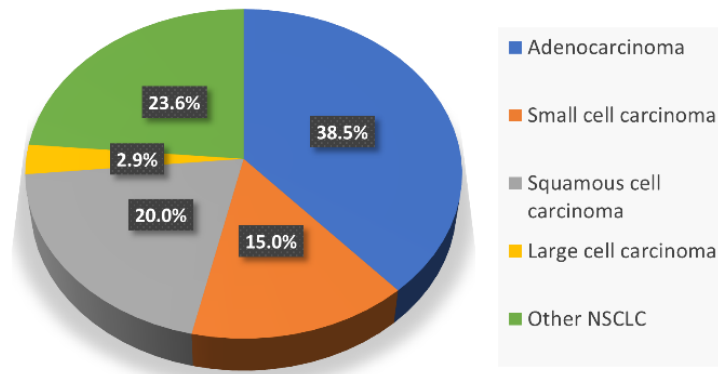


Figure 1.10 – Incidences of non-small cell lung cancers as compared to small cell lung cancer. Compiled from [95].

Although smoking increases the risk of all subtypes of lung cancer, squamous cell carcinoma is more strongly related to smoking and not often seen in non-smokers, whereas adenocarcinoma is seen in both smokers and non-smokers and is the most common type in never-smokers [95], [98], [99]. Several studies have reported the international lung cancer trends by histologic subtypes [100]–[102].

The behavior of carcinogenic cells has been related to several biological factors that could result in the deregulation of signaling pathways. The complexity and heterogeneity of these factors across different cancer types, combined with different phenotypes for the same cancer, hamper the identification of common pathways for the initiation and evolution of oncogenic behavior in cells [103], [104]. The bronchoalveolar subtype adenocarcinoma is the most common in non-smokers. Patients with this condition have a better prognosis in the early stage of the disease, but in an advanced stage, the prognosis is similar to other lung adenocarcinoma subtypes [105]. Mutations in this histological subtype are associated with the inhibitory action of tyrosine kinases on the epidermal growth factor receptor (EGFR) of transformed cells.

The epidermal growth factor receptor (EGFR) is a plasma membrane glycoprotein consisting of an extracellular EGFR-binding domain (ligand), a transmembrane region, and an intracellular tyrosine kinase domain [106], [107]. EGFR activation occurs by homodimerization with another EGFR or heterodimerization with members of the erbB/Her family. Receptor dimerization causes changes that induce activation of intracellular signaling cascades, mediated by effector proteins AKT, MAPK, and signal transducer and activator of transcription (STAT), which play a vital role in the processes of regulation, stimulating cell proliferation and survival [106]. Overexpression of the EGFR gene is associated with cancer aggressiveness, shorter survival, and higher metastasis [108]. Mutations in the EGFR gene are observed in about 15% to 40% of adenocarcinoma-type lung tumors, most prevalent in non-smokers or former smokers and rarely occur in squamous cell carcinoma-type lung cancer [109].

### 1.3.2 Implication of KRAS mutation

Another factor associated with the formation of lung cancer is the KRAS protein (oncogene in Kirsten RA Sarcoma virus), a protein that binds through lipid binding in the cytoplasmic region of the membrane. KRAS is critical in mitogenesis and, together with other proteins, acts by transmitting signals from the cell surface to other internal cell structures [110]. KRAS alternates between the activated state (when signals are transmitted) and the idle or quiescent state. When there is stimulation in the cell by growth factors or other receptor interactions, KRAS becomes active [111]. It is one of the proteins that control signaling pathways that regulate normal cell growth and malignant cell differentiation [110], [111] (Figure 1.11).

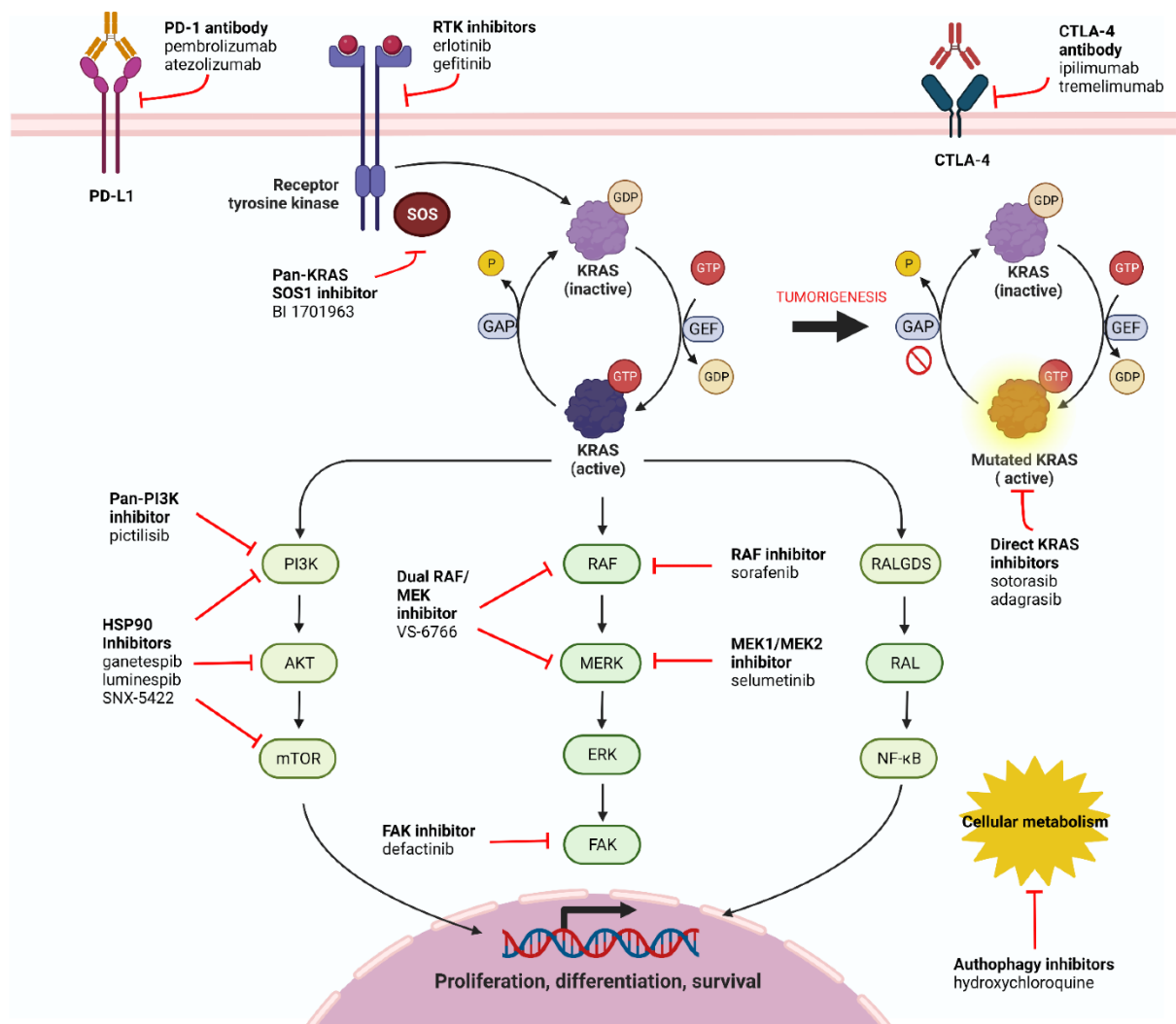


Figure 1.11 – Schematic representation of the KRAS pathways with various target inhibitors. The top section of the figure depicts the activation process of KRAS. KRAS gets activated upon interaction with GEF, binding to GTP, which represents its active state. The role of GAP in this sequence, which includes the release of a phosphate group, consequently, leads to the inactivation of KRAS. The right segment of the figure showcases a condition resultant from tumorigenesis where GAP is inhibited, causing a continuous activation state of KRAS. As a consequence of this persistent KRAS activation, a series of intracellular pathways are stimulated, culminating in cellular proliferation, differentiation, and survival mechanisms [112].

KRAS is different in most tumors due to the mutations that occur during their formation [111]. Mutations in the KRAS proto-oncogene are observed in 30% to 35% of neoplasms of patients with lung adenocarcinoma and are commonly associated with a poor prognosis [113]. Although therapeutic solutions exist for EGFR-mutated adenocarcinomas, this is not the case yet for KRAS-mutated tumors [114]. Many molecules, including mutated KRAS inhibitors or downstream effectors, have failed in clinical trials, questioning the validity of predictions from preclinical trials [115]. Therapeutic approaches such as directly targeting mutant KRAS with covalent KRAS-specific inhibitors [116], targeting KRAS membrane association [117], exploiting KRAS-regulated metabolic pathways [118], and reactivation of anti-tumor immunity [119] have been attempted, but with few promising results. Regardless of the numerous attempts in the past decades that covered multiple aspects of KRAS activation, KRAS mutant remains considered hardly druggable [120].

### 1.3.3 The expected benefit of using 2D mechano-mimetic culture plates

A hypothesis for this unsuccess in finding effective drugs against KRAS-mutated as well as other drug-resistant cancers might be associated with the environment where the cellular models are cultured and experimented. It is common knowledge that most animal cells *in vivo* experience a totally different mechanical environment offered by a plastic Petri dish and that they perceive and respond to the mechanical properties of their microenvironment [13]. Therefore, as mentioned [121]–[123], the stiffness of the extracellular matrix can significantly impact protein synthesis, transcriptional regulation and cell metabolism, as well as play an important role in the driving of an uncontrolled proliferation that may result in a malignant progression of cancer in humans. Despite the aforementioned facts, the majority of cell-based assays and cell culture procedures are carried out on plastic or glass substrates that possess rigidities in the order of gigaPascal (GPa), which are significantly higher than the physiological stiffness of kilopascal (kPa). Recent studies have established that conducting cell culture on such substrates can result in phenotypic drift, leading to alterations in the expression of basal genes and modification of basal cell characteristics [124]. Furthermore, repeated passages have been found to cause a reduction in the expression of typical melanoma markers [125], alterations in cell propagation capacity and endothelial cell migration [126], insulin secretion defects in pancreatic cells [127], and emergence of a secondary population of lung cancer cells not associated with drug resistance [128]. This phenotypic drift not only introduces significant bias but also poses a risk to the reliability and reproducibility of data, with considerable financial implications, particularly during the initial stages of pre-clinical drug discovery [129].

These observations indicate that the use of plastic substrates in cell culture leads to detrimental effects on the reliability of *in vitro* data, with particularly severe consequences in the context of drug candidate discovery. Additionally, research has demonstrated that incorporating the mechanical environment into the *in vitro* culture system has significant potential for optimizing cellular characteristics, including their differentiation capabilities, even after multiple passages. For example, a biomimetic rigidity substrate was shown to enhance myotube differentiation [130], and a mechano-mimetic substrate maintained the proliferative and multi-lineage potential of human MSCs during long-term expansion [131].

Therefore, the adverse scenario of lung cancer worldwide encourages research of innovative technologies to improve therapeutic arsenals [132]. As demonstrated, different genetic mutations arising from unhealthy habits or inherited disorders can lead to lung cancer. Some of them are known, and few solutions are available. The advent of immune checkpoint blockade therapy and targeted-drugs based on driver genes has changed the prognosis of lung cancer patients in the past few years, but the majority of them will not benefit from those treatments. Thus, the development of creative tools and techniques is mandatory to facilitate research and discovery of new treatments. A primary step involved in drug design is *in vitro* cell culture. As stated previously, to date, most cell cultures are performed on surfaces that do not reflect the mechanical properties of most tissues *in vivo*. The use of soft culture environments that have a similar mechanophysiology of *in vivo* conditions is seen as a promising route for the discovery of new cancer drugs and tissue engineering. Based on this context, it is essential to understand how the mechanical properties are distributed in human tissues to design cell culture substrates that mimic the mechanical properties of the *in vivo* physiopathology.

## 1.4 THESIS OBJECTIVES

The main objective of this thesis is to design lung 2D mechano-mimetic culture substrates and perform a basic cellular behavior assessment both on uniform and textured substrates. To achieve this objective, the work was subdivided into three specific objectives, described in the following subtopics.

### 1.4.1 Characterization of mechanical properties of healthy and tumor human lung tissues

This characterization is performed using IT-AFM (indentation-type atomic force microscopy) on 18 paired biopsies (18 healthy and 18 tumor tissues) from HCL patients (Lyon, collaboration Dr. Chalabreysse, anatomico-cytopathologist) with solid or acinar lung adenocarcinomas. From these data, cartography of the stiffness texture of physiopathological lung tissues with a micron resolution is extracted, as illustrated in Figure 1.12.

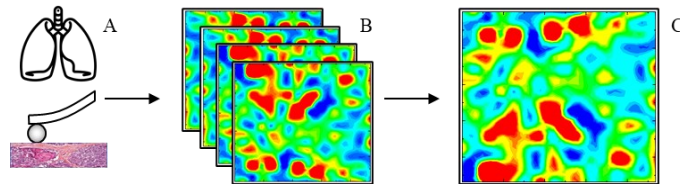


Figure 1.12 – (a) AFM measurements on human healthy and tumor lung tissue using a spherical tip to probe the rigidity at the micron scale. (b) Treated data translated to hundreds of 2D rigidity maps. (c) Statistical representation of the rigidity distribution of healthy or tumor lung tissue.

This step is followed by a statistical analysis to determine the most representative rigidity textures according to the histological types. Two types of outputs are expected: averaged elastic parameters of healthy and tumor lung tissues and statistical analysis of the stiffness texture of the tissue (Young's modulus) to provide inputs for the next objective.

### 1.4.2 Fabrication of a two-dimensional soft culture substrate presenting rigidity textures

This technological objective uses the expertise developed at LTM and operated by Cell&Soft. The principle consists of illuminating a photosensitive polyacrylamide aqueous solution through a gray-level mask, as shown in Figure 1.13.

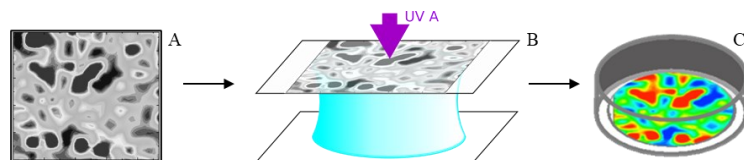


Figure 1.13 – (a) Fabrication of engineered hydrophobic gray level mask using contact optical lithography processes. (b) UV A illumination at a specific time to print a heterogeneous rigidity pattern onto the polyacrylamide hydrogel. (c) Polyacrylamide hydrogel with representative rigidity pattern at the  $\mu\text{m}$  scale of healthy and tumor human lung tissue.



Progressive crosslinking in response to the intensity level allows to modulate hydrogel's mechanical properties and print micron to centimeter-scale textures. As the intended textures are more complex than the printed geometric patterns, optimization steps are required to correct the diffusion of the reactive species that occur in this aqueous, gray-leveled lithographic process. Stiffness sensitive swelling may also require adjusting the geometric pattern. By completing this objective, we expect to provide a soft cell culture substrate that consist of a polyacrylamide hydrogel with physiopathological rigidity patterns that resemble the mechanical feature of healthy and tumor human lung tissues.

#### 1.4.3 Behavior analysis of tumor cell models on soft culture substrates

Basic cellular responses of A549 cells are assessed to get a first idea of the impact of stiffness texture compared to uniform mechanical properties. Cell adhesion, spreading, proliferation, and migration are compared in the presence and in the absence of stiffness texture on supports with identical mean mechanical properties. This preliminary study serves as a basis for a deeper analysis of the impact of stiffness texture on cell biology, as related in the Perspectives chapter.

### 1.5 THESIS ENVIRONMENT

Thesis activities took place at the LTM, under the scientific direction of Dr. Alice Nicolas (Laboratoire des Technologies de la Microélectronique – MINASEE Group). It was co-supervised by Camille Migdal, president of Cell&Soft, which financed the thesis ([www.cellandsoft.com](http://www.cellandsoft.com)). The thesis is integrated within the framework of two projects: CAMELEON, funded by the Cancéropôle Lyon Auvergne Rhone Alpes (CLARA), and MECAMIM, funded by the Auvergne Rhône Alpes Region. These two projects give the collaborative context (Lyon Cancer Research Center and Hospices Civils de Lyon), material support for the thesis, and CLARA's critical view of the project progress. LTM facilities and experimental resources (clean rooms, L2 cell culture laboratory) were made available. Human tissues are supplied by HCL (Lyon) in the part of the CAMELEON and MECAMIM projects and stored in an approved laboratory (Clnatec, CEA / Léti) according to the LTM hosting agreement with Léti. Mechanical characterization of tissues humans took place on the AFM platform of LiPhy (Grenoble) in compliance with the rules concerning the manipulation of human tissues. Cell&Soft facilities also were available for substrates development. They also provided orientation and expertise in the development a surface chemistry consistent with the tissue pulmonary physiology and expected cellular responses. Thus, Dr. Camille Migdal, as an expert biologist, brought an additional perspective to that of Cell&Soft Scientific Advisor (Dr. Alice Nicolas).

## 1.6 OUTLINE OF THE THESIS

Given this context, this doctoral thesis proposes a quantitative analysis of the mechanical properties of healthy and tumor lung tissue for the design of mechano-mimetic culture substrates. Each chapter starts with summary in French and in English. In the **first** chapter, the groundwork for this thesis is presented by providing the reader with the context and environment where the thesis took place. An exploration into cellular responses, specifically regarding rigidity sensing and mechanotransduction, is also included in this introductory chapter to prepare the reader for subsequent detailed investigations. Transitioning to the **second** chapter, an in-depth characterization of the mechanical properties of both healthy and adenocarcinoma human lung tissue is presented. The chapter elaborates on key concepts related to Atomic Force Microscopy (AFM) and contact mechanics on soft biological samples. This provides the theoretical framework that will support the understanding of the methods, data analysis, and interpretation of results that follow. Next, the **third** chapter shifts focus to studying stiffness textures in tissues. This includes an explanation of the fundamental concepts, such as stiffness heterogeneity in biological samples and shape descriptors. Further, the chapter outlines the materials and methods used for the research and the statistical analysis of the gathered data. The results from the comparison of stiffness measurements and analysis of tissue stiffness texture are also discussed. In the **fourth** chapter, the focus turns to the relationship between stiffness and lung tissue composition. Core concepts such as the role of collagen I,  $\alpha$ -SMA, and vimentin in lung tissue stiffness are elaborated upon. This chapter also provides a detailed account of the methods used in the study, which includes tissue preparation and immunofluorescence (IF) labeling. Qualitative results reveal the correlations between different components and tissue stiffness form an integral part of this chapter. Moving on to the **fifth** chapter, this thesis discusses the creation of hydrogels that mimics the lung tissue stiffness texture. The chapter explores relevant concepts like microfabrication techniques, hydrogel cross-linking strategies, polyacrylamide hydrogel, stiffness patterned hydrogel fabrication techniques, and hydrogel surface functionalization. Moreover, the materials and methods utilized in the process, as well as the results obtained from pattern design generation, mask fabrication, and hydrogel fabrication parameters, are all discussed. Finally, the **sixth** chapter presents an investigation into cell cultures on mechano-mimetic hydrogels. The chapter begins by establishing fundamental concepts like cell rigidity response, the influence of substrate chemical patterning on cell behavior, and the impact of stiffness patterning on cell behavior. The materials and methods applied in the research are thoroughly described, followed by a discussion and presentation of the results, which include the examination of cell spreading, cell velocity, cell growth dynamics, and cell movement. The thesis then concludes with a summative review of all findings, as well as the potential implications and future directions in the field.

## CHAPTER 2

---

# CHARACTERIZATION OF MECHANICAL PROPERTIES OF HEALTHY AND TUMOR HUMAN LUNG TISSUE

## 2 CARACTÉRISATION DES PROPRIÉTÉS MÉCANIQUES DES TISSUS PULMONAIRES HUMAINS SAINS ET TUMORAUX

Les propriétés mécaniques des tissus biologiques sont reconnues comme des indicateurs importants des conditions pathologiques et fournissent des informations sur les causes sous-jacentes des maladies [2],[133],[134]. Comprendre les propriétés mécaniques des tissus biologiques peut donc soutenir le développement de nouveaux outils de diagnostic, de stratégies de découverte de médicaments et d'approches thérapeutiques [135].

Dans ce chapitre, notre objectif est de proposer une mesure des propriétés mécaniques des tissus pulmonaires humains sains et tumoraux qui sera utilisée pour la fabrication de supports de culture souples aux propriétés mécaniques biomimétiques. Avant de nous plonger dans le sujet, il est important de se rappeler que les tissus biologiques sont hétérogènes en termes de composition et de propriétés physiques [69]. Alors que nous abordons la conception de supports mécano-mimétiques consacrés à la culture cellulaire, nous nous concentrons sur la mesure des propriétés mécaniques que les cellules peuvent détecter. Les chiffres typiques associés aux adhérences cellulaires impliquées dans la mécanotransduction, par exemple, les adhérences focales, sont en  $\mu\text{m}$  et  $\text{nN}$  [136] (ce qui résulte en une capacité de détection de la rigidité de l'ordre de  $\text{kPa}$ ). Dans ce contexte, nous nous concentrons sur la sonde locale des propriétés mécaniques de ces tissus à l'échelle du micron, avec des forces de l'ordre de  $1 \text{ nN}$ . Cela oriente le choix de la configuration expérimentale utilisée pour cette caractérisation vers la Microscopie à Force Atomique (AFM).

Dans la suite, une introduction de l'AFM et de sa variante de type indentation (IT-AFM) est fournie, avec un accent sur son applicabilité aux spécimens biologiques. Par la suite, une description des matériaux et des méthodologies utilisées dans la préparation des échantillons de tissus, la mesure de la rigidité et le traitement des données est réalisée.

Ce chapitre examine également la relation entre la rigidité des tissus et leurs caractéristiques histologiques respectives ainsi que les caractéristiques cliniques du patient. Cela se fait en comparant les résultats de la caractérisation mécanique AFM effectuée sur les tissus pulmonaires sains versus tumoraux. Nous mettons également l'accent sur le comportement élastique linéaire prédominant trouvé dans ces échantillons. De plus, le chapitre discute des interactions adhésives entre la pointe et le tissu et comment elles sont prises en compte dans le traitement des courbes force-distance. Il conclut enfin par une discussion qui intègre ces résultats et fournit une meilleure compréhension de leurs implications.

## 2 CHARACTERIZATION OF MECHANICAL PROPERTIES OF HEALTHY AND TUMOR HUMAN LUNG TISSUE

The mechanical properties of biological tissues have been recognized as important indicators of pathological conditions and to provide insight into the underlying causes of diseases [2], [133],[134]. Understanding the mechanical properties of biological tissues can thus support the development of new diagnostic tools, drug discovery strategies, and therapeutic approaches [135].

In this chapter, our goal is to propose a measure of the mechanical properties of healthy and tumor human lung tissues that will be used for fabricating soft culture substrates with biomimetic mechanical properties. Before delving into the topic, it is important to remember that biological tissues are heterogeneous in composition and physical properties [69]. As we address the design of mechano-mimetic supports devoted to cell culture, we focus on measuring the mechanical properties that cells can sense. Typical numbers associated with the cell adhesions involved in mechanosensing, for instance, focal adhesions, are  $\mu\text{m}$  and nN [136] (which result in the capability of sensing stiffness of the order of kPa). In this context, we focus on the local probing of the mechanical properties of these tissues at the micron scale, with forces of the order of 1 nN. This orients the choice of the experimental set-up used for this characterization toward Atomic Force Microscopy (AFM).

In the following, an introduction of AFM and its indentation-type variant (IT-AFM) is provided, with a focus on their applicability to biological specimens. Subsequently, a description of the materials and methodologies utilized in tissue sample preparation, stiffness measurement, and data treatment is carried out.

This chapter also investigates the relation of tissue stiffness to their respective histological characteristics and the patient's clinical characteristics. This is performed by comparing the AFM mechanical characterization results conducted on both healthy and tumor lung tissues. We also emphasize the predominantly linear elastic behavior found in these samples. Furthermore, the chapter discusses the adhesive interactions between the tip and the tissue and how it is accounted in force-distance curve processing. It ultimately concludes with a discussion that integrates these findings and provides a deeper awareness of their implications.

## 2.1 FUNDAMENTAL CONCEPTS

### 2.1.1 Atomic Force Microscopy (AFM)

Atomic force microscopy is a high-resolution imaging technique that has revolutionized the field of nanoscale science and technology. Invented in 1986 by Gerd Binnig, Calvin Quate, and Christoph Gerber [137], it has enabled researchers to visualize and manipulate surfaces at the atomic level. With its ability to produce three-dimensional topographical images and measure local properties, AFM has become an indispensable tool in a wide range of disciplines, including materials science, biology, chemistry, and physics.

Since its creation, the technology and uses of AFM have rapidly grown and diversified. Initially designed to view solid surfaces at the atomic level, a standard AFM configuration consists of a microcantilever featuring a sharp tip, a cantilever deflection sensor, a piezoelectric sub(nano)positioning device, and an electrical feedback system connecting the deflection sensor and the nanopositioner as shown in Figure 2.1.

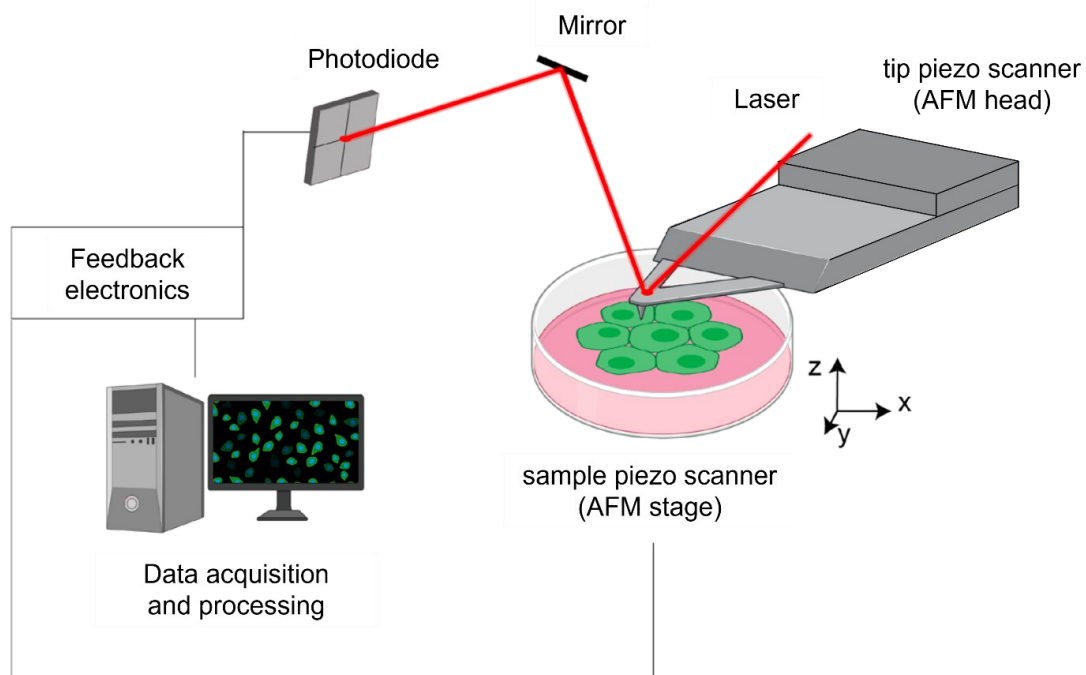


Figure 2.1 – A schematic illustration of the AFM working principle illustrates the key components and the fundamental mechanism of an atomic force microscope (Adapted from Müller et al. [138]). The interaction between the sharp tip and the sample surface results in cantilever deflection, which is monitored by the position-sensitive photodiode. The feedback mechanism and piezo scanner work together to maintain optimal tip-sample interaction, enabling high-resolution imaging and force measurements at the piconewton range.

The underlying principle of AFM lies in assessing the forces that occur between the tip and the specimen's surface. To measure these forces, a laser beam is directed towards the cantilever edge, reflecting towards a quadrant-based, position-sensitive photodiode. This photodiode

enables simultaneous monitoring of both normal and torsional deflections of the cantilever, with the bending of the cantilever directly proportional to the force experienced.

The location of the piezo scanner can differ based on the manufacturer and design of the AFM system. It may be positioned under the sample holder or stage, within the AFM head assembly, or integrated into a hybrid configuration. It is typically made of piezoelectric materials, such as lead zirconate titanate (PZT). When an electric voltage is applied to the piezoelectric material, it undergoes a dimensional change, causing it to expand or contract, depending on the voltage polarity. This deformation is highly controllable and can be fine-tuned by adjusting the applied voltage. Its role is to control the movement of the cantilever and probe tip in three dimensions relative to the sample surface, with typically  $100 \times 100 \times 15 \mu\text{m}^3$  scan volume. The sample is often placed on a separate sample stage or holder that can also be adjusted for coarse positioning. In hybrid configurations, an xyz sample piezo scanner can also be integrated with z scan ranging from  $100 \mu\text{m}$  to  $300 \mu\text{m}$ , ideal for large sample-area mapping.

Though initially designed for use in vacuum, AFM can function in both air and liquid environments at room temperature, which makes it especially valuable for analyzing biological molecules, cells, and tissues in their natural states. The microcantilever serves not only as an imaging tool but also to measure forces between various surfaces and materials. This includes electrical forces within thin layers [139], the behavior of liquids near surfaces [140], chemical forces such as interactions between hydrophilic or hydrophobic substances [141] and hydrogen bond formation. Acquisition of force-indentation or force-distance (FD) curves is crucial for these applications. This branch of AFM research ultimately led to the emergence of force spectroscopy.

### 2.1.2 Indentation-Type Atomic Force Microscopy (IT-AFM)

Indentation-type atomic force microscopy (IT-AFM) is a force spectroscopy technique that is commonly used to measure the elastic properties of both synthetic and biological materials. This technique involves the use of a specialized tip, such as a spherical or pyramidal tip, which is brought into contact with the sample surface at a specific velocity. The force is applied by a piezoelectric actuator, which then causes the tip to indent the sample to a depth of a few hundred nanometers or a few microns. This contact also causes a cantilever deflection, which is measured and used to calculate the force and tip-sample separation, providing mechanical information about the sample. The working principle and typical curve output are depicted in Figure 2.2, adapted from Kreig et al. [142].

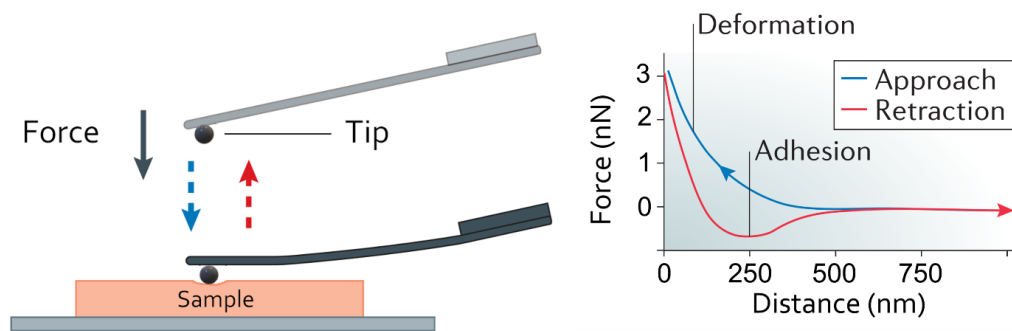


Figure 2.2 – In IT-AFM, a tip (e.g., colloidal probe) is used to indent and retract from a sample, enabling the measurement of local interactions and properties of the material (Left). The typical force-indentation curve (Right), also known as force-distance (FD) curve in literature, is characterized by the approach (blue) and retraction (red) curve, which describes the relationship between the force exerted by the cantilever and the indentation depth on the sample surface during measurement. (Adapted from [142]).

IT-AFM has been made possible through the advent of depth-sensing nanoindenter apparatus, which has allowed for a reduction in indentation dimensions and forces. This technique is highly effective due to its ability to provide high spatial resolution, making it useful for studying both synthetic and biological materials at the nano and microscale. One of the main benefits of IT-AFM is its non-destructive nature, which enables samples to be characterized repeatedly without causing significant damage to the sample. It can additionally provide information on a range of mechanical properties, including elasticity, stiffness, and adhesion force between the tip and the sample, allowing for comprehensive characterization at nano or microscale depending on the size of the tip [143].

### 2.1.3 Contact mechanics on soft biological samples

The use of contact mechanics models is essential in accurately describing the interactions between the tip and sample, thereby facilitating the extraction of pertinent mechanical information from force-distance curves. The problem of a rigid object indenting an elastic half-space, was initially investigated by Hertz in 1881 and Boussinesq in 1885. Since then, several researchers have contributed to the theoretical framework, which is widely employed in interpreting the results of indentation tests across all length scales. Exact solutions that relate force and indentation exist for axisymmetric indenter geometries, such as cylindrical, spherical, and conical [144]. These solutions are derived from various contact mechanics models that can be employed depending on the sample properties, specificities due to tip-sample interaction, probe geometry, and size.



IT-AFM is based on indenting the sample to a maximum setpoint force and fitting the resulting force-distance curve to a suitable contact mechanics model. Hertz and Sneddon models are among the most widely used approaches when the primary variable of interest is the elastic modulus of a material. These models provide a theoretical framework for understanding the relationship between the force applied by an indenter, the indentation depth, and the elastic properties of the sample being studied. The Hertz model specifically applies to contact between a spherical indenter and a flat surface, while the Sneddon model is an extension of the Hertz model that accommodates different indenter shapes, such as conical or pyramidal tips. Both models assume a linear elastic behavior of the material and neglect the effects of the adhesion of the tip, plastic deformation of the sample, and viscous damping [145]. Nonetheless, it should be noted that materials are susceptible to nonlinear elastic or plastic deformations in response to considerable applied forces or the presence of adhesion, thus necessitating the adoption of more pertinent modeling approaches.

Lin et al. have investigated the limitations of Hertzian models in the context of AFM nanoindentation [146], particularly regarding their inability to account for adhesive interactions between the tip and the sample when surface forces are present. They demonstrated that, due to these surface forces, the load-indentation behavior deviates considerably from the ideal Hertzian relationship. Therefore, they advocated that Hertzian models are inadequate when dealing with probe-sample adhesive interactions, which can frequently occur during the retraction of a rigid tip from a soft biological sample.

The foundation of adhesive contact mechanics theories can be traced back to the work of Johnson et al. [147], who established the Johnson-Kendall-Roberts (JKR) theory. This theory modified the classical Hertz theory of contact between spherical bodies to account for the influence of surface energy. In contrast, Derjaguin et al. [148] proposed a seemingly opposing theory called the Derjaguin-Muller-Toporov (DMT) theory. Tabor [149] resolved this apparent inconsistency by identifying the applicability of both theories to extreme cases of the influence of the adhesive force on the determination of sample compliance. In brief, it was shown that JKR approach is relevant for soft materials indented by a large tip compared to the characteristic length of the interaction potential and showing high adhesive interaction. In contrast, DMT model suits to stiffer materials, with a small tip radius and low adhesive interaction. More details on these theories are given later in this chapter.

Advanced models aiming at going beyond these extreme cases were developed in the 90s. In their numerical analyses, Muller et al. [150] and Greenwood [151] applied the Lennard-Jones potential to explore interactions within the intermediate regime. Maugis [152] derived closed-form solutions for the relationship between force, contact radius, and indentation in this regime by employing the Dugdale potential, which approximates the Lennard-Jones potential via a constant attractive force square well. Carpick et al. [153] refined the Maugis-Dugdale (MD) model for real-world indentation data by developing a general equation that connects force and contact radius (known as the Carpick-Ogletree-Salmeron or COS equation), closely mirroring the MD model. Similarly, Pietrement and Troyon [154] formulated a force-indentation relationship (Pietrement-Troyon or PT equation) that marginally deviates from the MD. As such, the COS and PT equations provide a practical approach for applying the MD model to experimental data.

Amidst various contact mechanics models, it is important to distinguish their differences and understand how the indenter behaves at each phase of the indentation and changes the force-distance curve. Lin et al. provided an insightful summary (Figure 2.3) that elucidated these differences. The initial column displays a diagram with the essential phases during the Hertzian indentation process with the respective force-distance curve for each phase. In the Hertz contact model, the indentation depth ( $\delta$ ), the exerted force ( $F_n$ ), and contact area ( $a$ ) are equal to zero at the point of initial contact (when the tip extends – approach – towards the sample surface) or at the separation point (also known as the pull-off point when the tip retracts from the sample surface). In the presence of adhesive forces, contact takes place due to these interactions. These non-zero interaction forces result in the deflection of the cantilever towards the sample surface.

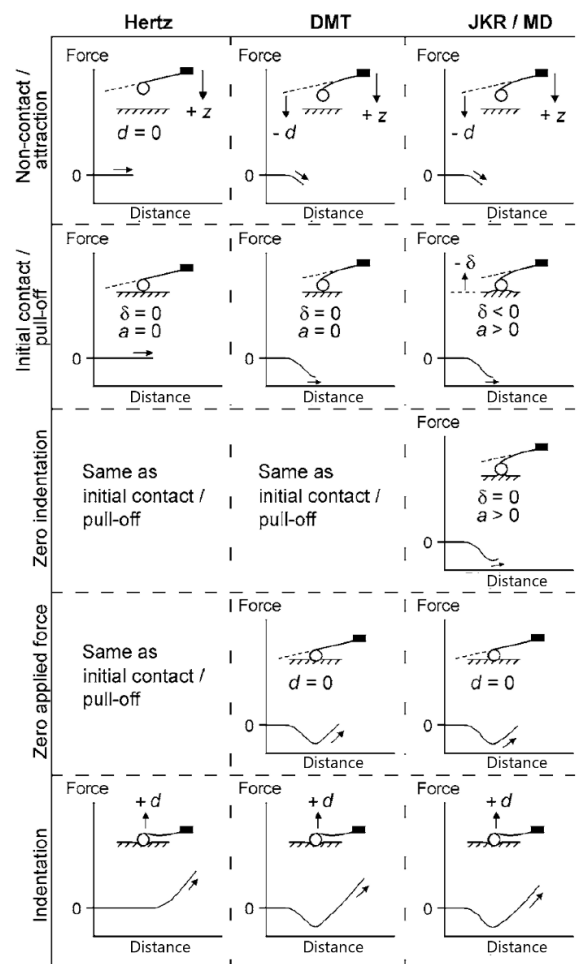


Figure 2.3 – Diagram of force-distance curves according to the Hertzian, DMT, JKR, and MD theories. Force-distance curves are displayed for the approach segment of the cycle. (Adapted from [146])

The relationship between the contact area and the force exerted is the primary factor that distinguishes the JKR and DMT theories. In DMT, when the cantilever restoring force balances the maximum adhesive force  $F_{ad}$ , the contact area becomes zero [155]. Thus, no indentation is observed. This phenomenon occurs during the initial contact as the tip comes close to the sample and at the pull-off point when the tip is retracted (Figure 2.3, second row from the top). In this same phase, in JKR theory, when the exerted force equals the adhesive force, the contact area is non-zero (Equation 3.4), causing a sudden contact or separation (during retraction) and negative indentation, justified by the sample deformation towards the indenter.

When probing soft biomechanical properties using AFM, the choice of the probe is a critical factor that determines the scales at which the physical quantities of interest are characterized. A micrometer-sized spherical probe averages the contribution of nano to the microscale contact area. This for instance allows to measure what stiffness is sensed by focal adhesion, which are  $\mu\text{m}^2$  pulling architectures. Nevertheless, due to the increased adhesion that can result from the larger contact area, it becomes necessary to use models that account for the adhesive interactions between the probe and the sample. While the MD theory offers an accurate way to account for the intermediate regime between the JKR and DMT models and includes negative indentation based on sample compliance, its practical application can be challenging. This is because of the absence of a direct relationship between force and indentation, which requires numerical iterations to determine multiple fitting parameters. As such, the MD theory will not be addressed in this work. Instead, the focus will be concentrated on the JKR and DMT models as they provide a straightforward analytical description of the adhesive interactions between the tip and sample. Nonetheless, careful consideration should be given when deciding on the most appropriate model to use for data processing when investigating the mechanical properties of soft biological samples. Integrating the concepts put forth by Lin et al. [146], Bouchonville and Nicolas developed a methodology [145] for AFM data processing, which offers guidelines for fitting adhesive force-distance curves. All these models address linear elastic deformations. But the experimental situation may deviate from the elastic regime. This can be checked by comparing the force-distance to curve to the elasto-adhesive fitting models. Indeed, for a spherical indenter, classic Hertz's model predicts that the force opposed by a material against an indenter, scales with the indentation as  $F_n \propto \delta^{3/2}$ , with  $F_n$  the loading force and  $\delta$  the indentation depth. Thus, when a material exhibits elastic behavior, plotting the indentation curve as  $F^{2/3}(\delta)$  yields a straight line. For experimental curves obtained on biological sample, the linear regime often limits to a range of deformation. This method thus allows to identify the elastic deformation range. This approach is analogous for conical or pyramidal indenters, but the plot should be  $F^{1/2}(\delta)$ .

However, as previously stated, this method can only be considered valid in the absence of adhesion between the tip and the sample. Nevertheless, Bouchonville et al showed that as a first-order assumption, adhesion contributes with similar scaling laws to the deformation of the material when indentation is performed with a spherical probe [70]. But even if the material responds elastically to the indentation, the quantification of the rigidity is biased by the adhesive interaction that pulls the probe into the material resulting in an overestimated Young's modulus [145]. As an example, Figure 2.4 shows a force-distance curve processed using the methodology proposed by Bouchonville and Nicolas.

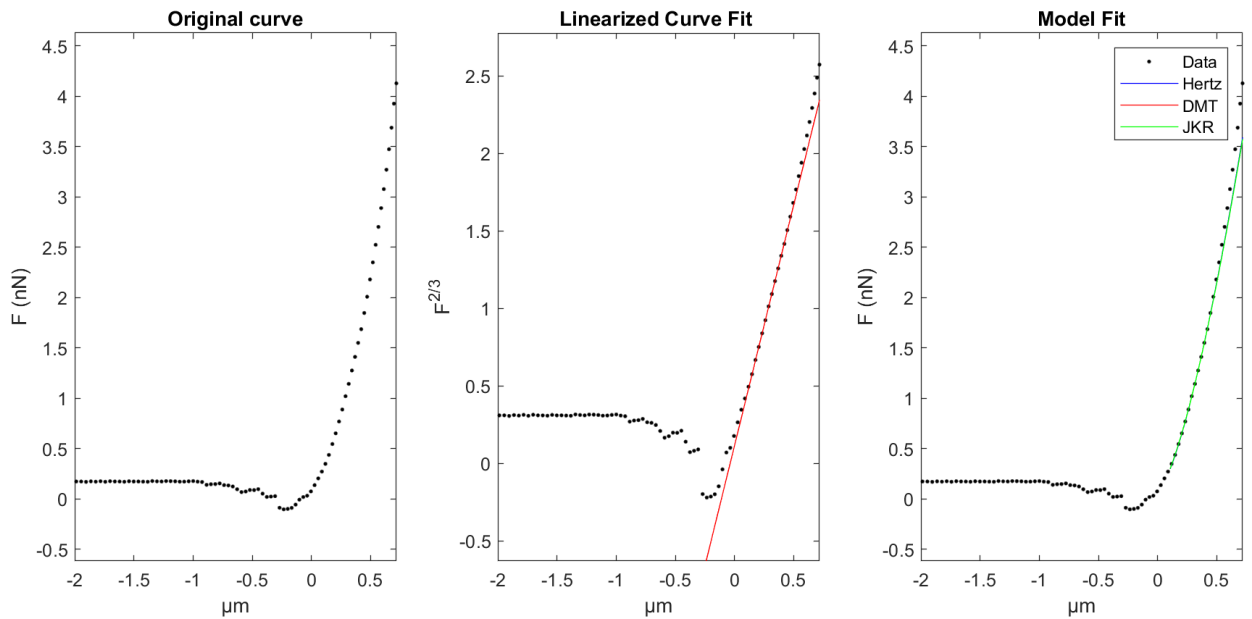


Figure 2.4 – On the left, the plot of the raw force-distance curve; on the middle, the linearization of the FD curve to select and fit the linear region; on the right, the original force-distance curve fitted for Hertz, DMT and JKR. In this example, using the Hertz model yielded a stiffness of 1.90 kPa, whereas DMT/JKR 1.52 kPa.

Assuming linear elasticity and no adhesion between the spherical probe and sample, the relationship between force and indentation is described by Hertz's law (Equation 3.1) with  $F_n$  the normal force,  $\delta$  the indentation depth,  $R$  the radius of the probe, and  $K$  the renormalized elastic modulus, related to the Young's modulus  $E$  and the Poisson's ratio  $\nu$  of the material:

$$F_n = KR^{\frac{1}{2}}\delta^{\frac{3}{2}} \quad (3.1)$$

$$K = \frac{4E}{3(1 - \nu^2)} \quad (3.2)$$

To account for adhesion between the tip and the sample, DMT and JKR models were both taken into consideration as we do not anticipate the relative strength of adhesion compared to compliance. JKR model applies to soft materials with high surface energies and probes with a large radius of curvature, thus concentrating elastic stresses at the edge of the contact. In this model, the adhesive interaction between the tip and the material dominates the elastic reaction force of the material, leading to surface attraction towards the tip [156]. JKR model is described by the following set of equations [147]:

$$\delta = \frac{a_{JKR}}{R} - \frac{4}{3} \sqrt{\frac{a_{JKR} F_{ad}}{RK}} \quad (3.3)$$

$$a_{JKR} = \frac{R}{K} (\sqrt{F_{ad}} + \sqrt{F_n + F_{ad}})^{\frac{2}{3}} \quad (3.4)$$

$$F_{ad} = \frac{3\pi}{2} \gamma R \quad (3.5)$$

where  $a_{JKR}$  is the contact radius and  $\gamma$  is the adhesion energy (in N/m or kPa· $\mu\text{m}$ ). Conversely, the DMT model is appropriate for materials with low surface energy and probes with a small radius. In this case, the adhesion energy barely deforms the surface. Adhesion behaves as a perturbation to the elastic response of the material, resulting in negligible indentation during the pull-off phase. DMT model is described by the following equations [148]:

$$\delta = \left( \frac{F_n + F_{ad}}{KR^{\frac{1}{2}}} \right)^{\frac{2}{3}} \quad (3.6)$$

$$F_{ad} = 2\pi\gamma R \quad (3.7)$$

For the sake of completion, the adhesion energy  $\gamma$  refers to the energy associated with the adhesive forces that occur when two surfaces come into contact. In the context of biological tissues being probed with a large tip, this would be the energy associated with the forces that cause the tip and the tissue to stick together. These forces can arise due to various factors, including van der Waals and electrostatic forces. Elastic energy, on the other hand, refers to the energy associated with the deformation of the material or tissue when a force is applied to it.

A dimensionless characteristic parameter [149], [150], [152] introduced by Tabor and further developed by Muller and Maugis allows for the distinction between the JKR and DMT models:

$$\mu \sim \left( \frac{R\gamma^2}{E^2} \right)^{1/3} / z_0 \quad (3.8)$$

with  $z_0$  representing the equilibrium distance associated with the attractive potential. This parameter measures the ratio of normal elastic deformation due to adhesion when no load is applied to the spatial range of adhesive forces themselves. Hence, large  $\mu$  indicates a strong short-range adhesion, favoring the JKR model, whereas values  $\mu \ll 1$  imply that adhesion forces beyond the contact region are significant, endorsing the DMT model. Ciavarella et al. [157] extensively reviewed the role of adhesion in contact mechanics and proposed a map to distinguish between the most appropriate model depending on the Tabor parameter and the dimensionless load (Figure 2.5).

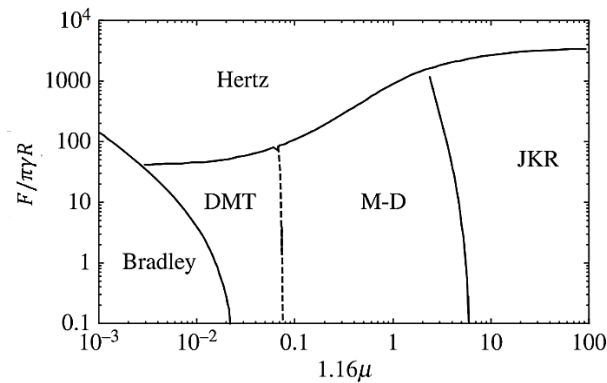


Figure 2.5 – Adhesion map for a spherical probe. The dimensionless load and the Tabor parameter  $\mu$  indicate the most appropriate model.  $F$  represents the normal indentation force. Adapted from [157].

Therefore, at a zeroth order approximation, the JKR model assumes that the indenting force,  $F_n$ , is essentially the interfacial force,  $F_{ad}$ . In contrast, under the DMT model, the loading force  $F_n$  opposes the elastic resistance of the material:  $F_n \gg F_{ad}$ , considering that this model presumes the deformation induced by indentation to align closely with Hertz's prediction. Thus, replacing  $F_{ad}$  by  $F_n$  in Equations 3.3 and 3.4 or neglecting  $F_{ad}$  in Equation 3.7 both lead to the same scaling law:  $F^{2/3} \propto \delta$ .

This scaling law aligns with the one outlined in Hertz's model (the purely elastic scenario), even though the adhesive interaction in the JKR model has a more significant impact on  $F_n$  than the elastic resistance resulting from indentation. Finally, this method allows finding the range of the force-distance curve that can be safely fitted to extract the elasto-adhesive parameters,  $K$  and  $\gamma$  of the material [145], and consequently the Young's modulus of the sample

## 2.2 MATERIALS AND METHODS

### 2.2.1 Preparation of the tissue sections

A total of 18 paired samples were obtained from Hospices Civil de Lyon (HCL). For each patient, one healthy and one cancerous lung biopsy were obtained, resulting in a total of 36 samples. Informed written consent was obtained from the patients or their families. We also received anonymized anatomopathology reports describing the gender, age, and grade of the tumor. Lung tissue samples were collected from the operating room during surgery and were immediately snap-frozen in liquid nitrogen. The unique morphology of lung tissue posed a few technical challenges for the cryopreparation and cutting of lung sections. To allow a precise and comprehensive evaluation of its structure, it was required to maintain the open architecture of the alveolar and bronchiolar spaces to preserve the tissue [158]. Non-fixed frozen tissues were embedded in OCT compound (optimal cutting temperature), then sections of 14  $\mu\text{m}$  thick – for histological staining – and its mirror sections of 100  $\mu\text{m}$  thickness – for AFM measurements – were cut using a cryostat (Leica Biosystems, 3050S) in triplicate. Thicker tissue sections were deposited on SuperFrost Ultra Plus™ GOLD glass slides (Thermo Scientific, USA) and immediately stored at  $-20^{\circ}\text{C}$ . Sections were characterized within two days of cutting. The thinner sections were quickly stained for toluidine blue, a basic thiazine metachromatic dye with a strong affinity for acidic tissue components [159]. The protocol consisted of a three-minute incubation at room temperature with a 1% Toluidine Blue (Sigma-Aldrich, USA) solution, followed by rinsing in distilled water and three minutes in 75% ethanol, full dehydration, and mounting with Eukitt ® (Kindler GmbH, Germany).

Stitched images of stained samples were captured using an inverted microscope (IX83, Olympus France, Rungis, France) at 10x magnification, which supported the selection of the region of interest (ROI) during AFM measurements. Tissue samples were incubated at  $37^{\circ}\text{C}$  on a hotplate for 10 minutes prior to measurement, and a hydrophobic pen (Dako pen, Agilent Technologies, USA) was used to draw an incubation space around the sample. Careful periodic washing was carried out with filtered PBS<sup>+/+</sup> buffer to remove OCT, detached cells or tissue debris. Next, the sample was immediately immersed in a droplet of filtered PBS<sup>+/+</sup> buffer + 0.01% Pluronic F-127 and measurements were performed within the next 1–2 hours per sample at room temperature. Given the restricted time frame of AFM experiments, it is unlikely that enzymatic activity exhibited by cells will significantly alter the resulting measurements and can therefore be considered negligible.

### 2.2.2 Biomechanical measurements of lung tissues using AFM

Young's moduli of lung tissue samples were measured on a Nanowizard II AFM (JPK Instruments, Berlin) in the force mapping or force volume mode. MLCT D tipless cantilevers (Bruker, Santa Barbara) with a nominal spring constant  $k = 0.03$  N/m were selected due to their capability to address Young's moduli between few tens of Pa and 100 kPa. Two types of measurements were performed on the tissue samples, one using the 15  $\mu\text{m}$  piezo scanner originally installed with the AFM and another of 100  $\mu\text{m}$  using the Cell Hesion® module, described in the next chapter. A polystyrene colloidal probe with a 10  $\mu\text{m}$  diameter was glued to the cantilever to average the elastic properties on a micron-sized area, i.e., averaging both cells and extracellular matrix mechanical properties. In this experiment, a Poisson's ratio of 0.42 was assumed [160]. Before initiating each experiment, optical sensitivity was determined by performing a single force curve on the surface of an infinitely stiff substrate, such as a plastic Petri dish filled with PBS<sup>+/+</sup> with 0.01% Pluronic F-127 and the cantilever spring constant was calibrated using the thermal noise method [161]. During this period, the tip was immersed in a PBS<sup>+/+</sup> solution with 0.01% Pluronic F-127 (poloxamer) to coat the probe, adding a hydrophobic layer to mitigate adhesion effects. Based on the unique characteristics of each sample, the approach, extension, and retraction parameters were slightly adapted to ensure optimal experimental conditions. Employing mirror sections from histological analysis, key target areas such as tumor or healthy regions were systematically probed in randomly distributed ROIs. Indentation depths were kept below 1  $\mu\text{m}$  by adjusting the nominal force set point within 2 to 4 nN to ensure exploitable force-distance curves. Feedback and approach parameters were: extend and retract speed 2  $\mu\text{m/s}$  setpoint force 4 nN, iGain 90 Hz, pGain 0.03. The acquired stiffness maps varied from 10x10 to 100x100  $\mu\text{m}$  with 5x5 to 10x10 pixels and represented at least from 25 to 100 force curves each. The significance was tested with a two-tailed t-test and a significance level ( $\alpha$ ) of 5%.

### 2.2.3 Data processing and analysis

Each force-indentation curve was pre-processed using the specialized processing software of the AFM, namely, JPKSPM Data Processing® 5.0.145, to extract the force-distance raw data of each curve. Exclusively retraction curves were considered, as they contain pertinent information regarding the potential contributions of adhesion forces to the collected data. To ensure the accuracy and relevance of the measured data, the selection of appropriate curves required careful consideration of the following criteria.



A well-defined baseline is necessary to serve as a reference point for determining the indentation depth. Additionally, the selected curve must exhibit an indentation depth exceeding 300 nm to ensure that the measured forces reflect the mechanical properties of the sample rather than tip-sample interactions. Moreover, the force range of the fit is desired to fall between 1 to 3 nN, which corresponds to typical cell-cell and cell-substrate interactions, but no strict limit was imposed. For each curve, a smooth filter was applied to remove noise, offset and tilt were subtracted to adjust the baseline, contact point was automatically determined with respect to the beginning of the vertical deflection, the slope was fitted using the Hertz model and elasticity was computed (Young's Modulus). Since the curve fitting performed by the JPK software uses Hertz model, it inevitably rejects the adhesion force between the tip and sample involved in this type of measurement. As this information is necessary to understand and retrieve the unbiased Young's modulus ( $E$ ) of the tissue, post-processing was imperative.

The force-distance curves, showcasing force (in nN) versus indentation (in  $\mu\text{m}$ ), were acquired and processed offline using a MATLAB-based custom algorithm. The algorithm allowed to highlight the region of the curve exhibiting elastic behavior, which was utilized for fitting. Subsequently, based on the methodology proposed by Bouchonville and Nicolas [145], data post-processing was conducted. By plotting the retract indentation curves with respect to  $F^{2/3}$ , the linear elastic behavior was transformed into a linear curve facilitating the identification of the curve segment accepting a straight line (Figure 2.6). Boundaries were manually marked after deviation of the curve, defining the indentation depth range on which the fitting model was applicable. Fitting models included Hertz, JKR and DMT models. Outputs of the fits were the Young's modulus, the adhesion energy, and the contact point. A proper estimation of the initial guess of the contact point proved to be a critical parameter necessary for data post-processing, particularly for adhesive force-distance curves, where its determination is often challenging [162].

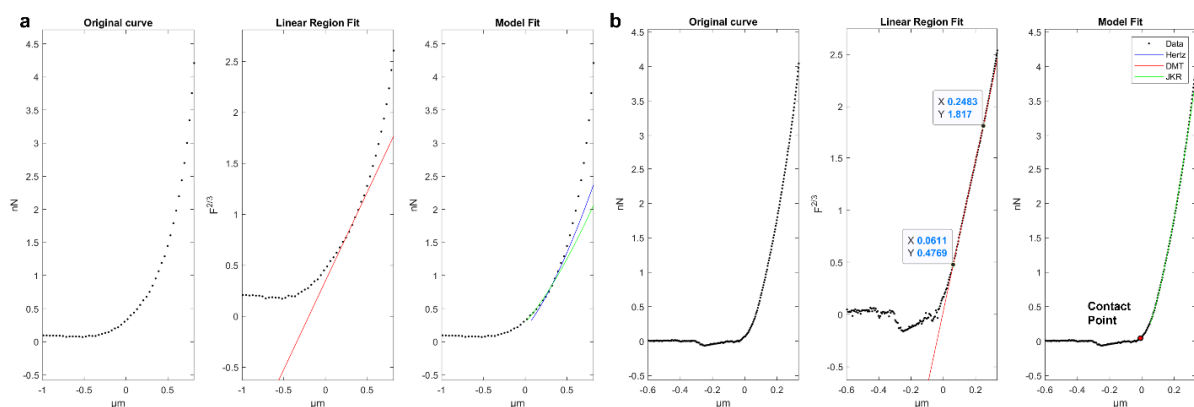


Figure 2.6 – Example of the original curve, linear region fit on  $F^{2/3}$ , model fit of rejected (a) and selected curve (b) with determination of contact point [77] and indentation values of the linear region.

The guess of this fit parameter is selected at the minimum of the adhesion well of the indentation curve for the DMT and JKR models and at the indentation that corresponds to  $F_n = 0$  for the Hertz model [70]. Finally, Young's moduli and adhesion energies were then calculated by fitting the curve in this range by Hertz, DMT, and JKR models with their respective residuals.

#### 2.2.4 Data selection for analysis optimization

AFM data acquisition can generate a substantial number of curves per sample, making post-processing analysis time-consuming and labor-intensive. In this study, each sample represents a biopsy from either healthy or tumor tissue, with each sample measured in triplicate. On average, 400 curves are obtained per sample, resulting in over 40,000 curves to process. Given the significant workload, data optimization was imperative. A criterion was established to include a minimum of 100 curves per patient for each tissue type. This selection criterion was chosen arbitrarily but validated for one sample by comparing two sets of data: the median of 100 randomly chosen points from the 400-point dataset and the overall sample median. The analysis demonstrated no significant statistical difference between the medians of the two sets. Moreover, it was observed that statistics fell within the standard deviation of the patient dataset. This approach effectively streamlined data handling without compromising the integrity of the results.

#### 2.2.5 Statistical analysis

Continuous data are presented as the mean of median values accompanied by their standard deviation, while categorical data are expressed as percentages. The Shapiro-Wilk test was employed to assess data normality. Depending on the data type and distribution, analysis was conducted using Student's t-test, Mann-Whitney U test, and Kruskal-Wallis test.

## 2.3 RESULTS

### 2.3.1 Histological comparison between healthy and tumor human lung tissues

The primary objective of conducting histological staining was to analyze tissue structures at the microscopic level, facilitating the selection of optimal sections for AFM measurements and pinpointing target locations to probe on the mirror cut of 100  $\mu\text{m}$ . Due to its high compliance and hollow architectural structure, lung tissue presents significant challenges in terms of sectioning for histological staining. Toluidine blue was selected as the staining agent, given its straightforward application and effectiveness. This staining method is based on the principle of metachromasia, a phenomenon wherein a dye absorbs light at distinct wavelengths depending on its concentration, thereby altering its color without any change in its chemical composition. Toluidine Blue thus stains acidic groups, such as DNA, nucleic acids, as well as polysaccharides and glycans, with blue levels that relate to the local concentration of electronegative groups on the surface of the tissue [159]. Figure 2.7 presents histological tissue staining for two sets of healthy and tumor sections from biopsies 14EX00110 and 13EX00166.

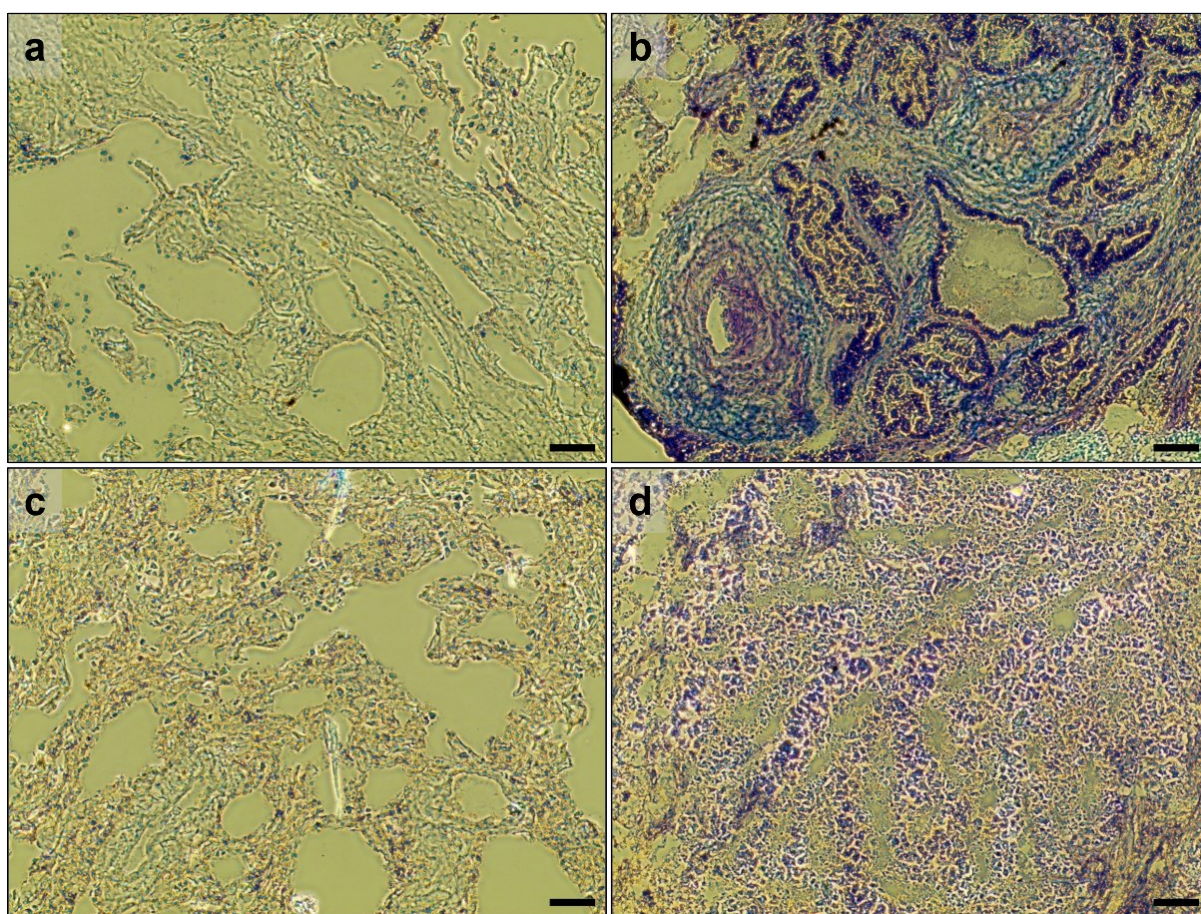


Figure 2.7 – Toluidine blue-stained tissue sections of paired biopsies. (a-b) Healthy and acinar adenocarcinoma tissues from patient 14EX00110. (c-d) Healthy and solid adenocarcinoma tissues from patient 13EX00166. Bars, 100  $\mu\text{m}$ .

Based on these histological sections and the evaluation by an anatomopathologist (Dr. Lara Chalabreysse, Hospices Civils de Lyon), it was possible to identify the main characteristics of healthy and both kind of tumor lung tissue. Healthy tissue samples displayed a lace-like characteristic lung morphology showing alveoli and bronchioles, whereas tumor tissues demonstrated a loss of typical morphology and regions with a more compact density of cells. Acinar adenocarcinomas showed rounded, oval-shaped malignant glands infiltrating fibrous stroma. Solid adenocarcinomas featured dense nests of large epithelial cells with abundant cytoplasm and pronounced nuclei (Figure 2.7b and d). Regions of interests (ROI) were pinpointed using microscopy before measurement and their positions were coarsely estimated during AFM assessment, relying on the corresponding mirror histological sections for reference.

### 2.3.2 Human tumor lung tissue is stiffer than healthy lung tissue

The methodology outlined in section 2.2.2 was utilized to measure the Young's modulus ( $E$ ) of human lung tissues as 18 paired samples of healthy and tumor tissues. This section presents the results of the AFM measurements conducted on these samples, considering both healthy and adenocarcinoma subtypes found in the tumor tissues. The samples were categorized as acinar and solid and analyzed for their respective mechanical properties.

In this thesis, a total of 20509 force-distance curves for healthy tissue and 21621 for tumor tissue were acquired through force volume mode that resulted in 321 and 384 maps, respectively. Map sizes varied from 10x10  $\mu\text{m}$  to 100x100  $\mu\text{m}$ , with resolutions ranging from 5x5 to 10x10 pixels, depending on the ROI. The overall scanned areas covered 0.16  $\text{mm}^2$  for healthy tissue and 0.17  $\text{mm}^2$  for tumor tissue, with an average biopsy surface of  $12 \pm 6 \text{ mm}^2$  and  $23 \pm 7 \text{ mm}^2$ , respectively. After the initial pre-processing, 52% of the curves were retained for further analysis, resulting in a total of 21792 curves. A quantitative summary of the analyzed data can be found in Table 2.1.

Table 2.1 – Summary of pre- and post-processing of force-distance curves.

	Healthy	Tumor	Total
# Curves	20509	21621	42130
Maps	321	384	705
Total Area ( $\text{mm}^2$ )	<b>0.16</b>	<b>0.17</b>	<b>0.33</b>
Pre-processing	11106	10686	21792
%	54%	49%	52%
Post-processing	<b>2224</b>	<b>2151</b>	<b>4375</b>
%	20%	20%	20%

Table 2.2 summarizes the median Young's Moduli, their respective multiplicative standard deviations, and dispersions. The dispersion is represented not by the standard deviation but by the interval containing approximately 2/3 (68.3%) of the values around the median (equivalent to one standard deviation). These results provide a comprehensive overview of the mechanical characteristics of healthy and tumor lung tissues and may serve as the foundation for future research on the mechanical properties of other tissues.

Table 2.2 – Median Young's moduli, dispersion, multiplicative standard deviation (SD), and number of curves (n) processed using JKR model.

Biopsy/ Patient	Median <i>E</i> Healthy (kPa)	Dispersion (kPa)	Mult. SD (*)	<i>n</i>	Median <i>E</i> Tumor (kPa)	Dispersion (kPa)	Mult. SD (*)	<i>n</i>	Type
13EX00024	1.8	[1.2; 2.8]	1.6	100	1.6	[1; 2.2]	1.5	98	Acinar
15EH04158	1.1	[0.3; 2.4]	2.5	114	2.7	[1.4; 5.1]	1.9	100	Acinar
14EX00110	2.0	[1.2; 4]	1.7	100	2.8	[1.1; 5.4]	2.4	100	Acinar
14EX00144	0.9	[0.6; 1.5]	1.5	109	2.9	[0.8; 4.2]	2.2	88	Acinar
15EH04592	1.7	[0.9; 3.8]	2.0	108	2.4	[1.4; 5.3]	2.0	98	Acinar
13EX00132	1.0	[0.4; 2.9]	2.7	128	1.6	[0.8; 4.2]	2.2	119	Acinar
14EX00043	1.8	[0.7; 3.3]	2.0	148	1.6	[0.8; 3.5]	2.1	151	Acinar
15EH06497	0.8	[0.4; 2.2]	2.4	147	2.4	[0.5; 7.6]	3.4	122	Acinar
15EH07257	1.6	[0.8; 3.6]	2.0	97	2.2	[0.7; 5.2]	2.9	110	Acinar
16EH00922	1.1	[0.4; 2.7]	2.7	140	3.8	[1.7; 6.7]	2.0	110	Acinar
16EH07456	1.3	[0.7; 3]	2.1	133	4.5	[1.8; 10.6]	2.2	147	Acinar
15EH08065	0.8	[0.3; 2.5]	2.8	132	2.3	[1.2; 4.8]	1.9	107	Solid
15EH09880	2.1	[0.8; 3.5]	2.1	139	2.3	[1.4; 4.7]	1.8	151	Solid
13EX00027	1.7	[0.9; 3.1]	1.9	134	2.4	[1.1; 4]	1.8	99	Solid
13EX00048	1.7	[1; 3.4]	1.9	109	2.0	[1.3; 4.7]	2.0	111	Solid
13EX00166	1.7	[0.8; 3.2]	2.0	151	3.2	[1.3; 6.9]	2.4	197	Solid
14EX00047	1.7	[0.9; 4]	1.9	120	2.9	[1.5; 6.4]	2.0	160	Solid
15EX00026	1.4	[0.6; 3.6]	2.5	115	2.3	[1; 4.9]	2.2	83	Solid
<b>Mean Acinar</b>	1.4	± 0.4	-	1324	2.6	± 0.9	-	1243	
<b>Mean Solid</b>	1.6	± 0.4	-	900	2.5	± 0.2	-	908	
<b>Mean All</b>	1.4	± 0.4	-	2224	2.5	± 0.7	-	2151	

Young's moduli were computed considering Hertz, JKR and DMT models. As explained later JKR model offers a better description of the tissues than Hertz or DMT models. For this reason, we mainly present results from the JKR model. Data optimization process, detailed in section 2.2.3, effectively reduced the post-processing workload while preserving the statistical significance of the data. Hence, after post-processing, 20% of the representative pre-processed curves were exploited. Figure 2.8 displays the lognormal stiffness distributions for healthy tissue compared to acinar and solid adenocarcinoma lung tissues, respectively (Appendix A).

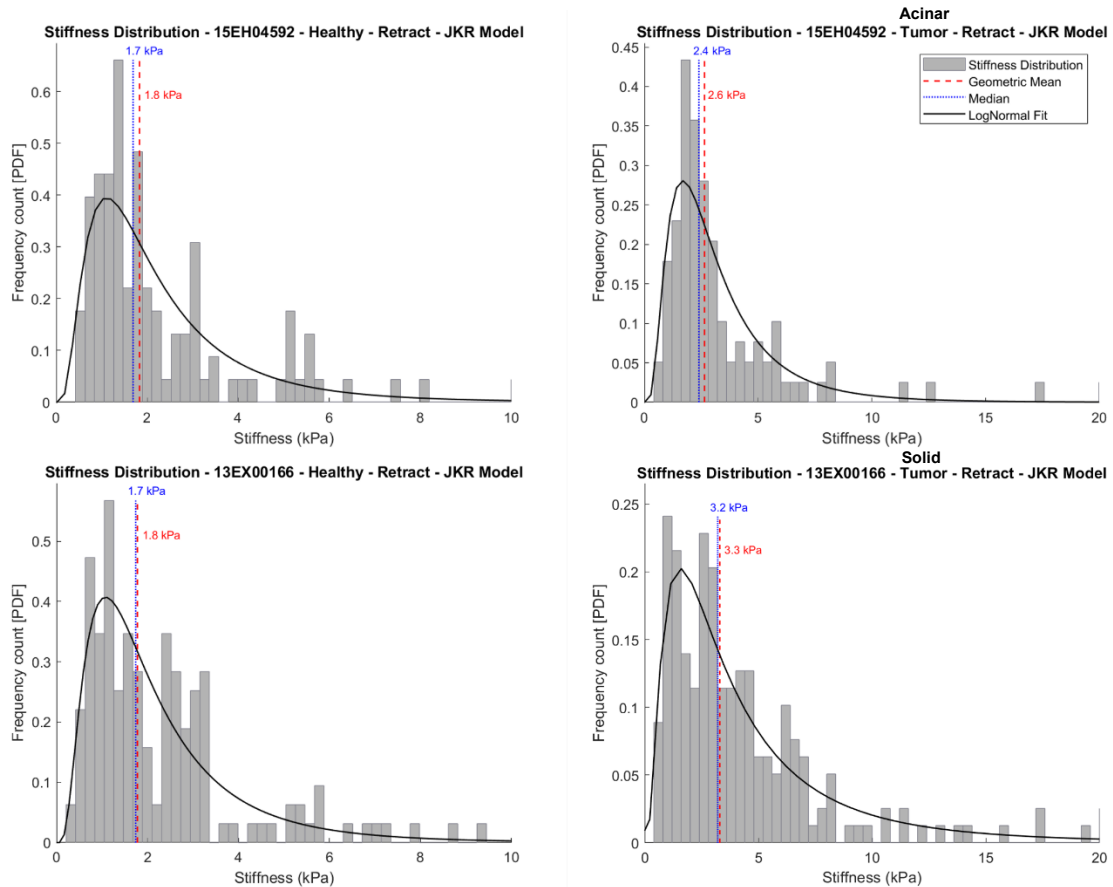


Figure 2.8 – Healthy and adenocarcinoma lung tissue stiffness distributions of 15EH04592 (acinar) and 13EX00166 (solid). Histograms are fitted for a lognormal distribution. The blue dotted lines represent the median and the red dashed lines the geometric mean of the distribution. Values are reported in Table 2.2.

A comparative analysis of the stiffness distribution in healthy and tumor lung tissues reveals a shift to the higher values for tumor tissue distribution. Mean stiffness values were obtained by averaging the median rigidities for each patient within each tissue type. Note that there was no significant difference in the mean stiffnesses of the histological adenocarcinoma subtypes, with values of  $2.6 \pm 0.9$  kPa for the acinar subtype and  $2.5 \pm 0.2$  kPa for the solid subtype (t-test,  $p=0.80$ ). The mean stiffness for tumor tissue is  $2.5 \pm 0.7$  kPa, while healthy tissue exhibits a mean stiffness of  $1.4 \pm 0.4$  kPa (Figure 2.8a). These findings indicate that adenocarcinoma lung tissue is not only stiffer than healthy lung tissue but also displays a higher degree of heterogeneity in stiffness values, as shown by the larger standard deviation between patients.

This is further evidenced by the wider distribution of stiffness values present in tumor tissue. Figure 2.9b provides a visual representation of the individual stiffness values for both healthy and tumor tissues in each patient. It is worth mentioning that only in two instances out of 18 (15EH09880 Solid and 15EX00026 Acinar) did the healthy tissue exhibit slightly higher stiffness than the tumor tissue.

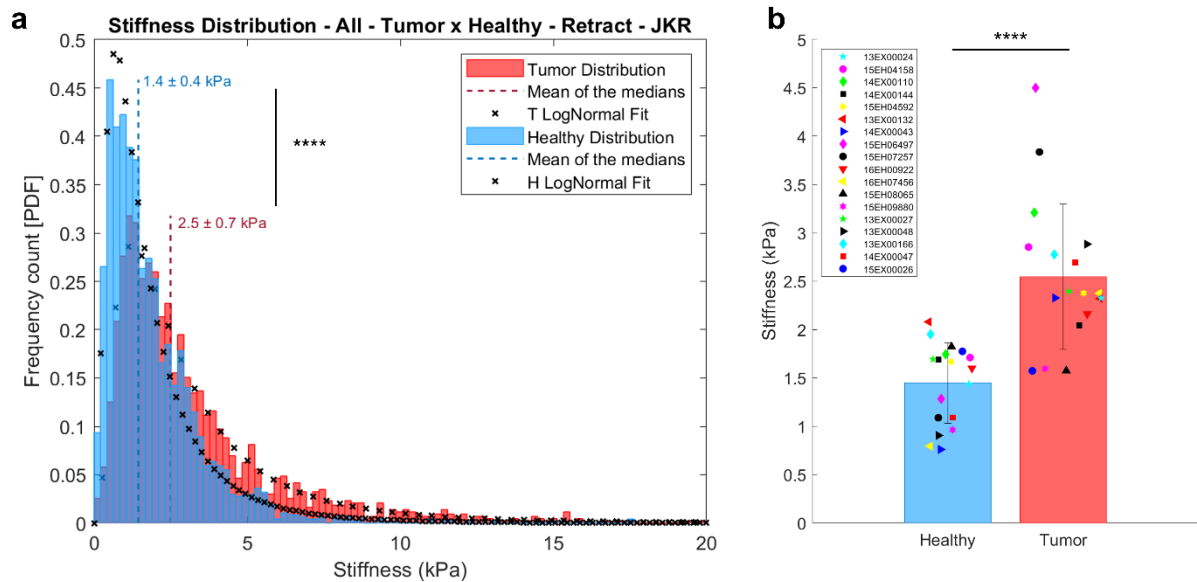


Figure 2.9 – (a) Healthy and tumor lung tissue stiffness distributions of the cohort; \*\*\*\*  $p < 0.0001$ ; (b) Box scatter plot of healthy and tumor tissue median stiffnesses.

Utilizing a two-tailed t-test and a significance level ( $\alpha$ ) of 5%, inferential statistical analysis of the datasets demonstrated a statistically significant difference between healthy and tumor tissues, with  $p < 0.0001$ . This indicates that the observed difference in stiffness between healthy and tumor tissues is not due to chance but rather a genuine difference in their mechanical properties. When examining acinar and solid tissues individually, as illustrated in Figure 2.10, this difference persisted despite the lower number of patients considered in the statistics: the p-values increased by one order of magnitude but remained below 0.01.

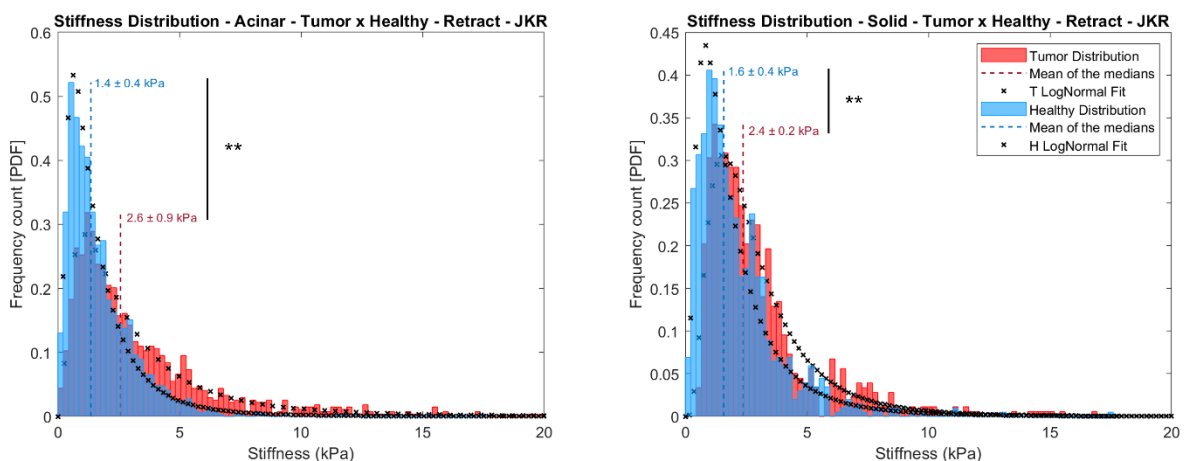


Figure 2.10 – Acinar (Left) and solid (Right) x healthy lung tissue stiffness distributions; \*\*  $p \leq 0.01$ .

It is also worth mentioning that the analysis was first conducted with 13 patients. In the second part of the thesis, five new samples were added, which did not substantially impact the mean stiffness values. However, the inclusion of more samples did strengthen the statistical analysis, leading to increased significance when compared to former datasets. This statistical analysis further supports the conclusion that there is a significant difference in stiffness between healthy and tumor lung tissues.

### 2.3.3 Both healthy and tumor lung tissues show a predominant linear elastic behavior at the microscale

Results from the micromechanical characterizations revealed a predominant linear elastic behavior in both healthy and tumor lung tissues. Upon post-processing, only a relatively small portion of curves deviated from this expected behavior. Specifically, rejection rates based on departure from linear elastic behavior were recorded at 6.8% for healthy tissues and 4.5% for tumor tissues post-processing. It is important to note that some curves were excluded during pre-processing due to the lack of an established baseline, insufficient indentation range, or the presence of discontinuity representing measurement artifacts.

### 2.3.4 Importance of considering the adhesive interaction of the tip with the tissue

In evaluating the benefits of an elasto-adhesive model compared to a Hertzian model, differences in the fitting parameters predicted by all described models were examined and are presented in Table 2.3. The mean stiffness obtained through the Hertz model exceeded the values from elasto-adhesive models on average by 27%. In the scenario where an elasto-adhesive model was unnecessary, it is anticipated that the fitting parameters would converge towards those defined by Hertz's model, consistent with a situation in which the interfacial energy tends to zero ( $\gamma \rightarrow 0$ ). However, results indicated otherwise comforting the need of using an elasto-adhesive description. Contact mechanics analysis of lung tissues revealed differences in the adhesion energy between healthy and tumor samples (Table 2.3).

Table 2.3 – Young's moduli, characteristic length and interfacial energies of healthy and tumor lung tissues obtained from the fits by Hertz, JKR and DMT models, and the intervals that account for 68.3% of the measurements.

	Healthy			Tumor		
	Hertz	DMT	JKR	Hertz	DMT	JKR
Median $E$ (kPa)	1.83	1.45	1.45	3.10	2.44	2.44
Dispersion for $E$ (kPa)	[0.8 4.0]	[0.6 3.1]	[0.6 3.1]	[1.4 7.3]	[1.1 5.7]	[1.1 5.7]
Mean of medians $E$ (kPa)	1.86	1.45	1.44	3.22	2.55	2.54
Standard Deviation $E$ (kPa)	0.53	0.42	0.42	0.92	0.75	0.75
$\mu z_0$ ( $\mu\text{m}$ )	NA	2.6	3.5	NA	1.2	1.6
Mean $\gamma$ (kPa $\cdot\mu\text{m}$ )	NA	3.0	4.4	NA	1.7	2.4



Approximately 75% of the analyzed curves exhibited no significant adhesion, suggesting that the Hertz model would be adequate for these instances. However, the remaining 25% displayed notable adhesion work, which was substantial enough to cause a shift in the Young's Moduli compared to values predicted by the Hertz model. Healthy lung tissues showed a mean adhesive energy  $\gamma_{HJKR} = 4.4 \text{ kPa}\cdot\mu\text{m}$ , nearly double the average for tumor tissues  $\gamma_{TJKR} = 2.4 \text{ kPa}\cdot\mu\text{m}$ . This decrease in adhesive energy for tumor tissues is suggestive of alterations in the properties of the extracellular matrix, potentially contributing to tumor progression and invasion. Moreover, the characteristic Tabor length  $\mu z_0$  (Eq. 3.8), indicative of the balance between adhesive forces and elastic deformation, was found to be on the order of micrometers. This substantial characteristic length indicates a significant interplay between adhesion forces and elastic deformation over a relatively large distance within the contact area compared to the characteristic distance of interaction of the surface potential,  $z_0$ . For  $z_0$  ranging from 100 to 400 nm, the typical distance between the zero-indentation position (contact point) and the zero-displacement position of the cantilever, the characteristic parameter  $\mu$  (Tabor parameter [149]) calculated for DMT and JKR was only one order of magnitude away from unity (Table 2.4), suggesting that JKR model would be more suitable than DMT, that is valid when  $\mu \ll 1$  (Figure 2.5).

Table 2.4 – Tabor parameter  $\mu$  for DMT and JKR analysis, for  $z_0$  ranging from 100 to 400 nm.

	Healthy		Tumor	
	DMT	JKR	DMT	JKR
$\mu (z_0 = 100 \text{ nm})$	26	35	12	16
$\mu (z_0 = 400 \text{ nm})$	7	9	3	4

Nonetheless, given the characteristic lengths identified in our study, it appears that the contact mechanics of both healthy and tumor lung tissues straddle between the DMT and JKR. Therefore, intermediate models like Maugis-Dugdale (MD) and Pietrement and Troyon (PT) should be considered, as they might offer a more accurate representation of the elasto-adhesive behavior. These models bridge the gap between the DMT and JKR models, accounting for the interplay of adhesion and deformation in a transitional regime. However, as DMT provides values not significantly different from those from JKR, for the sake of simplicity, we made the choice to limit them. Upon analyzing the fitting parameters from acinar and solid adenocarcinoma listed in Table 2.5, we confirmed the previous observations. For both tumor subtypes, characteristic lengths and adhesive energies were lower when compared to their healthy counterparts. These observations suggest that compositional differences may exist between solid and acinar adenocarcinomas, which could contribute to the slightly distinct mechanical properties.

Table 2.5 – Young’s moduli, characteristic length and interfacial energies for acinar and solid adenocarcinomas obtained from the fits by Hertz, JKR and DMT models, and the intervals that account for 68.3% of the measurements.

		Healthy Counterpart			Tumor		
		Hertz	DMT	JKR	Hertz	DMT	JKR
Acinar	Median $E$ (kPa)	1.71	1.32	1.32	3.04	2.35	2.35
	Dispersion for $E$ (kPa)	[0.7 3.8]	[0.7 2.9]	[0.7 2.9]	[1.3 7.4]	[1.0 5.5]	[1.0 5.6]
	Mean of medians $E$ (kPa)	1.76	1.36	1.36	3.29	2.59	2.59
	Standard Deviation $E$ (kPa)	0.52	0.42	0.42	1.13	0.93	0.93
	$\mu z_0$ ( $\mu\text{m}$ )	NA	3.1	4.1	NA	1.4	1.7
	Mean $\gamma$ (kPa- $\mu\text{m}$ )	NA	3.7	5.5	NA	2.1	2.8
Solid	Median $E$ (kPa)	2.06	1.65	1.65	3.17	2.51	2.51
	Dispersion for $E$ (kPa)	[0.9 4.1]	[0.6 3.2]	[0.6 3.2]	[1.5 7.2]	[1.2 5.8]	[1.2 5.8]
	Mean of medians $E$ (kPa)	2.00	1.59	1.59	3.10	2.49	2.49
	Standard Deviation $E$ (kPa)	0.56	0.42	0.42	0.48	0.40	0.40
	$\mu z_0$ ( $\mu\text{m}$ )	NA	1.8	2.5	NA	1.0	1.3
	Mean $\gamma$ (kPa- $\mu\text{m}$ )	NA	3.0	4.4	NA	1.7	2.4

### 2.3.5 Correlation of tissue stiffness with the clinical characteristics of the patients

The patient cohort analyzed in this thesis is summarized in Table 2.6. These parameters encompass demographic factors, stages of the disease, histological types, smoking status, and the presence of specific genetic mutations. The data in this table serves as a basis for correlating tissue stiffness with the clinical characteristics of patients.

Table 2.6 – Clinical characteristics of a cohort of 18 patients.

Clinical Characteristics	Statistics
Age, years [Median, 95% CI]	66 [58, 74]
Female	5/18 (28%)
Male	13/18 (72%)
Stage I (A&B)	7/18 (39%)
Stage II (A&B)	4/18 (22%)
Stage III (A)	7/18 (39%)
Acinar adenocarcinoma	11/18 (61%)
Solid adenocarcinoma	7/18 (39%)
Confirmed smoker	14/18 (78%)
Unconfirmed smoker	4/18 (22%)
KRAS mutation	9/18 (50%)
EGFR mutation	1/18 (6%)
Unconfirmed mutation	8/18 (44%)

In the analysis of the relationship between tissue stiffness and various patient characteristics, no statistically significant associations were found between stiffness and factors such as age, gender, tumor type, and cancer stage at the 0.05 significance level. The absence of significant differences in stiffness between genders (t-test:  $p = 0.93$ ) and tumor types (Mann-Whitney U test:  $p = 0.88$ ) suggests that these factors do not play a major role in determining stiffness (Figure 2.11a). Additionally, the Kruskal-Wallis test (non-parametric one-way ANOVA) of stiffnesses across cancer stages (Figure 2.11b) did not reveal any significant differences in median stiffness values ( $p = 0.16$ ). Furthermore, Figure 2.11c displays the lack of correlation between age and stiffness of the tumor (Spearman's rank correlation test:  $p = 0.63$ ) and healthy tissue (Spearman's rank correlation test:  $p = 0.23$ ).

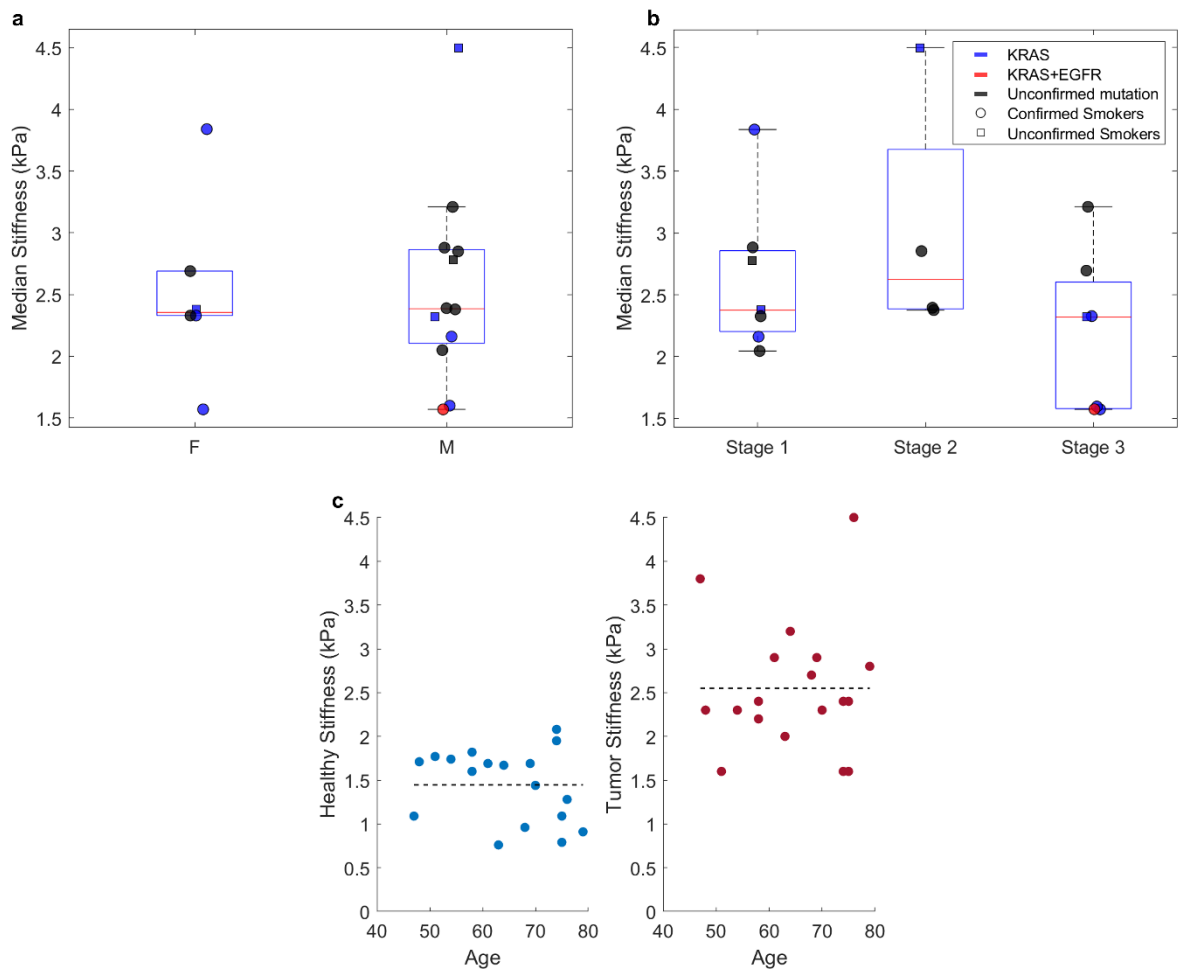


Figure 2.11– Comparative box plots illustrating the distribution of stiffness values. (a) Stiffness values are grouped by gender, with female (F) and male (M) samples shown side by side, highlighting the similarities in stiffness distributions between the two groups. (b) Stiffness values are categorized by cancer stage (1, 2, and 3), illustrating the distribution of stiffness within each stage and enabling a visual comparison of the medians and interquartile ranges across stages. (c) Scatter plots and linear regression lines for healthy and tumor tissue stiffness as a function of age. (Left) Healthy tissue stiffness (blue circles) plotted against age and (Right) tumor tissue stiffness (red circles) plotted against age with their respective mean stiffness values (black dashed line).

## 2.4 DISCUSSION

The mechanical properties of cells and tissues are intrinsically connected to vital physiological processes such as proliferation [163], morphogenesis [164], stem cell differentiation [165], migration [166], and adhesion [167]. Cells constantly experience mechanical pressure from various sources, including shear stress, contractile stress from their actomyosin cytoskeleton, neighboring cells, spatial confinement, gravity, and hydrostatic pressure [168]. These factors have been demonstrated to impact key molecular processes, such as ion channel activity, gene regulation, and protein expression [169],[170]. Disruptions in the biomechanical processes responsible for maintaining cellular equilibrium can result in modifications to the molecular and physiological characteristics of tissues, ultimately impacting organ function and leading to the development of various diseases. There has been an increasing focus on exploring how alterations in cellular mechanical properties may be associated with pathologies across a range of organs or play a role in the deterioration of tissue during the aging process [171],[172]. Moreover, over the last decade, an increasing number of studies have reported the importance of biomechanics in several aspects of tumor growth and notably in metastasis [173],[174]. Most of these studies have focused on ECM elasticity [58], [175], [176], while others on single cells nanomechanical signature [177],[178] and few on tissue elasticity [69],[70],[179]. Technical challenges in measuring complex and heterogeneous tissues, the interdisciplinary nature of the field requiring collaboration between multiple areas of expertise, a historical focus on cellular mechanisms and the difficulty of accessing biopsies might justify the fewer studies.

Lung mechanical properties, such as compliance, are crucial for proper biological functioning. The non-linear high elasticity of the whole organ and its mechanical robustness allow for hundreds of millions of respiratory cycles [180]. However, the lung is a mechanically and structurally heterogeneous tissue, featuring areas of high and low stiffness and porosity, making it challenging to characterize comprehensively at the cell scale. Normal lung parenchyma derives its mechanical integrity from the ECM, which is primarily composed of structural proteins (collagen and elastin), proteoglycan, glycosaminoglycan, and adhesion proteins [180],[181]. Similarly, during oncogenesis, lung tumor tissues develop mechanical integrity through the remodeling of the ECM [182]–[184]. A recent study demonstrated that human lung tumor tissue generates endogenous type I collagen, contributing to overall survival, cancer cell differentiation, and tumor clone formation [185], though the underlying mechanisms require further investigation. From a mechanical point of view, the modification of the content or nature of the ECM is expected to impact the microscale stiffness of the tissue [69], as we will discuss in Chapter 4.

The work described in this chapter sheds light on the fundamental properties of lung tissue mechanics, more specifically on the quantitative analysis of the stiffness of healthy and tumor lung tissue using IT-AFM. Probe functionalization with F-127 Pluronic [186] facilitated access to the tissue surface with reduced adhesion effects, enabling the acquisition of numerous force-distance curves. Indeed, in the absence of surface treatment, force-distance curves could not be obtained with a spherical probe of 10  $\mu\text{m}$  diameter: the AFM tip remained attached to the tumor tissue in the entire retraction length of the piezo, set at 12  $\mu\text{m}$ . A pyramidal tip was performing slightly better, although often failing to detach too. The use of a spherical probe was nevertheless important because the objective was to measure the stiffness of the tissue averaged over an area of the order of 1 square micron, which a spherical probe of this diameter allows. In contrast, a pyramid tip, whose apex is of the order of 20 nm, would have enabled the measurement of the stiffness of individual fibers of the ECM [179], thus providing stiffness data representative of the nanoscale texture. As mentioned in the introduction, we focus here on the microscale texture. Our hypothesis is that this scale plays a significant role in the mechanosensitive adaptation of cells to their environment because of the micrometer size of major players in stiffness sensing, namely, the focal adhesions. This does not exclude that nanoscale stiffness texture is also of importance. In the present chapter, where we focus on mean stiffness values, the use of a sharper tip could result in a larger dispersion of the data (and therefore, the need to acquire more) but not change the mean value. Using a probe with a larger contact area will, however, be of importance when analyzing the texture of the tissues in Chapter 3.

Regarding the clinical characteristics of the patients, no statistically significant correlations were found between stiffness and factors such as age, gender, tumor type and tissue type of the cohort. This result differs from the work by Sicard et al. [187], who showed that healthy lung tissues from the parenchyma were stiffening with age. Considering their findings, healthy tissues from the older patients should be, on average, 1 kPa stiffer than those of the youngest patients. This is clearly not the case (Figure 2.11). Several reasons could explain the difference: (i) the cohort we analyzed is composed of patients that suffer from cancer and that have been exposed to treatments while in their study, the tissues were collected from donors whose lungs were not suitable for transplantation; (ii) most of them have been exposed to cigarette smoke as active or passive smokers; (iii) they are aged of 46 to 80 years old, while their study was involving younger patients, aged of 11 to 60 years old; (iv) and finally their study did not account for the adhesive interaction of the tip with the tissue (a spherical probe of 2.5  $\mu\text{m}$  radius), which could lead to variability in the measurements that reflects changes in adhesiveness, rather than in stiffness.

These findings contribute to the understanding of the factors influencing stiffness in patients with cancer and emphasize the importance of further investigation to identify potential determinants of stiffness in this context.

Hertz or Sneddon are considered the most common models when the elastic modulus is the variable of interest. To accurately apply these models, certain assumptions must hold true, including a linear elastic correlation between indentation and the absence of viscosity or adhesion effects experienced by the AFM tip and sample [145]. Elasto-adhesive models were found to be necessary, given the presence of adhesion observed in the force-distance curves. As the portion of curves with a nonlinear behavior remained marginal (below 10%), elasto-adhesive models were considered as the most reliable description of the mechanics of these tissues.

Calculation of the adhesive energies  $\gamma$  and the Tabor parameter  $\mu$  suggest that the contact mechanics descriptions of the tissues orient to the JKR theory but also present some attributes of the DMT theory. This complexity arises due to the potential contribution of adhesion forces acting at larger distances beyond the immediate contact area. This observation is supported by the micrometer-sized characteristic length  $\mu z_0$ , which is comparable to the estimated contact radii, of the order of half the probe radius. This characteristic length demonstrates the wider impact area of these surface forces beyond just the contact points.

Thus, comprehensive models such as MD or PT are recommended to account for intermediate elasto-adhesive regime behavior. Comparative analysis of the biomechanical properties of both healthy and tumor tissues using Hertz, DMT and JKR has led to valuable observations. When applying the models to calculate Young's modulus, significant differences were observed. For tumor tissues, Young's modulus values derived from the Hertz model were consistently higher than those obtained using either the DMT or JKR models. Specifically, the Hertz model resulted in an average Young's modulus increase of 26.2%. This similar trend was observed in healthy tissues, resulting in a 28.1% increase in the average stiffness comparing Hertz to DMT or JKR models. This discrepancy between the models, particularly between the Hertz model and DMT or JKR models, can be attributed to the latter two models incorporating adhesive interactions, for which the Hertz model does not account. The adhesive forces considered in the elasto-adhesive models appear to decrease the effective stiffness, emphasizing that the impact of adhesion on the measured mechanical properties of tissues cannot be neglected. The stiffness differences between the DMT and JKR models proved to be non-significant. Due to the lack of significant differences, the choice between these two models may not considerably impact the final results in the context of this study.

Results showed that tumor tissues present greater stiffness when compared to healthy tissues. The mean stiffness of the healthy tissue was found to be  $1.4 \pm 0.4$  kPa considering 18 patients, while the mean stiffness of the tumor tissue was  $2.5 \pm 0.7$  kPa. This difference remains significant when acinar and solid histological subtypes are analyzed separately, with respectively 11 and 7 patients (t-test,  $p < 0.01$ ). It is to be noted that the mean stiffnesses of the histological adenocarcinoma subtypes are not significantly different:  $2.6 \pm 0.9$  kPa for the acinar subtype and  $2.5 \pm 0.2$  kPa for the solid subtype (t-test,  $p = 0.80$ ). Values obtained for the healthy tissue are in line with reported macro-scale measurements from porcine lung ( $1.4 \pm 0.4$  kPa) [188], micro-scale measurements from mice lung parenchyma (median  $E \sim 1.5$  kPa) [189] and  $1.87 \pm 0.95$  kPa human parenchyma [187]. Moreover, our findings demonstrate consistency with existing literature, even with its heavy reliance on the Hertz model. The stiffness calculated for healthy lung tissues of  $1.86 \pm 0.53$  kPa (Hertz) solidly aligns with previously reported values, adding robustness to the results.

This characterization of lung adenocarcinoma tissues is the first to be done locally, using an indentation technique, although some studies have been conducted on healthy tissues. A surprising result is the fact that acinar and solid histological subtypes do not exhibit significant differences in their mean mechanical properties, although the histological staining with toluidine blue showed quite different cell organizations, with more compact cells in the solid subtype and a more heterogeneous composition in the acinar subtype (Figure 2.6). It is, nevertheless, to be noted that the dispersion between patients is larger in the acinar subtype compared to the solid one (36% versus 8%) (Table 2.2). This large difference can hardly be attributed to the lower number of patients with solid subtypes (7 versus 11). It could, however, be related to the larger heterogeneity in the composition of the acinar subtype, as depicted in Figure 2.6. This aspect will be further discussed in Chapter 3.

The Poisson's ratio of 0.42 for lung tissue considered in this study is derived from the literature, specifically from macroscopic measurements [160]. Investigation of Poisson's ratio at the micro-scale has not been conducted yet. For most biomaterials, Poisson's ratio typically ranges between 0.4 and 0.5, mainly due to their high-water content. Within this range, the factor  $1/(1-\nu^2)$  from the Hertz model varies modestly from 1.19 to 1.33, indicating that reasonable fluctuations in Poisson's ratio exert only minor effects on the reported modulus [189].

The determination of Poisson's ratio for both tissue types falls outside the scope of this thesis, however, it is worth noting that a methodology was developed by Kalcioglu et al. [190] to investigate the poroelastic properties of a polyacrylamide hydrogel model at the microscale. This method include the Poisson's ratio among the fitting parameters, thus allowing its determination. This approach is anticipated to be adapted for tissues in future research.

The mean stiffness values were calculated as the average of the median rigidities for each patient in each tissue to provide a more representative measure of tissue stiffness. Median stiffness values were chosen for each patient because the median is less sensitive to outliers or extreme values than the mean. This is particularly important in the context of biological samples, where there can be substantial variability and heterogeneity. By calculating the median rigidity for each patient, the resulting statistic represents the central tendency of stiffness values for that patient. Moreover, the use of multiplicative standard deviations for representing the stiffness dispersion in Table 2.2 is justified by the nature of the lognormal distribution. The standard deviation for a lognormal distribution may not provide an accurate or intuitive representation of the dispersion. The reason is that the lognormal distribution is right skewed with a long tail, and the standard deviation can be heavily influenced by extreme values. This could lead to a misleading interpretation. On the other hand, the multiplicative standard deviation, which is derived from the standard deviation of the logarithm of the data, better captures the distribution's inherent multiplicative nature and provides a more meaningful understanding of the dispersion in the original scale.

In summary, this chapter has provided valuable insights into the mechanical properties of healthy and tumor lung tissues. In the upcoming chapter, the focus will be on describing the method to acquire large rigidity maps and analyze the stiffness texture in tissues. The analysis will generate output parameters essential for mask design, which will serve as critical inputs for fabricating gray-level masks. This comprehensive approach will not only deepen the understanding of stiffness texture in both healthy and tumor lung tissues but also facilitate the creation of relevant mechano-mimetic culture substrates.



## CHAPTER 3

---

### STUDY OF STIFFNESS TEXTURES IN TISSUES

### 3 ÉTUDE DES TEXTURES DE RIGIDITÉ DANS LES TISSUS

Dans ce chapitre, nous nous concentrons sur l'étude des textures de rigidité dans les tissus pulmonaires sains et tumoraux afin de développer des hydrogels mécano-mimétiques avec une hétérogénéité de rigidité pour les applications de culture cellulaire. Une étape cruciale pour atteindre cet objectif a impliqué le développement d'une méthodologie pour acquérir des cartes à grande échelle sur les tissus des patients en utilisant l'AFM. Contrairement aux précédentes mesures AFM utilisant un scanner avec un déplacement de 15  $\mu\text{m}$ , un scanner piézo plus grand était nécessaire pour éviter l'adhésion de la pointe pendant la rétraction et les obstacles pendant le mouvement latéral. Dans un premier temps, une analyse comparative des caractérisations d'hydrogel a été réalisée en comparant le scanner piézo 15  $\mu\text{m}$  et 100  $\mu\text{m}$ , en utilisant des pointes sphériques et pyramidales.

Par la suite, des cartes de rigidité de tissus pulmonaires sains et tumoraux provenant de treize patients ont été obtenues, suivies d'un traitement d'image et d'une analyse pour extraire les descripteurs de forme. Les descripteurs de forme sont des paramètres morphologiques utilisés pour caractériser et différencier les propriétés géométriques des objets ou des motifs. Une analyse statistique de ces descripteurs de forme a fourni des paramètres de conception qui ont aidé à la mise en œuvre d'un algorithme personnalisé innovant. Une analyse des attributs statistiques associés à ces descripteurs de forme a fourni les paramètres de conception nécessaires. Ceux-ci ont été employés dans la création de masques de niveau de gris, qui ont ensuite facilité la production de substrats mécano-mimétiques à base d'hydrogel. Ce processus est détaillé plus en profondeur dans le Chapitre 4.

Nous présentons ensuite les matériaux et les méthodes employés pour obtenir les résultats expérimentaux, y compris l'acquisition de cartes de rigidité, le traitement d'image, et l'analyse statistique des descripteurs de forme. Le chapitre présente également la comparaison des textures de rigidité saine et tumorale telles qu'elles sont représentées par leurs cartes de rigidité respectives et la procédure pour extraire les motifs de rigidité. Enfin, nous discutons des implications de la texture de rigidité des tissus dans la conception de motifs pertinents et des défis associés à ce développement technologique.

### 3 STUDY OF STIFFNESS TEXTURES IN TISSUES

In this chapter, we focus on investigating stiffness textures in healthy and tumor lung tissues to develop mechano-mimetic hydrogels with stiffness heterogeneity for cell culture applications. A critical step towards achieving this goal involved the development of a methodology for acquiring large force maps on patients' tissues using AFM. In contrast to previous AFM measurements employing scanners with 15  $\mu\text{m}$  displacement, a larger piezo scanner was required to circumvent tip adhesion during retraction and obstacles during lateral movement. Before measurements on patients' tissues, a comparative analysis of hydrogel characterizations was conducted using the 15  $\mu\text{m}$  and 100  $\mu\text{m}$  piezo scanners, employing spherical and pyramidal tips.

Subsequently, rigidity maps of healthy and tumor lung tissues from thirteen patients were obtained, followed by image processing and analysis to extract shape descriptors. Shape descriptors are morphological parameters used to characterize and differentiate the geometric properties of objects or patterns. A statistical analysis of the attributes associated with these shape descriptors supplied the requisite design parameters. These were employed in the creation of gray-level masks, which subsequently facilitated the production of hydrogel-based mechano-mimetic substrates. This process is delineated in more detail in Chapter 4. We next present the materials and methods employed in obtaining experimental results, including rigidity map acquisition, image processing, and statistical analysis of shape descriptors. The chapter also features the comparison of healthy and tumor stiffness textures as represented by their respective rigidity maps and the procedure for extracting rigidity patterns. Finally, we discuss the implications of tissue stiffness texture in designing relevant patterns and the challenges associated with this technological development.

### 3.1 FUNDAMENTAL CONCEPTS

#### 3.1.1 Stiffness heterogeneity in biological samples

As extensively described in Chapter 2, the straightforward method for assessing mechanical properties with AFM involves pressing the probe into the sample and tracking the force, which corresponds to the cantilever's deflection, as well as the probe's displacement in a force-distance curve. These force-distance curves, obtained during both the approach and withdrawal of the probe, capture the mechanical deformation and reaction of the sample when subjected to stress. They can be acquired in single-frequency (force modulation), where the probe sweeps the surface as a driving signal prompts the cantilever to oscillate (Figure 3.1a). Mechanical properties of the sample can be obtained from the AC component of the cantilever's deflection signal. In a position-dependent mode (force mapping) (Figure 3.1b), spectroscopy based on force-distance is used to map the mechanical properties of a biological system pixel-by-pixel during imaging, outputting a rigidity map or an elastograph [191]. Alternatively, the force can be charted against time in force-time curves, which are notably handy when maintaining the indenter at constant indentation depth [192] or exerting a steady force [193]. Those mechanical properties are especially valuable when samples exhibit viscoelastic [194] or time-dependent properties [195] (Figure 3.1c,d).

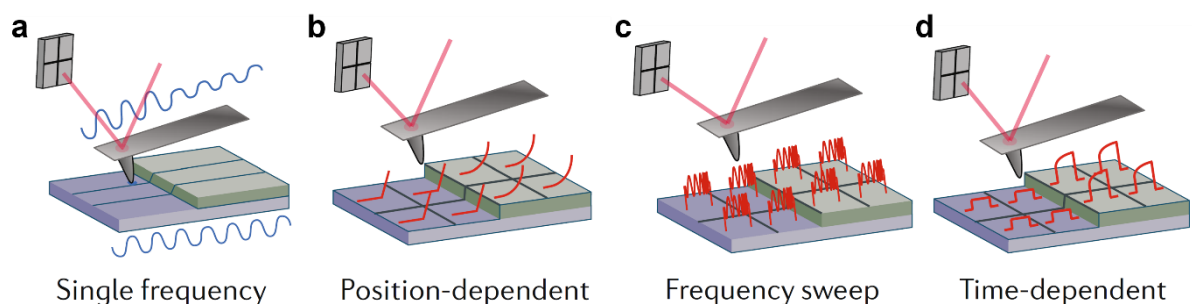


Figure 3.1 – Different modes of AFM force map acquisition (a) Single-frequency (b) Position-dependent (c) Frequency sweep (d) Time-dependent. Adapted from Krieg et al. [142]

In order to determine the Young's modulus from the apparent stiffness obtained through AFM measurements, it is crucial to compute the applied mechanical stress. This stress corresponds to the force exerted per unit contact area between the probe and the sample (expressed in Pa or  $Nm^{-2}$ ). Estimating probe-sample interactions becomes challenging with deeper indentations, especially when using common pyramidal probes. This issue can be mitigated by employing cylindrical or spherical probes. In the context of complex biological systems, sharp probes evaluate mechanical properties only at the local level, yielding nanomechanical signatures of tissue [174], [179],[196] or cell components [178]. This approach provides a characterization of the stiffness texture at the nanoscale.

Another scale of interest is the microscale, which is the scale of cell focal adhesions. Focal adhesions are assemblies of proteins that connect the extracellular matrix to the intern contractile machinery of the cell [197], [198] (Figure 3.2a). These structures transmit cell traction forces to the outside which in turn allow cells to sense the mechanical properties of the extracellular environment [167],[199] (Figure 3.2b) and are known to decrease their area in soft substrates [200] (Figure 3.2c).

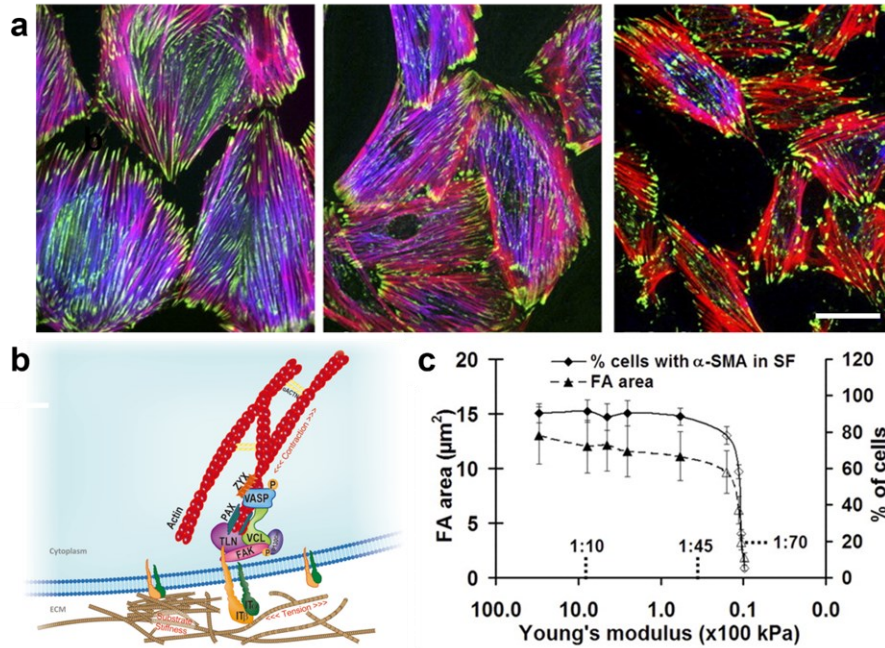


Figure 3.2 – (a) REF-52 myofibroblasts focal adhesions stained for vinculin (green),  $\alpha$ -SMA (blue), and F-actin (phalloidin; red) after standard fixation [200] Bar: 20  $\mu$ m). (b) Schematic representation of the main mechanosensing players involved in cell-ECM interaction at the focal adhesion (FA) site. Alterations in tension, stiffness, or other mechanical stimuli in the extracellular environment are detected by clusters of integrins, which respond by changing their morphology or distribution, and this in turn recruits focal adhesion kinases (FAK) [199]. (c) Focal adhesion size as a function of substrate stiffness [200].

The measured stiffness is of course dependent on the size of the indenter [201]. A sharp pyramidal indenter with a contact surface of few  $\text{nm}^2$  may measure individual stiff fibers from the extracellular matrix as well as soft cell bodies, while spherical probes with  $\mu\text{m}^2$  contact area may average them. Here we focus on the microscale texture of rigidity since it is known that stiffness sensing in focal adhesions is permitted by the collective organization of proteins at the microscale while sparse integrin molecules do not allow the construction of the complex molecular architecture at the origin of force transmission [202]. An effective solution has been the use of micrometer-sized spheres that can be glued at the edge of the cantilever and appropriately functionalized to reduce adhesion effects [186]. Using this approach, several publications demonstrated the heterogeneity at the microscale of different tissues such as healthy and tumor human pituitary gland [203], liver [204], breast, cervix [205] and murine

hippocampus [206]. Nevertheless, an important aspect present in a number of studies is the limited area over which force maps are acquired, typically confined to a few tens of micrometers squared [179]. This restricted region is inadequate for capturing a comprehensive representation of the texture of the tissue stiffness. Fortunately, with the advancement of AFM technology, manufacturers have begun to produce instruments with more extensive spatial capabilities, such as piezo scanners with xyz ranges of 300x300x300  $\mu\text{m}^3$  that allow for seamless stitching during imaging. This enhancement provides increased flexibility and robustness when measuring extensive areas.

Interestingly, although not considering adhesion models, a state-of-the-art study [205] published by Fuhs et al. in 2022 showcased the acquisition of rigidity maps for human breast and cervix carcinomas by automating the process across areas as large as 1  $\text{mm}^2$  while maintaining a spatial resolution of 10  $\mu\text{m}$  (Figure 3.3). Their results revealed broad rigidity distributions and the coexistence of jammed and unjammed areas in the tissues, contributing to cancer cell motility and mechanical stability.

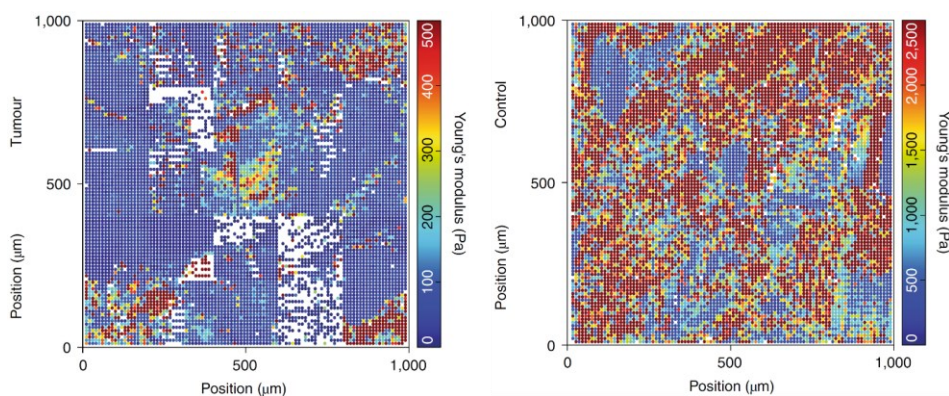


Figure 3.3 – Example of AFM rigidity maps of cervix healthy tissues (left) and tumor tissue (right) showing more heterogeneity in tumor tissue. Adapted from Fuhs et al. [205].

While numerous studies have primarily focused on understanding the fundamental aspects of mechanical properties heterogeneity in relation to specific oncological phenomena, one of the main objectives of this work is directed toward a practical application consisting in translating the stiffness heterogeneity or rigidity texture into hydrogels. By exploring tissue stiffness patterns present in rigidity maps and extracting their shape descriptors, we can develop novel mechano-mimetic hydrogels that approximate the mechanical environment of native tissues for cell culture studies. In this work, neither a large piezo scanner nor a motorized stage was accessible. The study was conducted by indenting individual force maps of size 100 x 100  $\mu\text{m}^2$ . A large extent piezo of 100  $\mu\text{m}$  (CellHesion module) was nevertheless required to analyze the lung tissues over these large areas, in order to overcome the topography (arising, for example, from the presence of alveoli) and high adhesion that was not sufficiently mitigated by the tip surface treatment described in Chapter 2.

### 3.1.2 Shape descriptors

In the historical context of image processing and machine vision, shape descriptors are central for object recognition, classification, and comparison [207]. Shape descriptors are quantitative features. They provide a mathematical representation of an object or pattern shape by capturing morphological attributes [208]. These parameters quantify the geometric and topological properties of objects in images, enabling efficient representation and comparison [209].

As early as the 1960s, researchers started investigating shape descriptors to analyze images. Pioneering work by Hu introduced a set of moment invariants, which provided a foundation for shape-based recognition methods [210]. Invariant moments played an essential role in object recognition, as they enabled the identification of objects despite alterations in position, orientation, and size. During the 1990s and early 2000s, the field witnessed the development of numerous shape descriptors, applied from biological shape analysis [211], [212] to enhancing machine vision system performance. Innovative methods, such as Fourier-based shape representation, boundary encoding using chain codes, and Zernike-based moment analysis, emerged as powerful tools for more precise shape characterization [213]. Shape descriptors were valuable in extracting meaningful features from images, paving the way for comprehensive image analysis tasks such as identifying objects, classifying patterns, and retrieving similar images.

The 2010s witnessed a paradigm shift as deep learning and convolutional neural networks (CNNs) revolutionized the field. Krizhevsky, Sutskever, and Hinton's seminal work on AlexNet demonstrated the immense potential of CNNs, leading to their widespread adoption [214]. At present, the fusion of shape descriptors with these advanced machine learning approaches has significantly expanded the potential of image processing and machine vision systems and are deeply rooted in diverse applications, including autonomous vehicles, facial recognition, medical imaging, and augmented reality, reshaping industries, and our daily lives.

Although modern deep learning architectures have shifted towards learning hierarchical features automatically, the knowledge of shape descriptors remains essential in certain applications where traditional techniques are still effective or when simplified interpretability is sufficient.

Following a simplified approach, which will be further elaborated in the discussion section, basic shape descriptors are extracted from threshold binary images of rigidity maps. A rigidity map is an output of force mapping AFM, comprised of a 2D matrix that exhibits a set of rigidity values (kPa) measured at a fixed pitch throughout a specific area, as depicted in Figure 3.4.

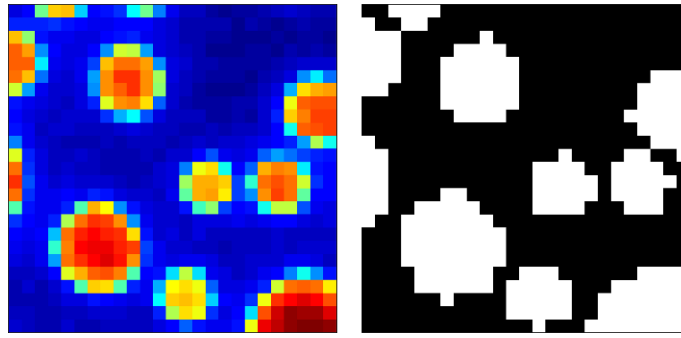


Figure 3.4 – Example of rigidity map (left) and binarized map after applying an arbitrary rigidity threshold.

Binarization using a threshold or ceiling value is a common technique for converting grayscale or color images into binary images [215]. This step requires selecting a specific rigidity value as the threshold. Values that exceed the threshold are given a value of one (white), marking the foreground, while those beneath the threshold are assigned a value of zero (black), representing the background. Determining the appropriate threshold is crucial for delineating the rigidity patterns and their surrounding environment. This decision strongly influences the size of patterns employed in the mask design and can ultimately impact the resulting stiffness heterogeneity of the hydrogel.

The most used class of numerical shape descriptors combines size parameters to produce dimensionless ratios. Among dozens of simple shape descriptors that have been described [216], [217], only a few of them are necessary for this incipient approach. The description of each shape descriptor considered, and their respective formula is listed in Table 3.1.

Table 3.1 – Basic shape descriptors definitions and their corresponding formula.

Shape Descriptor	Definition	Formula
Aspect Ratio	Ratio of the major axis length to the minor axis length of an object, reflecting the elongation of the shape	$\frac{Major\ axis\ length}{Minor\ axis\ length}$
Circularity	Compares a shape to a circle by relating its area and perimeter, with values close to 1 indicating more circular shapes	$\frac{4\ \pi\ Area}{Perimeter^2}$
Solidity	Measures a shape's convexity by comparing its area to the area of its convex hull, with values closer to 1 indicating higher convexity	$\frac{Area\ of\ shape}{Area\ of\ convex\ hull}$



## 3.2 MATERIALS AND METHODS

### 3.2.1 Mechanical characterization using AFM with CellHesion Module

After cryosectioning thirteen paired biopsies to a thickness of 100  $\mu\text{m}$ , the tissue sections may not be entirely flat when placed on glass slides, resulting in height variations of around 20  $\mu\text{m}$ . The use of the CellHesion module was justified due to the need to access distances beyond this height. Designed for integration with the JPK NanoWizard AFM II head and controller, it replaces the standard stage by incorporating the AFM with an optical microscope. Equipped with an additional z-piezo the module reaches 100  $\mu\text{m}$  range, enabling the mechanical characterization of individual cells, substrates, and tissues that demand large pulling distances. In standard AFM mode, the AFM head piezos control all three axes of movement while the sample remains stationary. In CellHesion mode, the head piezos manage x- and y-axis movements, while the CellHesion stage piezo handles z-movements moving the sample vertically, keeping the head z-piezo fully retracted throughout the process. During acquisition, the PI closed-loop PIFOC mounted on the objective moves synchronously with the sample stage, maintaining the plane of interest in focus throughout force measurements. Rigidity maps should be large enough to assess the rigidity texture of tissue samples. As the scanning area increases, so does the step the cantilever travels, meaning that lateral tip movement can potentially encounter obstacles on the tissue, disrupting the cantilever or even halting the measurement. The module provides an extended pull range, sufficient to avoid such obstacles during the measurement process.

In contrast to the standard piezo scanner with a 15  $\mu\text{m}$  range, the CellHesion module has a different measurement mechanism: the cantilever remains stationary while the sample stage lifts, causing an indentation. Despite the reversed mechanism, it respects the same contact mechanics law derived for a spherical tip indentation. To maintain a similar indentation depth as in the measurements with the smaller piezo scanner, we used the same 10  $\mu\text{m}$  diameter probe functionalized with F-127 Pluronic, and the following parameters: maximum force, 4 nN; z-speed, 2  $\mu\text{m s}^{-1}$ ; retract z-length, 30  $\mu\text{m}$ ; capture rate, 2048 Hz. Feedback and approach parameters were adjusted: z-closed-loop was enabled, relative setpoint force 1 nN, iGain 3 Hz, pGain 0.001, with a target height of 10  $\mu\text{m}$  and a timeout of 10-15 seconds. The z-length for extension was reduced since the extend curve was not exploited. In force mapping mode, at least two 100x100  $\mu\text{m}$  maps, spaced by a 10  $\mu\text{m}$  step, were acquired per patient, enabling visualization of rigidity variations in large fields sampled at the cell-sized scale. The biopsies of the 18 patients were analyzed, although the initial five biopsies were discarded because the characterization protocol was still being implemented. Acquisition time varied from 25 to 50

min for one map. The long acquisition time was due to the low scanning velocity used for the indentation of 2  $\mu\text{m/s}$ . Faster scanning velocities were not tested as lung tissues may show a viscoelastic behavior [218]. The scanning velocity was chosen in reference to brain tissues that are known to show viscoelasticity [219].

### 3.2.2 Image processing of rigidity maps

We addressed whether tumor or healthy tissues have intrinsic features in their rigidity maps. Shapes and sizes of the rigidity patterns were therefore analyzed after image processing. 52 rigidity textured maps ( $100 \times 100 \mu\text{m}^2$ ), two per patient per tissue type, with  $10 \times 10$  pixels were processed in MATLAB and ImageJ. A custom-made MATLAB algorithm was implemented to generate rigidity threshold binary masks. Then, ImageJ was used to isolate the areas in the maps above the predefined rigidity threshold and calculate their shape descriptors such as area, aspect ratio, circularity, and solidity (Table 3.1). The rigidity threshold was arbitrarily set to 2.9 kPa, corresponding to the 70<sup>th</sup> percentile of the tumor stiffness distribution. This threshold was applied to both healthy and tumor tissues to enable a comparison between the two. The selection of two maps per sample proved adequate for providing a statistically significant representation of the stiffness textures of the tissues, as each map contained at least 60 data points that were exploitable out of 100 indented points.

### 3.2.3 Statistical Analysis

Statistical analysis was conducted on the shape descriptors and rigidity patterned area distributions for the thirteen healthy and tumor tissues. Prior to applying the Mann-Whitney U test, Shapiro-Wilk test was used to assess the normality of the datasets. For non-normally distributed data, both tests were applied to the rigidity patterned areas of both datasets, considering a significance level ( $\alpha$ ) of 5%.

### 3.3 RESULTS

#### 3.3.1 Comparison of stiffness measurement using the standard piezo scanner and CellHesion

Before acquiring rigidity maps, measurements from different piezo scanners were compared to assess their reliability in determining rigidity. Polyacrylamide hydrogels with varying uniform stiffness values were fabricated (details in section 5.2.3) by controlling photopolymerization through timed UV exposure [220]. These hydrogels were then characterized using both piezo systems, along with 10  $\mu\text{m}$  diameter spherical and pyramidal tips (Figure 3.5). On a given gel, indentations were carried out at neighbor positions keeping speed and z-length (ZL) constant. Single force-distance curves and force maps ranging from 2x2 to 8x8 pixels, covering 10x10  $\mu\text{m}$ , were collected.

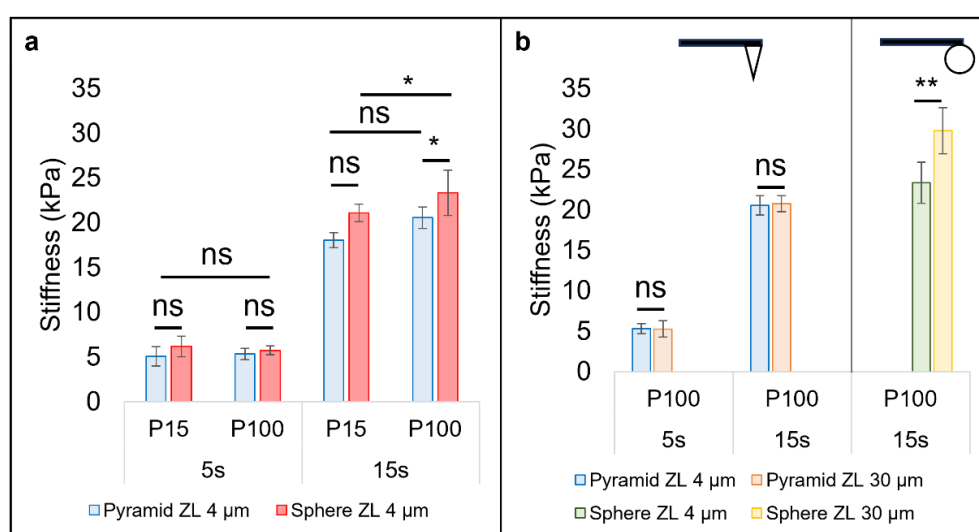


Figure 3.5 – (a) Hydrogel stiffness as a function of indenter type and piezo size at different UV illumination times with fixed set-point force at 4 nN, retract speed at 2  $\mu\text{m}/\text{s}$  and z-length at 4  $\mu\text{m}$ . (b) Comparison between measurements made with 4 and 30  $\mu\text{m}$  retract z-length. Values are represented as mean  $\pm$  SEM.

For pyramidal probe measurements, curve fitting was performed considering the Sneddon Model, which inherently neglects the adhesion force between the tip and the sample. Similarly, data processing for spherical probes utilized the Hertz model. For 5s hydrogels, no statistically significant differences were observed between measurements from the 15  $\mu\text{m}$  and 100  $\mu\text{m}$  (CellHesion) piezo scanners or between indenters. However, a statistically significant difference was observed for stiffer hydrogels (15s) when using the longer piezo (Figure 3.5a). Moreover, the use of the CellHesion module and spherical probe at 30  $\mu\text{m}$  retract z-length led to higher stiffness (Figure 3.5b). A reason could be due to non-linearity of the piezo when travelling at large distance or the impact of hydrodynamic drag force on the cantilever.

### 3.3.2 Acquisition of large rigidity maps

Rigidity maps were acquired for 13 paired biopsy samples. As a result, a total of 52 rigidity maps, consisting of 26 for healthy and 26 for tumor tissues. Experimental constraints, such as measurement speed, acquisition time, and tissue section biological viability, limited the number of obtained maps. However, the collected data were sufficient for conducting a statistically meaningful analysis. Figure 3.6 and Figure 3.7 illustrates examples of textured rigidity maps of acinar and solid lung adenocarcinoma and their healthy counterpart, respectively.

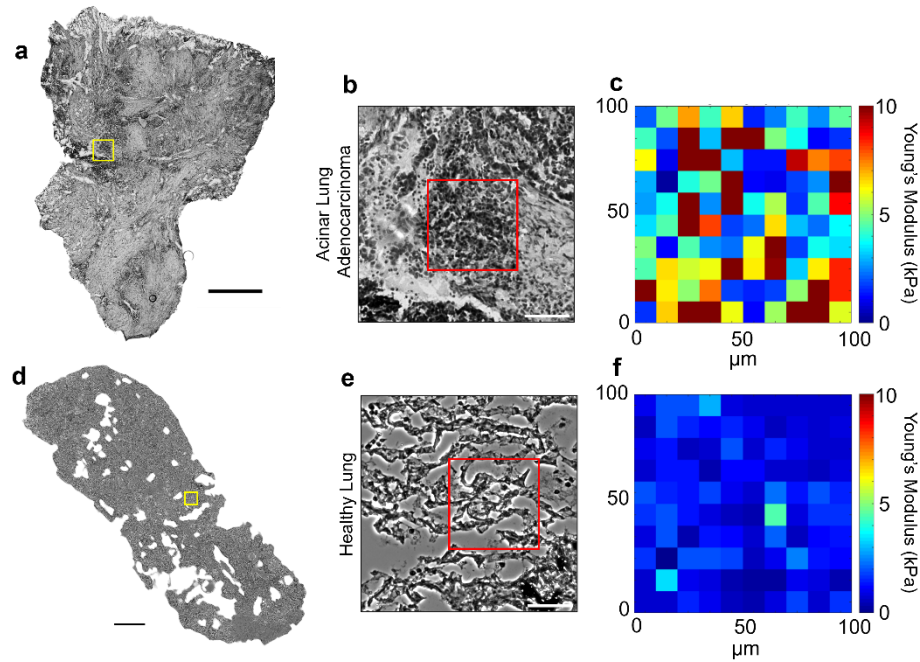


Figure 3.6 – Example of rigidity map from acinar adenocarcinoma and healthy lung of patient 16EH07456. **(a,d)** Reference Toluidine-blue stained sections (Bars: 500 μm). **(b,e)** Bright field optical images zoomed at the tumor region and healthy region, respectively (Bars: 50 μm). **(c,f)** Rigidity maps (100x100 μm<sup>2</sup>, 10x10 pixels) with 85% and 75% of the curves exploitable, respectively.

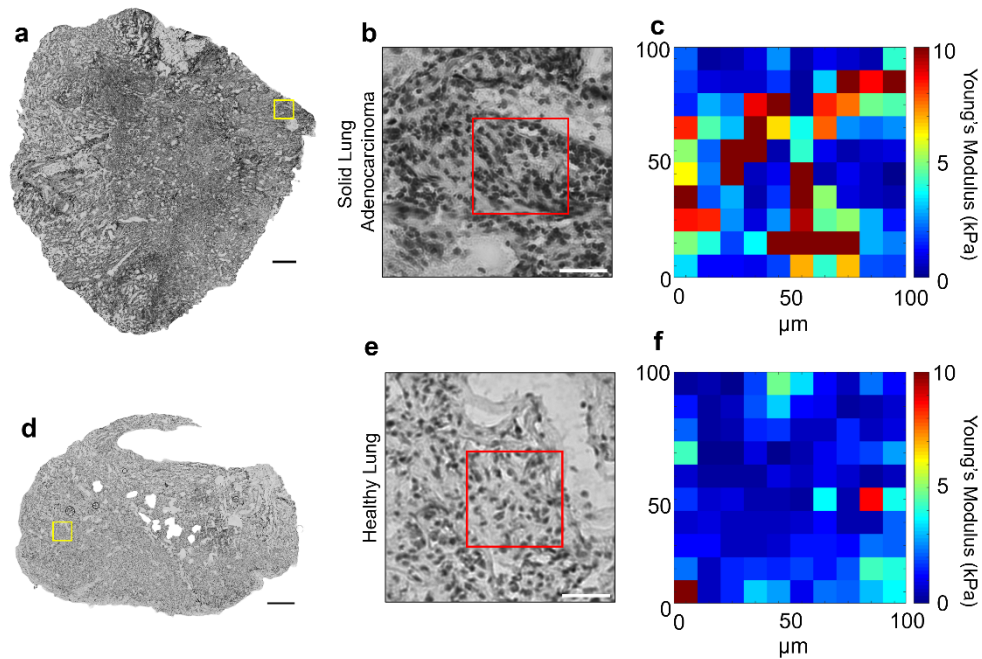


Figure 3.7 – Example of rigidity map from solid adenocarcinoma and healthy lung and of patient 13EX00166. **(a,d)** Reference Toluidine-blue stained sections (bars: 500  $\mu\text{m}$ ). **(b,e)** Bright field optical images zoomed at the tumor region and healthy region, respectively (bars: 50  $\mu\text{m}$ ). **(c,f)** Rigidity maps (100x100  $\mu\text{m}^2$ , 10x10 pixels) with 89% and 90% of the curves exploitable, respectively.

It is important to note that some of the maps are incomplete; therefore, linear interpolation was employed to replace NaN values. With the 15  $\mu\text{m}$  piezo, linear elastic behavior was observed in 93.2% of curves for healthy tissues and in 95.5% for their tumor counterparts. Switching to the 100  $\mu\text{m}$  piezo, these quantities dropped to 92.1% (n=1854) and 92.7% (n=1762), respectively. Incompleteness occurs in rigidity maps when certain curves are excluded during data processing as previously. Moreover, toluidine blue-stained sections were used as a reference to probe the ROIs during measurement. Tumor tissues visually presented more heterogeneous rigidity maps, with increased stiffness dispersed throughout most of the regions of interest, consistent with the previously presented stiffness distributions (Figure 2.9). While healthy tissues occasionally revealed localized areas of increased stiffness, they predominantly exhibited a less dispersed rigidity texture.

### 3.3.3 Analysis of tissue stiffness texture for stiffness heterogeneity pattern design

In this section, we focus on the analysis of rigidity maps and the subsequent image processing to identify rigidity patterns. Visual examination of the spatial organization of the patterns, suggested that they are randomly positioned. It is to be noted that the low resolution of the maps (10 x 10 pixels) prevented the use of tools to identify any positional order. Nevertheless, the Toluidine blue staining did not show any regular organization of tissue components, thus leading to the conclusion that a positional order of stiff compounds is quite improbable. A

custom-made MATLAB algorithm was utilized to transform the generated textured rigidity maps into rigidity threshold binary masks. In these masks, measurements above 2.9 kPa are represented by white regions, while black regions represent those below the threshold. Figure 3.8 illustrates the conversion of a textured rigidity map into a binary mask.

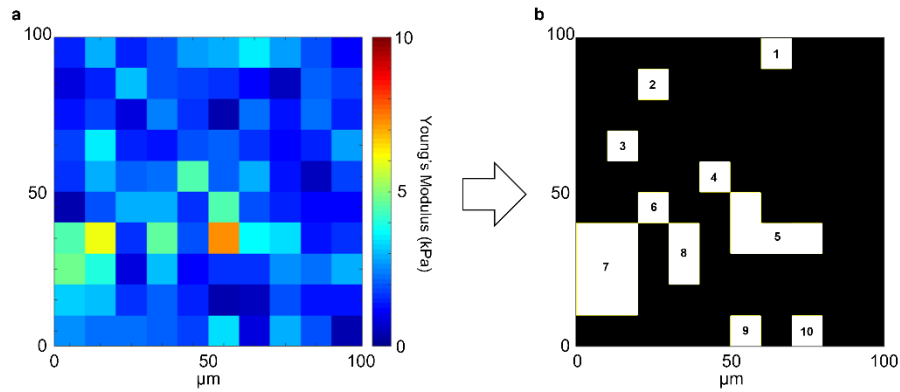


Figure 3.8 – Conversion of a rigidity map (a) into a binary mask (b) applying a 2.9 kPa rigidity threshold.

The same threshold was applied to healthy and tumor rigidity maps for a meaningful comparison. After the conversion, the resulting binary masks retained their original 10x10 pixel resolution. These maps were then processed using ImageJ to upscale them 10x without interpolation, facilitating proper patterns segmentation through watershed or manual methods. Following segmentation, particle analysis was conducted to calculate the shape descriptors of the numbered areas. When investigating the stiffness pattern areas of all patients, it became apparent that the data followed a non-normal distribution ( $p < 0.001$ , Shapiro-Wilk test for both distributions), with a tendency towards a quasi-log-normal distribution (Figure 3.9).

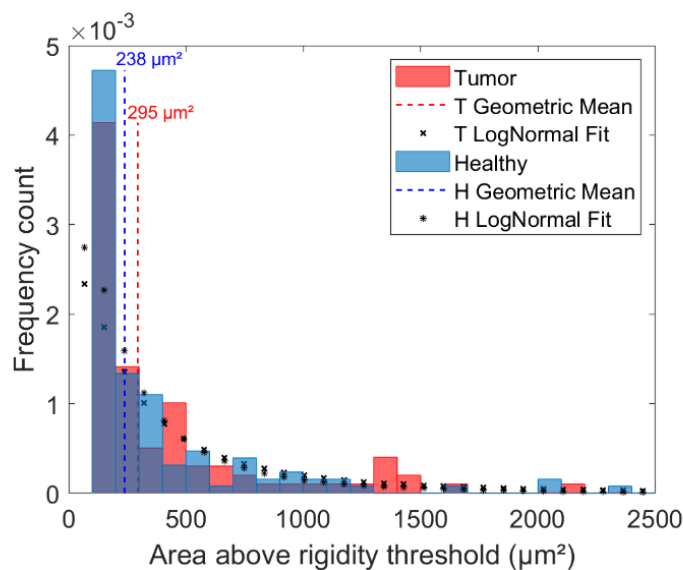


Figure 3.9 – Distribution of pattern areas above the rigidity threshold for healthy and tumor tissues.

As the distribution of the size of the stiffness patterns above the threshold follows a log-normal or quasi-log-normal distribution, the geometric mean was used to characterize the mean properties of the distribution. This quantity is a more appropriate measure of central tendency as it is less sensitive to extreme values and skewed data [221]. Instead of exclusively examining individual patients, the analysis of the stiffness pattern area was performed at the population level by calculating the overall geometric mean of the stiffness patterned areas. To quantify variability around the geometric mean, we used the multiplicative standard deviation, which considers the multiplicative nature of the geometric mean and provides a better representation of data spread in such distributions. Table 3.2 presents the summary statistics obtained from the statistical analysis of the shape descriptors from healthy and tumor tissue rigidity maps.

Table 3.2 – Summary statistics of analyzed rigidity maps with surface coverage or % of surface over the rigidity threshold (%SORT), geometric means of rigidity pattern areas, and basic shape descriptors.

	%SORT	Pattern Area ( $\mu\text{m}^2$ )	Aspect Ratio	Circularity	Solidity
<b>Healthy</b>	24%	238	1.40	0.605	0.91
<b>Tumor</b>	31%	295	1.45	0.591	0.90
Acinar	42%	423	1.60	0.526	0.86
Solid	22%	221	1.33	0.649	0.93

Table 3.2 indicates that the patterns are primarily convex (with a solidity close to 1) and have an elliptical shape (with an aspect ratio of 1.5). The circularity of the patterns is consistent with the angular patterns, which result from data pixelation. Another critical parameter investigated was the surface coverage percentage, namely the surface over the rigidity threshold (%SORT) present in each textured rigidity map. As shown in Figure 3.10, on average,  $31 \pm 21\%$  and  $24 \pm 17\%$  of the surfaces were above the defined rigidity threshold in tumor and healthy tissues, respectively. Overall, tumor tissues exhibited stiffer regions, as observed in the colored rigidity maps and their stiffness distribution. The surface filling percentage will be used as an input parameter in the custom-made algorithm that generates the mask design in Chapter 4.

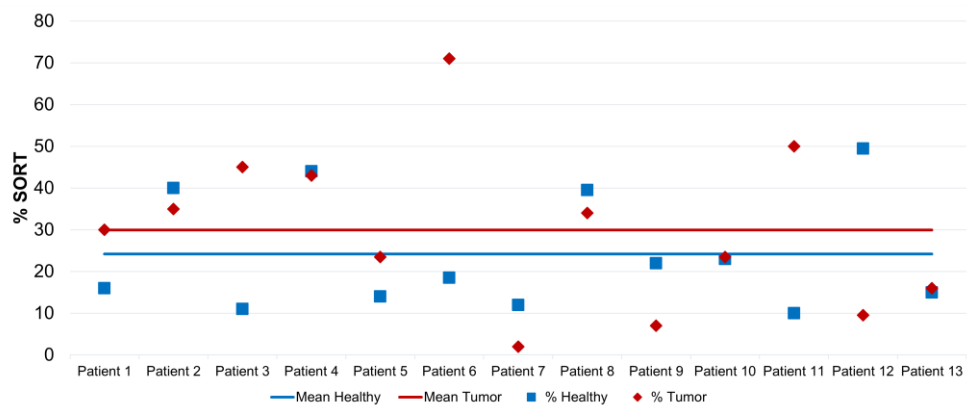


Figure 3.10 – % of surface over the rigidity threshold (% SORT) per patient.

Under the assumption of non-normal distributions, to rigorously evaluate the differences between groups, we employed the Mann-Whitney U (MWU) test. In conclusion, the results indicate no statistically significant difference between healthy and tumor tissue rigidity patterned areas (MWU,  $p = 0.22$ ). However, tumor tissues exhibited more heterogeneity compared to healthy tissues, as demonstrated by the %SORT. A statistical significance was observed between acinar and solid patterns (MWU,  $p = 0.02$ ), with acinar presenting higher %SORT compared to solid. Considering the computed shape descriptors, the average pattern shape is showed in Figure 3.11 for both healthy and tumor tissues.



Figure 3.11 – Average shape considering the shape descriptors for healthy and tumor tissues with Aspect Ratio = 1.73, Circularity = 0.58 and Solidity = 0.90, 1 pixel = 1.0851  $\mu\text{m}$ .

The analysis of these statistical outcomes provided a primary understanding of tissue stiffness heterogeneity. The rationale behind this simplified approach is to provide a morphological understanding of tissue stiffness patterns and quantification of the inputs for designing and fabricating gray-level masks that approximate tissue heterogeneity.

#### 3.3.4 Extraction of mask design parameters

The rigidity threshold plays a critical role in highlighting stiffness patterns, which is essential for the subsequent calculation of shape descriptors and determination of the average pattern shape. Implementing a statistical law that reproduces variations of the calculated pattern shape in Figure 3.11 would be excessively complex. Moreover, due to physicochemical constraints such as diffusion of the free radicals during hydrogel polymerization, printing large patterns with small details can be challenging.

As a result, we reduced the problem to a zero-order approach by selecting a disk (circle) as the simplest representation of a convex pattern, owing to its ease of use in design. Considering the broad variation in stiffness distribution observed for tumor tissue and the quasi-log-normal nature of its rigidity patterned area distribution, an effective strategy was to create a log-normal distribution consisting of randomly generated circles with radii (areas) centered around the geometric mean radius, ranging from the calculated minimum and maximum radii. Table 3.3 shows the design parameters that will be considered to generate the mask design to approximate the stiffness heterogeneity of tumor tissues, including the geometric mean radius and standard deviation, maximum and minimum radii.



Table 3.3 – Circular pattern design parameters obeying the lognormal distribution as the patterns measured on patient tissues.

<b>Geometric Mean Radius (μm)</b>	<b>Geo Standard Deviation (μm)</b>	<b>Ln of Geo Standard Deviation</b>	<b>Max Radius (μm)</b>	<b>Min Radius (μm)</b>
9.7	1.84	0.61	48.9	5.6

The dispersion of the geometric mean radius was determined by calculating the geometric standard deviation (GSD). When implementing this lognormal distribution, it was first assumed that the rigidity patterned areas corresponded to circular areas. Then, the radii were calculated, and the natural logarithm was applied to generate a normal distribution. Since the exponential of a normal distribution results in a lognormal distribution, the GSD could be exponentiated to obtain the standard deviation ( $\sigma$ ) of the underlying distribution.

In summary, this approach provides a simplified yet effective way to extract mask design parameters that capture tissue heterogeneity. By employing a disk representation, we can generate a random circle distribution corresponding to the rigidity patterned areas, which will serve as input for creating gray-level masks that approximate the intricate stiffness texture observed in tumor tissues.

### 3.4 DISCUSSION

Stiffness heterogeneity stems from the intricate and irregular distribution of mechanical properties within the tissue, influenced by variations in cellular composition and extracellular matrix components [58]. In tumor tissues, heterogeneity typically manifests as increased stiffness and disorganized structure relative to healthy tissues [222], [223]. It has been demonstrated that the stiffness of the ECM is a critical factor in the progression of various cancer forms [222]. In solid neoplasms, like those found in breast [224] and pancreatic cancer [225], the tumor tissue often demonstrates abnormal rigidity, which can be attributed to the rigid extracellular matrix due to the processes of accumulation, contraction, and cross-linking. This increased rigidity in the extracellular matrix induces mechanotransduction, a mechanism that translates mechanical cues, such as matrix stiffness, into intracellular biochemical signaling. As a result, this influences the phenotypic characteristics of both neoplastic and stromal cells within the tumor microenvironment [226].

In addition to an altered mean stiffness, tumor tissues often show an altered stiffness texture [174], [179], [203]. Cells are known to be sensitive to subcellular texture of rigidity [220], [227]. It is thus of interest, for instance for fundamental analysis or drug screening purpose, to analyze cell behavior *in vitro* when grown on substrates that mimic this pathological stiffness heterogeneity. But addressing the mechanical complexity of lung tissue and accurately replicating it within a relevant cell culture substrate poses a considerable challenge. In an effort to handle this challenge, our research began with the quantification and analysis of stiffness texture in both healthy lung tissue and lung adenocarcinoma specimens. Following this initial investigation, we developed a simplified approach to derive design parameters from rigidity maps.

The use of the CellHesion module was imperative for investigating larger tissue regions. Despite its challenging operation, conducting tests on hydrogels enabled the optimization of experimental parameters and the successful acquisition of large rigidity maps. Our statistical analysis revealed that the stiffer hydrogel (15s) displayed a statistically significant difference in measurements between the 15  $\mu\text{m}$  and 100  $\mu\text{m}$  piezo scanners, whereas the softer hydrogel did not exhibit such differences (Figure 3.5). This bias coming from CellHesion module could not be explained. Nonetheless, one should not disregard the impact of hydrodynamic drag force on the AFM cantilever, particularly at increased z-lengths and speeds when using the spherical probe.

These novel findings about the microscale mechanical properties of lung adenocarcinoma strongly indicate that, besides their *de visu* difference observed in histological analysis, their stiffness distribution also differs from healthy tissue, as shown in Chapter 2. A broader stiffness distribution indicates more heterogeneity. Here we could associate the broadening of the distribution of the Young's modulus of the tumor tissue to a stiffness texture. Highly localized increases in stiffness were observed ( $>10$  kPa) as exemplified by one elastograph of tumor biopsy 16EH07456 (stage IIB), shown in Figure 3.6c. In comparison, healthy lung tissue of the same patient showed far less heterogeneity. Considering the premise that lung adenocarcinoma possesses regions rich in collagen expression and typically are associated with pulmonary fibrosis, these intrinsic characteristics corroborate for a stiffer environment and will be investigated in Chapter 5.

After the characterization of the mechanical properties in lung tissues, 52 large rigidity maps were acquired, representing localized stiffness at  $10\ \mu\text{m}$  intervals across  $100\times 100\ \mu\text{m}^2$ . Subsequently, a criterion was established to isolate any rigidity patterns potentially present within these maps. To achieve this, a rigidity threshold of 2.9 kPa was arbitrarily determined, representing the 70th percentile of tumor tissue stiffness distribution. Binary masks were generated using MATLAB, featuring black (below the threshold) and white (above the threshold) shapes, by applying this threshold to the original rigidity maps. Although sophisticated statistical texture methods exist, a simple iterative procedure was employed to analyze and extract basic shape descriptors from rigidity maps, with subsequent categorization achieved using ImageJ.

The rigidity patterned areas for all patients exhibited a non-normal distribution as evidenced by the Shapiro-Wilk test. Due to the log-normal-like behavior of the data, the geometric mean was utilized as a measure of central tendency, offering a more accurate representation within the population. Despite the non-significance of rigidity patterned areas between both tissues, lung adenocarcinoma exhibited stiffer regions, with 31% of the surface exceeding the rigidity threshold, compared to 24% in healthy tissues. Furthermore, despite their similar mean stiffness reported in Chapter 2, a statistically significant difference was found between the acinar and solid rigidity patterned areas, highlighting a probable inherent stiffness texture that could be associated with each lung adenocarcinoma subtype.

The limited number of maps acquired per patient, arising from experimental and technological limitations, could potentially explain the lack of statistical significance. By probing millimeter-size areas and increasing the sample size, future studies may be able to provide more robust and conclusive evidence regarding the differences in tissue stiffness texture between healthy and tumor tissues. Another possibility could be that the difference in stiffness texture is beyond the resolution of the scanned maps, of 10  $\mu\text{m}$ . Acquiring more precise maps is necessary to test this hypothesis. Both strategies, acquiring larger maps or increasing the resolution of the scan, require exposing the samples to longer acquisition times. Although the scanning velocity may be optimized to higher values, the limited lifetime of the tissue will remain a major limitation. Despite the present analysis could certainly be improved, it is noteworthy that this represents the first characterization of rigidity pattern morphology derived from lung tissues, with potential applicability to other biological samples. The significance of this strategy remains to be assessed in the context of cell culture models.

The resulting average pattern displayed an elliptic shape with high convexity. Reducing to a zero-order approach, a disk pattern was the obvious choice. Thus, we derived circular pattern design parameters. These design parameters will be used to generate a random circle pattern which in turn will be essential for the fabrication of a gray-level mask (Chapter 4).

The choice of the stiffness threshold is arbitrary, it will be validated when fabricating hydrogels by the use of the gray level photomask designed with the resulting patterns: the distributions of stiff areas and of the Young's modulus of the hydrogel should resemble those measured in tissues. The value of the threshold is therefore tightly linked to the photochemistry of the hydrogel. Here we use this value to evaluate a potential difference between healthy and tumor tissues. No difference in the shape of the stiff patterns is found with the chosen value, nonetheless %SORT was different suggesting that different texture parameters can be chosen to design soft substrates that mimic the healthy or tumor tissue stiffness. Only the surface density of the stiff patterns has to be adjusted. This conclusion is however partial since only a small portion of the surface of the tissue is analyzed. Any difference in stiffness texture is better evaluated by comparing the stiffness distribution obtained through out the sample, in the absence of threshold, by looking at the dispersion of the stiffness values. Table 2.2 in Chapter 2 consistently revealed a higher variability in tumor stiffness compared to healthy tissue across all patients.

Although larger rigidity maps have been successfully acquired in recent studies [205], reproducing stiffness heterogeneity on *in vitro* cell culture substrates has not been a primary focus. Furthermore, most studies employing colloidal probes continue to process data using the Hertz model, neglecting the contribution of adhesion, and generating untrustworthy results [205]. Additionally, other investigations [191] have relied on particularly thin sections of 10  $\mu\text{m}$  for AFM characterization, which might be insufficient to probe a comprehensive average of cell and ECM stiffness and to screen the stiffness of the glass bottom. In conclusion, our study shed light on the complex nature of tissue stiffness heterogeneity in both healthy and lung adenocarcinoma tissues. Our approach to acquiring and processing rigidity maps, coupled with a procedure to extract mask design parameters, provides a valuable framework for comprehending the mechanical landscape of lung tissues and establishing the groundwork for developing pathophysiological stiffness textures on hydrogels.

Before navigating the domain of hydrogel fabrication and achieving a degree of control over their mechanical properties in Chapter 5, we now turn our attention to an intriguing new perspective. In Chapter 4, we will delve into the relationship between the mechanical properties of tissues, specifically their stiffness, and their inherent biological composition. We move beyond the microscale and into a broader context, using the knowledge and tools gained thus far to explore how variations in tissue stiffness can reveal insightful details about their composition.

## CHAPTER 4

---

# CORRELATION BETWEEN STIFFNESS AND LUNG TISSUE COMPOSITION

## 4 CORRÉLATION ENTRE LA RIGIDITÉ ET LA COMPOSITION DU TISSU PULMONAIRE

Le chapitre 4 rentre dans la dynamique complexe de la composition des tissus et de la rigidité dans les tissus de l'adénocarcinome du poumon, en se concentrant particulièrement sur les rôles du collagène, de l' $\alpha$ -SMA, et de la vimentine, protéines connues pour être surexprimées dans les tissus tumoraux et pouvant influencer la rigidité des tissus. Nous cherchons à comprendre comment ces composants interagissent pour influencer la rigidité des tissus, un aspect important de la progression des tumeurs et potentiellement significatif pour déterminer les approches de traitement. Dans la section matériaux et méthodes, la préparation des échantillons de tissus et les techniques utilisées pour les analyser sont décrites, y compris la coloration de Trichrome Goldner pour le collagène, l'immunofluorescence (pour la vimentine et l' $\alpha$ -SMA), l'acquisition d'images, et les mesures AFM. La section des résultats se concentre sur les associations entre la rigidité des tissus et la teneur en collagène, vimentine et  $\alpha$ -SMA. Le résultat majeur du chapitre 4 indique que, de manière globale, aucune corrélation n'a été observée entre la rigidité des tissus de l'adénocarcinome du poumon et les niveaux de collagène, de vimentine, et d' $\alpha$ -SMA, malgré le fait que ces protéines soient reconnues dans la littérature existante comme des facteurs influençant la rigidité des tissus tumoraux. Cependant des corrélations sont suspectées en fonction des sous-types histologique, qui demandent à être confirmés en élargissant le jeu de données. De plus, nous identifions une similitude frappante entre la distribution de la vimentine dans les cellules A549 et les cellules présentes dans le tissu de l'adénocarcinome du poumon.

Dans la section de discussion, nous réfléchissons aux implications potentielles de ces résultats. Les corrélations identifiées entre le collagène, la vimentine, l' $\alpha$ -SMA, et la rigidité des tissus dans les sous-types histologiques fournissent des informations sur les mécanismes moléculaires sous-jacents aux propriétés biomécaniques. Ces résultats améliorent notre compréhension de la façon dont les tissus de l'adénocarcinome du poumon se développent et répondent à leur environnement, potentiellement en informant des stratégies thérapeutiques plus efficaces et ciblées. En conclusion, ce chapitre offre un aperçu initial sur les protéines structurales clés et leur influence sur la rigidité des tissus dans l'adénocarcinome du poumon.

## 4 CORRELATION BETWEEN STIFFNESS AND LUNG TISSUE COMPOSITION

Chapter 4 dives into the complex dynamics of tissue composition and stiffness in both healthy and lung adenocarcinoma tissues, with a particular focus on the roles of some proteins that are known to be overexpressed in tumor tissues and that could influence tissue stiffness, an important aspect of tumor progression and potentially significant in determining treatment approaches. To this end, we investigate the contribution of collagen,  $\alpha$ -SMA, and vimentin to tissue stiffening. In the materials and methods section, the focus is on the preparation of the tissue samples and the techniques used to analyze them, including Trichrome Goldner staining for collagen, immunohistochemistry, image acquisition, and AFM measurements. These procedures are meticulously detailed to give readers a full understanding of the process and provide a roadmap for similar future studies. The results section concentrates on the associations between tissue stiffness and the content of collagen, vimentin, and  $\alpha$ -SMA. The primary findings of this investigation are that despite known relationships in the literature, within the specific dataset analyzed that combines acinar and solid histological subtypes, no correlation was observed between the stiffness of lung adenocarcinoma tissues and the contents of collagen, vimentin, and  $\alpha$ -SMA. However, correlations are suspected according to histological subtypes, which need to be confirmed by enlarging the dataset. In addition, we identify a compelling similarity between the distribution of vimentin in A549 cells and cells present in lung adenocarcinoma tissue, which suggests that A549 cells might serve as a useful model for studying vimentin's role in lung adenocarcinoma. In the discussion section, we ponder the potential implications of these findings. The identified correlations between collagen, vimentin,  $\alpha$ -SMA, and tissue stiffness in histological subtypes provide insights into the molecular mechanisms underlying the altered biomechanical properties. These findings enhance our understanding of how lung adenocarcinoma tissues develop and respond to their environment, potentially informing more effective and targeted therapeutic strategies. In conclusion, this chapter offers an incipient overview about key structural proteins and tissue stiffness in lung adenocarcinoma.



## 4.1 FUNDAMENTAL CONCEPTS

### 4.1.1 Healthy and adenocarcinoma lung tissue composition

As illustrated in the first chapter and evidenced in Figure 2.7, healthy and tumor lung tissues showcase not just visually compelling contrasts but also significant compositional differences. The healthy human lung tissue is characterized by a well-organized extracellular matrix (ECM), which provides structural support to the resident cells and modulates various physiological processes. Primarily composed of proteins like collagen and elastin, glycosaminoglycans, and proteoglycans, the ECM of lung tissue exhibits specific biomechanical properties, including compliance and stiffness, which maintain tissue homeostasis [34],[180],[181]. A variety of cell types reside within the healthy lung tissue, each with specific functions (Figure 4.1b). Epithelial cells, which line the respiratory tract, provide a barrier against environmental pollutants and pathogens. Smooth muscle cells control bronchial constriction and dilation, influencing airflow. Fibroblasts synthesize ECM components, maintaining the structural integrity of lung tissue. Additionally, various immune cells, like alveolar macrophages and lymphocytes, contribute to immune surveillance and response [228].

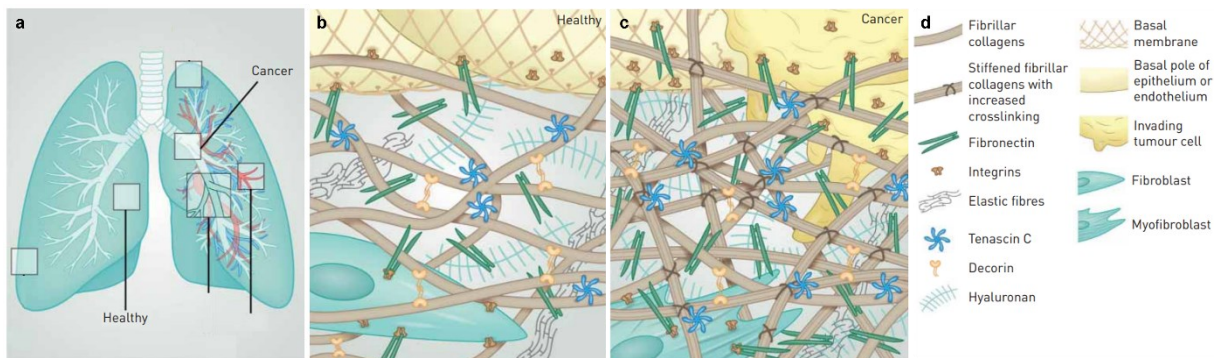


Figure 4.1 – Pathological transformations within the lung's interstitial extracellular matrix (ECM) in healthy and cancerous conditions. (a) General view of the lung, highlighting the parenchyma on healthy and cancer locations. (b) The integrity of a healthy interstitial ECM, which is a flexible network of collagens, elastin, and fibronectin, tethered to the basal membrane of the epithelial cell layer, is upheld by the activity of resident fibroblasts. (c) In the context of cancer, primary and metastatic tumors are encapsulated by a dense, rigid stroma, rich in highly crosslinked collagens, along with amplified levels of fibronectin, tenascin C, and hyaluronan. (d) Legend with components present on both conditions. Adapted from [34].

On the contrary, the lung tissue in adenocarcinoma, exhibits significant alterations. Solid adenocarcinoma is characterized by dense, tumor cell-packed regions with scant stroma and mucin production, whereas acinar adenocarcinoma is defined by gland-like or acinar structures formed by tumor cells [229] (Figure 2.7). In both types, the ECM becomes disorganized and excessively stiff, leading to the disruption of normal tissue architecture [34] (Figure 4.1c). The predominant cell type within adenocarcinoma tissues are the cancer cells themselves, which exhibit abnormal morphology, uncontrolled proliferation, and the ability to invade surrounding tissues. Other cells such as cancer-associated fibroblasts (CAFs) [230] and tumor-infiltrating immune cells, such as tumor-associated macrophages (TAMs) [231] and T-cells, also inhabit the tumor microenvironment. These cells often contribute to tumor progression and remodeling, creating a highly complex dysregulated cellular ecosystem. The next sections the focus will be some specific proteins that are known to plays a role the tissue stiffness.

#### 4.1.2 The role of collagen in cell and tissue stiffness

Collagen, one of the main components of the ECM, plays a central role in determining tissue stiffness and integrity. It is a structural protein that forms a fibrous network within the ECM, providing mechanical stability and strength to tissues. This network imparts tensile strength and contributes to the tissue's biomechanical properties, such as stiffness and elasticity [58],[121]. Indeed, the mechanical stability of lung parenchyma is predominantly attributed to the ECM, which mainly consists of collagen. Various studies highlight the role of this structural protein in determining the mechanical attributes of tissues and their influence on cell mechanics [181],[189],[232]. At the cellular level, Stylianou et al. [233] investigated the role of collagen content and extracellular matrix in causing cytoskeletal remodeling in pancreatic fibroblasts. This study found that collagen matrix stiffening increases Young's modulus of fibroblasts and cancer-associated fibroblasts (CAFs) as seen in Figure 4.2. On the same note, a recent study from Koorman et al. showed that spatial collagen stiffening promotes collective breast cancer cell invasion by reinforcing extracellular matrix alignment [234].

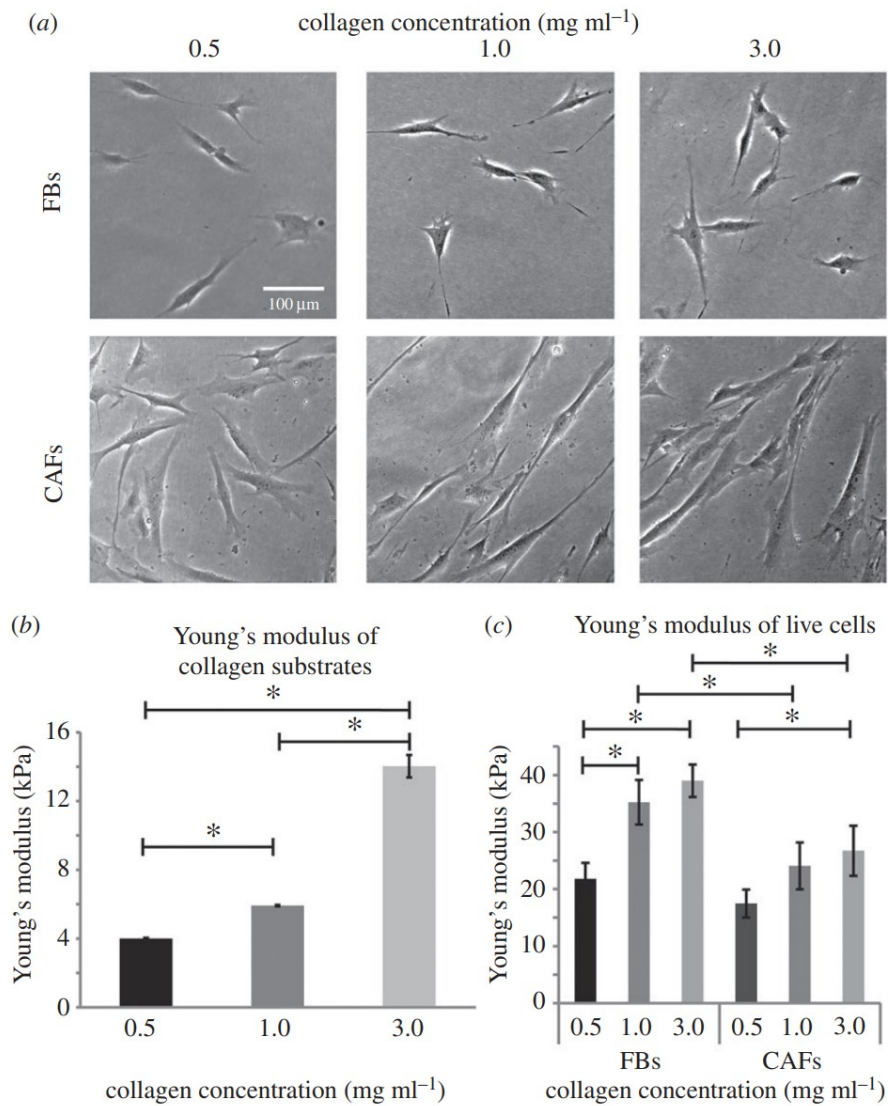


Figure 4.2 – Impact of matrix rigidity on the Young's modulus of cells. **(a)** FBs and CAFs using optical microscopy, grown on collagen substrates of varying concentrations, **(b)** Relative Young's modulus of the substrate, and **(c)** AFM-measured Young's modulus of live cells [235].

Changes in ECM stiffness are largely driven by alterations in type I collagen deposition, as corroborated by numerous studies [25], [236], [237]. At the tissue level, the quantification of tumor rigidity by elastography (ultrasound) has shown strong correlations with collagen content, collagen crosslinking, activated fibroblast density, and blood vessel density, implying a critical role of collagen in dictating tumor stiffness. Inherently, the fibrillar structure of collagen I furnishes a resilient mechanical scaffolding that confers both rigidity and durability to tissues [238]. Across different organ systems, the concentration and organization of collagen fibrils vary, thereby modulating the distinct mechanical and biological properties of each organ. Hence, alterations in collagen deposition, post-translational modifications, or cross-linking - frequently observed in pathological states such as fibrosis and cancer - can drastically reshape tissue biomechanics, remodel the stroma, potentially catalyzing disease initiation and progression [239], [240], [241].

#### 4.1.3 The role of $\alpha$ -SMA in cell and tissue stiffness

Alpha-smooth muscle actin ( $\alpha$ -SMA) is another important player in regulating cell and tissue stiffness. This protein is found in smooth muscle cells and plays a significant role in maintaining cell contractility. It is involved in cellular processes such as migration, cell shape maintenance, and most importantly, modulation of cellular tension and stiffness [242]. Moreover, the expression of  $\alpha$ -SMA is upregulated in myofibroblasts, a specialized fibroblast subtype that emerges during tissue injury and repair. Myofibroblasts are characterized by high contractility, driven by  $\alpha$ -SMA incorporation into stress fibers. This elevated contractility contributes to wound closure by generating tension, but also enhances tissue stiffness, influencing cellular behavior and ECM organization [243].

In pathological conditions such as cancer, an abnormal increase in  $\alpha$ -SMA expression often indicates an increased population of cancer-associated fibroblasts (CAFs), which contribute to tumor progression. These CAFs exhibit increased contractility and can remodel the ECM, by secreting matrix metalloproteinases (MMPs) and other enzymes that break down or alter the existing matrix, thereby increasing tissue stiffness and creating a tumor-permissive environment [47]. In lung adenocarcinoma, a significant correlation has been observed between  $\alpha$ -SMA overexpression and tumor progression [244]. This overexpression is suspected to participate in enhancing tissue stiffness. To corroborate, Lee et al showed that the ACTA2 gene, responsible for encoding  $\alpha$ -SMA, was overexpressed in lung adenocarcinoma cells and acted as a pivotal agent, concurrently modulating cancer cell mechanics and regulating signal protein expression, thereby profoundly impacting the trajectory of lung adenocarcinoma outcomes [245].

#### 4.1.4 The role of vimentin in cell and tissue stiffness

Vimentin, an intermediate filament protein typically expressed in mesenchymal cells, plays a significant role in maintaining cell shape, integrity, and elasticity. In addition to providing structural support, vimentin is involved in a variety of cellular processes, including adhesion, migration, and signal transduction, all of which contribute to the overall biomechanics of the cell and thereby to the tissue stiffness [246]. At the cellular level, vimentin forms a network around the nucleus that helps to resist mechanical stress and distributes forces throughout the cell, as extensively reviewed by Danielsson et al. [247]. This role becomes particularly important in the context of lung tissue, where cells are regularly subjected to mechanical stress during breathing. Alterations in the vimentin network can affect the mechanical properties of

cells, such as their stiffness, and contribute to pathological conditions in lung tissue [247],[248]. For instance, increased expression of vimentin has been linked to pulmonary fibrosis, a condition characterized by stiffening of the lung tissue [34]. On this note, a 2016 case report detailed an occurrence of lung adenocarcinoma where both the symptoms and clinical imagery bore a striking resemblance to pulmonary fibrosis [249].

In the context of cancer progression, vimentin also hold a central role in facilitating invasion, particularly in confined environments. Tumor cells navigate through the ECM either as individual entities or in a collective manner, maintaining intercellular connections. Navigating through confined spaces demands a fine-tuned orchestration of cytoskeletal dynamics, tension and rearrangement, crucial not only for sustained locomotion but also for counteracting frictional and elastic resistance against the cell surface [250]. Thus, vimentin intermediate filaments, given their unique mechanical properties, provide cancer cells with elasticity [251] and fuel the vicious cycle of tumor tissue stiffening [252]. On this note, it was shown that oncogenes can reinforce cellular stiffness via HDAC6-dependent reorganization of the vimentin filament network. The study found that treatment with tubacin, which blocks HDAC6 activity, resulted in a significant suppression of SV40T-induced vimentin reorganization and a recovery of the peripheral vimentin intermediate filament network. This recovery of the vimentin network was associated with a decrease in cell stiffness, suggesting that HDAC6 activity by SV40T is required for the oncogene-induced increase in cell stiffness (Figure 4.3).

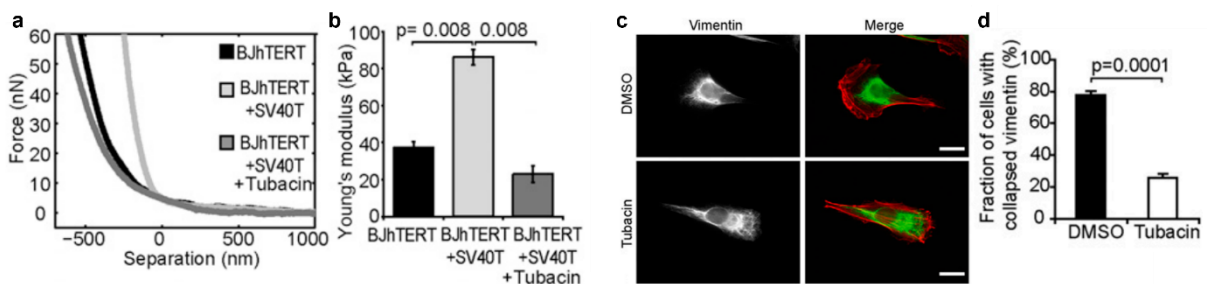


Figure 4.3 – SV40T induces increased cell stiffness via HDAC6. **(a)** Force curves acquired on BJhTERT cells (black), BJhTERT+SV40T cells (light gray), and BJhTERT+SV40T cells treated with tubacin (dark gray). **(b)** Quantification of cells stiffnesses at 30 nN load. **(c)** Representative BJhTERT+SV40T cells treated with DMSO and tubacin analyzed for organization of vimentin intermediate filaments. Black and white images show vimentin and merged images show vimentin (green) and F-actin (red). **(d)** Quantification of the collapse of the vimentin IF network in cells [253].

It was also demonstrated that breast carcinoma cells, when lacking vimentin, exhibit greater pliability, reduced contractility, and diminished directional persistence in migration, as summarized by Liu et al [254] in Figure 4.4.

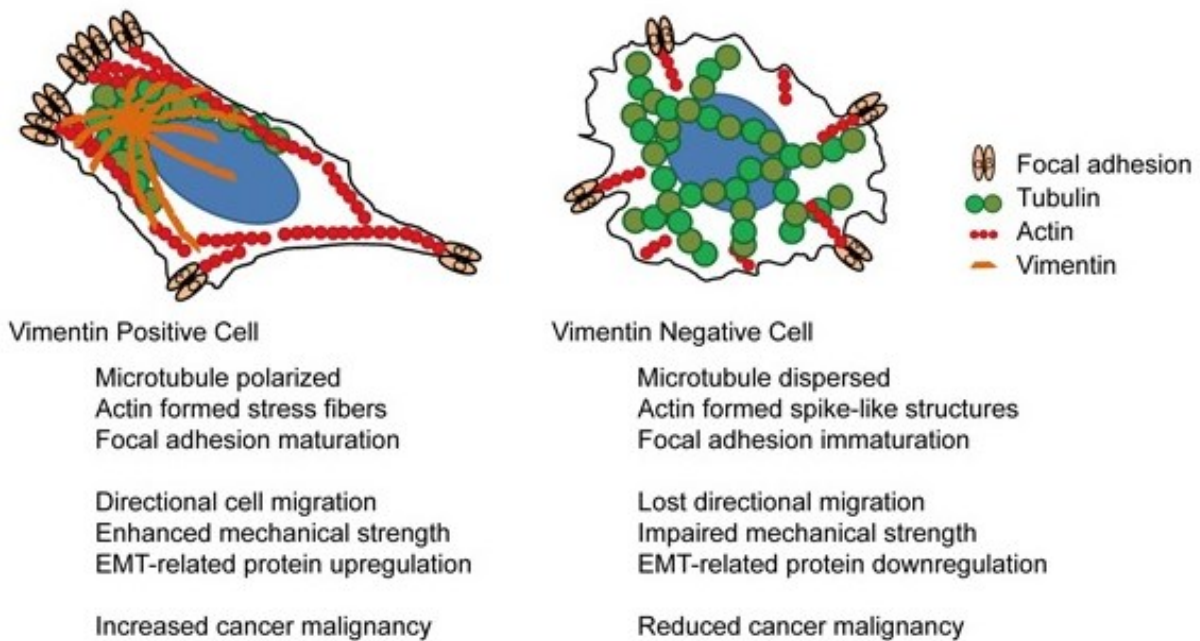


Figure 4.4 – Schematic of the cellular orientation of tubulin (green), actin (red), and focal adhesion (light orange) in cells positive and negative for vimentin (dark orange). In vimentin-positive cells, microtubules are located near the cell nucleus, with actin forming stress fibers at the cell base, indicating EMT-related protein expression. When vimentin is depleted, microtubules disperse, and actin forms spike-like structures at the cell edges, along with cell membrane extension. This also reduces focal adhesion. These changes weaken the cells and affect their directional movement, showing the role of vimentin in EMT-related mechanoregulation and cancer progression. From [254].

Additionally, vimentin has been revealed as essential for generating compartmentalized pressure, driving cell migration in 3D [255]. From a mechanistic standpoint, vimentin filaments have been shown to grant resistance to deformation in migrating cells. Experimentation involving AFM and microfluidic optical stretcher revealed that cells lacking vimentin, specifically in MDA-MB-231, became noticeably more deformable and stretchable [256]. This likely occurs due to vimentin intermediate filaments adopting a front-to-rear polarity, forming a cage-like structure encapsulating the nucleus with individual filaments extending to the trailing edge of the cell [257].

Building upon these observations, vimentin is increasingly recognized as a fundamental player in cellular mechanics and the evolution of cancer. Its function goes beyond just providing structural support but also regulates cellular elasticity and malleability [258]. Notably, vimentin is thought to play a significant role in tumor tissue stiffening, further underlining its participation in cancer invasion and metastasis. Given these roles, vimentin is drawing attention as a potential biomarker for cancer diagnosis, prognosis and treatment [258]–[263], providing a promising avenue for future advancements in cancer research and treatment options.

## 4.2 MATERIALS AND METHODS

### 4.2.1 Tissue preparation

In the present analysis, three tumor biopsies were utilized, including two solid (14EX00047 and 13EX00166) and one acinar type (15EH06497). These were non-fixed, frozen tissues that were encapsulated in an optimal cutting temperature (OCT) compound. Using a cryostat (Leica Biosystems, 3050S), four serial sections were generated from each biopsy (Figure 4.5). The sections had varying thicknesses: 14  $\mu\text{m}$  for toluidine blue staining, 7  $\mu\text{m}$  for both Trichrome Goldner staining and immunohistochemistry, and a mirrored section of 100  $\mu\text{m}$  thickness specifically intended for AFM measurements.

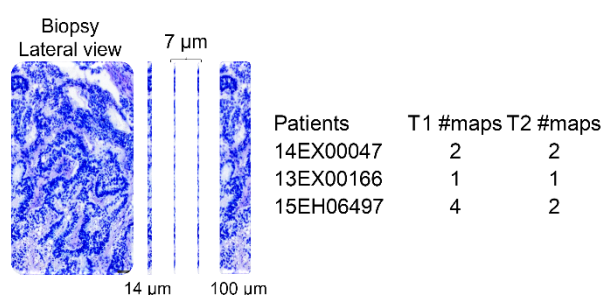


Figure 4.5 – Schematic depicting the positions of the sections in the biopsy and the varying section cut thicknesses utilized for different procedures such as toluidine blue staining, trichrome Goldner, immunohistofluorescence, and AFM, from the left to right. The table shows the number of maps analyzed with AFM. T1 and T2 denote 2 ensembles of sections performed at 2 different depths in the biopsies.

Tissue sections were deposited on SuperFrost Ultra Plus™ GOLD glass slides (Thermo Scientific, USA) and immediately stored at  $-20^{\circ}\text{C}$ . Sections were characterized within two days of cutting. The thinner sections were quickly stained for toluidine blue, a basic thiazine metachromatic dye with a strong affinity for acidic tissue components [159]. The protocol consisted of a three-minute incubation at room temperature with a 1% Toluidine Blue (Sigma-Aldrich, USA) solution, followed by rinsing in distilled water and three minutes in 75% ethanol, full dehydration, and mounting with Eukitt® (Kindler GmbH, Germany).

### 4.2.2 Trichrome Goldner staining

Tissue sections were thawed and then sequentially immersed in absolute, 90%, and 70% ethanol solutions, followed by distilled water, for 15 seconds each to remove residual OCT. Once the excess water was drained, sections were allowed to dry completely. A circle was drawn around each tissue sample with a hydrophobic pen and allowed to dry for one minute. Subsequently, 300-400  $\mu\text{l}$  of 4% PFA solution was added to each sample for fixation, which was allowed to proceed for five minutes before the solution was discarded. Following fixation, samples were subjected to Goldner's Trichrome staining. First, the tissue sections were treated with a mixture of Iron hematoxylin acc. Weigert Reagents A and B for ten minutes, followed by a thorough

wash under running tap water for five minutes. Sections were then immersed in Picric acid saturated alcohol for five minutes and washed briefly in distilled water. This was followed by a ten-minute incubation with Fuchsin Ponceau according to (acc.) Masson, and a four-minute incubation with Phosphomolybdic Acid acc. Masson without washing the sections between these two steps. Samples were then treated with Light Green acc. Goldner for four minutes. Post-staining, sections were rapidly dehydrated through sequential washes with distilled water, absolute ethanol, 90% ethanol, and 70% ethanol. After the removal of excess liquid, sections were left to dehydrate thoroughly. Finally, a small volume (5-10  $\mu$ l) of Eukitt® was applied to each section, and a mounting coverslip was placed. The stained tissue samples were then left to dry for at least 15 minutes prior to image acquisition. In the stained adenocarcinoma lung sections, nuclei appeared dark red to black, muscle fibers, keratin, and cytoplasm were bright, collagen and mucus displayed green to blue hues, and erythrocytes were visualized as orange to yellow. Following staining, sections were stored at 15°C to 30°C for best preservation.

#### 4.2.3 Immunofluorescence

All steps were carried out under low light conditions. The tissue sections were first washed twice with PBS<sup>+/+</sup> to remove dead cells or loose tissue. The sections were then permeabilized with a solution containing PBS<sup>+/+</sup>, 4% PFA, and 0.5% Triton 100x, and left to incubate for 15 minutes at room temperature. Following the permeabilization step, sections were fixed in a solution of PBS<sup>+/+</sup> and 4% PFA for 45 minutes at room temperature. Post-fixation, sections were saturated with a solution containing PBS<sup>+/+</sup>, 0.1% Tween 20, and 2% BSA, and incubated for 1 to 2 hours under slow agitation at room temperature. For primary antibody incubation, monoclonal anti-vimentin (mouse) (clone V9; Santa Cruz, Dallas, USA) and polyclonal anti- $\alpha$ -SMA (rabbit) antibodies (PA5-16697; Thermo Fisher Scientific, Waltham, USA) were diluted in PBS<sup>+/+</sup>, 0.1% Tween 20, and 2% BSA to 5  $\mu$ l/ml and 8  $\mu$ l/ml, respectively. The sections were incubated in the antibody solutions for one hour under slow agitation at room temperature. This was followed by three washes and a 30-minute incubation with PBS<sup>+/+</sup>, 0.1% Tween 20, and 2% BSA. Secondary antibody incubation was performed using Alexa Fluor A488 anti-rabbit antibody (Invitrogen) and CY5 conjugated anti-mouse antibody (Jackson ImmunoResearch Laboratories), both diluted to 5  $\mu$ L/mL in PBS<sup>+/+</sup>, 0.1% Tween 20, and 2% BSA,. The sections were incubated with the secondary antibodies for one hour under slow agitation at room temperature protected from light. This was followed by three washes and a 30-minute incubation with PBS<sup>+/+</sup>, 0.1% Tween 20, and 2% BSA. Finally, nuclei staining was performed by incubating the sections with Hoechst (diluted 1/1000 in PBS<sup>+/+</sup>, 0.1% Tween 20, and 2% BSA) for 15 minutes at room temperature. The Hoechst solution was then replaced with PBS<sup>+/+</sup>, 0.1% Tween 20, and 1% ATAM and stored at 4° C for further image acquisition.



#### 4.2.4 AFM measurements

Tissue samples were incubated at 37°C on a hotplate for 10 minutes prior to measurement, and a hydrophobic pen (Dako pen, Agilent Technologies, USA) was used to draw an incubation space around the sample. Careful periodic washing was carried out with filtered PBS<sup>+/+</sup> buffer to remove OCT, detached cells or tissue debris. Next, the sample was immediately immersed in a droplet of filtered PBS<sup>+/+</sup> buffer + 0.01% Pluronic F-127. Measurements were performed within the next 1–2 hours at room temperature. At least two maps of 100x100 µm were acquired per biopsy using the Cell Hesion module using similar operational parameters as Chapter 3.

#### 4.2.5 Image acquisition

Stitched images of toluidine blue and trichrome Goldner stained samples were captured using an inverted microscope (IX83, Olympus France, Rungis, France) at 20x magnification and a color camera (CAM SC50, Olympus France), which supported the selection of the region of interest (ROI) during AFM measurements. For immunofluorescence, phase contrast, DAPI, CY5 and GFP images were captured for the tissue morphology, nuclei, vimentin and  $\alpha$ -SMA, using a digital CMOS camera (ORCA-Flash4.0, Hamamatsu Photonics, Japan) with exposure times of 100 ms, 1 s, 500 ms, 500 ms and 350 ms, respectively.

In the absence of a motorized stage on the AFM, the positions where the stiffness was measured were manually located on the toluidine blue stained mirror section. 660 x 660 µm<sup>2</sup> were drawn on the image of the mirror section stained with toluidine blue at these positions. Capture of images on the sections stained for collagen or proteins were performed at these marked positions, by using visual recognition of specific patterns present on the mirror section stained with toluidine blue.

#### 4.2.6 Data and statistical analysis

Data processing consisted of analyzing colored bright field images of Trichrome Goldner stained samples and fluorescence for nuclei, vimentin and  $\alpha$ -SMA. For Trichrome Goldner images, ImageJ was used to split the RGB channels. Blue channel image was used to measure the collagen density at the corresponding positions. Background was removed by the use of a threshold. The outside part of the biopsy was used to set the value of the threshold. The intensity density (unit/µm<sup>2</sup>) was computed by dividing the sum of the intensity of the pixels by the total area minus the area of the background. For the quantification of the immunofluorescence signal, phase contrast images were used to create a mask of the tissue. This allowed to remove bias that could come from different degree of compacity of the tissue (for example in the presence of a lacy morphology compared to dense nests). Using the process tool Image Calculator, the generated mask was subtracted from the CY5 (far-red) channel image corresponding to the

vimentin content. Vimentin intensity was computed as intensity divided by the working area from the mask (unit/ $\mu\text{m}^2$ ). Similar procedure was undertaken for  $\alpha$ -SMA captured on the GFP channel. Spearman's rank correlation was employed to evaluate the relationships between tissue stiffness and the content of the proteins of interest, namely collagen, vimentin, and  $\alpha$ -SMA. This non-parametric measure was chosen given its ability to detect both linear and non-linear associations, providing a comprehensive evaluation of potential correlations. Additionally, to understand the relationships between the different proteins themselves, pairwise Spearman's correlations and Shapiro-wilk test for normality were also computed between the content of collagen, vimentin, and  $\alpha$ -SMA. A p-value less than 0.05 was considered statistically significant in these analyses.

### 4.3 RESULTS

#### 4.3.1 Correlation between collagen content and tissue stiffness

Understanding the correlation between collagen content and tissue stiffness was a key aspect of our research. Using Trichrome Goldner staining, collagen was identified and quantified by measuring the intensity of the blue channel per  $\mu\text{m}^2$  for each selected region. Only one acinar and one solid biopsies could be analyzed. For the solid subtype, tissue stiffness varied from 1.6 to 7.1 kPa, with collagen content ranging from 168.6 to 184.9 units/ $\mu\text{m}^2$ . Despite the variability in tissue stiffness, collagen content remained relatively constant, implying that collagen does not significantly influence the variations in tissue stiffness within this subtype. In the acinar subtype, tissue stiffness varied from 1.1 to 7.2 kPa, while collagen content fluctuated between 114.2 and 177.4 units per  $\mu\text{m}^2$ . Again, there was a lack of direct correlation between tissue stiffness and collagen content. For instance, the maximum collagen content of 177.4 units per  $\mu\text{m}^2$  was seen at a moderate stiffness value of 7.2 kPa, while the lower collagen content of 114.2 units per  $\mu\text{m}^2$  corresponded with the minimal stiffness value of 1.1 kPa. Figure 4.6 the dispersion values of collagen intensity versus stiffness for all subtypes.

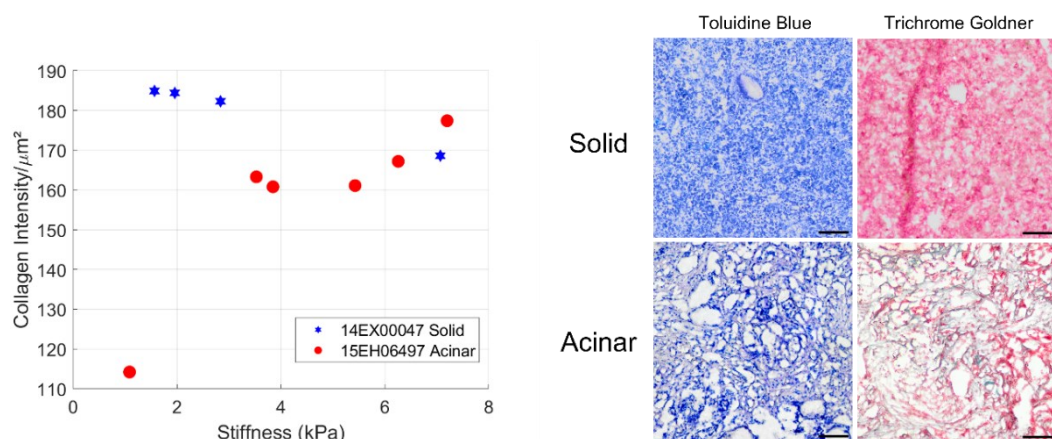


Figure 4.6 – Collagen intensity as a function of stiffness for both tumor subtypes.

In the examination of the association between tissue stiffness and collagen content, the Spearman correlation analysis produced a p-value of 0.85, demonstrating the absence of correlation between the local collagen content and the local stiffness of the tissue. When analyzing individually, the results suggest that the impact of collagen content on tissue stiffness may vary between solid and acinar subtypes of adenocarcinoma, with a direct correlation observed in acinar (Spearman test:  $\rho = 0.83$ ;  $p = 0.04$ ) and an inverse correlation in solid ones (Spearman test:  $\rho = -1$ ;  $p < 0.001$ ). While these correlations are significant ( $p < 0.05$ ), they nevertheless suggest that collagen content may impact the stiffness of both histological subtypes in a different manner, thus preventing a global analysis to be conducted. Consequently, within the constraints of this study, it appears that collagen content does not substantially affect the local tissue stiffness when all samples are considered collectively, although it has been demonstrated in the literature that an increased collagen concentration correlates to a stiffer matrix [264]–[266]. Moreover, this analysis does not rule out the existence of a relationship, as additional unconsidered factors (i.e., different ECM components, cross-linking, fiber orientation in both tissue subtypes and subtypes-dependent stiffness of the cells) could potentially impact these findings.

#### 4.3.2 Analysis of correlation between stiffness and vimentin

For this analysis, 2 solid and 1 acinar biopsies were analyzed. Upon examining the relationship between tissue stiffness and the intermediate filament protein vimentin, significant variations were observed based on the tissue subtype. Figure 4.7b shows the immunofluorescent labelling of the nuclei (DAPI) and vimentin (CY5 far-red). In the solid subtype of adenocarcinoma, vimentin levels varied considerably across different stiffness measures, ranging from 1.2 to 22.9 units/ $\mu\text{m}^2$  (Figure 4.7). The vimentin content did not exhibit a consistent trend with changes in stiffness. For instance, a high vimentin concentration was observed both at lower stiffness (2.0 kPa, vimentin: 22.9 units/ $\mu\text{m}^2$ ) and higher stiffness (7.1 kPa, vimentin: 21 units/ $\mu\text{m}^2$ ). Conversely, the lowest vimentin level was noted at a mid-range stiffness value of 2.8 kPa (vimentin: 1.2 units/ $\mu\text{m}^2$ ). In the acinar subtype, the vimentin content, which fluctuated between 9.8 to 16.2 units/ $\mu\text{m}^2$ , showed less variability compared to the solid subtype. Even with changes in stiffness ranging from 1.1 to 7.2 kPa, vimentin levels maintained a relatively narrow range with no apparent trend correlating increased stiffness with increased vimentin. Intracellular vimentin will be presented in topic 4.3.5.

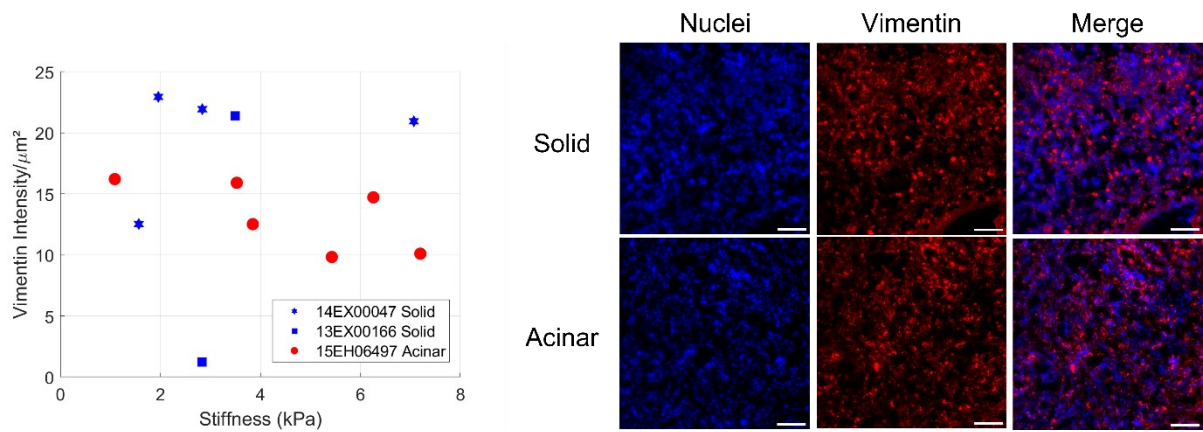


Figure 4.7 – Vimentin intensity as function of stiffness for both tumor subtypes.

Moreover, statistical analysis using Spearman's rank correlation test further substantiated this lack of correlation between tissue stiffness and vimentin, with p-value of 0.38 . The statistical analysis indicates no significant correlation in the case where the data from solid and acinar tumors were pooled. When each tumor type was analyzed individually, the Spearman's correlation did neither evidence any correlation. The p-value was of 0.87 for the solid tumors and 0.11 for the acinar tissue. These findings suggest a need for a larger data sets to provide more definitive insights into the correlation patterns.

#### 4.3.3 Analysis of correlation between stiffness and alpha-smooth muscle actin ( $\alpha$ -SMA)

In solid adenocarcinomas, we see a broad range of tissue stiffness values, from a low of 1.6 kPa to a high of 7.1 kPa. Correspondingly,  $\alpha$ -SMA expression also varies considerably, with values as low as 6.2 units/ $\mu\text{m}^2$  at the high end of stiffness, and as high as 25.9 units/ $\mu\text{m}^2$  at a mid-range stiffness level. Interestingly, the data shows no apparent consistent correlation between increased tissue stiffness and  $\alpha$ -SMA expression within this subtype (Figure 4.8). In acinar adenocarcinomas, stiffness values fluctuate between 1.1 kPa and 7.2 kPa. However, the associated  $\alpha$ -SMA expression remains comparatively steady, mostly within the lower range from 4.13 to 6.21 units/ $\mu\text{m}^2$ , with a single higher instance at 9.44 units/ $\mu\text{m}^2$  (Figure 4.8). Statistical analysis revealed a Spearman's coefficient of -0.61 with *p* value of 0.036, suggesting a negative correlation between stiffness and  $\alpha$ -SMA. Conversely, the analysis for both solid and acinar tumors did not reveal any correlations, with *p*-values of 0.70 and 0.47 for solid and acinar tumors, respectively. Overall, these results suggest a complex interplay between tissue stiffness and that  $\alpha$ -SMA content may inversely correlate with tissue stiffness, although it is suspected that the overexpression by activated fibroblast in lung tumor may lead to increased stiffness [244]. It must be noted, however, that the lack of statistical significance observed in correlations for individual tumor subtypes highlights the necessity for larger datasets to affirm these findings, thereby strengthening the statistical reliability.

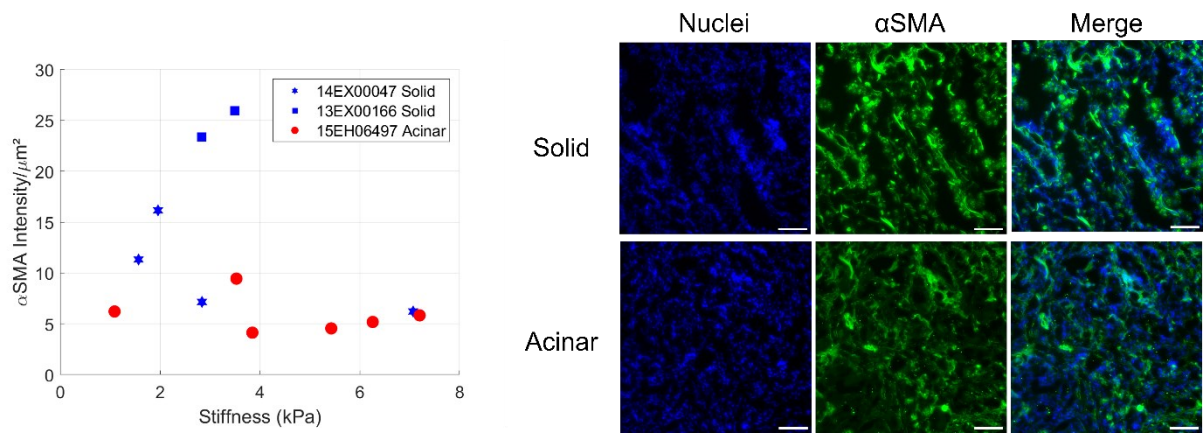


Figure 4.8 –  $\alpha$ -SMA intensity as function of stiffness for both tumor subtypes.

#### 4.3.4 Correlation between collagen, vimentin, and $\alpha$ -SMA

For two patients (out of 2), we obtained a correlation between the local stiffness of the tissue and the collagen content, the correlation being positive for the patient with acinar histological subtype and negative for the patient with solid histological subtype. However, neither the vimentin nor the  $\alpha$ -SMA contents were correlating to the local stiffness for these patients. We therefore wondered whether there might be a correlation between collagen, vimentin and  $\alpha$ -SMA content. For example, it could be that vimentin or  $\alpha$ -SMA content, which should contribute positively to tissue stiffness, correlate negatively with collagen content and prevents any clear correlation with stiffness.

The analysis reveals interesting patterns when exploring the correlation between vimentin,  $\alpha$ -SMA, and collagen. For instance, a positive correlation was observed between vimentin and  $\alpha$ -SMA expression with a p-value of 0.038 ( $\rho = 0.66$ ), suggesting an associated increase in  $\alpha$ -SMA expression with the rise in vimentin expression (Figure 4.9a). These results indicate a potential cooperative effect of the two proteins in contributing to tissue stiffness. On the contrary, the relationship between vimentin and collagen appears to be not statistically significant, with a Spearman p-value of 0.37 (Figure 4.9b). Nevertheless, a significant positive correlation is found between  $\alpha$ -SMA and collagen with a Spearman correlation coefficient of 0.64 with p-value of 0.048 (Figure 4.9c). This could potentially point to a concerted action of these two proteins in modulating tissue stiffness. These results suggest that since  $\alpha$ -SMA positively correlates with collagen content and with vimentin, collagen and vimentin contents should also positively correlate. This points to the need to enlarge the dataset with additional patients.

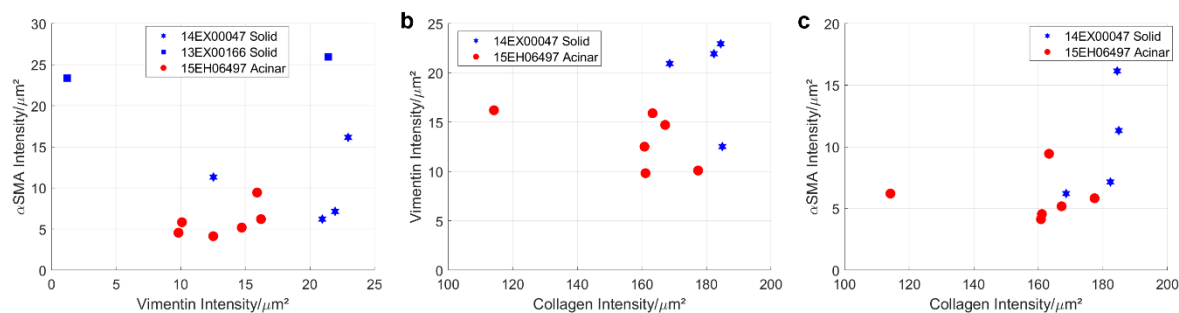


Figure 4.9 – Correlation analysis of vimentin,  $\alpha$ -SMA, and collagen contents. (a) Scatterplot showing the correlation between vimentin and  $\alpha$ -SMA ( $\rho = 0.66$ ;  $p = 0.038$ ). (b) Scatterplot showing the correlation between vimentin and collagen ( $\rho = 0.32$ ;  $p = 0.37$ ). (c) Scatterplot showing the correlation between  $\alpha$ -SMA and collagen ( $\rho = 0.64$ ;  $p = 0.048$ ).

#### 4.3.5 Vimentin distribution in A549 cells appears to be similar to that observed in cells present within lung adenocarcinoma tissue

The distribution of vimentin was examined in A549 cells, a human lung adenocarcinoma cell line, and compared to that of cells present in lung adenocarcinoma tissue samples (both solid and acinar subtypes). Interestingly, the intracellular distribution of vimentin in A549 cells showed similarities to the pattern observed in the tissue samples. In both A549 cells and lung adenocarcinoma tissue, vimentin predominantly localized in the cytoplasm, forming a filamentous network that extended to the cell periphery as shown in Figure 4.10. This observation aligns with vimentin's well-established role as an intermediate filament protein responsible for maintaining cell shape and integrity, and with the organization that is expected in tumor cells [254]. In both types of samples, the distribution was non-uniform, with certain regions appearing to have a higher concentration of vimentin. Furthermore, instances of extracellular vimentin were observed in the lung adenocarcinoma tissue samples. Extracellular vimentin has been implicated in various pathological conditions, including cancer, and has been shown to facilitate cell adhesion, migration, and immune response evasion [247], [267]. Although the function of extracellular vimentin in lung adenocarcinoma requires further investigation, the presence of vimentin outside the cell boundary may play a role in modulating tissue stiffness and promoting cancer progression. In conclusion, similarities in intracellular vimentin distribution between A549 cells and lung adenocarcinoma tissues was noticeable and confirmed the relevance of using A549 cells as a model cell line for cellular tests performed for this study (Chapter 6). The presence of extracellular vimentin in the tissue samples further suggest a potentially expanded role for vimentin in lung adenocarcinoma beyond its traditional intracellular functions.

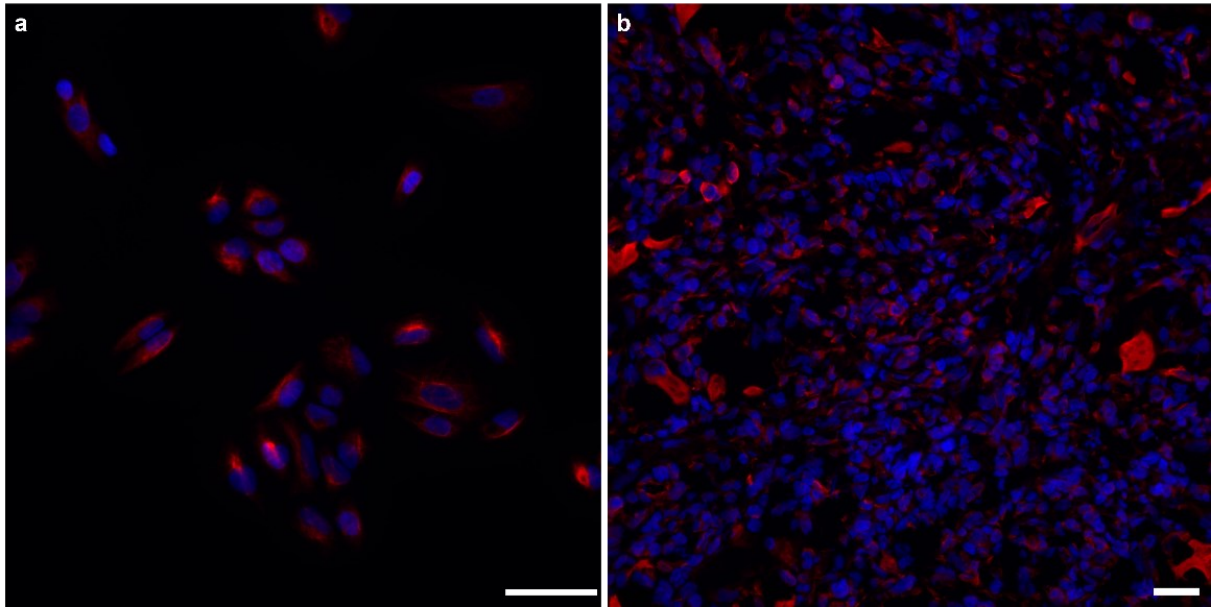


Figure 4.10 – Comparative analysis of vimentin in A549 cells and lung adenocarcinoma tissue: The figure depicts the relative expression of vimentin, a type III intermediate filament protein, in A549 lung carcinoma cells and tissue samples from patients with lung adenocarcinoma. (a) shows immunofluorescence staining of vimentin (red) in A549 cells, while (b) presents similar staining in lung adenocarcinoma tissue, potentially presenting a mesenchymal state. Bars in 50  $\mu\text{m}$ .

#### 4.4 DISCUSSION

The results presented in this chapter reveal intriguing patterns concerning the role of collagen, vimentin, and  $\alpha$ -SMA in the stiffness of lung adenocarcinoma tissues. Although this work explored the interplay between these structural proteins and tissue rigidity, it is important to bear in mind the limitations of the study. The scope was constrained by the size of the dataset and the observational nature of the experiment, with data gathered from a relatively limited number of tissue samples. As a result, these findings serve as an early investigation into the relationship between these proteins and tissue stiffness in lung adenocarcinoma, rather than establishing definitive patterns or relationships. Therefore, these insights should be interpreted with a degree of caution, and broader generalizations must be substantiated by further studies using larger datasets.

It is known that these proteins have distinct but overlapping distributions in various cell types. Collagen, for instance, is mainly produced by fibroblasts and myofibroblasts in the stroma of tissues [268]. Vimentin is a type III intermediate filament protein ubiquitously expressed in mesenchymal cells, which include fibroblasts, endothelial cells, and various immune cells such as macrophages [246],[267],[254].  $\alpha$ -SMA is a marker for myofibroblasts and smooth muscle cells but can also be expressed in fibroblasts during processes like wound healing or fibrosis [244],[269].

While increased collagen content compared to the healthy tissue contributes to increase the mean stiffness of the tumor tissues [181],[189],[232] the analysis of the local collagen content and tissue stiffness demonstrated a lack of a significant correlation, albeit some subtype-specific trends are suspected: increased collagen content could positively reinforce tissue stiffness in acinar subtype ( $p = 0.04$ ) but have no or a negative influence in solid subtype ( $p < 0.001$ ). Consistently, the Shapiro-Wilk test revealed that the collagen distribution neither follows a normal distribution within each patient (14EX00047:  $p = 0.036$ ; 15EH06497:  $p = 0.014$ ) nor across the whole patient population ( $p = 0.008$ ). While more data are needed to confirm it, differences between both subtypes are not unexpected, the solid subtype exhibits a dense cellular organization while the acinar subtype shows a lacier organization (Figure 2.7). Thus, the ECM scaffold could have a different density in both subtypes that results in a different impact on tissue stiffness. For example, physical properties of collagen fibers, such as cross-linking or orientation as previously described in section 4.1.2 could correlate with an increased stiffness in the acinar tissue while variation of density in a more uniform network of collagen fibrils would have less impact on the local stiffness. In addition, other ECM components could contribute to the local stiffness, which expression is subtype-dependent. Therefore, a deeper exploration of the tissue microenvironment and composition might help elucidate the factors contributing to tissue stiffness.

The complexity of these results is further exemplified by the findings concerning vimentin and  $\alpha$ -SMA. Mirroring the findings regarding collagen, vimentin did not exhibit an overall clear correlation with tissue stiffness. Intriguingly, this study revealed a significant negative correlation between  $\alpha$ -SMA and tissue stiffness, contrary to expectations based on previous literature [244]. Yet, when analyzed individually by histological subtypes, the correlations, albeit negative, did not reach statistical significance. These observations suggest the presence of intricate regulatory mechanisms governing these proteins expression and their impact on tissue stiffness, which might be specific to the tumor subtype. Importantly, the interplay between these proteins emerged as a significant factor. Upon Shapiro-Wilk normality test,  $\alpha$ -SMA displayed a normal distribution within each patient but not across the collective patient set (14EX00047:  $p = 0.509$ ; 15EH06497:  $p = 0.116$ , patient set;  $p = 0.032$ ). This divergence points to data insufficiency, which hinders a concrete conclusion. Interestingly, two patients displayed relatively constant spatial  $\alpha$ -SMA quantities, which were somewhat similar. In contrast, the third patient values noticeably differed. However, a positive correlation was found between  $\alpha$ -SMA and vimentin content, consistent with the idea that  $\alpha$ -SMA presence is more likely in mesenchymal tissue. As for vimentin, it was found to conform to a normal distribution both within each patient and across the patient cohort (14EX00047:  $p = 0.076$ ; 15EH06497:  $p$



= 0.248, patient set;  $p = 0.308$ ). However, no correlation emerged between vimentin content and stiffness, regardless of whether the data were analyzed as a whole, by subtype, or by patient. Additionally, no correlation between vimentin and collagen content was observed, suggesting that vimentin's influence on rigidity may not be the dominant factor. The intricacy of the role of vimentin extends beyond its relationship with other proteins and tissue stiffness. The presence of vimentin in both intracellular and extracellular spaces observed in this study aligns with the growing body of research acknowledging the expanded functional scope of this protein. Emerging evidence indicates that vimentin is actively secreted through the Golgi apparatus, interacting with specific cell-surface receptors and thereby initiating various cellular responses. This extracellular form of vimentin secreted by macrophages [267] or astrocytes [270] participates in diverse processes, such as tissue inflammation, wound healing, and axonal growth.

While these findings shed some light on the correlation between structural proteins and tissue stiffness in lung adenocarcinoma, the observed extracellular vimentin has been known to tissue remodeling, immune evasion, and potentially, tumor progression [247],[248]. Though the relevance of these modifications to lung adenocarcinoma has yet to be determined, they could provide additional information about disease state or progression.

# CHAPTER 5

---

## MIMICKING TISSUE STIFFNESS TEXTURE ON HYDROGEL

## 5 REPRODUIRE LA TEXTURE DE RIGIDITÉ DES TISSUS DANS UN HYDROGEL

Ce chapitre plonge au cœur de cette thèse, en commençant par une exploration exhaustive des concepts fondamentaux. La première section introduit le domaine de la fabrication d'hydrogels, expliquant des concepts tels que la photolithographie et les stratégies de réticulation des hydrogels. Elle décrit également les caractéristiques des hydrogels de polyacrylamide et leur pertinence pour cette recherche. Les techniques de fabrication d'hydrogels à rigidité modulée, ainsi que les considérations pour la fonctionnalisation de surface des hydrogels, sont également discutées.

En passant aux matériaux et méthodes, le chapitre détaille le processus de conception de masques à niveau de gris et les étapes impliquées dans leur fabrication. Cela pose les bases pour une exploration approfondie de la façon dont les hydrogels de polyacrylamide à rigidité modulée sont créés, leur caractérisation mécanique, et les étapes nécessaires pour la fonctionnalisation de surface.

Le cœur du chapitre présente les principales conclusions de la recherche. Il balaye la génération des motifs jusqu'à la fabrication de masques ainsi que l'optimisation des paramètres pour la conception de masques et de la fabrication d'hydrogels. La géométrie résultante et la rigidité des motifs de cercles aléatoires à l'échelle micronique sur des hydrogels de polyacrylamide sont examinées, suivies d'une discussion sur la fonctionnalisation de surface optimisée pour permettre la culture de cellules A549 sur ces substrats. Le chapitre se conclut par une discussion approfondie qui lie les différents aspects de la fabrication d'hydrogels à rigidité modulée et les différentes stratégies utilisées pour réaliser une fonctionnalisation efficace de la surface.

## 5 MIMICKING TISSUE STIFFNESS TEXTURE ON HYDROGEL

This chapter delves into the core of this thesis, beginning with a comprehensive exploration of fundamental concepts. The initial segment introduces the domain of hydrogel fabrication, explaining concepts such as photolithography and hydrogel cross-linking strategies. It also describes the characteristics of polyacrylamide hydrogels and their relevance to this research. The techniques for fabricating stiffness-patterned hydrogels, along with considerations for hydrogel surface functionalization, are also discussed.

Moving on to the materials and methods, the chapter elaborates on the process of pattern mask design and the steps involved in the gray-level mask fabrication. This sets the groundwork for an in-depth exploration of how stiffness-patterned polyacrylamide hydrogels are created, their mechanical characterization, and the steps needed for surface functionalization.

The core of the chapter presents the main findings of the research. It follows the process from pattern design generation to mask fabrication and optimization of both mask design and hydrogel fabrication parameters. The resulting geometry and rigidity of micron-scaled random circle patterns on polyacrylamide hydrogels are examined, followed by a discussion on the refined surface functionalization needed to enable A549 cell culture on these substrates. The chapter concludes with an extensive discussion that links the different aspects of stiffness-patterned hydrogel fabrication and the different strategies used of to achieve effective surface functionalization.

## 5.1 FUNDAMENTAL CONCEPTS

### 5.1.1 Microfabrication techniques

#### 5.1.1.1 Photolithography

The utilization of standard planar lithography techniques, first employed in the 1960s during the rise of the semiconductor industry, remains a prevalent method for the fabrication of transistors and integrated circuits (ICs) within the field of microelectronics [271]. Photolithography, which was later referred to as microlithography, and now as nanolithography, has unquestionably been one of the major driving forces behind the progress made in the semiconductor technology. Since its inception, the semiconductor industry has been focused on miniaturization, in order to increase the number of devices that can be integrated into a small area on a chip. The miniaturization of features in the semiconductor industry has been an ongoing objective since its early days and has been achieved through the utilization of photolithography or optical lithography. This technique has not only enabled the production of smaller and more complex devices, but also played a significant role in the advancement of mask making, which is an essential aspect of photolithography.

This well-established microfabrication technique uses light to transfer a geometric pattern from a photomask to a light-sensitive material, known as a photoresist, on a substrate [272]. The process typically involves several steps, including substrate preparation, photoresist application, prebaking, exposure to light through a photomask, post-exposure baking, development, and hard baking [272]. The photomask contains the desired pattern, which can be created through various methods such as electron beam lithography or laser writing [273], [274]. The photoresist can be either positive or negative, with the former becoming more soluble upon exposure to light, and the latter becoming less soluble. Upon exposure, the photoresist undergoes chemical changes that enable selective removal during the development stage [275].

The transfer of the pattern from the mask substrate to the artifact substrate is typically accomplished by utilizing a change agent, such as light, that can pass through the transparent artifact substrate. Conversely, the patterned media on the mask substrate is typically less transparent or opaque to this change agent [271]. The transmitted image may pass through a lens, with either demagnification or 1:1, or it may be contact printed directly to the receiving substrate, as shown in Figure 5.1.

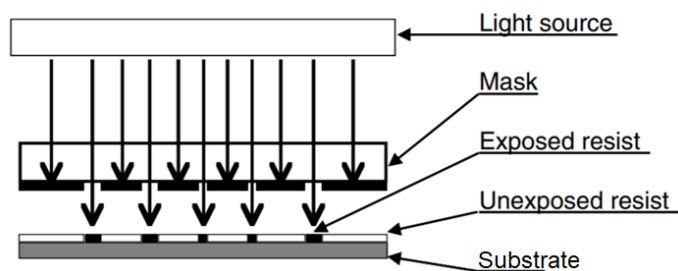


Figure 5.1 – Schematic of substrate exposure using a mask.

There have been significant advancements in photolithography in recent years, with the emergence of techniques such as extreme ultraviolet lithography (EUVL) and nanoimprint lithography (NIL) [276], [277]. EUVL employs extreme ultraviolet light with a wavelength of 13.5 nm to achieve higher resolution and pattern density compared to traditional photolithography [276], [277]. NIL, on the other hand, is a direct patterning technique that involves the mechanical deformation of a resist material using a patterned mold or stamp, which allows for high-resolution patterning without relying on light [276]. In brief, photolithography is a microfabrication technique used to selectively remove unwanted materials from a thin film surface or substrate bulk by utilizing light, such as ultraviolet (UV) radiation, to transfer a geometric pattern from a photomask onto a light-sensitive chemical substance known as a photoresist.

#### 5.1.1.2 Grayscale lithography

Grayscale lithography is an advanced yet moderately underutilized form of photolithography that enables the fabrication of three-dimensional (3D) microstructures with varying heights [278] or 2D topological features in photosensitive materials [227]. Unlike conventional binary photolithography, grayscale lithography uses photomasks containing a range of grayscale tones, known as gray-level masks. These masks generate varying levels of light transmission. They are obtained by depositing nanometer-scale layers of a metal material onto a substrate.

Prior to other microfabrication processes, physical vapor deposition (PVD) is commonly utilized in the fabrication of gray-level masks. A variety of PVD methods are available, such as thermal evaporation, sputtering, ion plating, and molecular beam epitaxy (MBE). Thermal evaporation involves heating the metal material through resistive heating, electron beam, or laser, leading to vapor formation [279]. The vapor condenses on the glass substrate, creating a thin metal film. Sputtering employs high-energy ion bombardment to eject atoms from a metal target, which then condense as a thin film on the substrate [280]. Ion plating uses a similar approach, with the addition of a reactive gas [281]. MBE can be considered as a precise form of PVD where a beam of metal atoms is directed toward the substrate, favoring the formation of a thin layer [282]. By fine-tuning the parameters of the PVD process, such as the type of

metal, the reactive gas, and the deposition rate, precise control over the thickness of the metal film can be achieved. This, in turn, determines the degree of light transmission through the mask, allowing for the creation of various grayscale tones on the mask. Therefore, given the varied transmittance levels, as light permeates through the mask, it illuminates the photoresist with different intensities. This difference in energy dose results in distinct levels of polymerization, for instance, within a hydrogel, which consequently manifests as a range of mechanical properties or microstructures.

Maskless lithography is another technique that enables exposing resists with different levels of light intensity [283]. For instance, DMDs enable the generation of grayscale patterns by spatially modulating the light intensity, thus varying the polymerization within the photoresist. This means complex structures can readily be produced. This technique is less resolved than the use of mask photolithography but it allows rapid prototyping and it eliminates the manufacturing stage of a gray level mask that can be cost prohibitive or time intensive.

#### 5.1.2 Hydrogel cross-linking strategies

Hydrogel cross-linking is an essential aspect of fabricating stable cell culture scaffolds, as it governs properties such as swelling behavior, porosity, and mechanical strength. The choice of a suitable cross-linking strategy relies on the specific application of the biomaterial. This section offers an overview of the primary factors to contemplate when selecting a hydrogel cross-linking strategy, along with a few commonly used methods.

The consideration of biocompatibility is paramount when selecting an appropriate cross-linking strategy. In instances where cells are encapsulated within a hydrogel for 3D culture systems, it is crucial that the cross-linking chemistry employed is non-toxic, ensuring cell viability and proper functioning. Conversely, for 2D scaffolds, the reduced direct contact between cells and cross-linking agents permits the adoption of more robust cross-linking approaches without significantly jeopardizing cell viability. By carefully selecting a cross-linking strategy in accordance with the intended application, the sustained vitality and functionality of the cells within the hydrogel scaffold can be achieved.

Moreover, the swelling or shrinking behavior (swelling kinetics) of cross-linked hydrogels must be considered. This behavior depends on factors such as hydrogel material, cross-linking density, and osmolarity of the incubating solution. Densely cross-linked materials such as polyacrylamide exhibit less swelling compared to loosely cross-linked hydrogels [284]. It is vital to consider swelling behavior during the design phase of a biomimetic cell culture scaffold, as it influences hydrogel shape over time. Another important factor is the degree of porosity and pore size, which are determined during the cross-linking process. These properties directly

affect nutrient and waste exchange for encapsulated cells in 3D [285] configurations. Hydrogels can be classified based on their pore sizes as nanoporous, microporous, or macroporous. Achieving higher porosity involves increasing the distance between cross-linking points or using double networks polymers, where one serves as a scaffold and the other modulates the pore size.

Degradability can be an important aspect in some applications, as controlled degradation of the hydrogel scaffold allows for matrix remodeling [286]. The majority of natural polymers can undergo enzymatic degradation by mammalian cells; however, hydrogels without inherent cleavage sites can be engineered by incorporating functional moieties that enable enzymatic breakdown [287] or facilitate activation through light exposure [288].

Common cross-linking strategies include physical cross-linking, which involves non-covalent interactions such as hydrogen bonding, hydrophobic interactions, or ionic interactions between polymer chains [289]. This cross-linking is reversible and might be less toxic to encapsulated cells. Another approach is chemical cross-linking, which involves covalent bonds between polymer chains formed through various reactions, such as Michael addition [290], click chemistry [291], or free radical polymerization that can be chemically, thermally or photo initiated [10]. The latter being advantageous due to gel-formation *in situ* and accurate spatiotemporal control. By modifying illumination parameters like distance, wavelength, power, and exposure time, hydrogel mechanical rigidity and biochemical properties can be precisely controlled [292]. A recent review by Zang et al. emphasized the elaborate interplay between macroscopic stability and microscopic dynamics in achieving structurally dynamic hydrogels with potential for biomedical applications [293]. Thus, chemical cross-linking generally results in more stable and mechanically robust hydrogels. Moreover, hybrid cross-linking integrates both physical and chemical cross-linking methods to attain particular properties and attributes of the hydrogel [294]. In essence, the selection of an appropriate hydrogel cross-linking strategy necessitates a thorough evaluation of the specific application demands, as well as the potential implications on cell viability, mechanical properties, and degradation kinetics.

### 5.1.3 Polyacrylamide (PA) hydrogel

Hydrogels are crosslinked polymer networks swollen with water, known for their high-water absorption capacities and tissue-like elastic properties, making them ideal candidates as supports or scaffolds for studying cell-substrate mechanical interactions. Certain types of hydrogels formed from biocompatible macromolecular precursors and mild gelation conditions



are often used to encapsulate cells in 3D scaffolds or serve as 2D supports [295]. Both natural and synthetic materials can be utilized in the fabrication of hydrogels (Table 5.1). To promote crosslinking, functional groups or crosslinking agents are introduced, which enable the formation of stable network structures. Natural materials, such as alginate, chitosan, and gelatin, can be modified with methacrylate groups to enhance crosslinking via physical or chemical interactions. Synthetic materials like polyethylene glycol (PEG) also require engineering to contain unsaturated groups, such as acrylate groups. In contrast, polyacrylamide is inherently equipped with amide groups, eliminating the need for additional functionalization before crosslinking. The tailored crosslinking process allows for the customization of hydrogel properties, such as mechanical strength, degradation rate, and swelling behavior.

Table 5.1 – Advantages and disadvantages of polymer precursors used for hydrogel synthesis. Adapted from Tenje et al. [296]

Polymer	Advantages	Disadvantages
<b>SYNTHETIC POLYMERS</b>		
Poly (ethylene glycol) (PEG) PEG-diacrylate PEG-dimethacrylate PEG-azide	<ul style="list-style-type: none"> <li>▪ Biologically inert</li> <li>▪ Dissolvable in different solvents which enables easy functionalization reactions</li> <li>▪ Inexpensive</li> <li>▪ No batch-to-batch variation</li> </ul>	<ul style="list-style-type: none"> <li>▪ No promotion of cell attachment</li> <li>▪ Not enzymatically degradable</li> <li>▪ Difficult to attain low stiffness (below 10kPa)</li> </ul>
Poly (acrylamide)	<ul style="list-style-type: none"> <li>▪ Stiffness modulation in a wide range of rigidities, between hundreds of Pa to several tens or hundreds of kPa, thus enclosing physiological rigidities of the in vivo ECM</li> <li>▪ Weak non-specific adsorption of the proteins to uncoated gel surface</li> <li>▪ Non degradable, preventing degradation by cells</li> <li>▪ Transparency</li> <li>▪ Cell penetration is avoided thanks to the existence of pores in the range of 100 nm</li> </ul>	<ul style="list-style-type: none"> <li>▪ No promotion of cell attachment</li> <li>▪ Monomers are cytotoxic</li> <li>▪ Not enzymatically degradable</li> </ul>
<b>NATURAL POLYMERS</b>		
<i>Polysaccharides</i>		
Hyaluronic acid (HA) HA-acrylate HA-methacrylate HA-thiol HA-norbornene	<ul style="list-style-type: none"> <li>▪ Enzymatically degradable</li> <li>▪ Biocompatible</li> <li>▪ Interacts with CD44 receptors</li> </ul>	<ul style="list-style-type: none"> <li>▪ Viscous solution</li> <li>▪ No promotion of cell attachment</li> </ul>
Alginate Alginate methacrylate	<ul style="list-style-type: none"> <li>▪ Inexpensive</li> <li>▪ Mild crosslinking conditions</li> <li>▪ Rapid gelation</li> <li>▪ Can be used as sacrificial layer</li> </ul>	<ul style="list-style-type: none"> <li>▪ Hydrogels can dissolve within days due to Ca<sup>2+</sup> loss</li> <li>▪ Diffusion dependent gelation that might result in heterogeneous cross-linking</li> <li>▪ Gelation leads to increase of viscosity and might clog chip</li> </ul>

### Proteins

Collagen	<ul style="list-style-type: none"><li>▪ Biocompatible</li><li>▪ Provides ligands for cell adhesion</li><li>▪ Can be gelled without chemical modification</li><li>▪ Enzymatically degradable</li></ul>	<ul style="list-style-type: none"><li>▪ Highly viscous in solution which makes handling difficult</li></ul>
Gelatin	<ul style="list-style-type: none"><li>▪ Inexpensive</li></ul>	<ul style="list-style-type: none"><li>▪ Rapid degradation</li></ul>
Gelatin methacrylate	<ul style="list-style-type: none"><li>▪ Low viscosity, easy handling</li></ul>	<ul style="list-style-type: none"><li>▪ Weak mechanical properties</li></ul>
Gelatin-thiol	<ul style="list-style-type: none"><li>▪ Enzymatically degradable</li></ul>	
Gelatin norbornene	<ul style="list-style-type: none"><li>▪ Provides ligands for cell adhesion</li></ul>	
Chitosan	<ul style="list-style-type: none"><li>▪ Anti-microbial activity</li></ul>	<ul style="list-style-type: none"><li>▪ Poor stability that restricts applications</li></ul>
Chitosan methacrylate		

---

Among the various materials for hydrogel synthesis, polyacrylamide was selected primarily due to its mechanical properties [29], [297]: a high deformability, with a linear response in a large range of deformation in the kPa range. However, as polyacrylamide is not permissive to cell adhesion, considerable work has been done to establish protein coupling strategies and make it suitable to cell culture applications [298]. Upon polymerization, acrylamide and bis-acrylamide combine to create elastic gels that exhibit consistent time-independent responses to stress. Charrier et al. demonstrated that incorporating linear polyacrylamide as a dissipative element within crosslinked gels creates a viscoelastic gel (Figure 5.2). The combination of entrapped and slowly relaxing linear chains forms a viscoelastic gel with distinct shear storage modulus ( $G'$ ) and loss modulus ( $G''$ ). Both  $G'$  and  $G''$  increase during polymerization, highlighting the confinement of linear molecules as the source of viscoelasticity [299].

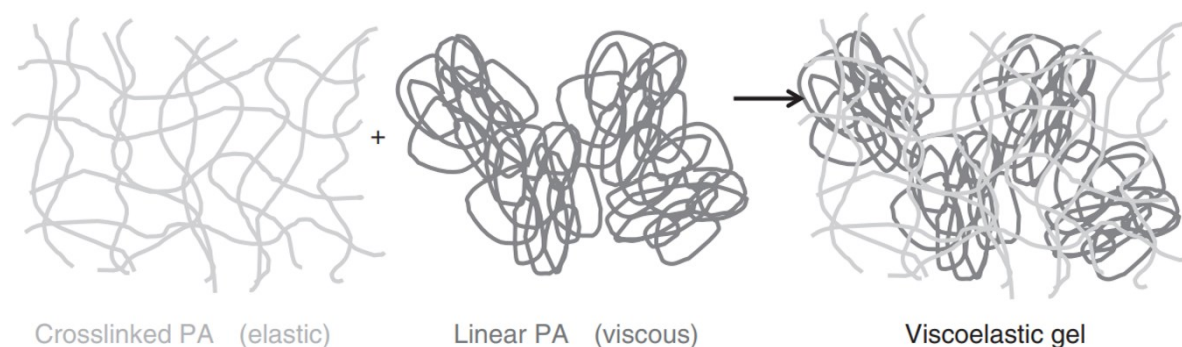


Figure 5.2 – Graphic representation from [299] of the combination of an elastic polyacrylamide network with a viscous solution of linear polyacrylamide, resulting in the formation of a viscoelastic gel. The entrapment of linear chains within the network is responsible for generating the viscoelastic properties of the hydrogel, highlighting the non-viscous nature of polyacrylamide.

Polyacrylamide hydrogels do not inherently interact with cell surface receptors or integrins, thus enabling user-defined control over these interactions. While not appropriate for 3D culture due to the toxicity of hydrogel precursors, polyacrylamide is well-suited for 2D long-term culture as its non-degradable nature ensures stable mechanical properties over time. It is particularly well-suited for mechanobiology investigations requiring precise manipulation of hydrogel stiffness [10]. This has been evidenced by recent studies demonstrating the effects of substrate stiffness on cell differentiation [299], spreading and migration [300]. In the context of this work, these attributes make polyacrylamide an attractive material for designing biomimetic culture supports that emulate the mechanochemical environment of human tissues.

#### 5.1.4 Stiffness pattern hydrogel fabrication techniques

The previously mentioned techniques have been instrumental for advancing microfabrication across various fields, notably including biology and medicine, significantly contributing to the development of innovative microdevices, such as those employed in tissue engineering [294], [301], microfluidic devices [302], biosensors [303], drug delivery systems [304] and cell culture platforms [305], [306]. Within the field of hydrogel fabrication, a diverse array of techniques has been devised to engineer hydrogels with distinct stiffness patterns and structures to mimic the mechanical properties of tissue microenvironment.

Among these techniques are microfluidic-based hydrogel fabrication, stereolithography, micropillars, photodegradation and photopolymerization. Microfluidic-based hydrogel fabrication employs microfluidic devices to manipulate small fluid volumes, generating hydrogel structures with precise control over stiffness, geometry, size, structure, composition, and physicochemical properties [307] (Figure 5.3a). This method also facilitates the integration of functional components, such as cells or biomolecules, during the fabrication process. Stereolithography is a 3D printing technique that utilizes a light source to selectively polymerize a liquid photopolymer resin [308]. A platform is submerged into the resin, and the light source traces a pattern on the surface of the resin, solidifying it layer by layer. By adjusting the exposure time, light intensity, and the type of photopolymer resin used, stiffness patterned hydrogels with varying mechanical properties can be fabricated (Figure 5.3b [309]). The micropillar technique involves the use of an array of pillar structures to manipulate the cellular microenvironment, offering mechanical and topographical control [310] (Figure 5.3c). The stiffness of hydrogels can also be controlled by using a photodegradation reaction, which involves a photodegradable cross-linker and monomers. In this technique, a photodegradable ether in the cross-linker can be cleaved by irradiation, leading to the degradation of the hydrogel network and a decrease in stiffness. By varying the light exposure time and intensity, patterns

of stiff and soft regions can be created on the hydrogel surface. This technique was used in a recent study to investigate the effects of spatially patterned matrix elasticity on stem cell fate [227] (Figure 5.3d). Lastly, photopolymerization has emerged as a predominant method for achieving two-dimensional (2D) stiffness patterning in hydrogels. Photopolymerization leverages the controlled exposure of light to initiate polymerization and crosslinking reactions within photosensitive hydrogel precursors. By precisely modulating the intensity, duration, and spatial distribution of light exposure, in combination with a patterned mask or not, hydrogels can present specific topological stiffness patterns [311] (Figure 5.3e). This high degree of spatial resolution, coupled with rapid processing times and compatibility with various photosensitive materials, makes photopolymerization particularly advantageous.

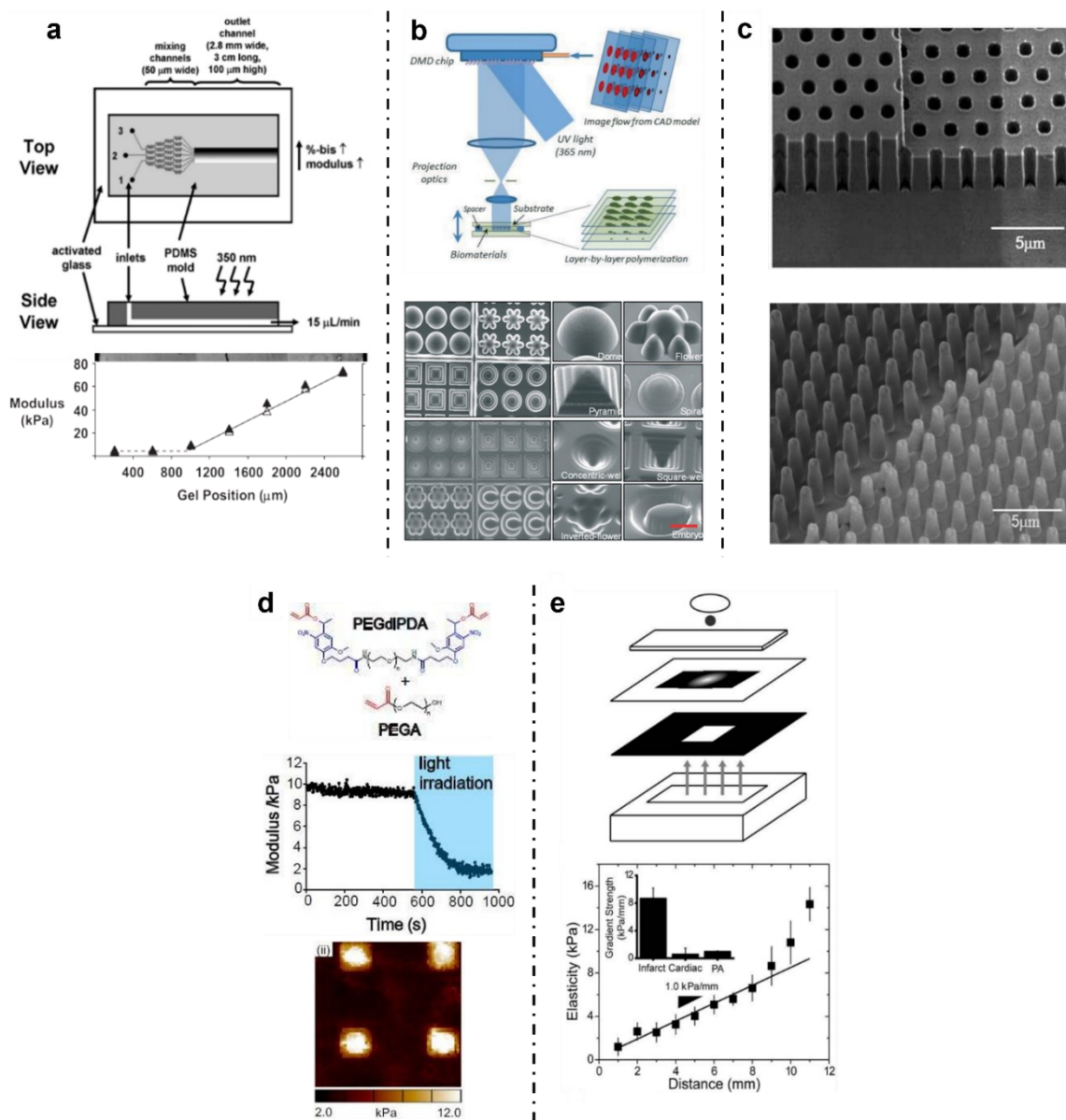


Figure 5.3 – Different fabrication techniques to engineer hydrogels with stiffness patterns and structures. (a) Microfluidics, (b) Stereolithography, (c) Micropillars, (d) Photodegradation and (e) Photopolymerization.

Li et al. have recently demonstrated the potential of a novel closed-loop control algorithm using digital holographic microscopy-based stiffness imaging feedback for high-accuracy control of mechanical properties in hydrogel microstructures [312]. This breakthrough holds promise for regenerating complex biomimetic extracellular matrices in tissue engineering and biomedical research applications. However, to expedite industry-oriented product development focused on high throughput analysis for drug discovery, a simpler strategy is preferable. By fabricating a gray-level mask with tissue-specific pattern distribution using standard optical lithography and using photopolymerization to pattern the hydrogels, we aim to achieve heterogeneous stiffness in a more efficient and scalable manner. This streamlined approach not only focuses on relevance but also emphasizes scalability, flexibility, and customization, ultimately enabling the design of mechanomimetic hydrogels of diverse human organs.

#### 5.1.5 Hydrogel surface functionalization

Surface functionalization of hydrogels refers to the process of modifying the surface properties of hydrogels by introducing specific functional groups or molecules. The purpose of this modification is to tailor the hydrogel characteristics, such as biocompatibility, cell adhesion, mechanical strength, and responsiveness to environmental stimuli. Functionalization can be achieved through various methods, such as covalent attachment of functional groups, physical adsorption of molecules, or the incorporation of specific biomolecules during hydrogel synthesis.

The chemical inertness of polyacrylamide presents both notable benefits and drawbacks. This property effectively prevents nonspecific cell adhesion when employed as a culture substrate, allowing controlled regulation of adhesive interactions, offering a distinct advantage when exploring the mechanical influence of specific receptors or adhesive proteins. However, the extent of this inertness also poses a constraint, as its chemical characteristics can hamper straightforward covalent attachment, thus requiring the use of linker molecules, plasma treatment, or photoinitiated reactions. A variety of protein conjugation strategies have been introduced [298], highlighting the use of heterobifunctional reagents Sulfo SANPAH or Sulfo-LC-SDA for the functionalization of polyacrylamide. Sulfo-LC-SDA being more reactive than Sulfo SANPAH thanks to its photosensitive diazirine group [313]. This chemistry offers increased stability and reactivity compared to alternative compounds [298].

Recent studies [220], [306] have successfully demonstrated the capacity to decouple hydrogel stiffness and adhesive ligand functionalization allowing for a more comprehensive understanding of complex cellular responses to these factors, which would be challenging to achieve using natural materials. Previous studies have not explored this decoupling, as the

materials utilized were either conducive to cell adhesion [314] or not assessed [315]. For instance, numerous cell types, including human MSCs, exhibit increased spreading and proliferation as stiffness rises. However, when cultured on laminin-coated hydrogels, MSCs spread to a lesser extent compared to other ECM protein coatings. This example highlights how the interplay between hydrogel stiffness and adhesive ligand presentation can be tailored to manipulate cellular responses [316].

### 5.1.6 From rigidity maps to mechano-mimetic hydrogels

Thus, to coherently incorporate the AFM measurements presented in Chapter 2 and extracted texture parameters from Chapter 3 with the goal of integrating these specifications within a hydrogel, a structured approach was adopted. As a reminder, our process begun with the AFM measurements, capturing the mechanical properties of the lung tissue samples. Subsequently, the extraction of texture parameters from rigidity maps provided an in-depth understanding of the rigidity patterns and attributes. Now we proceed to emulate these stiffness texture in a polyacrylamide hydrogel. Figure 5.4 provides a visual summary of these integral stages involved in our fabrication process. Consequently, in the Materials & Methods section that follows, we detail the procedure corresponding to the mask and hydrogel fabrication steps.

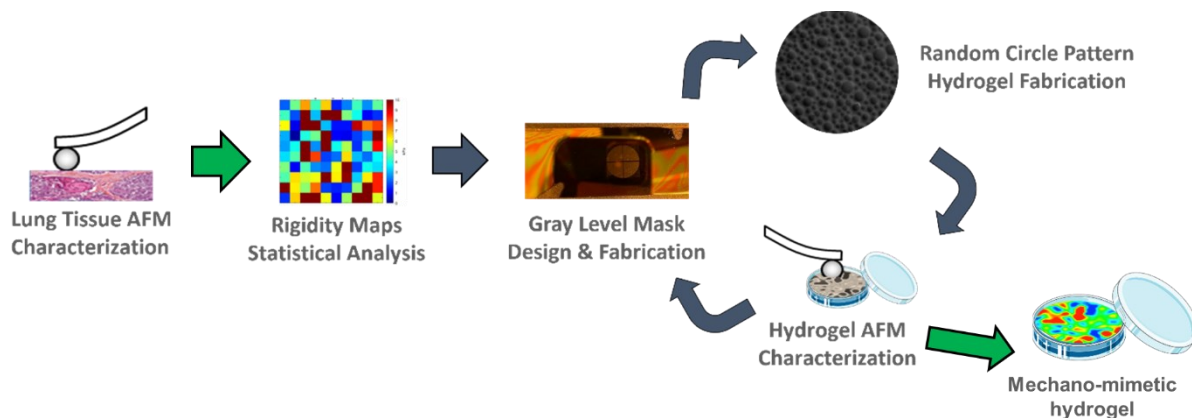


Figure 5.4 – Roadmap for developing mechano-mimetic hydrogels, going AFM characterization of lung tissue to mechano-mimetic hydrogel..

## 5.2 MATERIALS AND METHODS

### 5.2.1 Pattern mask design

Random circle patterns were generated using an algorithm implemented both in MATLAB and Python. Initially, only data from acinar tissues was available, thus mask design parameters were obtained considering different shape descriptors. These data were used for initial experiments for determining mask fabrication parameters. Furthermore, final mask design took into consideration the tumor lung (acinar and solid) tissue rigidity maps shape descriptors described in section 3.3.4.

Pixel size of the design is dependent of the tool that will be used to transfer the pattern onto the photomask. Here, it is given by the resolution of the tool, the SmartPrint UV (Microlight3D, France) with a 5x objective, with a pixel size  $pix = 1.0851 \mu\text{m}$ . The smallest feature possible at this magnification is  $3 \mu\text{m}$ , offering sufficient precision for this application. The area covered by the patterns, which is a disk with a diameter of 32 mm, is then defined and converted into pixels. This area composes a matrix S, which is initially filled with zero logical values.

In the algorithm, a new Gaussian distribution G of the radii natural logarithm  $\ln(R)$  was generated by considering the statistical parameters extracted from the natural logarithm of the rigidity patterns radii distribution. The mean of this normal distribution is the median, hence,  $\text{Median} = \ln(R_{\text{geomean}} = 2.27)$  with standard deviation  $\sigma = 0.61$  (Figure 5.5a). To position the disks, a pixel is randomly selected in the matrix S (x and y coordinates), then, the new gaussian distribution is exponentiated to obtain the radii log-normal distribution (Figure 5.5b).

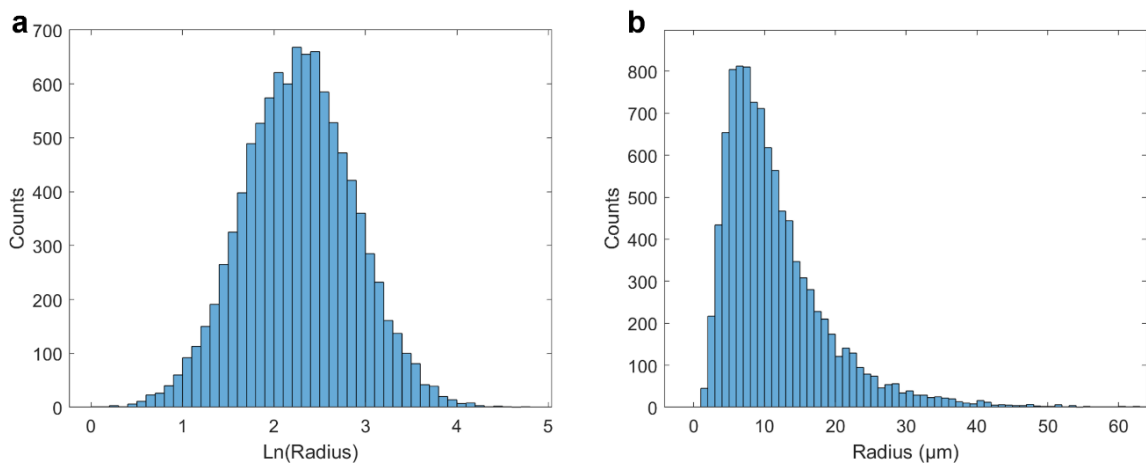


Figure 5.5– (a) Generated random circle radii gaussian distribution with 10000 values center at  $M = 2.27$  and  $\sigma = 0.61$ , corresponding to natural logarithm of the geometric mean of the rigidity pattern radii distribution. (b) Exponential of the gaussian distribution with geometric mean =  $9.7 \mu\text{m}$ , hence the radii log-normal distribution from where random radii will be selected.

A random radius within the previously defined maximum and minimum radii range is selected from the log-normal distribution and pixelized as  $R/pix$ . The algorithm evaluates if the selected circle does not overlap with an existing circle by checking whether the distance between the centers of the new circle and the nearest neighbors is greater than the sum of their radii, plus an optional constant allowing for proper separation of the patterns by the lithographic tool – for instance, in this work, the smallest distance was chosen to be 2  $\mu\text{m}$  after a few iterations. If this condition is not met, a new pixel is selected randomly along with a new radius, and the test is repeated until the new disk is properly positioned relative to its neighbors, without overlap. After obtaining a list associating centers and radii, each disk area is transferred to the matrix  $S$  by replacing the values 0 (false) with the value 1 (true) for the respective pixels. The matrix  $S$  is then converted to an 8-bit binary image. Moreover, the algorithm to generate the pattern had to be adapted to deliver a file that was compatible with lithography operation software (Phaos, Microlight3D). The image was then saved in .tif format for further analysis and processing. Due to the large file size ( $\sim 800$  Mb), the image was divided in six equal parts and stitched during photolithography process (Phaos software only accept files below 140 Mb). The mask design resulted in random distribution of hundreds of thousands of circular patterns and can be further adapted to any pattern shape.

### 5.2.2 Gray-level Mask Fabrication

Gray-level masks were engineered from the textured rigidity maps. Compressed  $\text{N}_2$  was used to remove any visible macroscopic elements from the surface of the 76x26x1.2 mm glass slides. The slides were then thoroughly rinsed with a jet of DI water to remove nonvisible particles. Next, a fiber-free cloth was soaked in acetone, and each glass slide was manually cleaned. The slides were then immersed in a piranha solution (a 2:1 mixture of 97% sulfuric acid and 30% hydrogen peroxide) for 10 minutes. After removal from the piranha solution, the slides were rinsed vigorously with DI water three times to eliminate any residual particles and dried under compressed  $\text{N}_2$ . Glass slides underwent plasma treated at 100%  $\text{O}_2$  for 5 min and were then immediately transferred to the chamber of a Plassys type electron gun (MEB550, electron gun 10 kW, Marolles-en-Hurepoix, France). The latter was employed to deposit 1 nm of titanium and 17 nm of chromium on activated surface. This resulted in a transmission coefficient of 13% at 365 nm UV light. For the photolithography, 1 ml of TI Prime (MicroChemicals, Germany) was spin-coated at 2000 rpm, and 5000 rpm/s for 30 s on the substrate to promote adhesion of the photoresist. The glass slide was heated at 100  $^\circ\text{C}$  for 50s on a hot plate. 2 ml of AZ1512s (MicroChemicals, Germany), a positive tone photoresist commonly used for micro and



nanofabrication, was spin-coated at 2000 rpm and 5000 rpm/s for 30 s to obtain a 600 nm layer. The glass slide was soft-baked at 100 °C for 50s on a hot plate to remove any residual solvents and enhance the adhesion of the photoresist to the substrate. This ensures a clean and stable resist layer for exposure, preventing resist lifting or peeling during subsequent steps. Then, each part of the random circle pattern .tif (previously split in six) was loaded to the software and automatically divided in 86 subimages, adjusted for alignment and stitching. Next, the substrate was exposed to UV light (385 nm) for 0.6 seconds per subimage – writing field (2.1 x 1.2 mm) – with a 5× objective using a Smart Print-UV (Microlight3D, France) maskless photolithography system. After exposure, the substrate was hard-baked at 120°C for 50 s. In this step the substrate was heated to harden and reinforce the recently exposed photoresist, enhancing its chemical and mechanical stability. This process is essential for achieving high-resolution patterns and ensuring the photoresist can withstand subsequent etching processes. Next, the resist pattern was developed by immersing it in 1:3 AZ-400K (MicroChemicals, Germany):de-ionized water mixture, which removed the exposed areas while leaving the unexposed areas intact. The optimal development time ranged from 15 to 20 seconds to ensure high pattern fidelity and reduced defects. Chromium wet etching was performed using TechniEtch Cr01 (MicroChemicals, Germany) to remove the exposed chromium areas, transferring the pattern to the mask. Immersion time is dependent on Cr thickness layer. At 20°C etching speed is estimated to be around 60 nm/min or 1 nm/s [317]. Consistently, the region of interest becomes *de visu* transparent after 18 to 20 s immersion. After etching, the substrate was slowly agitated for 5 min in two subsequent DI water baths and further dried using compressed N<sub>2</sub>. Finally, to remove the photoresist, the mask was immersed in acetone for four minutes, stirring manually. Afterward, a double rinse was performed, first with 96% ethanol and then with isopropanol. Subsequently, the mask was dried out using an N<sub>2</sub> air gun and stored in a clean container. To summarize, Figure 5.6 illustrates the procedure used to transfer the generated design on the gray-level mask.

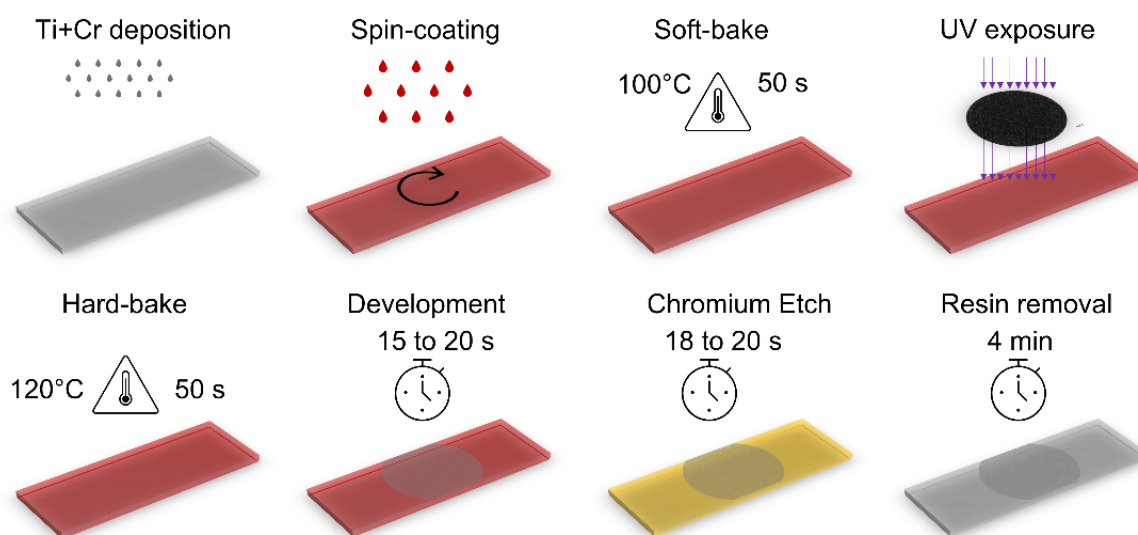


Figure 5.6 – Mask fabrication processing steps. From left to right: Ti+Cr layer is deposited, positive resin is spin-coated, soft-baked for 50 s at 100 °C , then pattern is transferred using SmartPrint UV, next development using AZ400K for 18 to 20 s, finally removing resin with acetone.

Utilizing a glass slide as a lithographic mask for the polymerization of monomers in an aqueous solution necessitates the application of a hydrophobic treatment to minimize material adhesion during the process. The slide is rendered hydrophobic through the covalent grafting of fluorinated chains (Optool, Daikin DSX, Japan). This is achieved by immersing it for 1 minute in Optool, diluted at 1/1000 with perfluorohexane. Subsequently, the slide is exposed to water vapor at 65°C for 1 hour. Lastly, it is gently rinsed for 10 minutes in perfluorohexane with slow agitation.

### 5.2.3 Fabrication of stiffness-patterned polyacrylamide hydrogel

Hydrogels with random circle pattern mimicking tissue stiffness heterogeneity were obtained from the rapid photopolymerization of an acrylamide/bis acrylamide solution through a gray-level mask. The preparation of the solution of monomers is described in reference [306]. In summary, 2 mg of a highly efficient UV-sensitive initiator Irgacure 819 (Ciba Specialty Chemicals, Basel, Switzerland) is dissolved into 10 µL of propylamine (Sigma-Aldrich, Saint Quentin Fallavier, France) at 52 °C for 10 min. 490 µl of deionized water, 250 µl of a 40% solution of acrylamide and 250 µl of a 2% solution of N, N-methylene-bis-acrylamide (Bio-Rad) were mixed, leading to a 10%-0.5% mixture of monomers. The solution was used 7 days after resting and for a month. During this time, the stock solution of monomers keeps a stable reactivity to UV exposure. 30 mm diameter coverslips were chemically activated using Bind Silane (Fisher Scientific) to allow stable, covalent bonding of the polyacrylamide hydrogels: the coverslips were first cleaned in a 0.1 M NaOH solution for 10 min, then rinsed first in

deionized water then in ethanol and dried using dry air. A solution containing 484  $\mu\text{l}$  of acetic acid, 56  $\mu\text{l}$  of BindSilane completed up to 15 ml with absolute ethanol was prepared. 500  $\mu\text{l}$  of this solution was pipetted to each coverslip and wiped off with a dust-free wiper. Masks remained for 5 minutes in perfluorohexane to enhance its hydrophobicity. 30  $\mu\text{l}$  of the prepolymer solution were deposited in the center of a silanized 30 mm diameter glass slide and reticulated by exposing the precursor solution sandwiched between the activated coverslip and the hydrophobic mask to UV-A ( $2 \text{ W/cm}^2$ , Eleco UVP281). The duration of the illumination tuned the mechanical properties of the hydrogel, depending on the experiment. Next, the glass slide and the mask were placed in deionized water for at least 25 minutes and carefully detached from the mask. The hydrogel was rinsed three times with deionized water to remove unreacted compounds and stop the polymerization reaction. Finally, it was placed in deionized water to swell overnight.

#### 5.2.4 Mechanical characterization of the hydrogel and stiffness patterns

Mechanical properties of the patterned hydrogels were measured using the NanoWizard II AFM (JPK Instruments, Berlin, Germany) in the force mapping mode with a pyramidal tip on a MLCT C cantilever (Bruker, Palaiseau, France) with a nominal spring constant of 0.01 N/m. Young's moduli were fitted from the indentation curves using a Hertz–Sneddon mode. Rigidity maps were acquired randomly, independent on the size of the pattern. Stiffness characterization was conducted in at least 16 random locations with force-maps of  $2 \times 2 \mu\text{m}$  consisting of  $2 \times 2$  pixels on soft (background) and rigid areas (circle patterns). Moreover, the characterization of the stiffness texture of the hydrogel was performed by acquiring force-maps of  $100 \times 100 \mu\text{m}$  with  $20 \times 20$  to  $25 \times 25$  pixels. At least 60 random circles diameters were characterized by image analysis in parallel to the acquisition of force/indentation curves using the AFM microscope.

### 5.2.5 Surface functionalization of stiffness-patterned hydrogels

The patterned polyacrylamide hydrogel was made compatible with cell culture by covalently grafting collagen I to its surface via the photosensitive NHS-ester diazirine heterobifunctional crosslinker sulfo-LC-SDA (Sulfosuccinimidyl6-(4,4'-azipentanamido) hexanoate). Figure 5.7 shows the chemical reaction involved in this process.

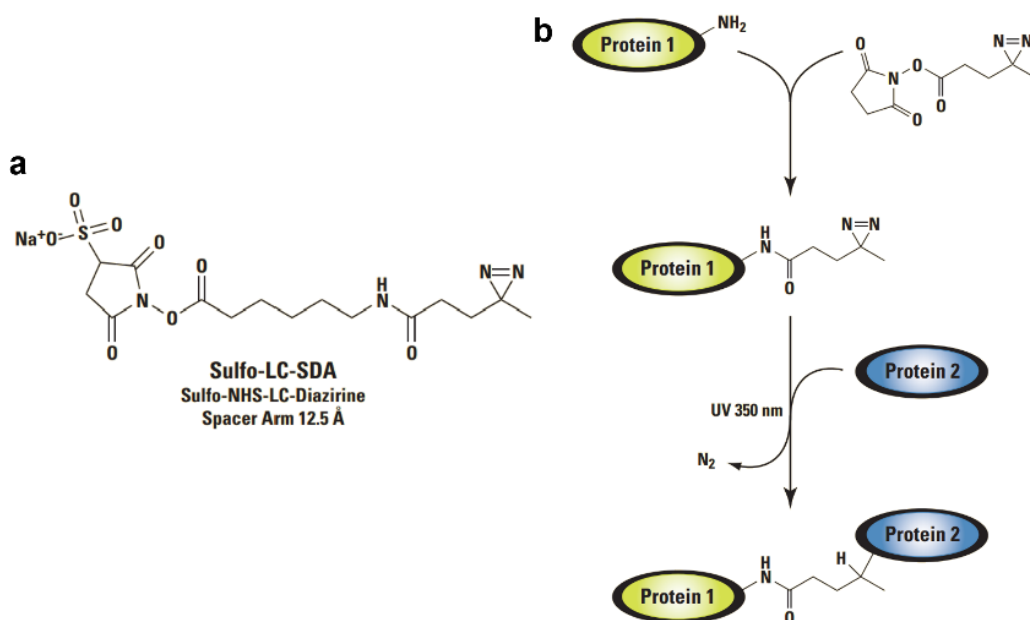


Figure 5.7 – (a) Structure of the heterobifunctional sulfo-LC-SDA. (b) NHS-ester diazirine crosslinking mechanism involves NHS esters reacting with primary amine groups (-NH<sub>2</sub>) within pH 7-9 buffers, forming stable amide bonds and releasing NHS. Photoactivation of diazirines with long-wave UV light (330-370 nm) results in reactive carbene intermediates [313].

The NHS end of the sulfo-LC-SDA reacts with primary amines and the diazirine group reacts under UV activation to any unsaturated group (among which, polyacrylamide).

Different protocols were attempted to favor uniform functionalization, functionalization of the background (soft regions) and overfunctionalization of the stiff patterns of the hydrogel. To ensure the grafting of a sufficient number of proteins at the surface of the hydrogel, the protocols involved slight or more intense dehydration steps of the solutions of crosslinker or of proteins, whose efficacy was already demonstrated for polyacrylamide hydrogels with uniform stiffness [306]. Nevertheless, previous work already observed that dehydration steps can lead to a non-uniform coating when the hydrogel bears a stiffness texture of few microns [220]. Here the stiffness patterns being larger, the effect of dehydration steps was investigated. The proof of concept was performed with fluorescently labelled fibrinogen (Molecular Probe), with the aim of transferring it to collagen I, a protein that is dominant in lung tissues.

Initially, the gels were dehydrated after fabrication to enhance their ability to fill with the crosslinker solution. This also made it possible to seal them at the bottom of drilled Petri dish using an UV sensitive glue (Norland 68), following a patented process (FR3098525). The crosslinker solution was added at a concentration of 0.6 mg/ml. After 1h, the crosslinker solution was removed and the gels were slightly dehydrated (for 20 min, until the surface appears dry). The gels were then exposed to UV light for 5 min. This enabled the attachment of the crosslinker to the polyacrylamide chains. Figure 5.8 show the attempted surface functionalization protocols.

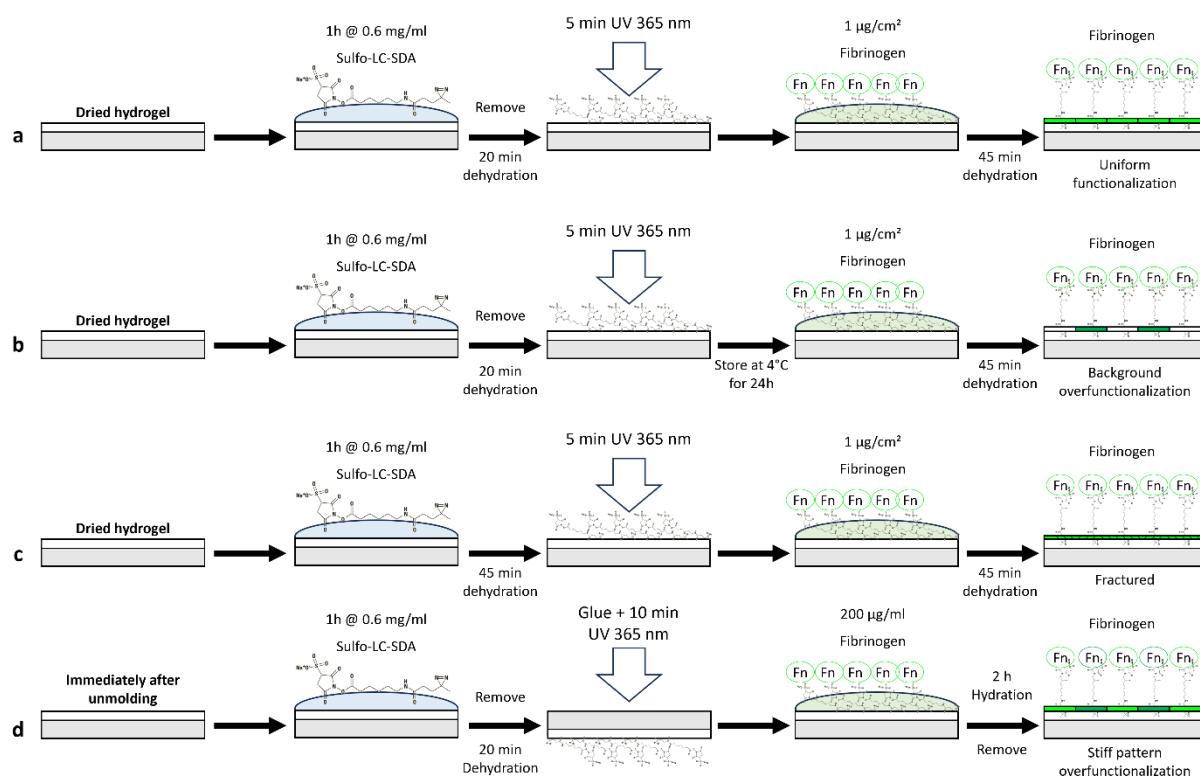


Figure 5.8 – Schematic representation of the different protocols employed for surface functionalization of the hydrogel. Each protocol is characterized by a unique sequence of steps, including immersion in sulfo-LC-SDA, UV exposure, and dehydration steps.

(a) To obtain a uniform protein coating (Figure 5.20a), the solution of fluorescently labeled fibrinogen was deposited on the hydrogel at a theoretical surface density of  $1 \mu\text{g}/\text{cm}^2$  and let to evaporate under a laminar flow hood until the surface was dry (1h30 to 2h). (b) This step allowed to concentrate the protein solution close to the surface of the hydrogel and enhance the reaction of the NHS group of the crosslinker with the amine groups of the protein. To enhance the surface functionalization on the soft regions (around the stiff patterns), the hydrogel was let for resting overnight at  $4^\circ\text{C}$  after binding the crosslinker to the hydrogel (Figure 5.20b). Identical steps were performed afterward with the solution of fluorescently labeled fibrinogen. (c) Finally, overfunctionalization of the stiff patterns was initially obtained by following the same protocol as in (a) but with strongly dehydrating the protein solution (more than 2 h, Figure 5.20c). When the mean stiffness of the hydrogel was set to low values consistent with the ones


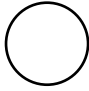
measured in lung tissues, this unfortunately resulted in the appearance of fractures at the surface of the hydrogel. To limit fractures, the protocol was reconsidered and the dehydration steps were limited. (d) Instead of working with initially dry samples, the gel was immersed in sulfo-LC-SDA solution (same concentration as before) for 1h right after the fabrication. The gel could then fill with the crosslinker solution when swelling. After 1h, the crosslinker solution was removed and the gels were slightly dehydrated (for 20 min, until the surface appears dry). Crosslinking of the sulfo-LC-SDA was then performed at the same time as the sealing of the gel at the bottom of the drilled Petri dish, by UV illuminating the assembly backward for 10 min. Subsequently, to reduce dehydration, fluorescently labelled fibrinogen solution was promptly deposited at 200  $\mu\text{g}/\text{ml}$  and let for react for 2 h. Finally, the solution of proteins was removed and the functionalized gel immediately rinsed with water and immersed in PBS ++ to swell overnight. As shown on Figure 5.20d, we observed that this protocol prevented the formation of fractures and led to a non-uniform surface functionalization, the stiff patterns having a higher concentration of protein than the soft background.

## 5.3 RESULTS

### 5.3.1 Random circle pattern design generation

Generation of the pattern mask design was implemented based on the previously described design parameters. These design parameters were extracted after image and statistical analysis of the pattern areas above an arbitrarily defined rigidity threshold from healthy and tumor lung tissues. The rigidity threshold and the distance between circles (spacing) emerged as critical parameters and were subjected to iterative optimization after hydrogel mechanical characterization. A custom-made MATLAB algorithm was implemented to generate a randomized array of non-overlapping circular patterns, distributed across a circular surface with a diameter that matched or exceeded the glass slide supporting the hydrogel. Basic geometric parameters were sourced from the rigidity maps and employed to generate the mask design (Table 5.2). The standard shape derived from the shape descriptors was simplified into a circle as explained in topic 3.3.4.

Table 5.2 – Input parameters from rigidity patterns and resulting design parameters.

Parameters	Rigidity maps Parameters	Generated Design
Standard Shape		
Median ( $\mu\text{m}$ )	8.0	7.6
Max ( $\mu\text{m}$ )	48.9	40.1
Min ( $\mu\text{m}$ )	5.6	4.6
Geomean ( $\mu\text{m}$ )	9.7	8.1
Geo Std. Dev. ( $\mu\text{m}$ )	1.8	1.4
Minimum Spacing ( $\mu\text{m}$ )	-	2
%SORT	30.92%	30.92%

The generation of the random circle pattern mask design initially posed a computational challenge, due to the necessity of scanning the entire matrix every time a new circle was added. This exhaustive approach led to significant delays, with computation times averaging around 60 hours. To address this, a new approach was implemented to accelerate the pattern generation process. Instead of scanning the entire matrix, a virtual window matching the circle size was created for each new circle. The logical values were then altered only within this confined area. Through this localized approach, the computation times were dramatically reduced to just a few minutes, without compromising the integrity or precision of the pattern design. Figure 5.9 shows the final random circle pattern design.

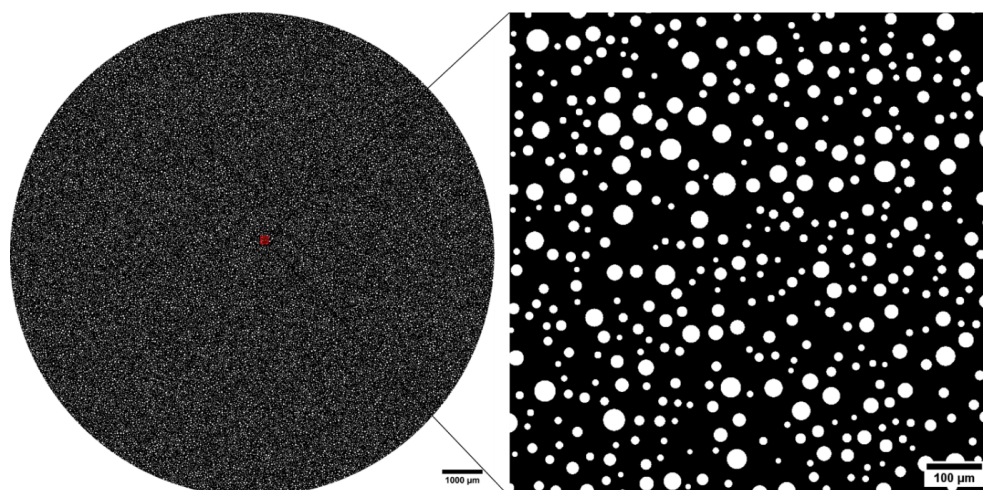


Figure 5.9 – Random circle pattern generated using a custom-made algorithm implemented in MATLAB.

As a result, over 700000 disks were randomly positioned without overlap occupying 30.92% of a circular surface of 32 mm of diameter.

### 5.3.2 Random circle pattern mask fabrication

In this section, we present the results from the fabrication of a gray-level mask with random circle patterns. The mask fabrication process consists of a series of steps, each with specific objectives, designed to ensure the accurate transfer of the pattern onto the hydrogel substrate. The first step involves the deposition of titanium and chromium layers on the substrate using a Plassys-type electron-gun. This step is critical in creating an adhesion layer (Ti) and a pattern transfer layer (Cr) that will serve as the basis for the subsequent photoresist coating. This adhesion layer is necessary because previous experiments in the lab have shown that the polymerization of the hydrogel is very aggressive for the surface of the mask, although it is treated with an inert anti-sticking layer. The absence of adhesion layer resulted in the detachment of grains of chromium after few uses of the mask.

It is important to mention that errors in alignment (before UV exposure), development or etching at any stage of fabrication can adversely affect the accuracy of the intended pattern, therefore they must be mitigated. For instance, the maskless lithographic tool we used (SmartPrint UV, Microlight3D) can print these large number of patterns only by dividing the image in 6 parts. To ensure seamless alignment, careful calculation of the coordinates was carried out and considered during stitching. Remarkably, the initial results, demonstrated a high degree of correspondence between the fabricated masks and the original design, as illustrated in Figure 5.10, although parameters were not yet optimized regarding the precision of the lithography (for instance, no gap between the circles was imposed at this stage).



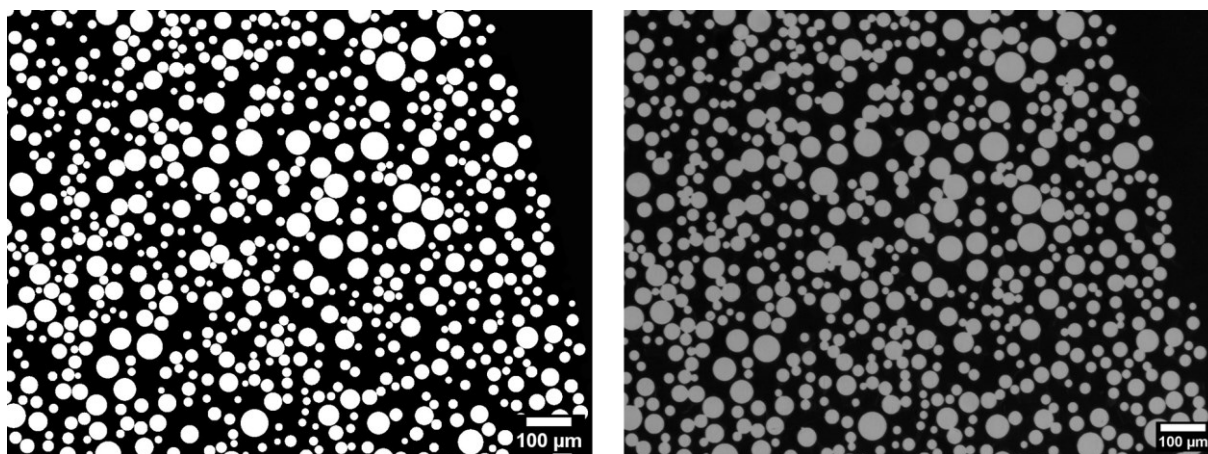


Figure 5.10 – (Left) Random circle pattern design template. (Right) Example of a fabricated gray-level mask with random circle patterns after chromium etching.

Nevertheless, analysis of the circles dimensions transferred to the mask showed to be slightly bigger than the design, requiring design optimization. Image analysis was conducted on both the design and the mask to assess the resulting circle radius distribution. Circle radius ranged from 5.8 to 32.9  $\mu\text{m}$ , with a geometric mean radius of 12.7  $\mu\text{m}$ . This value was found to be approximately 8% smaller than the geometric mean radius of the circles in the fabricated mask, which was 13.7  $\mu\text{m}$ , as summarized in Table 5.3.

Table 5.3 – Circle size analysis of Figure 5.9 representing the random circle pattern design and the fabricated mask without optimization. Values are in micrometers.

Parameters	Design	Mask	Difference
Median	12.6	13.57	8%
Max	32.9	34.13	4%
Min	5.8	6.26	8%
Geomean	12.7	13.70	8%
Geo Std. Dev.	1.43	1.40	-2%
%SORT	34.07%	37.66 %	11%

The reduction in circle dimensions was determined to be essential on the design phase, as the pattern dimensions on the mask can increase after chrome etching and also after hydrogel swelling. Moreover, the selection of an appropriate deposition thickness for the mask was a critical aspect of the fabrication process, as it can significantly impact the resulting hydrogel stiffness distribution. To determine the optimal deposition thickness, two masks with distinct deposition thicknesses - one with 15 nm (1 nm Ti + 14 nm Cr) and another with 18 nm (1 nm Ti + 17 nm Cr) - were fabricated. Hydrogels were then produced using each mask, with an illumination time of 12 seconds and intensity of 9.6  $\text{mW}/\text{cm}^2$  (60% of the maximum intensity) applied to both. The stiffness of the resulting hydrogels was evaluated to assess the influence of the metal thickness on hydrogel properties. AFM measurements revealed stiffness values of 4.4 kPa and 3.3 kPa (MWU-test:  $p < 0.0001$ ) for hydrogels fabricated using the 15 nm and 18

nm masks, respectively. Given that the 18 nm mask yielded a hydrogel with a stiffness distribution exhibiting a median value closer to the typical tumor stiffness distribution, it was selected for further mask fabrication and hydrogel production (Figure 5.11).

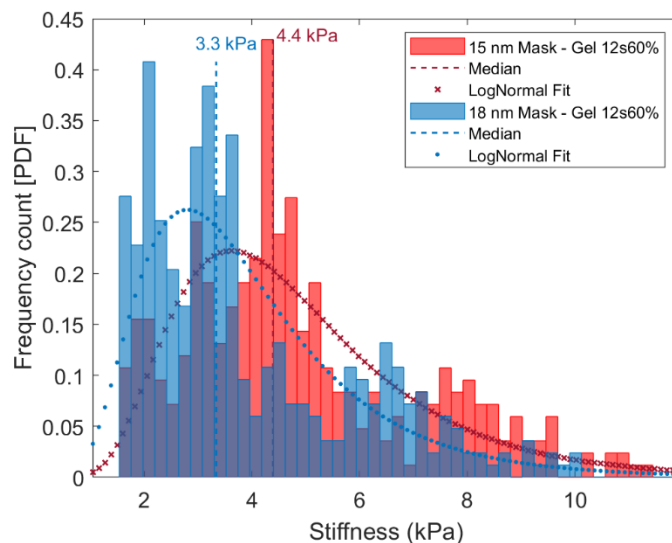


Figure 5.11 – Stiffness distribution of 12s60% hydrogels fabricated with (a) 15 nm and (b) 18 nm of chromium gray-level mask.

### 5.3.3 Optimization of mask design and hydrogel fabrication parameters

Mask design parameters optimization was fundamental for achieving a stiffness distribution in polyacrylamide hydrogels that closely resembles the one found in tumor tissues characterized in this work. The mask optimization design was guided by the following objectives:

1. To consider the circle size distribution based on the parameters calculated from both adenocarcinoma types, obeying a log-normal distribution with defined geometric mean and between the minimum and maximum circle radii range.
2. To create micron-scaled random circle patterns on the hydrogel surface that would yield the desired stiffness distribution found on the lung tumor tissues.

The final mask design was determined to have a circular surface with a diameter of 32 mm, which is slightly larger than the glass slide diameter of 30 mm or the size of a well in 6 wells plate. This provided enough margin for positioning the glass slide containing the hydrogel. The median surface density, represented by the Surface Over the Rigidity Threshold (SORT) percentage, was kept at 30.92% obtained from the texture statistical analysis (Topic 3.3.3). Circle radius distribution was designed to follow a log-normal law: this choice was arbitrary, as there was not enough experimental data to draw the population distribution of the sizes of the texture patterns. It is equivalent to assuming that the stiffness texture comes from a local increase of the content in extracellular matrix that is randomly scattered in the biopsy. An

examination was conducted to draw comparisons between the final mask and the constructed hydrogel, with a focus on assessing the accuracy of pattern replication. As delineated in Table 5.4, there were distinct similarities between the design parameters of circles in the fabricated hydrogel and those in the final mask design.

Table 5.4 – Comparison of parameters across different stages of pattern mask design and hydrogel fabrication.

Parameters	Input Parameters	Optimized Design	Gray-level Mask	Hydrogel 18s30%
Median	8	7.6	7.9	8.4
Max	48.9	40.1	43.5	43.1
Min	5.6	4.6	4	4.9
Geomean	9.7	8.1	8.3	8.8
%SORT	30.92 %	30.92 %	26.45 %	26.95 %
# Circles	-	738620	3185	5781

The last line of the table, representing the number of circles, refers to the count utilized in the circle size analysis. Due to the extensive size of the mask and hydrogel, the analysis was conducted on a subset of data, specifically, three large, representative images were chosen from both the mask and hydrogel stages. This selection process explains why the %SORT did not reach the anticipated 30.92%. Nonetheless, the sampled approach provided a representative dataset for the comparative analysis, while maintaining the general characteristics of the entire mask and hydrogel.

The median, maximum, minimum, and geometric mean radius of the circles in the hydrogel were mostly in line with those of the optimized design and the gray-level mask. However, the median and geometric mean circle sizes in the hydrogel did register a slight increase after swelling. While the differences were small, they suggest room for further improvements in pattern replication accuracy. The comparisons made, thus, underline the efficacy of the fabrication procedure in producing mask patterns in the hydrogel structure, albeit with some degree of variation. A visual demonstration of this comparative analysis is provided in Figure 5.12, showing the mask design and the corresponding hydrogel obtained with 18s of UV exposure at power 4.8 mW/cm<sup>2</sup> (noted 18s30% hereafter).

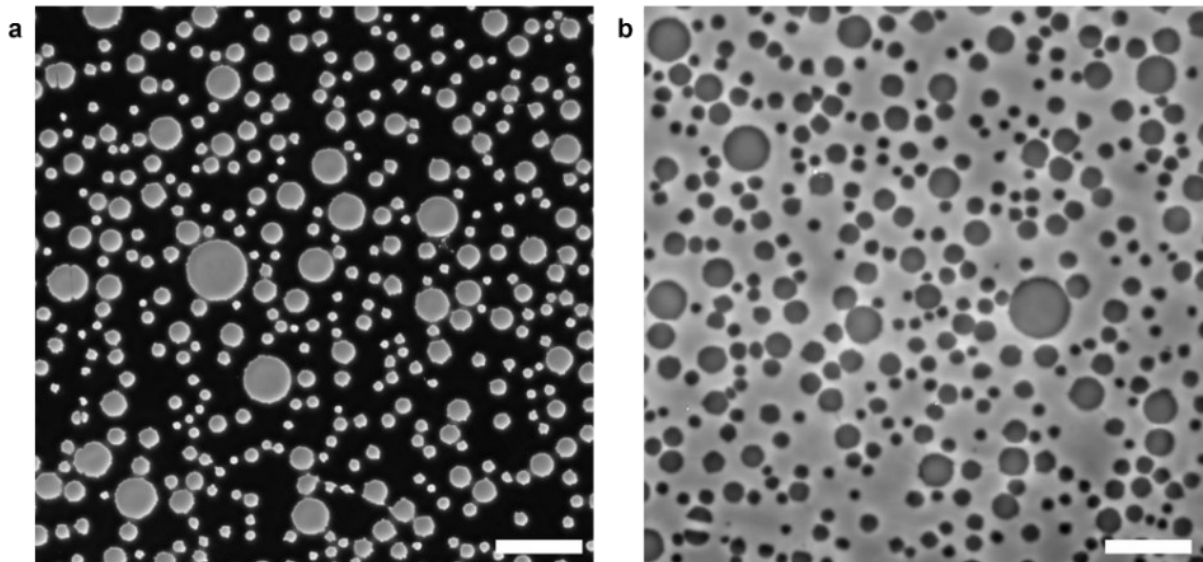


Figure 5.12 – Comparison between (a) the optimized gray-level mask and (b) the hydrogel obtained with 18s UV exposure at 4.8 mW/cm<sup>2</sup> (18s30%). Bars: 100  $\mu\text{m}$ .

The distribution of circle sizes across the optimized design, mask, and fabricated hydrogel was examined to further evaluate the replication accuracy. The optimized design served as the reference point, with its circle distribution acting as the target for the mask creation and hydrogel fabrication stages. Upon evaluation, as represented in Figure 5.13, the optimized mask exhibited a similar radius distribution to the optimized design, affirming the efficacy of the pattern transfer process during mask creation. The hydrogel, while demonstrating a comparable distribution, exhibited a slightly shifted circle size distribution, possibly due to swelling post-fabrication. These comparative assessments, emphasize the reproducibility and accuracy of the pattern replication process from design to hydrogel.

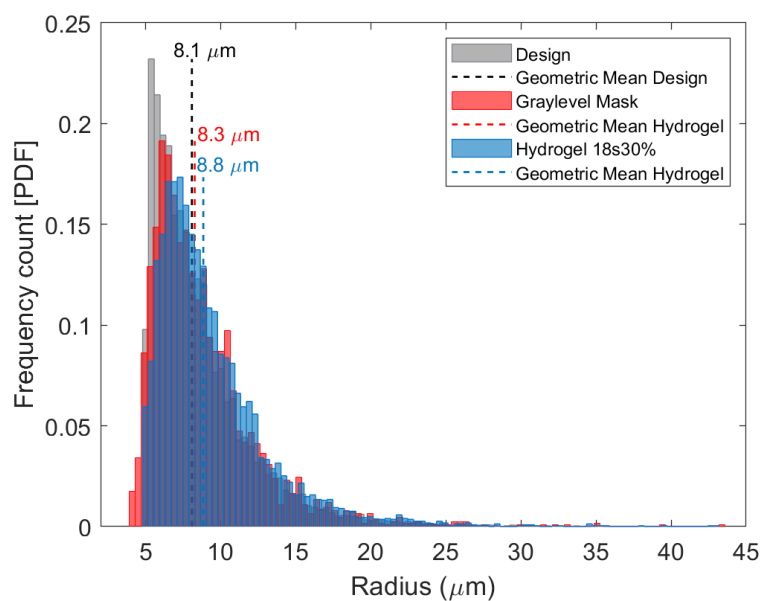


Figure 5.13 – Comparative analysis of circle size distributions across the optimized design, gray-level mask, and the fabricated hydrogel for 18s30%. A slight shift in the distribution is noted between stages, underscoring the variations that occur throughout the fabrication process.

The stiffness texture was transferred into the polyacrylamide hydrogel and the resulting stiffness distribution was compared to the one found in the analyzed tumor tissues. Multiple iterations were necessary to fabricate a mask that incorporate the ideal design parameters derived from the rigidity maps. This involved investigating the impact of UV dose (Eq. 5.1) on hydrogel stiffness, by employing varying combinations of intensities and illumination times, and subsequently characterizing the hydrogel mechanical properties using AFM.

$$\text{UV Dose} = \text{UV lamp power} \times \text{exposure time} \quad (5.1)$$

Figure 5.14 illustrate the relationship between the total energy delivered for reticulation (dose), and the median Young's moduli of the hydrogels.

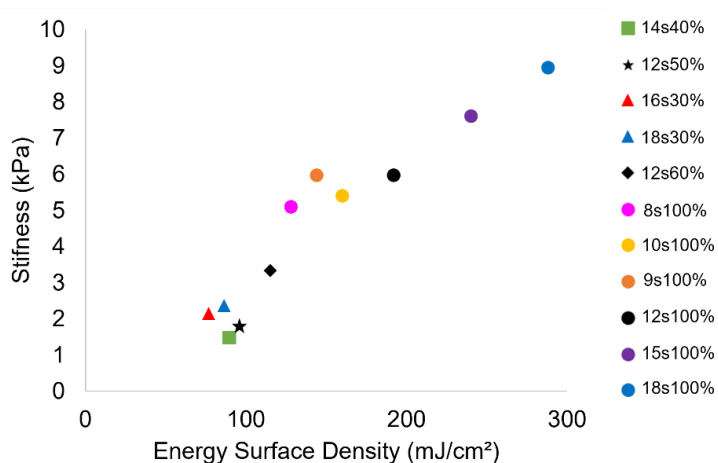


Figure 5.14 – Optimization of hydrogel fabrication parameters. Median stiffness of the gel as a function of the surface energy transmitted for reticulation. The optimal combination of illumination time 18s and 30% of maximal lamp intensity (4.8 mW/cm<sup>2</sup>) represented by the blue triangle marker was determined based on the closest match to the median stiffness of the tumor distribution.

Upon data analysis, an illumination time of 18 seconds at a power of 4.8 mW/cm<sup>2</sup>, which corresponds to an energy dose of 86.4 mJ/cm<sup>2</sup>, resulted in hydrogel with a median stiffness of 2.4 kPa, closely approximating that of the tumor tissues (2.5 kPa). Moreover, the data reveals a linear correlation ( $R^2 = 0.9033$ ) between stiffness and energy dose applied to the hydrogel. In principle, as evidenced by Sheth et al. [318], at lower energy surface densities, the correlation exhibits a linear trend; conversely, with extended exposure times and thus, higher energies, the correlation becomes exponential reaching a plateau (steady-state regime), characterized by the full hydrogel polymerization. Here the parameters we tried did not allow to reach the plateau.

### 5.3.4 Micron-scaled random circle patterns geometry and rigidity on polyacrylamide hydrogels

In this section, we investigate the relation between the size of the micron-scaled circle patterns and the local rigidity of the polyacrylamide hydrogels. Two distinct patterned hydrogels were fabricated, one at an exposure of 18s30% (86.4 mJ/cm<sup>2</sup>) and another at 22s30% (105.6 mJ/cm<sup>2</sup>). This second dose allowed to test the dose effect on the relation between the size and the stiffness of the patterns. Their mechanical properties were then characterized using AFM. Using a pyramidal probe, force maps were captured at various locations on the hydrogel surface. This included 2x2 pixels in 2x2 μm areas on the background (soft regions) and on the circles (rigid regions). Additionally, larger force maps of 25x25 pixels within 100x100 μm areas were captured at randomly chosen positions to ensure heterogeneity and complete the statistics. Before measurement, an image of each circle was taken to measure its size using ImageJ, considering a pixel size of 1.097 μm. Figure 5.15 showcases the correlation between the stiffness and the radius of the circles. Interestingly, a quasi-linear correlation was observed for both hydrogel conditions. The equations represent the relationship of the stiffness and radius of a patterned hydrogel at a certain exposure. For the 18s30% exposure hydrogel, the slope of 0.085 indicates a moderate increase in stiffness with increasing circle radius. Conversely, the 22s30% exposure hydrogel exhibits a steeper slope of 0.197, indicating a more pronounced increase in stiffness with increasing circle radius.

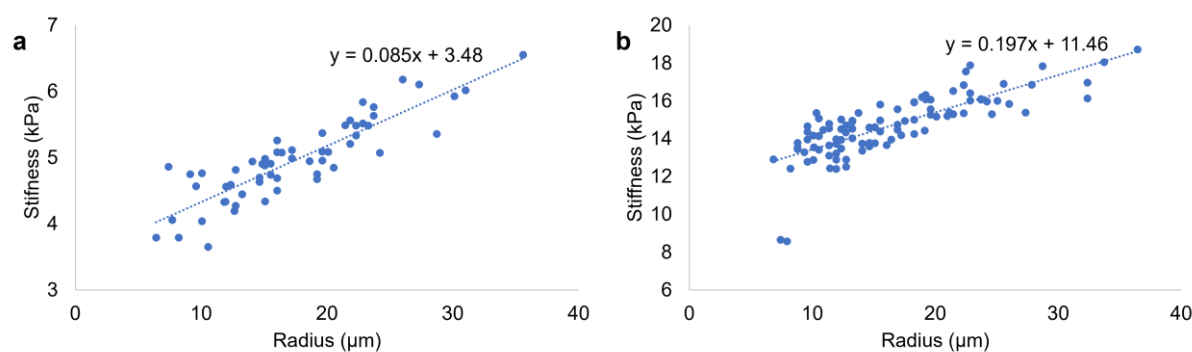


Figure 5.15 – (a) Stiffness x Radius of 18s 30% hydrogel n=60 circles , (b) Stiffness x Radius 22s 30% hydrogel n=72 circles.

This quasi-linear correlation supports the conclusion that larger circles are stiffer than smaller ones. There are several reasons for this observation. As the reticulation process occurs in a water-based solution, the diffusion of the monomers and the photoinitiator contributes to the final reticulation [319] leading to rigidity gradients, which are demonstrated by the wide range of rigidities present in the characterized hydrogel. Larger transparent circles on the mask allow for more monomer pumping. Additionally, the longer diffusive pathways in larger patterns ensure a slower and more controlled diffusion of monomers and initiators, allowing for a more

complete polymerization and crosslinking. Consequently, this results in the formation of a denser and more rigid polymer network. Moreover, the gradual stiffness gradient observed from the center to the periphery of these larger circles could be indicative of the diffusion dynamics during polymerization (Figure 5.16).

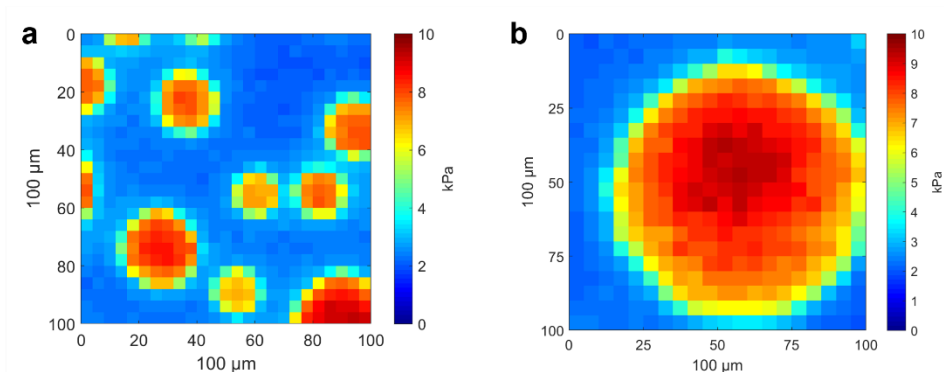


Figure 5.16 – AFM acquired rigidity maps showing the stiffness variation within the 18s30% polyacrylamide hydrogel. (a) It clearly indicates that the smaller circles present a lower stiffness as compared to their larger counterparts, illustrating the relationship between pattern size and mechanical properties within the hydrogel structure. (b) Stiffness variation across a large circle pattern.

In addition, an in-depth mechanical characterization of a 18s30% hydrogel was undertaken. This involved combining rigidity maps of 100x100  $\mu\text{m}$  size with a resolutions varying from 20x20 pixels and 25x25 pixels and localized measurements of the rigid circles and background. This resulted in a comprehensive dataset of 2652 datapoints, comparable to the dataset acquired from the tumor tissue, comprising 2151 datapoints. An overview of the statistics for soft, rigid regions, and the hydrogel as a whole is provided in Figure 5.17.

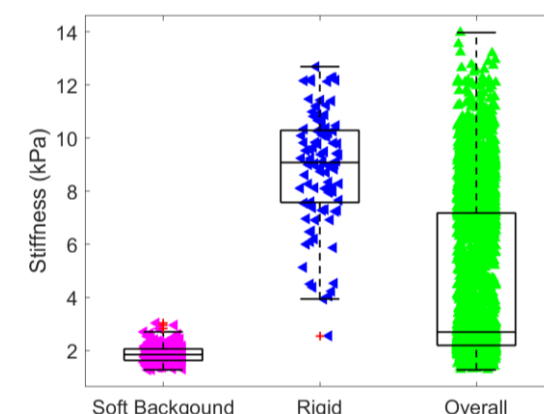


Figure 5.17 – Boxplots with detailed mechanical characterization of a hydrogel 18s30%. Each boxplot represents the distribution of datapoints for soft background (n=203), rigid circles (n=100), and overall random regions (n=2652) within the hydrogel. Overall datapoints obtained from rigidity maps with dimensions of 100x100  $\mu\text{m}$ , in resolutions of 20x20 and 25x25 pixels. The comparison is made with a similar dataset from tumor tissue consisting of 2151 datapoints.

### 5.3.5 Stiffness distribution of polyacrylamide hydrogel and compared to tumor stiffness distribution

Tumors are characterized by a broad spectrum of stiffness values, largely attributable to the diversity of tissue constituents and a multifaceted interplay of tumor microenvironmental factors. This variability in stiffness has been linked to significant implications in cancer behavior and is therefore of relevancy in the field of cancer biology [121]. To recapitulate this biomechanical heterogeneity of tumor tissues within our *in vitro* model, we embarked on a comparative study between the stiffness distribution found on the lung tumor tissues and the fabricated polyacrylamide hydrogels. The journey towards fabricating hydrogels with a stiffness distribution mimicking that of tumor tissues started with an extensive experimentation phase. This involved creating initial versions of hydrogels, and meticulously refining the fabrication parameters in response to AFM characterization results.

It is worth emphasizing that this endeavor was not a mere replication exercise. Instead, it provided an avenue for uncovering the intricate relationships between the design parameters of the mask, the photopolymerization process, and the resulting hydrogel stiffness. These insights are invaluable not only for optimizing the hydrogel fabrication process, but also for enabling the production of mechanically representative hydrogels that closely mimic the diverse stiffness landscape observed within tumor microenvironments.

Preliminary tests demonstrated that the hydrogels exhibited a median stiffness that exceeded anticipated values. Specifically, a hydrogel exposed for 9 seconds at 100% intensity resulted in a median stiffness of 6 kPa, equivalent to an energy dose of 144 mJ/cm<sup>2</sup>. The use of shorter exposure times at similar intensity resulted in fractured hydrogels. Such observations underlined the necessity to recalibrate the photopolymerization parameters, specifically, the UV exposure duration and intensity. Consequently, a systematic process of fine-tuning was undertaken. By adjusting the illumination duration and concurrently modulating the UV intensity, a balance was struck at 18 seconds of exposure at 30% intensity, which corresponded to an energy dose of 86.4 mJ/cm<sup>2</sup>. This adjustment facilitated the creation of a softer hydrogel background and also permitted the generation of stiffness-varied patterns within the hydrogel. The outcome was a heterogeneous mechanical distribution with a median stiffness of 2.4 kPa, as illustrated in Figure 5.18.



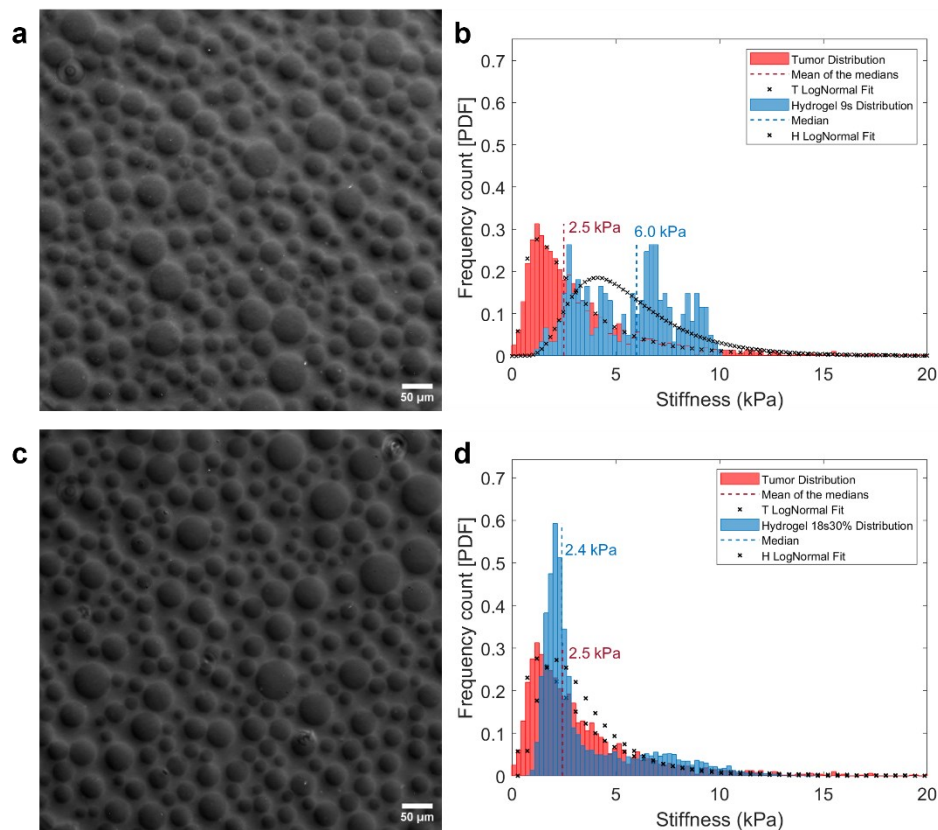


Figure 5.18 – Comparative AFM characterization of hydrogels polymerized under different conditions. (a) Phase image captured at 20x magnification of a hydrogel exposed at 9s 100% intensity, illustrating the random pattern across the hydrogel. (b) Corresponding stiffness distribution derived from the hydrogel in (a), demonstrating the unsought range of mechanical properties. (c) Phase image captured at 20x magnification of a hydrogel exposed at 18s30% intensity. (d) Corresponding stiffness distribution, demonstrating the achieved replication of tumor-like mechanical heterogeneity in the hydrogel, as a result of fine-tuning the fabrication parameters.

Through this iterative approach of fabricating, testing, and adjusting parameters, it was possible to create hydrogels whose stiffness distributions closely mimics those observed in tumor tissue Figure 2.9, thereby enhancing the pathophysiological relevancy of this cell culture *in vitro* model that is yet to be evaluated.

The stiffness distribution of the fabricated hydrogels presents two pronounced peaks, corresponding to the soft (2 kPa) and stiff (7.8 kPa) patterned areas by the single gray-level mask design. While this approach yields a clear demarcation between these two zones, it implies a compromise, specifically, the limited representation of intermediate stiffness values that are natively present in lung tumor tissues. However, it is important to note that the presence of intermediate stiffness values is not entirely absent in these hydrogels. The smooth stiffness gradients present around the patterned areas on the hydrogel provide a transition zone that essentially embodies these intermediate stiffness values. As explained previously, these stiffness gradients, although not explicitly designed, result from the spatial variation in illumination during the photopolymerization process, and they may play a role in more closely emulating the native tumor microenvironment. While intermediate stiffness values do exist

within the fabricated hydrogels, their scarcity compared to native tumor tissues introduces a level of mechanical complexity to the hydrogel and could constrain the complete representation of the tumor full mechanical spectrum.

Nonetheless, it should be noted that the single gray-level approach was a strategic choice made to simplify the fabrication process, and not a limitation of the methodology itself. The mask design could be modified to include additional gray levels, which would allow the fabrication of hydrogels with more complex stiffness distributions, potentially filling in the intermediate stiffness range. Future studies may consider this approach to better mimic the highly heterogeneous mechanical landscape of tumor tissues.

### 5.3.6 Fine-tuned surface functionalization

For cellular adhesion and proliferation, surface functionalization of the polyacrylamide hydrogels was deemed essential. This requirement is due to the fact that, inherently, polyacrylamide hydrogels exhibit a non-adhesive surface which is incompatible with cell culture. To accomplish surface functionalization, sulfo-LC-SDA, a photo-activatable crosslinker, was employed. The role of sulfo-LC-SDA is to bind to the proteins and attach to the hydrogel surface. The surface functionalization process employed two proteins – collagen I and fibrinogen each having unique attributes contributing to the efficiency of the process. Collagen I was selected due to its prevalence in the ECM of lung tissues and enables cell culture. On the other hand, fibrinogen was employed for its specific benefits during the characterization stage. Being coupled with a green fluorescent dye, the fibrinogen coating can be rapidly evaluated by confocal imaging, allowing promptly modification of the protocol, although not suitable for cell culture. Nevertheless, it is to be noted that collagen organization may differ from fibrinogen as the former easily aggregates in thick fibers. This point is discussed below.

The initial experiment involved stiffness patterned hydrogels, UV-illuminated at 18s to 22s at 30%, with rigidity ranging from 2.4 to 5 kPa. These hydrogels first showed fractures post-functionalization (data not shown). For this reason, functionalization studies were then first conducted with slightly stiffer hydrogels 30s exposure at 30% lamp power, with rigidity approximately 10 to 12 kPa. These were selected based on the premise that a more robust reticulation of polymer chains would a more robust hydrogel, mitigating the occurrence of fractures. Figure 5.19a illustrates that no fractures were visible on the unswollen hydrogel post sulfo-LC-SDA grafting. Post protein grafting, however, fractures emerged, albeit less frequently than on the softer hydrogel (Figure 5.19b). The presence of these fractures was further evidenced by fibrinogen GFP labelling, as seen in Figure 5.19c. Upon full swelling of the hydrogel and seeding with A549 cells, they showed a tendency to align along the fracture lines, potentially driven by the elevated concentration of collagen I in these areas. (Figure 5.19d).

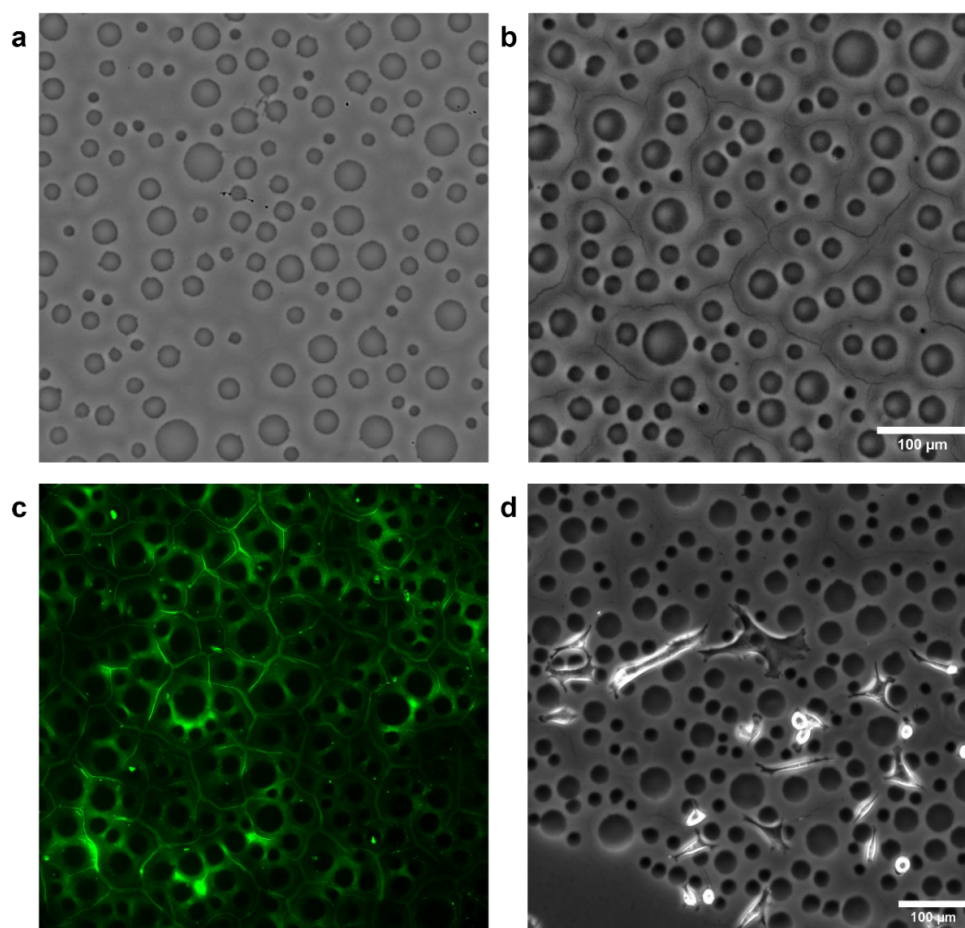


Figure 5.19 – (a) Post sulfo-LC-SDA grafting, the hydrogel illuminated for 30s at 30% UV showed no fractures. (b) Following collagen, I deposition, fractures were observed on the same sample. (c) Fractures were evident with GFP-labeled fibrinogen functionalization at  $1 \mu\text{g}/\text{cm}^2$ . (d) A549 cells seeded on the hydrogel (b) adhered and aligned along the fractures, where collagen I was abundant. Magnification: at 20x, Bars:  $100 \mu\text{m}$ .

In these functionalization attempts, a specific protein deposition protocol based on different dehydration steps was employed. This involved dehydration of the sulfo-LC-SDA (1-2 hours after removal), UV illumination for 5 min, protein deposition for 1h and full protein dehydration (at  $1 \mu\text{g}/\text{cm}^2$ ). However, this method led to undesired fractures in both rigid and soft hydrogels, as shown in Figure 5.19c and Figure 5.20a, respectively. All these dehydration steps help in concentrating the crosslinker and the protein at the surface of the hydrogel which in principle results in an efficient and controlled coating [306]. A plausible explanation for the appearance of fractures might be that the intense dehydration conditions induced mechanical stress which subsequently resulted in fractures. In an effort to overcome this challenge, the protocol was tailored to minimize the dehydration steps involved. A variety of alternative strategies were assessed and tested. A schematic representation of the distinct protocol steps employed in these different strategies is provided in Figure 5.8, while their corresponding results are depicted in Figure 5.20.

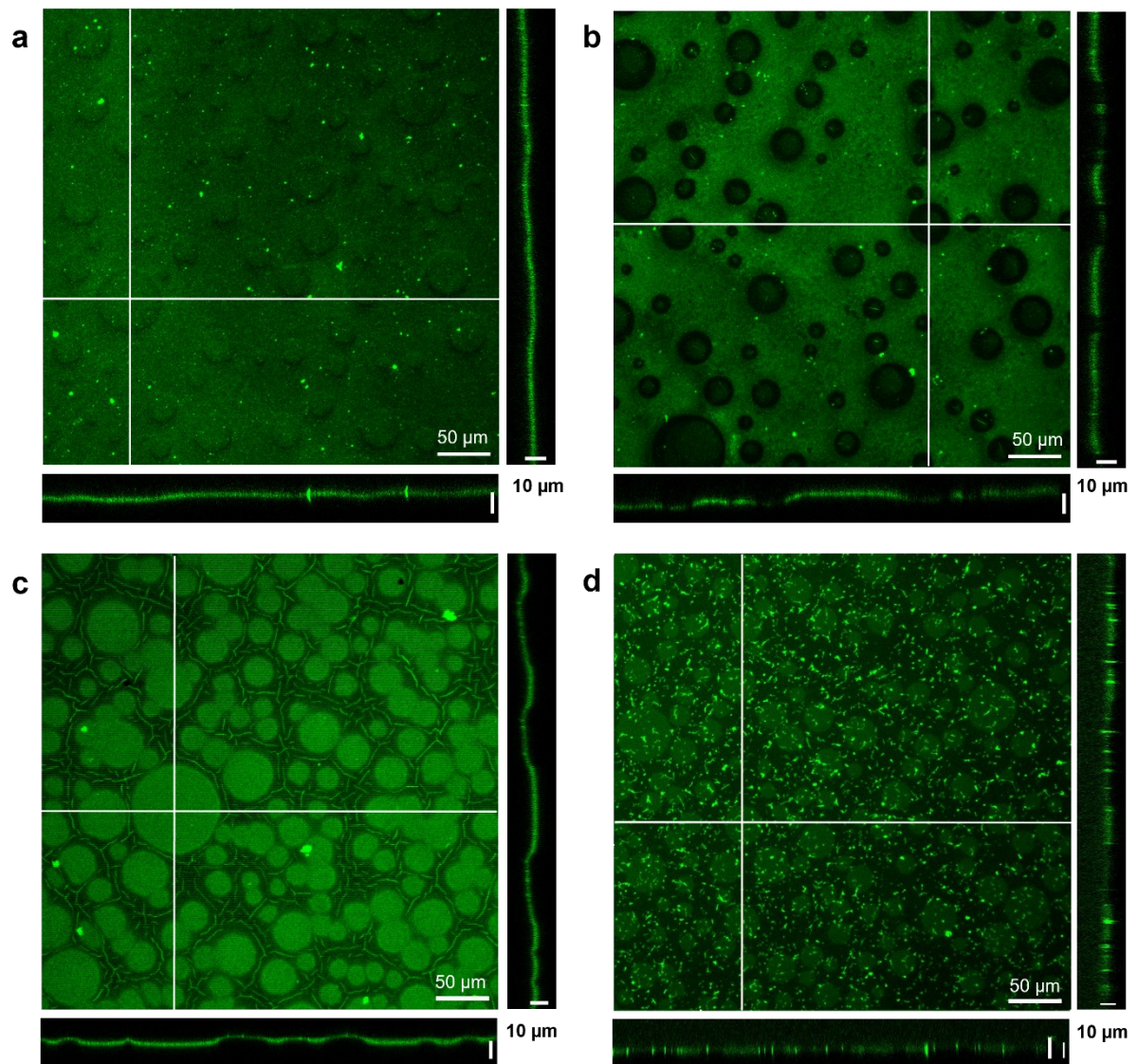


Figure 5.20 – Different surface functionalization protocols on 22s30% hydrogels with GFP labeled fibrinogen. **(a)** Uniformly functionalized hydrogel achieved via sulfo-LC-SDA dehydration, immediate UV exposure, and protein deposition. **(b)** Overfunctionalization of the hydrogel background. **(c)** Overfunctionalization of the stiff patterns with fractures due to prolonged sulfo-LC-SDA dehydration and protein drying. **(d)** Optimized protocol outcome showcasing successful overfunctionalization with 200  $\mu\text{g/ml}$  fibrinogen and fracture prevention. The bright dots are aggregates of fibrinogen coming from inappropriate storage conditions.

In conclusion, these findings emphasize the importance of carefully tailoring the surface functionalization of polyacrylamide hydrogels for cell culture applications. A balance must be struck between achieving sufficient protein attachment for cellular adhesion and avoiding extreme conditions that can lead to hydrogel degradation. Further understanding of the interplay between functionalization conditions and hydrogel mechanical properties is essential for the development of advanced cell culture platforms and could lead to more sophisticated *in vitro* models of the tumor microenvironment.

## 5.4 DISCUSSION

In the Chapter 3, we had determined the statistical texture of stiffness of normal and tumor lung tissues. Here we use these parameters to design a gray level mask and use standard photolithography technology to fabricate mechano-mimetic polyacrylamide hydrogels. In principle, maskless lithography could be more suitable since it allows to vary the design of the projected light very easily. In the context of our experiments, limitations have been encountered while utilizing the SmartPrint UV technology for direct grayscale printing of patterns on the hydrogel. The primary challenge arose due to our sample size, which exceeded the printing field of the SmartPrint. This required stitching, a process that can introduce variability. This variability stems from the diffusion factor; subsequent illuminated areas may not achieve the same degree of polymerization, thereby potentially influencing the overall stiffness of the hydrogel. Specifically for hydrogel applications, it is paramount to UV expose all the sample simultaneously or devise a strategy to efficiently manage the diffusion process, mitigating discrepancies in polymerization degrees across the sample.

Here the resist is an aqueous solution composed of monomers and a photoinitiator. The diffusion coefficient of these entities is of the order of  $10^{-9} \text{ m}^2/\text{s}$  [320], meaning that entities diffuse on distances of order of  $30 \text{ }\mu\text{m}$  every second. Then, it is expected that the local reticulation rate in an exposed field is highly sensitive to the reservoir of monomers or photoinitiator of the neighboring fields.

The ambition of fabricating a mask that reproduces the stiffness heterogeneity of a tissue on a hydrogel required overcoming significant microfabrication challenges. The use of gray-level technology has been well-documented in various applications. However, the literature falls short when it comes to fabricating masks using random pattern designs. Our approach of depositing a single layer of chromium proved to be a particularly effective strategy. This technique allowed us to leverage the property of chromium to attenuate UV light by adjusting the thickness of the chromium layer during deposition. This was confirmed by differences in stiffness distributions favoring a higher stiffness for hydrogel fabricated with a mask with a thinner layer of chromium (Figure 5.11). Used for hydrogel polymerization, where the diffusion coefficient of the free radicals can be as high as  $1000 \text{ }\mu\text{m}^2/\text{s}$ , this technology facilitated the creation of patterns with intricate rigidity gradients, as confirmed by the results. The rigidity maps showed in Figure 5.16a clearly demonstrate the presence of a range of stiffnesses, showing that smaller circles present lower stiffness compared to larger ones. The capacity to generate these varied mechanical environments within a single hydrogel construct proved to be an incipient step to emulate the complex mechanical heterogeneity found in actual tumor tissues.

The fabrication of masks and hydrogels entailed two distinct but interrelated sets of parameters that were carefully controlled and adjusted. Regarding the mask fabrication, the optimization process necessitated the fine-tuning of parameters including the thickness of chromium, UV illumination time of resin, development time, chromium etch time, and mask design parameters. Each of these elements was instrumental in shaping the final mask characteristics, including its feature resolution, uniformity, and reproducibility. In parallel, the patterned hydrogel fabrication process also required careful control of various factors. The photopolymerization exposure time and intensity significantly influenced the hydrogel's stiffness distribution. These conditions, when carefully adjusted, are expected to promote the formation of longer polymer chains, leading to a more uniform network of crosslinked chains with less dangling strands and more regular chain lengths [320]. A better resistance to fractures is then expected, leading to an overall increase in its mechanical stability.

The results showed a quasi-linear correlation between the stiffness of the hydrogel and the radii of the circles. This correlation underpins the fact that larger circles, due to the potential for more monomer pumping, are composed of a denser polymer network. Nevertheless, their mechanical properties are not uniform, as they demonstrate a stiffness gradient from their center to the periphery, reflecting the diffusion dynamics during photopolymerization (Figure 5.16b). The current single gray-level mask design, though it successfully reproduces a broad stiffness distribution, could be further developed to yield a more comprehensive representation of the tumor mechanical profile. The incorporation of multiple gray-levels in the mask fabrication process could enrich the spectrum of intermediate stiffness values within the hydrogel, allowing for a more precise mimicry of the mechanical heterogeneity observed in tumor tissues. Future work should focus on advancing mask design and fabrication to better replicate its stiffness distribution.

Since the resulting stiffness can hardly be predicted, AFM characterization was necessary to accurately measure the mechanical properties of the fabricated hydrogels. Together, the iterative optimization steps in both mask and hydrogel fabrication ensured the creation of a biomechanically-relevant *in vitro* model, which exhibits a wide range of stiffnesses across its surface, closely mimicking the natural variability found within the lung tumor microenvironment (Figure 5.18b). These findings unveil the complexity of the mechanical properties of the fabricated hydrogels and suggest that manipulating the geometry of the patterns could be a viable approach to fine-tuning the stiffness distribution of the hydrogels.

To better replicate the stiffness texture observed in lung adenocarcinoma, we refined the photopolymerization parameters in response to AFM characterization results. We established that a UV exposure of 18 seconds at 30% (4.8 mW/cm<sup>2</sup>) resulted in a hydrogel with a median stiffness of 2.4 kPa, closely similar to the median tumor distribution. However, it should be noted that our approach, while creating a clear distinction between soft and rigid zones, underrepresents the intermediate stiffness values that are natively present. The presence of these intermediate stiffness values may not fully encapsulate the entire mechanical spectrum present within the lung tumor tissue studied in this thesis, thereby potentially limiting the complete representation of its biomechanics. The ramifications of this aspect of the fabrication process remain unclear and demand deeper exploration. This inherent complexity within the tumor stiffness distribution presents a compelling challenge for future efforts to refine hydrogel fabrication techniques.

An essential part of this work was to optimize a surface functionalization protocol to enable cell culture. Given the naturally non-adhesive surface of polyacrylamide hydrogels, a protocol was established to ensure appropriate protein attachment, which was necessary for the subsequent cell adhesion and proliferation studies. Observations indicated that maintaining a consistently hydrated environment throughout the functionalization process was fundamental in preventing fractures in the hydrogel. This protocol resulted in the pattern overfunctionalization while maintaining hydrogel integrity, indicating an effective balance between achieving the necessary protein attachment and preserving the structural properties of the hydrogel. In the condition showed in Figure 5.20b, the obtained results and observations propose a seemingly counter-intuitive phenomenon in surface functionalization, where dehydration, which was expected to lead to heterogeneous functionalization, resulted in a homogeneous one in our experimental setup. This outcome contradicts previous studies by Mgharbel et al. [220], who reported overfunctionalization of motifs via dehydration. In their work, protein dehydration led to the overfunctionalization of the stiff motifs because the capillary forces involved in dewetting were tuned by the stiffness-dependent kinetics of evaporation at the surface of the hydrogel. Stiff polyacrylamide hydrogels dehydrate slower than soft ones, so the surface of the stiff dots is expected to retain more water and to remain hydrated for a longer time than the surface of the soft background, resulting in the overfunctionalization of the stiff regions of the hydrogel. The difference with Mgharbel's work could be the size and the spacing of the stiff patterns, of few tens of microns here compared to few microns in Ref. [220]. The attraction of the proteins lying in the soft regions by capillary forces toward the hydrated stiff patterns could be indeed limited to a distance of few microns.



A unique aspect of the protocol applied in this study is that it challenges the conventional methodology which typically avoids dehydration during the functionalization process. Traditional protocols primarily rely on maintaining hydration to ensure the effective grafting of proteins onto the hydrogel surface, often employing protein concentrations ranging from 15 to 200  $\mu\text{g}/\text{ml}$ . Our approach, on the contrary, incorporates strategic dehydration steps. Although seemingly counter-intuitive, we found that these dehydration steps can, in fact, facilitate a uniform and effective protein attachment, thus enhancing the overall efficacy of the hydrogel surface functionalization.

The overfunctionalization of the hydrogel background in Figure 5.20c brings forth an intriguing phenomenon. After sulfo-LC-SDA was activated by UV exposure and the sample subsequently stored at 4°C for 24 hours, an unexpected overfunctionalization occurred. This suggests that the sulfo-LC-SDA molecules could diffuse towards the surface during the night-long incubation and that the NHS group remained functional. This is unexpected and counter-intuitive as one would anticipate that the cross-linker is bound to the hydrogel. This thus probably evidences the presence of free polymer chains, which can diffuse in the gel and consequently, more material can reach the surface in the soft regions that are more porous. Further investigation is warranted to fully understand the precise mechanisms at play in this unexpected result.

Moreover, the overfunctionalization of the stiff patterns with hydration might be a consequence of the differential absorption characteristics of hydrogel regions with varied stiffness (Figure 5.20d). Stiffer regions could possibly retain more water due to their higher mechanical resistance to dehydration, leading to a longer presence of the water-soluble sulfo-LC-SDA in these regions. During the sulfo-LC-SDA immersion process, it is conceivable that the reagent permeates the hydrogel more deeply in areas where water is retained for longer periods. This could lead to an increased availability of sulfo-LC-SDA in the stiff regions, ultimately resulting in more substantial functionalization in these areas compared to softer ones when the protein is subsequently introduced. In essence, the distribution of sulfo-LC-SDA on the hydrogel surface governs the subsequent dispersion and attachment of proteins.

# CHAPTER 6

---

## CELL CULTURE ON MECHANO- MIMETIC HYDROGELS

## 6 CULTURE CELLULAIRE SUR HYDROGELS MÉCANO-MIMÉTIQUES

Le comportement cellulaire est influencé par une myriade de facteurs, parmi lesquels la rigidité et la composition chimique de l'environnement cellulaire jouent un rôle significatif. Et, tout comme l'environnement chimique, la rigidité est variable spatialement comme discuté dans le chapitre 3. Comprendre comment les cellules répondent à la texture de rigidité est essentiel pour le développement d'applications biomédicales avancées et l'ingénierie tissulaire. Cette question est rarement abordée, et encore moins avec des cellules cultivées sur des textures de rigidité biomimétiques. Ainsi, ce chapitre vise à combler au moins partiellement cette lacune. Il se penche sur les effets de la texture de rigidité du substrat sur les comportements cellulaires, tels que l'étalement, la motilité et la prolifération.

Ce chapitre est organisé comme suit. Les discussions initiales présentent des concepts fondamentaux, fournissant un aperçu des réponses cellulaires à la rigidité et de l'influence du patterning chimique et mécanique sur le microenvironnement cellulaire. Une revue des méthodes analytiques, à savoir l'étude de diffusion et l'autocorrélation de vitesse, fournit les bases nécessaires pour comprendre les études menées. Dans la section expérimentale, une description détaillée de la fabrication et de la fonctionnalisation des hydrogels de polyacrylamide à motifs de rigidité est donnée, qui sont utilisés comme substrats pour la culture cellulaire. Le processus d'ensemencement des cellules, d'acquisition d'images et d'analyse de données ultérieure par vélocimétrie d'images de particules et de calcul de longueur de corrélation est également discuté. Les résultats sont ensuite présentés, éclairant de multiples aspects du comportement cellulaire en réponse aux motifs de rigidité. Cela inclut des observations sur la propagation initiale des cellules, la motilité cellulaire, le comportement diffusif, la dynamique de croissance cellulaire et la densité cellulaire à confluence. Les différences de comportement cellulaire lorsqu'elles sont cultivées sur des hydrogels uniformes et à motifs offrent des aperçus des effets du patterning du substrat sur l'activité cellulaire.

Le chapitre se conclut par une discussion complète sur les résultats observés, établissant des liens avec la littérature existante et fournissant des suggestions pour de futures recherches. Les aperçus tirés de ce travail ont des implications pour la conception de substrats de culture biomimétiques et pour une meilleure compréhension de la mécanobiologie des interactions cellule-substrat.

## 6 CELL CULTURE ON MECHANO-MIMETIC HYDROGELS

Cellular behavior is influenced by a myriad of factors, among which the stiffness and chemical composition of the cellular environment plays a significant role. And, as with the chemical environment, the stiffness is spatial variable as discussed in Chapter 3. Understanding how cells respond to stiffness texture is integral for the development of advanced biomedical applications and tissue engineering constructs. This question is rarely addressed, and even less so with cells grown on biomimetic stiffness textures. Thus, this chapter aims to at least, partially bridge this gap. It delves into the effects of substrate stiffness texture on cellular behaviors, such as spreading, motility, and proliferation.

This chapter is organized as follows. Initial discussions present fundamental concepts, providing an overview of cellular responses to rigidity and the influence of chemical and mechanical patterning on the cellular microenvironment. A review of analytical methods, namely diffusion study and velocity autocorrelation, provides the necessary background to comprehend the studies conducted. In the experimental section, a detailed description of the fabrication and functionalization of stiffness-patterned polyacrylamide hydrogels is given, which are used as substrates for cell culture. The process of cell seeding, image acquisition, and subsequent data analysis through Particle Image Velocimetry and correlation length calculation are also discussed.

The results of the investigation are then presented, shedding light on multiple aspects of cell behavior in response to stiffness patterns. These include observations on initial cell spreading, cell motility, diffusive behavior, cell growth dynamics, and cell density at confluency. The differences in cell behaviors when cultured on uniform and patterned hydrogels offer insights into the effects of substrate patterning on cellular activity.

The chapter concludes with a comprehensive discussion on the observed findings, drawing connections to existing literature and providing suggestions for future research. The insights garnered from this work have implications for the design of biomimetic culture substrates and further understanding the mechanobiology of cell-substrate interactions.

## 6.1 FUNDAMENTAL CONCEPTS

### 6.1.1 Cells respond to rigidity

The in-depth investigation of mechanical interactions between cells and their surrounding matrices represents an intense field of study with promising implications for tissue engineering and drug development [298]. As contractile entities, cells are inherently capable of perceiving and reacting to the mechanical properties of their environment through exerted forces [321]. Vital to various biological processes, the ability of cells to sense and respond to rigidity has become a focal point in understanding cellular behaviors. This sensitivity to rigidity plays a vital role throughout different stages of cellular life, thereby underpinning its significance as detailed in the introduction chapter [322]. Traditionally, research into cell rigidity sensitivity has been conducted primarily by cultivating cells on soft hydrogel or elastomeric substrates possessing uniform mechanical attributes [323], [324]. However, natural tissues exhibit non-uniform stiffness, often extending down to the subcellular scale [321]. Thus, an alternative and complementary approach to further understand the influence of rigidity on cell culture is to construct stiffness textured culture substrates. Such platforms would integrate both micron-scale stiffness patterns and adjustable surface chemistry, thereby more accurately mimicking the mechanical heterogeneity observed in biological tissues.

### 6.1.2 Chemical patterning of the substrate influences cell behavior

Cells are dynamic entities that respond to various physical and chemical cues present in their environment. The concept of chemical patterning of the substrate as a means of controlling cell behavior has gained increasing attention in the last 25 years. With the use of micropatterning techniques, scientists can manipulate the spatial distribution of adhesive ligands, guiding cell attachment and growth. The pioneering study by Watt et al., in 1988, effectively harnessed micropatterning techniques to control cell shape, subsequently influencing cell growth and differentiation of human epidermal keratinocytes.

Expanding on the influence of micropatterning on cell life, the work of Chen and Ingber [163] illustrated that not only the cell shape but also the cell's entire life cycle can be affected by geometrical constraints obtained with chemical patterns. They demonstrated that cells cultured on micropatterned substrates exhibited differences in cell growth and viability compared to cells grown on unpatterned substrates. In their experiment, it appears that the pivotal determinant of the transition between apoptosis, survival, and growth was not only the degree of cell adhesion, but rather the area available for the cell to spread.

Since the mid 2000's, Théry and colleagues made a significant leap in 2006, demonstrating the influential role of cell shape on the cell's orientation and division axis [325]. This was followed by his influential work [326] about micropatterning as a tool to decipher cell morphogenesis and functions, describing a variety of micropatterning techniques such as microcontact printing, photo-patterning, laser-patterning, stamping, and sequential exposure-grafting. These methodologies have gained widespread use in biomedical research, providing insights into how the physical aspects of the cellular microenvironment influence cell physiology.

Micropatterning has also been used to study cell migration, a key process in many biological phenomena, such as embryonic development, wound healing, and cancer metastasis. An interesting example of this is "The first World Cell Race" by Maiuri et al. [327], wherein cells were cultured on micropatterned adhesive proteins tracks and their migration speeds were compared. This provided valuable insights into the variables influencing cell migration, such as cell type, environment, and the influence of genetic modifications. Building on these insights, cumulative research has further elucidated the complex interplay between the physicochemical cues presented by the microenvironment and their influence on cellular morphology and differentiation potential. In the field of stem cell research, understanding the factors that influence lineage commitment is of utmost importance. One intriguing aspect that has garnered significant attention is the role of cell shape in directing the differentiation of mesenchymal stem cells (MSCs). Kilian et al. explored the impact of geometric cues on MSC differentiation. Their research demonstrated that cell shape, independent of soluble factors, exerts a strong influence on the fate determination of MSCs derived from bone marrow. By manipulating the shape of adherent MSCs, the researchers observed distinct trends in lineage commitment (osteogenic, adipogenic, or neurogenic), even with subtle geometric variations. Their study provides compelling evidence of how geometric cues from the environment can steer the fate of cells, thereby influencing their differentiation [328].

In a complementary perspective, the work by Dupont et al., has provided a molecular link between the physical properties of the cell environment and cell behavior. They demonstrated that YAP (Yes-associated protein) and TAZ (transcriptional coactivator with PDZ-binding motif), both being key players in the Hippo signaling pathway, respond to changes in cell shape and substrate rigidity. This provides mechanistic insights into how cells translate geometric and mechanical cues into biochemical signals and changes in cell behavior [329].

These studies together elucidate the potential of chemical patterning and geometrical cues to control cell behavior, highlighting the important role of the physicochemical microenvironment in determining cellular outcomes.

### 6.1.3 Stiffness patterning also impacts cell behavior

While the influence of chemical patterning on cell behavior is well established, recent developments have emphasized the role of mechanical properties, particularly stiffness patterning, in modulating cellular responses. The work of Fu et al., reported on how cells interact with their environment utilizing hydrogels and micropost arrays as investigative tools [330]. The researchers observed that the alteration of hydrogel density, derived from natural ECM proteins, significantly impacted cell morphology, and function. Synthetic ECM analogs further provided insights into substrate rigidity's role in stem cell differentiation. The silicon micropost arrays, offering a broad range of rigidities, enabled the team to examine cell-material interactions closely. When cultured on rigid microposts, human mesenchymal stem cells (hMSCs) exhibited a well-spread morphology characterized by highly organized actin stress fibers and large focal adhesions. In contrast, the culture of these cells on soft microposts resulted in a rounded cellular morphology characterized by distinct microvilli, disorganized actin filaments, and smaller adhesion complexes. A strong correlation between traction force and cell spreading was observed, with a substantially smaller independent effect of micropost rigidity on traction force, confirming the hypothesis that mechanical cues from the microenvironment can influence cell behavior.

In addition to influencing cell morphology, the mechanical properties of micropillars can also exert a significant effect on cell motility, an essential cellular process implicated in wound healing and cancer metastasis. A recent study conducted by d'Alessandro et al. investigated cell migration guided by long-lived spatial memory [331]. The study reveals that cells have the ability to actively alter their surroundings, leaving behind enduring physicochemical markers that influence their subsequent trajectory. The authors introduced the concept of self-interacting random walks, which explains large-scale exploration in cell migration.

In the cell adhesion domain, stiffness patterns have been demonstrated to play a role as well. Cell adhesion, a critical step in cell migration and tissue development, is sensitive to the rigidity of the microenvironment. Expanding on this, recent work by Mgharbel et al. investigated the ability of cells to sense and respond to local stiffness patterns on hydrogels. They observed that cells exerted tensile forces on the extracellular environment, adapting their forces to the subcellular stiffness variations [220].

Beyond influencing cell adhesion and migration, stiffness patterns can also guide cell differentiation. Yang et al. showed that spatially patterned matrix elasticity can direct stem cell fate, and that irregular, disorganized variations in matrix mechanics appear to disrupt actin organization and lead to different cell fates [332]. The study also elucidates a novel spatial mechanical dosing mechanism that correlates to both the magnitude and organization of spatial stiffness, suggesting that the organization of the matrix environment acts as a mechanical switch for cell lineage decisions. Moreover, Hadden et al. [332] analyzed the behavior of stem cells on hydrogels with varying stiffness levels, shedding light on the mechanisms behind stem cell migration and mechanotransduction. It was found that stem cells exhibit dose-dependent responses to intermediate stiffness values on linear stiffness gradient hydrogels, rather than switch-like responses. They showed that substrate stiffness has a significant impact on stem cell differentiation. The expression of various differentiation markers, such as MyoD for myogenic differentiation and CBFA1 for osteogenic differentiation, was found to be highest at specific stiffness values.

More recently, the hydrogel platform developed by Yip et al. [333] and the subsequent work by Mattiassi et al. [334] have provided an adaptable system for studying the effects of topography and stiffness on neuronal differentiation and maturation in the absence of biochemical factors. They were able to demonstrate a significant enhancement of the propensity of multipotent neural progenitor cells (mNPCs) to commit to the neuronal lineage and increase the rate of neuronal maturation [335]. Taken together, these studies highlight the influence of stiffness patterning on cellular behavior, emphasizing the intricate interplay between cells and their mechanical environment.

#### 6.1.4 Characterization of cell motility by Mean Square Displacement and Velocity autocorrelation function

Cell motility is an integral aspect of various biological processes, including development, wound healing, immune responses, and metastasis in cancer. Understanding and quantifying this dynamic behavior requires specialized tracking tools and methods. One such measure extensively used in mechanobiology is the Mean Square Displacement (MSD), a mathematical tool to statistically describe diffusive behaviors like random walks. The MSD is derived from the tracking of cell movement over time. It provides a way of characterizing the spatial-temporal trajectory of a cell and allows to discern different types of cell movement patterns, from simple diffusion to directed migration. MSD analysis is particularly useful in determining whether cell movement is random or directional, and it can further discern whether cells are sensing and responding to environmental gradients or substratum mechanical properties.



In essence, it quantifies the average squared distance that a cell moves in a given time interval. From the assessment of the MSD plot, information about the mode of motion can be determined (Figure 6.1). A linear increase of the MSD with time indicates a random walk, or diffusive motion, implying the absence of external cues. Conversely, a quadratic relationship suggests directed motion, indicating the presence of a guiding stimulus. Further, a plateau in the MSD could be indicative of confined motion, as often observed within dense cellular environments or when cells are subject to physical constraints [336]. Figure 6.1 illustrates these three possible interpretations.

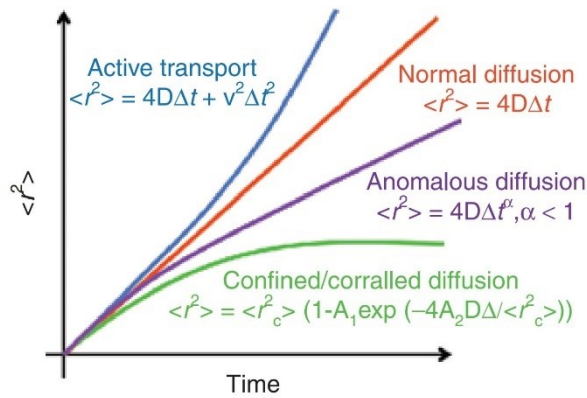


Figure 6.1 – The diffusional behavior can be classified based on the time-dependent properties of the Mean Squared Displacement (MSD). Adapted from de Bruin et al. [336].

In combination with live-cell imaging techniques, MSD analysis offers a powerful method to track and quantify cell movement patterns. Such analysis can be useful for understanding how cells sense and navigate their physical environment and interpret mechanical cues.

Similarly, the velocity autocorrelation function is another important mathematical tool used to study cell motility. It quantifies the correlation of cells movements in space or over time, providing valuable insights into the inherent and external factors governing cellular behavior.

Cellular motion encompasses two integral characteristics: direction and speed. Although mean squared displacement is effective in detecting directional persistence, it does not provide insights into speed fluctuations. The velocity autocorrelation function fills this gap by considering both the direction and magnitude of the velocity, offering a more comprehensive view of cellular motion dynamics. When considering temporal correlations, it is calculated as the average of the product of the cell velocity at a given time and its velocity at a subsequent time.

$$C(\tau) = \frac{\int dt \vec{v}(\vec{r}, t) \cdot \vec{v}(\vec{r}, t + \tau)}{\int dt \|\vec{v}(\vec{r}, t)\|^2} \quad (6.1)$$

When this value is positive, it implies persistent motion, indicating that the cell maintains its speed and direction over time. In contrast, a negative value suggests anti-persistent motion, implying frequent alterations in the cells speed or direction. When considering spatial correlations, it is calculated similarly, but considering space coordinates instead of time.

$$C(\vec{r}) = \frac{\int d\vec{r}' \vec{v}(\vec{r} + \vec{r}', t) \cdot \vec{v}(\vec{r}', t)}{\int d\vec{r}' \|\vec{v}(\vec{r}', t)\|^2} \quad (6.2)$$

It provides information on a potential coordination of cell movement that may occur over several cell sizes [337]. One of the key parameters in the analysis of the velocity autocorrelation function to be extracted is thus the correlation length (spatial analysis) or the persistent length (temporal analysis).

In the context of mechano-mimetic hydrogels, investigating the velocity autocorrelation function provides a valuable approach to study how the mechanical properties of the microenvironment where the cells are cultured influence their interactions. Cells cultured on different stiffness or patterned hydrogels may display distinct MSD and velocity autocorrelation functions. These differences could reflect the diverse ways in which cell motility dynamics are modulated by substrate rigidity.

## 6.2 MATERIALS AND METHODS

### 6.2.1 Fabrication of stiffness-patterned polyacrylamide hydrogel

Similar to section 4.2.3, 30  $\mu\text{l}$  of the polyacrylamide solution were deposited in the center of a silanized 30 mm diameter glass slide. The precursor solution was sandwiched between the activated coverslip and the transparent mask (for unpatterned hydrogel) or the random circle pattern gray-level mask (for patterned hydrogel) designed as described in Chapter 4. Reticulation was achieved by exposure to UV-A light (Eleco UVP281, Gennevilliers, France, 2  $\text{W}/\text{cm}^2$ ). The duration of the illumination was adapted to tune the mechanical properties of the hydrogel. 8 seconds UV illumination at 100% of the bulb power (112  $\text{mJ}/\text{cm}^2$ ) were used for polymerizing a gel with uniform stiffness of mean Young's modulus of  $4.2 \pm 0.2$  kPa (median 4.2 kPa). 22 seconds at 30% intensity (105.6  $\text{mJ}/\text{cm}^2$ ) were used to reticulate the gel with the textured stiffness, which resulted in a median stiffness of 5.2 kPa with dispersion ranging from [2.7; 9.3 kPa] as shown in the stiffness distribution presented in Figure 6.2.

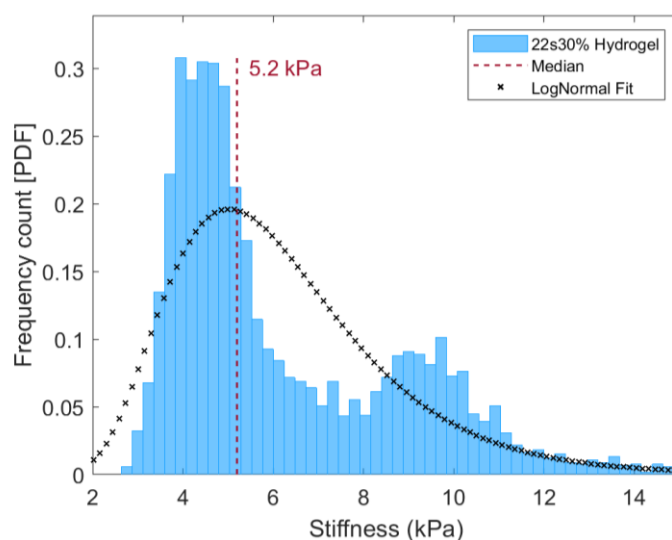


Figure 6.2 – Stiffness distribution of 22s30% polyacrylamide hydrogel.

These values, which are slightly above the values measured on the human tissues (Section 4.2), were used as a proof of concept. The true mechano-mimetic gels, with a lower stiffness, were under testing at the moment of writing the manuscript.

### 6.2.2 Calibration of the surface density of the protein coatings

The polyacrylamide hydrogels are made compatible with cell culture by covalently grafting an adhesion protein to its surface via the photosensitive NHS-ester diazirine heterobifunctional crosslinker sulfo-LC-SDA (Sulfosuccinimidyl-6-(4,4'-azipentanamido) hexanoate, Pierce). In order to properly control the surface density of the coating, the standard protocol used at LTM dehydrates the protein at the surface of the gel so that all the proteins are in contact with the

heterobifunctional crosslinker that has been grafted in excess to the hydrogel. Preliminary tests presented in Chapter 4 had shown that the stiffness patterned hydrogels are not robust to the dehydration processes (Figure 5.19). A protocol with limited dehydration was thus developed as described in Section 4.3.6. However, this protocol does not allow to anticipate the surface density of the protein since the solution of protein is let for react a certain amount of time and then removed. To solve this issue, the surface density of the grafted proteins was compared in between a protocol involving a complete dehydration of the protein solution at the surface of the hydrogel and a second protocol with limited dehydration as described in Chapter 4 and below. This comparison allowed to choose the proper concentration of proteins for the second protocol so that both protocols lead to the same surface density. Basically, it was observed that hydrogel surface functionalization at 200  $\mu\text{g}/\text{ml}$  of fibrinogen without dehydration resulted in a similar fluorescence intensity than using 1  $\mu\text{g}/\text{cm}^2$  with complete protein dehydration.

This comparison was performed by Céline Hadji (R&D Engineer at Cell&Soft). It was conducted by grafting Alexa Fluor 488 conjugated fibrinogen from human plasma (Thermofisher, Ref. F13191) at the surface of hydrogels with identical stiffness. Fluorescence intensities were compared using confocal microscopy (Zeiss LSM880): a stack of images with 0.42  $\mu\text{m}$  spacing was captured at a wavelength of 488 nm, thick enough to ensure the capture of the whole intensity signal. The mean of the intensity was calculated and compared between both conditions from three images of 375  $\mu\text{m}$  x 375  $\mu\text{m}$  acquired for every condition (Figure 6.3).

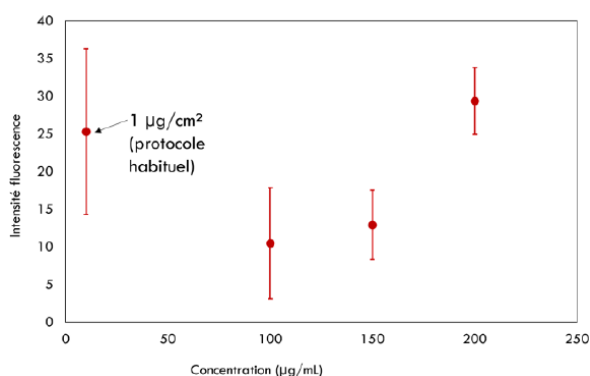


Figure 6.3 – Mean intensity of fibrinogen at varying concentrations. 200  $\mu\text{g}/\text{ml}$  fibrinogen concentration present similar fluorescence compared to 1  $\mu\text{g}/\text{cm}^2$  fibrinogen.

### 6.2.3 Surface functionalization of the hydrogels

The uniform hydrogel was coated with Collagen I at a surface density of 1  $\mu\text{g}/\text{cm}^2$ , following the protocol that involves the dehydration of the protein solution. In brief, after the polymerization and the rinsing of the hydrogel, the gel was immediately soaked for 1h in sulfo-

LC-SDA at a concentration of 0.6 mg/ml in deionized water. After this time, the solution was removed and the gel was let for drying for 20 min under laminar flow, until its surface appears dry. Then the glass slide with the hydrogel layer on one side was glued at the bottom of a drilled culture plate of 35 mm using a UV sensitive glue. The 10 min UV exposure needed to polymerize the glue also allowed to crosslink the sulfo-LC-SDA to the gel. A solution of Collagen I at 12  $\mu\text{g}/\text{ml}$  in water was deposited on top of the hydrogel. It was let for dehydrate under a laminar flow hood and under agitation until the surface appeared dry (approximate duration, 2h30). This led to the theoretical grafting of 1  $\mu\text{g}/\text{cm}^2$  of Collagen I. Finally, the gel was rinsed 3 times with PBS<sup>+/+</sup> and immersed in PBS<sup>+/+</sup> to swell overnight.

The stiffness patterned hydrogel was coated with Collagen I following the protocol with limited dehydration steps. In brief, the first steps of functionalization were similar to those of the uniform hydrogel until the UV exposure step. Collagen I solution in PBS<sup>+/+</sup> was then added at a concentration of 200  $\mu\text{g}/\text{ml}$  to match a similar mean surface density as the uniform gel (Figure 6.3). It was let to react with the NHS end of sulfo-LC-SDA for 2h. Finally, the solution was removed, and the gel was rinsed 3 times with PBS<sup>+/+</sup> and immersed in PBS<sup>+/+</sup> to swell overnight.

#### 6.2.4 Cell culture and seeding

A549 cells were cultured in Dulbecco's Modified Eagles Medium (DMEM) (Sigma Aldrich, Dorset, UK) supplemented with 10% v/v Fetal Bovine Serum (FBS) and 2mM L-Glutamine. Proliferative cultures were incubated at 37°C with 5% CO<sub>2</sub> and subculture passed out by washing the cell monolayers with calcium and magnesium-free phosphate buffered saline (PBS<sup>-/-</sup>) [111]. Then, 1x Trypsin/EDTA solution (Sigma Aldrich) was added and cells were incubated at 37°C until they detached from the BP100 surface. Trypsin was deactivated by adding complete growth medium before seeding. The cells were seeded on the hydrogels at a density of 21000 cells/cm<sup>2</sup>.

#### 6.2.5 Image acquisition

Phase contrast images were captured using an IX83 Olympus inverted microscope, equipped with a temperature and CO<sub>2</sub>-controlled incubation chamber (Olympus France, Rungis, France). The temperature was set to 37°C and CO<sub>2</sub> was maintained at 5%. Image acquisition was launched 4 hours post-seeding, permitting the cells to initially attach and spread on the hydrogel surfaces. Images were obtained at three distinct periods during 4 days, each corresponding to different stages of cell behavior on the hydrogel surfaces. Medium was changed after 2.5 days. Three to four positions, each showing a field of view of 660 x 660  $\mu\text{m}^2$ , were acquired on each hydrogel. The positions were chosen far away from each other in a disk of radius 1.4 cm.

The first period, lasting for 5 hours starting from the 4th hour post-seeding, focused on the initial cell spreading and adhesion. High-resolution images were captured at a 20x magnification (NA 0.8) to document details of cell morphology and initial spreading behavior. For this experiment, only the first frame was analyzed. Images were taken every 30 minutes throughout this period. The second period, extending for 10 hours focused on monitoring cell proliferation as the sub-confluent cells spread to cover the hydrogel surface. This study was conducted at the beginning of day 2. Cell diffusive movement was analyzed using MSD and the kinetics of the surface coverage was quantified. Images were once again captured at four distinct fields of view per sample with similar capture rate.

The final period consisted of three hours and was conducted on confluent monolayers at day 4. This period focused on studying cell dynamics at confluence, including velocity and correlation length analysis using Particle Image Velocimetry (PIV). During this period, images were taken more frequently, every 10 minutes.

#### 6.2.6 Image analysis

Different methods were used depending on cell density. At low cell density, cell counting and the quantification of cell area was performed by manually contouring each cell in the captured images using the ImageJ software. The percentage of surface coverage by the cells was determined by the cumulative area of all cell outlines in a given image divided by the total area of that image. Similarly, the velocity was obtained by manually tracking the cells using the manual tracking plugin on ImageJ. When the cells were near confluency, the surface coverage was obtained by subtracting empty spaces to the image area. Cells were manually counted and the mean cell size was obtained by dividing the cells number by the surface coverage. Velocity measurement at confluency were performed using PIV, as explained below. All data generated from the image analysis were subjected to statistical analysis using the Student's paired t-test. The aim was to determine if there were statistically significant differences between the mean values obtained from the cells cultured on patterned and uniform hydrogel surfaces. For the presentation of results, all values were expressed as mean  $\pm$  standard deviation or standard error when indicated.

#### 6.2.7 Particle Image Velocimetry and Correlation length

Particle Image Velocimetry (PIV), a method predominantly used in fluid dynamics, is incorporated in this study to assess the velocity field within a monolayer, circumventing the concept of cells. Unlike traditional approaches that introduce small light-diffusing tracer particles into the fluid, this study utilizes phase contrast image details directly. Phase contrast images were first processed using ImageJ to adjust the contrast and highlight cell edges,

improving the visibility of individual cells and their boundaries. This preprocessing step enhances the accuracy of subsequent PIV analysis. Subsequent analysis was carried out using the PIVLab tool [338], a MATLAB software package for PIV analysis. The Fast Fourier Transform (FFT) algorithm was employed for performing cross-correlation, with three passes implemented to gradually refine the interrogation areas and provide accurate velocity measurements. The first pass used an interrogation area of 128 x 128 pixels, the second pass an area of 64 x 64 pixels, and the third pass an area of 32 x 32 pixels. For each pass, the interrogation areas were advanced by 64 pixels, 32 pixels, and 16 pixels, respectively.

Sub-pixel velocity estimation, an essential step for improving the spatial resolution of PIV measurements, was performed using the Gaussian 2x3 point algorithm, providing standard correlation robustness. This algorithm estimates the location of the peak of the correlation map with sub-pixel accuracy by fitting a Gaussian function, thereby enhancing the precision of velocity vector determination. Vector validation step was subsequently applied to all frames to remove outlier vectors, which could potentially distort the velocity field. This validation was conducted using a standard deviation filter with a threshold set at 8 times the standard deviation, and a local median filter with a threshold of 3. This process ensures that only reliable vectors, consistent with their local neighborhood, are retained in the final velocity field. Additionally, image-based vector validation was performed using the low contrast filter and bright object filter, both applied with the suggested thresholds. These filters help eliminate vectors derived from regions with insufficient contrast for accurate cross-correlation or overly bright regions that could bias the cross-correlation peak. Given the presence of gaps or holes in the cellular monolayer at the beginning of the image acquisition, no interpolation was performed to fill missing vectors. This decision was made to prevent artificial modification of the velocity field. The resulting velocity component vectors and velocity magnitudes were computed for each frame pair and position. All data were saved in .mat format for each position, facilitating further analysis and post-processing.

The correlation length of cells on uniform and rigidity textured hydrogel surfaces was explored after PIV analysis. The PIV analysis measured pixel displacements between successive frames, thus providing the components of velocity in the x and y directions. The spatial autocorrelation function of the velocity was calculated as described in Eq. 6.1. A radial averaging was performed to represent the correlation function in terms of distance. Two fitting models were explored. First, a decaying exponential model of the form  $e^{-x/\xi}$  was tested, and the correlation length  $\xi$  was computed. The correlation length is the characteristic length scale over which velocity fluctuations are correlated, it is defined as the distance at which the correlation function

has decayed to a specific value, often  $1/e$ . Secondly, a faster decaying function was tested, of the form  $1/\left(1 + \frac{x}{\xi}\right)^a$ . This procedure was performed for every frame pair, resulting in a series of fitting parameters.

### 6.3 RESULTS

#### 6.3.1 Initial cells spreading is higher on uniform hydrogel than on patterned hydrogel

The experiment was conducted by seeding A549 cells onto unpatterned (uniform) and patterned (RCP - Random Circle Pattern) hydrogels. Images of the hydrogels were taken 4 hours post-seeding, capturing three distinct positions per hydrogel type to ensure a robust analysis (Figure 6.4).

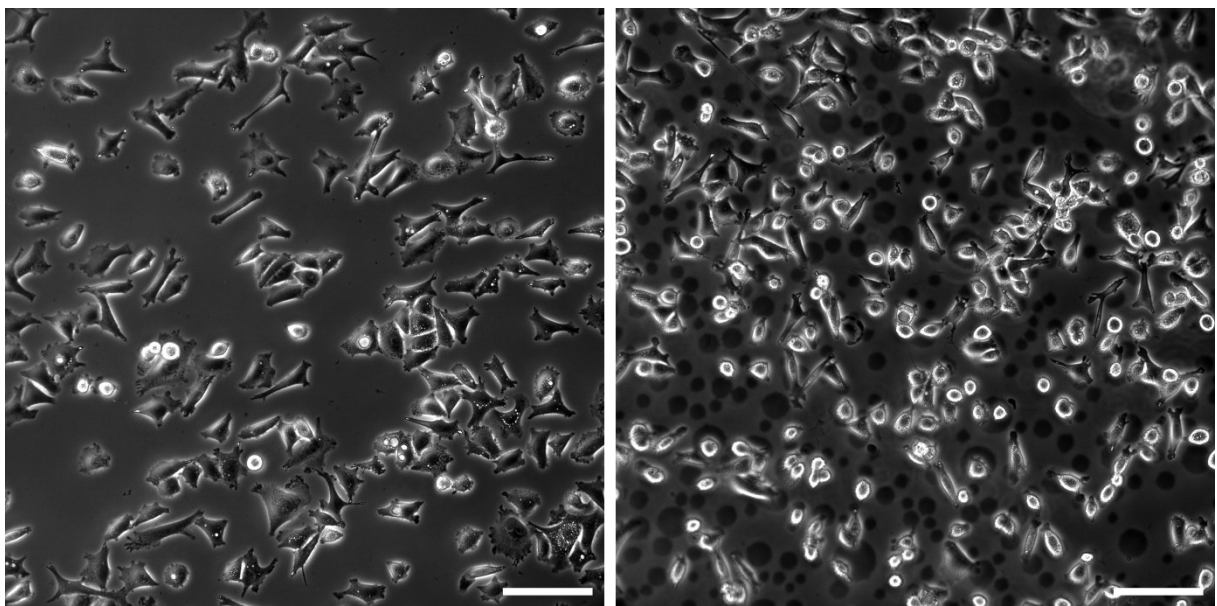


Figure 6.4 – Comparative analysis of cell morphology and distribution on unpatterned (left) and patterned (right) hydrogels. Both images were captured 4 hours post-seeding, at the same magnification (20x), and are representative of the typical cell morphology and distribution observed in each condition. Bars: 100  $\mu\text{m}$ . Differences in cell distribution, size, and shape between the two conditions can be visually noted, underscoring the effect of micrometer-sized stiffness texture on cellular behavior.

The subsequent analysis was focused on cell initial adhesion and cellular morphology, taking into account the total cell count, total and mean cell area, and the percentage of hydrogel surface covered by cells, summarized in Table 6.1.



Table 6.1– Comparison of cell count, total area, mean area, and percentage surface coverage between unpatterned (uniform) and patterned (RCP) hydrogels. Mean value presented is accompanied by the corresponding standard deviation.

	Cell Count	Total Area ( $\mu\text{m}^2$ )	Mean Area ( $\mu\text{m}^2$ )	% Surface Coverage
Uniform P1	100	72274	723	16.3%
Uniform P2	124	87473	705	19.7%
Uniform P3	167	125167	750	28.3%
<b>Mean <math>\pm</math> SD</b>	<b>130 <math>\pm</math> 34</b>	<b>94971</b>	<b>726 <math>\pm</math> 22</b>	<b>21.4%</b>
RCP P1	250	74887	328	18.5%
RCP P2	266	101570	382	22.9%
RCP P3	218	94702	434	21.4%
<b>Mean <math>\pm</math> SD</b>	<b>245 <math>\pm</math> 22</b>	<b>90386</b>	<b>381 <math>\pm</math> 53</b>	<b>20.9%</b>

The cell count was found to be higher on the patterned hydrogel, with an average of  $245 \pm 22$  cells, compared to an average of  $130 \pm 34$  cells on the unpatterned hydrogel. There was also a significant difference in the mean area occupied by individual cells for the two conditions (t-test,  $p = 0.003$ ). The uniform hydrogel presented larger cells with a mean area of  $726 \pm 22 \mu\text{m}^2$ , while cells on the patterned one had a smaller mean area of  $381 \pm 53 \mu\text{m}^2$ .

Interestingly, despite these differences in individual cell size and count, the overall surface coverage by cells (% Surface Coverage) demonstrated no significant difference between the two conditions, with a mean of around 21% for both unpatterned and patterned hydrogels. This indicates that despite the individual cells being smaller on patterned hydrogels, the higher cell count resulted in similar overall coverage, with  $94971 \mu\text{m}^2$  for cells on uniform hydrogel compared to  $90386 \mu\text{m}^2$  for the patterned one. These results collectively indicate that the introduction of patterned heterogeneity in hydrogel stiffness has an impact on cellular morphology.

### 6.3.2 Subconfluent cells move with a lower velocity on patterned hydrogel

The influence of hydrogel patterning on cell motility was first explored at sub confluency. At each of four different positions for each hydrogel type, five cells were selected for tracking, resulting in a total of 20 individual cells examined per hydrogel condition. The movement of these subconfluent cells on both unpatterned and patterned hydrogels was monitored over 10 hours period, with images captured every 30 minutes. Differences in cell movement characteristics were evident between the two types of hydrogels. Figure 6.5 clearly shows that cell movement is influenced by the stiffness texture: on the right panel, cell tracks go from a stiff disk to another (represented in yellow).

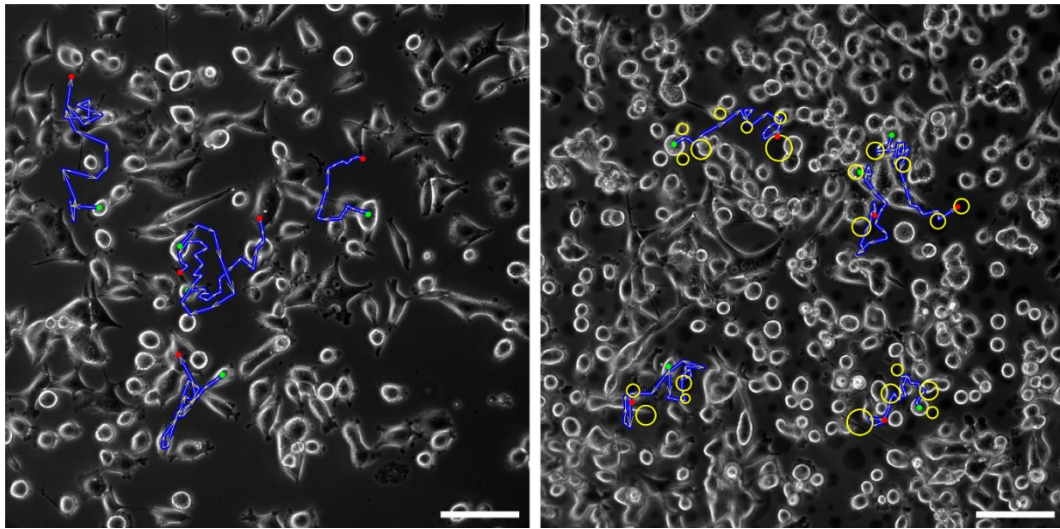


Figure 6.5 – Superimposed cell trajectories on microscopy images of unpatterned (left) and patterned (right) hydrogels. Images are shown at the final time. Each trajectory is depicted as a blue line showing the path taken by a single cell during a 10-hour period. The starting point of each trajectory is marked in green, and the ending point is marked in red. Yellow arrows indicate the direction of movement along each trajectory and yellow circles shows the circle patterns. Bars: 100  $\mu\text{m}$ .

On average, the cells step was smaller on the patterned hydrogel (mean  $\text{Step}_{\text{RCP}} = 12.9 \pm 2.8 \mu\text{m}$ ) compared to the uniform hydrogel (mean  $\text{Step}_{\text{U}} = 20.3 \pm 9.1 \mu\text{m}$ ). This observation was also reflected in the velocity of cell movement, with cells on the patterned hydrogel displaying a lower average velocity (mean  $V_{\text{RCP}} = 27.2 \pm 6 \mu\text{m/h}$ ) than cells on the uniform hydrogel (mean  $V_{\text{U}} = 35.1 \pm 9.5 \mu\text{m/h}$ ) (Figure 6.6). These disparities in both total distance traveled and velocity were found to be statistically significant between hydrogels (for Step and V,  $p < 0.01$ ), underscoring the influence of the substrate patterning on cell motility.

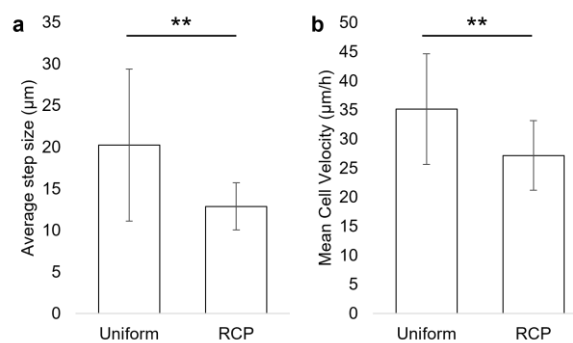


Figure 6.6 – (a) Mean cell step and (b) mean cell velocities with their respective standard deviations on uniform and patterned (RCP) hydrogels after 10-hours of culture.

In conclusion, our observations indicate that the imposition of spatial heterogeneity in hydrogel stiffness, similar to the mechanical microenvironment of tumor tissues, seemingly imposes constraints on the motility of subconfluent cells in comparison to their counterparts cultured on a hydrogel with homogeneous stiffness. This intimates a pronounced influence of the mechanical cues of the microenvironment on cellular locomotive behavior. However, a comprehensive understanding of the fundamental mechanisms orchestrating these detected divergences in cellular motility requires further investigations.

### 6.3.3 Analysis of the diffusive behavior of cells on both hydrogels

A deeper exploration of cellular motility at low cell density was undertaken through the analysis of mean square displacement (MSD) from cell tracking data. Despite the distinct stiffness texture of the hydrogels, cells on both surfaces demonstrated similar MSD profiles over the time course. An important observation was the linear increase in MSD with time for both hydrogel types, a pattern indicative of a random walk or diffusive motion. This pattern suggests that the cells are moving in a non-directed manner, indicating an absence of effective external cues guiding their migration. Moreover, the slopes of the MSD progression for cells on both hydrogel types were similar, as seen in Figure 6.7. This further validates the observation of comparable random walks, implying that the degree of randomness in cell movements remained largely unchanged regardless of the hydrogel stiffness texture.

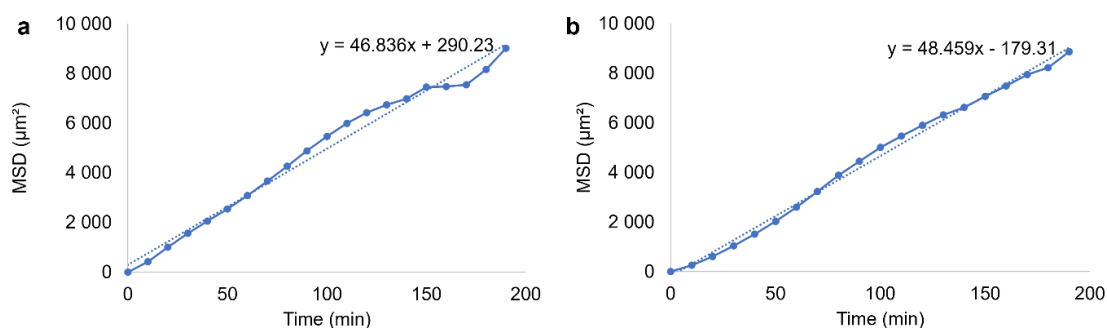


Figure 6.7 – Comparative analysis of cell mean square displacement (MSD) on unpatterned (a) and patterned (b) hydrogels. Each point on the graph represents the average MSD for 5 cells.

### 6.3.4 Measure of the dynamics of cell growth at subconfluency

The dynamics of cell growth on both the uniform and patterned hydrogels were also closely tracked for 66 h beginning at day 2, when the cells were subconfluent. The total area occupied by cells and the resulting surface coverage was measured at two positions for each hydrogel type at four equal time intervals. At the beginning of the experiment (beginning of day 2 post seeding), both types of hydrogels displayed comparable cell coverage, with 42-51% surface coverage on the uniform (Figure 6.8a) and 50-52% on the patterned one (Figure 6.8b).

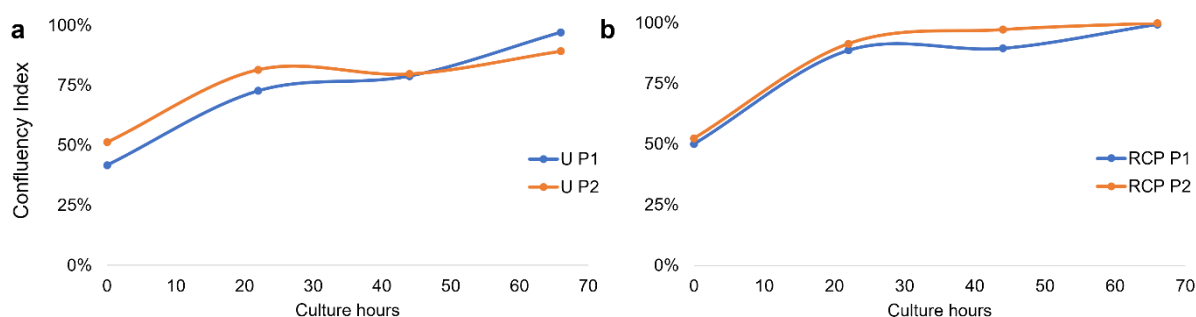


Figure 6.8 – Temporal progression of cell confluency on uniform (a) and patterned (RCP) (b) hydrogels. Red and blue curves show the confluency index of two positions in the culture plate.

However, the total area occupied by cells was slightly higher on the patterned hydrogel, and the cell count almost double that on the uniform (Table 6.2). This indicates a higher cell density on the patterned hydrogel despite similar surface coverage, possibly suggesting a different growth pattern influenced by the presence of microscale stiffness patterns. As the observation period progressed, the uniform hydrogel showed a marked increase in surface coverage but did not reach confluency (Figure 6.8a). In contrast, on the patterned hydrogel, the increase in surface coverage was faster: after 22 hours, the surface coverage was of 89-91% on the patterned hydrogel while it was only of 79-80% on the uniform gel. By the end of the observation period, full confluency was observed on the patterned hydrogel, ranging between 99-100%, while confluency was not attained on the uniform hydrogel yet (surface coverage at 66 h: 89-97%).

Table 6.2 – Quantitative analysis of cell growth dynamics at subconfluency on different hydrogel positions and hours.

<b>Hydrogel Position Hour</b>	<b>Total Covered Area (um<sup>2</sup>)</b>	<b>% Surface coverage</b>	<b>Mean cell Area (μm<sup>2</sup>) ± SD</b>	<b>Initial Cell Count</b>
Uniform P1 0h	184690	41.7%	901 ± 569	205
Uniform P1 22h	321958	72.7%	-	-
Uniform P1 44h	349234	78.8%	-	-
Uniform P1 66h	430001	97.1%	-	-
Uniform P2 0h	227150	51.3%	931 ± 568	244
Uniform P2 22h	361121	81.5%	-	-
Uniform P2 44h	353158	79.7%	-	-
Uniform P266h	395188	89.2%	-	-
RCP P1 0h	221864	50.1%	537 ± 343	413
RCP P1 22h	392900	88.7%	-	-
RCP P1 44h	396471	89.5%	-	-
RCP P1 66h	440364	99.4%	-	-
RCP P2 0h	232387	52.5%	533 ± 294	436
RCP P2 22h	404956	91.4%	-	-
RCP P2 44h	430594	97.2%	-	-
RCP P2 66h	442491	99.9%	-	-

Overall, while both hydrogel types supported cell growth and expansion, the cells on the patterned hydrogel exhibited a higher cell density and faster surface coverage. These results indicate that the stiffness heterogeneity of the substrate could influence not just cell movement, as previously observed, but also cell proliferation and spreading dynamics.

### 6.3.5 Cell density at confluency is higher in RCP hydrogel resulting in lower mean cell size

From each hydrogel type, images were captured from three distinct positions at the final stage of confluency. The images were subsequently subjected to careful analysis, with the main parameters of interest being cell density and the mean cell size at confluency. Upon reaching confluency, the cell populations on the uniform and patterned hydrogels exhibited distinct characteristics. A higher cell density was observed in the patterned hydrogel at confluency, averaging  $278089 \pm 30764$  cells/cm<sup>2</sup>, in comparison to the uniform hydrogel with an average of  $163077 \pm 11642$  cells/cm<sup>2</sup> (t-test,  $p < 0.01$ ) (Figure 6.9a). This increase in cell density corresponded with a reduction in the mean cell size in the patterned hydrogel. Cells in the patterned hydrogel demonstrated an average size of  $362 \pm 38$  μm<sup>2</sup>, substantially smaller than cells in the uniform hydrogel, which had a mean size of  $615 \pm 43$  μm<sup>2</sup> (t-test,  $p < 0.05$ ) as shown in Figure 6.9b.

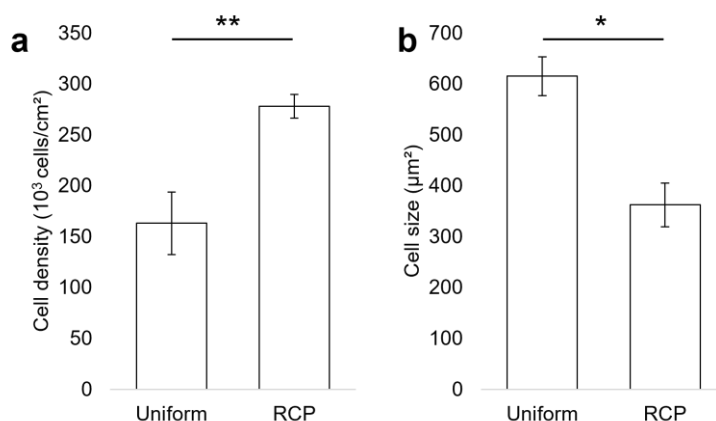


Figure 6.9 – Cell density and mean size at confluency on uniform and patterned (RCP) hydrogels: (a) Comparison of cell density, (b) Comparison of average cell size. Mean values are derived from three distinct positions for each hydrogel type, with error bars indicating standard deviation.

The unique mechanical properties of patterned hydrogels appear to influence not only cell motility and growth patterns but also cell size and density at confluency. Future work should delve deeper into these findings to further unravel the precise mechanisms by which the heterogeneity in hydrogel stiffness modulates cellular behavior.

### 6.3.6 Analysis of cell movement at confluency

The initial attempt to model the velocity autocorrelation function produced poor fits to the observed data, suggesting a non-exponential decay in cell velocities (Figure 6.10a). This rendered the extraction of a conventional correlation length problematic, as it relies on the assumption of an exponential decay. To address this, an alternative approach was taken. A model of the form  $\left(1 + \frac{x}{\zeta}\right)^{-a}$  was proposed for fitting the data, where  $\zeta$  denotes the characteristic length and  $a$  an exponent related to the correlation function. As visible on Figure

6.6b, this function provides a much better fit of the autocorrelation function, meaning that at this degree of confluency, cell movement is poorly correlated. This methodology resulted in the identification of a subcellular characteristic length scale and of a decay exponent for both hydrogel conditions.

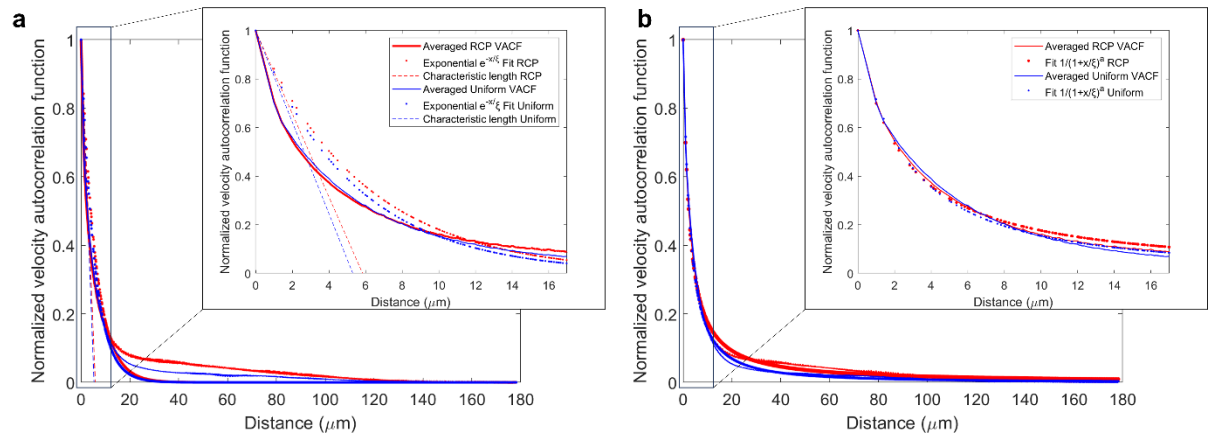


Figure 6.10 – Velocity autocorrelation function (VACF) and fits for cells on uniform and patterned (RCP) hydrogels. VACF for three different positions, represented by bright blue, blue and red, respectively are shown. (a) The VACF are fitted by an exponential decay  $e^{-x/\xi}$  (dashed lines). The inset on the right shows a zoomed-in view of the initial region, which illustrates the divergence of the experimental data from the expected exponential decay. (b) Fit by a faster decaying function  $\left(1 + \frac{x}{\xi}\right)^{-a}$  (dashed lines). The dotted lines represent the fitted function, which provides a better representation of the observed decay in the correlation function compared to the exponential fit. The inset shows a close-up view of the initial region, which emphasizes the characteristic length ( $\xi$ ) and its differences between cells cultured on uniform and RCP hydrogels.

Fitting autocorrelation functions at given time and position showed that the fitting parameters keep stationary in time and oscillate around a mean value for each type of hydrogel. The characteristic length  $\xi$  and the decay exponent  $a$  were thus obtained by fitting the time-averaged autocorrelation curves for each position. Notably, the analysis across the average three distinct positions revealed that cells cultured on uniform hydrogels exhibited larger mean exponent decay (t-test:  $p = 0.010$ ) and mean characteristic length (t-test:  $p = 0.066$ ) compared to those cultured on the patterned hydrogels, as presented in Figure 6.11.

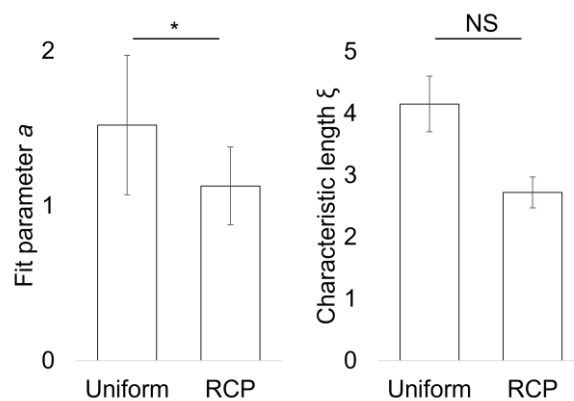


Figure 6.11 – Computed (a) Mean decay exponent  $a$  and (b) Mean characteristic lengths  $\xi$  obtained from the average autocorrelation function fits of the three positions for cells cultured uniform and patterned (RCP) hydrogels with their respective standard errors.

Fit results, their mean values and the associated standard errors for both uniform and RCP hydrogel conditions are presented in Table 6.3.

Table 6.3 – Mean fitting parameters for the velocity autocorrelation function for cells cultured on uniform and RCP hydrogels.

Statistic	Uniform	RCP
Mean $a \pm SE$	$1.52 \pm 0.14$	$1.13 \pm 0.58$
Mean $\xi \pm SE$ ( $\mu\text{m}$ )	$4.15 \pm 0.45$	$2.72 \pm 0.25$

This might suggest a more extensive spatial correlation of cellular motion within the context of the uniform stiffness hydrogel environment. However, it is essential to consider that this interpretation only stems from the perspective of a characteristic length scale and not the traditional correlation length. Therefore, caution must be exercised when attributing this observed difference to physical manifestations of cell velocities correlation.

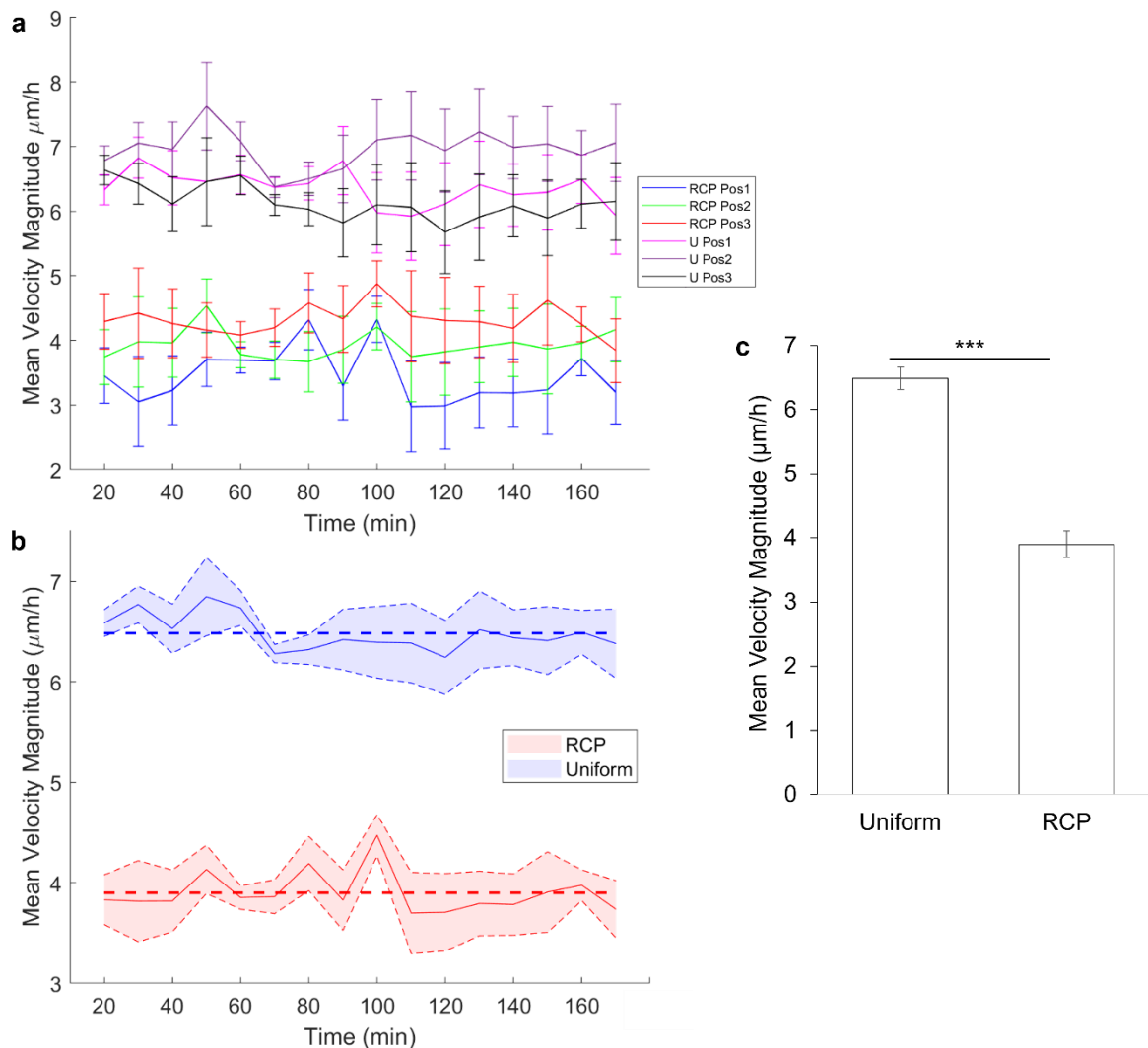


Figure 6.12 – Mean velocity magnitudes of cells cultured on uniform and patterned (RCP) hydrogels. (a) The plot displays the computed velocity magnitudes at 3 positions for both types of hydrogels. (b) Mean velocity magnitudes of cells cultured on uniform and RCP hydrogels, with their respective standard error. (c) Comparison of velocity magnitude presenting statistically significant difference with  $p < 0.001$ .

Furthermore, we found that cells moved faster on average when cultured on uniform hydrogels compared to patterned hydrogels (Figure 6.12a-c) with  $V_U = 6.5 \pm 0.2 \mu\text{m/h}$  and  $V_{RCP} = 3.9 \pm 0.2 \mu\text{m/h}$ . Despite both hydrogel types having similar median stiffness, the either higher or lower stiffness present in the circle patterns (dispersion ranging from 2.7 to 9.3 kPa, to be compared to  $\pm 0.2$  kPa on the uniform gel) may hinder to cell movement. The rapid proliferation and early attainment of confluency on patterned hydrogels may also limit cell motility due to increased cell-cell interactions and reduced available space. These findings are in alignment with existing literature. Prior studies by Garcia et al. [339] and Petitjean et al. [340] have reported drastic reductions in cell velocities upon reaching confluency, often down to a few micrometers per hour. This feature was also observed in this study, reinforcing the understanding that confluent states reduce cell motility.

#### 6.4 DISCUSSION

The impacts of patterned functionalization on cellular behavior are widely recognized. Patterns have been known to confine single cells and shape their form [163], and the specific geometry of these patterns can alter the stability of intercellular junctions, especially in the case of cell doublets [341]. In addition to these effects on individual cells or small assemblies, confinement can also influence the larger picture by changing the propagation of cellular stresses in cell assemblies and decreasing the correlation length [342]. Significant attention has also been given to the investigation of cell movements within monolayers. Many studies have analyzed correlation in cell movements on stiff matrices without patterns, and on soft substrates with a focus on measuring cellular stresses. The role of stiffness patterns has been specifically highlighted in their capacity to guide cellular stresses in single cells [343].

Here we compared cell behavior on hydrogels with uniform stiffness or randomly distributed stiffness patterns, both having the same mean surface density of Collagen I coating. In the early stages of our cell culture experiment, it was found that the presence of stiffness patterns significantly impacted A549 cell morphology and distribution (Figure 6.4). A higher cell count was observed on the patterned (RCP) hydrogel, and consistently the individual cells exhibited a smaller average area compared to those on the uniform hydrogel (Table 6.1) This disparity appeared far from intuitive. It is well documented that cells sense and respond to the variations in stiffness patterns by altering their spreading behavior. But in general, the spreading area increases with stiffness, at least in the range of the rigidities that are explored in this work [344]. Here the disk patterns have a higher stiffness than the uniform hydrogel (Figure 6.2). As their size and their spacing is of the order of the cell size (Figure 5.13 shows the geometric mean



circle size on patterned hydrogel of 8.8  $\mu\text{m}$ ; mean cell size at confluency 10.7  $\mu\text{m}$ , Figure 6.9), the cells are expected either to be confined on large patterns or to adhere to several patterns [220]. This latter situation is well visible on Figure 6.5. As the patterns are randomly distributed, there is no geometrical limitation to cell spreading, and therefore no obvious reason for the cells to be less spread. Interestingly, despite the differences in cell count and individual cell size, the overall surface coverage by cells remained similar between uniform and patterned hydrogels (Table 6.1). This observation suggests that, although individually smaller, cells on patterned hydrogels adopt a more densely packed arrangement to achieve similar coverage to the larger cells on uniform hydrogels. This observation points to the potential influence of cell-cell interactions and collective cell behavior in modulating cell distribution in response to variations in substrate stiffness.

Stiffness patterning emerged as a modulator of cell motility in the subconfluent phase of cell culture. This phase typically involves a higher level of cell migration as cells proliferate and spread to occupy the substrate, and any changes in their motile behavior can significantly impact the overall dynamics of cell population growth and spatial distribution. Cells on the patterned hydrogel exhibited slower velocities and presented shorter average step compared to their counterparts on the uniform hydrogel. These results suggest that the spatial heterogeneity of stiffness present to the patterned hydrogel may have constrained cell movement [345].

This is congruent with previous studies showing that mechanical properties can influence cell motility. Cells navigate their environment by sensing physical cues, such as the stiffness of the substrate, which subsequently direct their movement for instance along stiffness gradients [346], [347]. The patterned hydrogel, with its more complex mechanical landscape, may provide cues that encourage a more conservative, slower migration pattern. These results also mirror observations in more complex biological systems, such as tumor tissues, where heterogeneous mechanical properties have been associated with altered cell motility patterns [166].

The analysis of mean square displacement (MSD) provides a closer look at cell motility on both unpatterned and patterned hydrogels. Mean square displacement is often used as a way to quantify the random motion of particles (in this case, cells), with a linear increase in MSD over time indicating diffusive motion, also known as a random walk.

In the experiment, cells exhibited a linear increase in MSD over time on both unpatterned and patterned hydrogels, indicative of a random, non-directed mode of movement. This behavior suggests an absence of effective external cues guiding cell migration. The similarity in the slopes of the MSD progression for cells on both hydrogel types further supports this conclusion,

implying that the randomness of cell movements remains largely unaffected by differences in hydrogel stiffness or patterning. Hence, while substrate properties like patterning and stiffness can influence cell velocity and travel distance (as observed in section 6.3.2), they seem to not significantly impact the randomness or diffusivity of cell movement. This observation is not surprising as the stiff patterns are randomly distributed. They should not provide a specific orientation to the movement but they could affect cell velocity by forcing non-natural steps from a stiff pattern to another one, as Figure 6.5 suggests. This is precisely what is observed. The fact that the amplitude of the velocity is lower suggests that the cells are hampered in their movements, probably because the density of the stiff disks is not sufficient to ensure a continuous movement.

The monitoring of cell growth dynamics for 66 hours revealed distinct patterns on uniform and patterned hydrogels (Figure 6.8). At the beginning of the experiment, both hydrogel types displayed similar cell coverage, yet the patterned hydrogel housed nearly twice the number of cells, suggesting a denser cell growth behavior potentially influenced by the stiffness heterogeneity. As the culture period progressed, the patterned hydrogel exhibited a more accelerated expansion, achieving full confluency by the 66th hour. In contrast, the uniform hydrogel, while also showing increased cell surface coverage, did not reach full confluency within the same time frame. Therefore, these results indicate that the presence of substrate stiffness heterogeneity could play a role not only in affecting cell movement, as observed in previous sections, but also in impacting the dynamics of cell proliferation and spreading.

Moreover, substrate stiffness has been widely recognized to regulate cell behavior through mechanotransduction, the process by which cells convert mechanical stimuli into biochemical signals [348]. A key pathway implicated in this process is the Rho/ROCK (Rho-associated coiled-coil kinase) pathway [349]. When cells encounter a stiff environment, they often respond by increasing the formation of stress fibers and focal adhesions, which are mediated by the Rho/ROCK pathway [350]. This pathway is known to modulate cell adhesion, spreading, migration, and proliferation [351], all of which appear to be influenced by the stiffness patterning observed in our study. In our experimental setting, the higher cell density and faster coverage on the patterned hydrogel could be a result of enhanced activation of the Rho/ROCK pathway. The mechanical stimuli provided by the stiffness patterns might be promoting an increase in cell-matrix adhesions and stress fibers, leading to increased cell spreading and proliferation. Another pathway that might be involved is the YAP/TAZ pathway, which is a key downstream effector of the Hippo pathway and is known to be sensitive to mechanical cues including substrate stiffness [351]. When cells are on a stiffer regions, YAP/TAZ is activated

and translocated into the nucleus to promote the transcription of genes involved in cell proliferation and anti-apoptosis [352],[353], potentially explaining the increased cell density observed on the patterned hydrogel. Therefore, the differential cell growth dynamics observed on the uniform and patterned hydrogels could be influenced by the activation of mechanosensitive signaling pathways like the Rho/ROCK and YAP/TAZ pathways. Further studies are needed to confirm the involvement of these pathways and uncover the precise molecular mechanisms underlying the observed behaviors.

It was demonstrated that, upon reaching confluency, the patterned and uniform hydrogels displayed unique cell population traits. The patterned hydrogel was observed to have a higher cell density, with approximately 280000 cells/cm<sup>2</sup>, compared to 160000 cells/cm<sup>2</sup> on the uniform hydrogel. This rise in cell density was accompanied by a decrease in average cell size on the patterned hydrogel, where cells had an average size of  $362 \pm 38 \mu\text{m}^2$ , significantly smaller than the  $615 \pm 43 \mu\text{m}^2$  average size observed in cells on the uniform hydrogel (Figure 6.9).

Our results also revealed that cells moved more quickly on average ( $6.5 \pm 0.2 \mu\text{m/h}$ ) when cultured on uniform hydrogels as opposed to patterned hydrogels ( $3.9 \pm 0.2 \mu\text{m/h}$ ) even at confluency (Figure 6.12). This observation suggests that the intercellular interaction does not drastically modify the cell interaction with the substrate as it was reported for other cell types such as HUVE cells for instance [342].

The analysis of the velocity autocorrelation function unveiled a non-exponential decay in cell velocities, necessitating an alternative approach to extract the characteristic length (Figure 6.10a). This process led to identifying a subcellular length scale under both hydrogel conditions, in agreement with the work of Petitjean et al. [340] and more recently Garcia et al. [339] (Figure 6.11). However, this interpretation is strictly from the perspective of the characteristic length scale, not a traditional correlation length, necessitating careful analysis when relating this difference to physical manifestations of cell velocity correlation. Further investigation is needed to elucidate the biophysical mechanisms accountable for this observed difference. Nonetheless, as observed from the previous results of this chapter, the stiffness pattern had an influence on the cell sizes, and cell size has been shown to have a direct effect on cell velocity [340]. Our analysis revealed that cells cultured on patterned hydrogel surfaces near confluency exhibited a lower characteristic length compared to cells on uniform hydrogel surfaces. The shorter characteristic length observed would suggest more localized velocity fluctuations and restricted cell motion within the crowded cellular environment near confluency. The high cell density imposes mechanical constraints and promotes increased cell-cell interactions. These factors are known to contribute to reduced freedom of movement.

These results align with prior studies that report a significant decrease in cell velocities upon reaching confluency. Garcia et al. showed that the distance over which cell displacements are correlated first increases drastically and then decreases back to cellular or subcellular sizes, while the speed of the cells slows down over time [339]. These changes are not controlled by cell density but rather by a maturation of the cell–cell and cell–substrate contacts. The authors also suggested a possible underlying mechanism leading to cellular slowing down. Counterintuitively, Pinto et al. recently investigated the impact of substrate disorder on cell motility in a model confluent tissue using the self-propelled Voronoi model. The researchers found that when the characteristic length scale of the preferred geometry is smaller than the cell size, the tissue is less rigid than its homogeneous counterpart, resulting in an increase in cell motility [354]. The study suggests that the underlying structure supporting the tissue, such as the extracellular matrix (ECM) or a culture substrate, should not be described using generalized bulk metrics since heterogeneities can play a relevant role in the tissue mechanics.

Since these experiments focused mostly on the confluent period of cellular monolayers, future research endeavors could aim to expand on these findings by investigating earlier stages of monolayer formation including a range of uniform and stiffness patterned hydrogels. For a comprehensive understanding of correlation length in the context of this work, future studies must encompass longer observation periods and consider the potential role of cell-cell and cell-substrate maturation in dictating cell motility. Moreover, understanding the non-exponential behavior of the velocity correlation function could uncover the complex interplay of factors that shape collective cell behavior and its implications for various biological contexts. This holistic understanding could provide a foundation for interpreting our current findings and furthering our knowledge of cell motility in confluent monolayers.

# CHAPTER 7

---

## CONCLUSIONS

## 7 CONCLUSIONS

This doctoral thesis has concentrated on a quantitative analysis of the mechanical properties of healthy and tumor lung tissue, with the aim of designing mechano-mimetic culture substrates that emulate the stiffness texture of adenocarcinoma lung tissue. Utilizing AFM, the study delved into a comprehensive analysis of the mechanical properties of lung tissues. This work spun multiple fields of knowledge across the various chapters, each contributing to the theoretical framework and practical methodologies used and addressing different aspects such as stiffness texture heterogeneity, protein tissue composition, hydrogel fabrication with textured rigidity, and a comparative investigation into A549 cell culture on uniform *versus* pattern mechano-mimetic hydrogels.

The intrinsic relationship between the mechanical properties of cells and tissues with essential physiological functions like proliferation, differentiation, and the development of various diseases emphasizes the significance of biomechanics in cellular behavior and disease progression. Within this context, the compliant nature of the lung (either healthy, or with two subtypes of adenocarcinoma) makes it relatively difficult to characterize, requiring a methodological approach and repetition until consistent force-indentation curves can be acquired. These technical challenges were overcome with specific probe functionalization to mitigate adhesion, leading to the acquisition of the microscale mechanical properties of lung tissues. The clinical characteristics of patients, the contact mechanics different models used in the analyses, and the adhesive interaction effect on the measured mechanical properties were carefully explored. Stiffness values highlighted significant differences between healthy and tumor tissues, with tumor tissues showing greater stiffness. Surprisingly, acinar and solid subtypes of adenocarcinoma did not reveal significant differences in mechanical properties, despite their histological differences. The implemented methodology in this work could be easily adapted and used to characterize other biological tissues.

The use of the Cell Hesion module enabled the exploration of larger tissue areas and the acquisition of textured rigidity maps. . Application of a threshold corresponding to the 70th percentile of tumor tissue stiffness distribution allowed the creation of binary masks using a custom algorithm, and, by using a straightforward iterative process, this approach facilitated the analysis and extraction of basic shape descriptors from the rigidity maps, leading to subsequent statistical analysis.

This analysis yielded an average pattern that demonstrated an elliptical shape with pronounced convexity. By adopting a zero-order approach, a circle pattern emerged, and was instrumental in generating a random circle pattern design which served as inputs for the fabrication of a single layer gray-level mask. The stiffness threshold, though arbitrarily selected, has been revealed as a key factor tied to the photochemistry of the hydrogel, offering insights into custom-tailored strategies for replicating the tissue stiffness texture. While the current data do not discern a difference in the shape of the stiff patterns between healthy and tumor tissues at the chosen threshold value, the difference in surface coverage and the observed tumor stiffness variability underscore the potential of this methodology.

Despite the success in obtaining larger rigidity maps in recent studies, the focus on replicating stiffness heterogeneity in *in vitro* cell culture substrates has been largely overlooked. Consequently, our approach to obtaining and interpreting rigidity maps (though constrained by a limited number of maps and technological limitations), combined with a specialized process for deriving mask design parameters, offers a valuable framework for understanding the mechanical properties of biological tissues and lay the ground for creating pathophysiological stiffness textures on hydrogels.

The insights gathered in this thesis also shed light on the relationship between known structural proteins such as collagen, vimentin, and  $\alpha$ -SMA, and the stiffness of lung adenocarcinoma tissues. The analysis in this study revealed a complex link that defies a simplistic correlation between collagen content and stiffness across the different subtypes. Interestingly, when examined individually, the tumors subtypes exhibit inverse correlations (acinar positive and solid negative) that are statistically significant. Vimentin and  $\alpha$ -SMA also reveal unexpected relationships:  $\alpha$ -SMA showed a significant negative correlation with tissue stiffness, contrary to prior expectations. On the contrary, for vimentin, no significant correlation was found. This study provided insights into the relationship between structural proteins and tissue rigidity, although certain limitations constrain the findings (restricted size of the dataset, observational character of the experimentation, data collection from a relatively narrow selection of tissue samples). Therefore, further research is required to elucidate the definitive patterns and relationships, and to potentially uncover additional information about disease state or progression.

The development and fabrication of mechano-mimetic polyacrylamide hydrogels using the statistical texture of stiffness in lung tissues represents a complex yet successful endeavor. The utilization of chromium in gray-level technology to create intricate stiffness gradients in hydrogels and the fine-tuning of various parameters led to an effective emulation of mechanical

heterogeneity found in actual tumor tissues. The work successfully achieves a heterogeneous stiffness distribution despite inherent limitations, such as the underrepresentation of intermediate stiffness values, and challenges in using SmartPrint UV technology.

Simultaneously, optimizing the surface functionalization protocol with the goal of overfunctionalizing the rigid patterns to enable cell culture was paramount in this work, resulting in an effective balance between protein attachment and preservation of hydrogel integrity. The seemingly counter-intuitive phenomenon observed in surface functionalization, such as the dehydration process's positive effect and the overfunctionalization of hydrogel backgrounds, offers new insights that may contradict traditional methodologies.

The study exploring the effects of patterned functionalization on cells helped us understand the intricate relationships between stiffness patterns, cell structure, and motion. Stiffness patterns were found to significantly alter A549 cell morphology and distribution, leading to a more densely packed arrangement of smaller cells on patterned hydrogels compared to uniform ones. These patterns modulate cell motility in both the subconfluent and confluent phases. The random distribution of stiffness, although affecting the velocity, did not significantly impact the diffusivity of cell movement, underscoring its limited role in guiding cell interactions and movement. The exploration in confluent monolayers highlighted intriguing traits, such as higher cell density and reduced cell size on patterned hydrogels, as well as the non-exponential decay in the velocity autocorrelation function. These insights illuminate a new understanding of how substrate properties like stiffness patterning can transcend individual cellular levels to influence collective cell behavior, affecting processes such as cell proliferation, spreading, and motion. Although this study elucidates several basic aspects of cellular behavior in response to stiffness patterns, it also opens new avenues for research to refine the comprehension of the mechanobiology of cells and tissues, and further research is required to identify the mechanotransduction pathways involved in the distinctive cell growth dynamics between patterned and uniform hydrogels. The complexities revealed in the interaction between cells and their substrate will advance our understanding of cell behavior in *in vitro* and may guide future developments in tissue engineering and medical applications.

Overall, the innovative approaches and detailed analyses in this doctoral thesis could significantly contribute to the current understanding of lung tissue mechanics, laying the groundwork for future research, and serve as inputs for potential applications in the biotechnology field, as presented in the next chapter (Perspectives).



# CHAPTER 8

---

## PERSPECTIVES

## 8 PERSPECTIVES

The insights gained through these chapters underscore the complexity and intricacy of lung tissue mechanics, as well as the importance of considering the technological factors to better reproduce the tissue micromechanical environment. As we look ahead, our research aims to unravel the influence of textured rigidity on cellular behaviors and compare it to other conditions, including, uniform rigidities and the standard plastic/glass supports. The balance of the influence of the stiffness of the culture plate and the density of surface ligands are also interesting areas of exploration, given their distinct impact on cellular constituents. The potential correlations between textured rigidity, cellular adhesion, and the actin cytoskeleton are worth elucidating in future work, providing new directions for improving our understanding of cell-ECM interactions. Furthermore, we aim to carry out a comprehensive suite of biological experiments, including the analyses of signaling pathways and transcriptomics, in collaboration with the CRCL. The goal of these experiments is to better understand the impact of textured rigidity on cell cycle, gene expression and the preservation of cellular phenotypes when the cells are grown *in vitro* on 2D mechano-mimetic substrates (Figure 8.1). It is indeed well documented that cell proliferation is slowed down when cultured on soft substrates of uniform stiffness (with some exceptions for some cell types) [170]. In a recent study, the CRCL group led by C. Chaveroux in collaboration with A. Nicolas (LTM) and C. Migdal (Cell&Soft) has shown that in human bronchial epithelial cells, which are alveolar progenitors, this slowed proliferation was attributed to the nonstandard arrest of cell cycle in S phase (Figure 8.1a), which proved to be consistent with data reported for mice and pork [355],[356]. They also proved that the differentiation capability of these cells was preserved in the cells grown on uniformly soft substrates for 20 passages while it was lost on plastic plates (Figure 8.1b). This conducted to the conclusion that the culture of these cells on uniformly soft substrates (3 kPa) was limiting cellular drift compared to the culture on plastic dishes. The influence of stiffness texture is now to be addressed to see if it brings specific traits to the cells as we anticipate from our preliminary study on cell morphology, proliferation and migration. We also anticipate that these outcomes will provide a significant contribution to the field of biomechanics and its links to lung oncology.

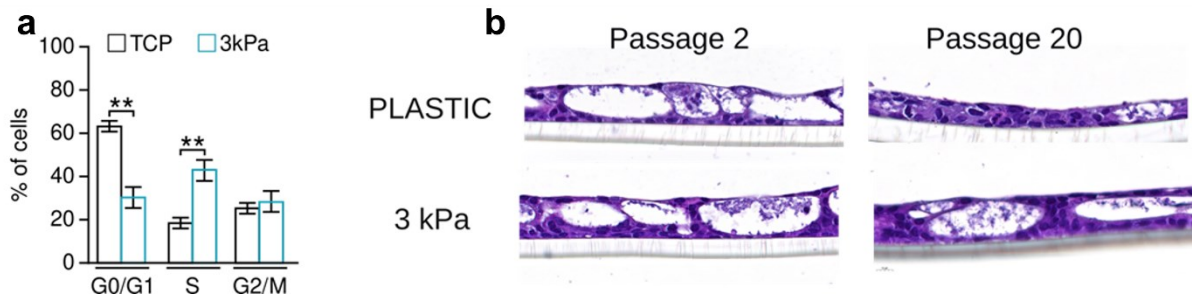


Figure 8.1 – (a) HBECs grown on uniformly soft substrates accumulate in S phase, meaning that the traditional program is partly halted. (b) Cell passages limit the differentiation capabilities of HBECs in an alveolar tissue when they are grown on plastic but not on a uniformly soft substrate. Hematoxylin & Eosin staining.

Investigations into stem cell biology could also be foreseen in our future studies. By analyzing the responses of stem cells to variations in rigidity and surface chemistry conditions, novel perspectives on cellular behavior could be attained. In particular, this research aims to provide a deeper understanding of how these factors affect stem cell differentiation and the maintenance of their phenotypic characteristics. These insights could potentially contribute for the development of innovative regenerative therapies.

Moving forward, our research efforts will not only focus on stem cells and immortalized cell lines but will also integrate primary cells into our experimental framework. Primary cells offer a more physiologically relevant model and could potentially reveal unique responses to substrate rigidity and surface chemistry that might not be observable in immortalized cell lines. This broader approach to cell type will expand the scope of our understanding of cell-matrix interactions and improve the reliability and applicability of our findings.

From a biophysical standpoint, utilizing cellular contractility measurements could pave the way for a deeper understanding of fundamental cellular mechanisms. By employing advanced techniques such as Traction Force Microscopy and Intracellular Stress Microscopy, we aim to quantify and interpret the forces exerted by cells. Examining how these forces correlate with the physicochemical properties of their culture substrates could lead us to new insights into how cells interact with their environment at a fundamental level. At LTM, this question has been addressed in the past years by growing cells on soft substrates with a periodic texture of rigidity [220]. This study has unveiled that the cells are adherent to the stiff and the soft part of the substrate, although focal adhesions mainly localize on the stiff patterns. This observation resulted from the fact that cellular traction forces were exceeding noise level in both places as seen in Figure 8.2.

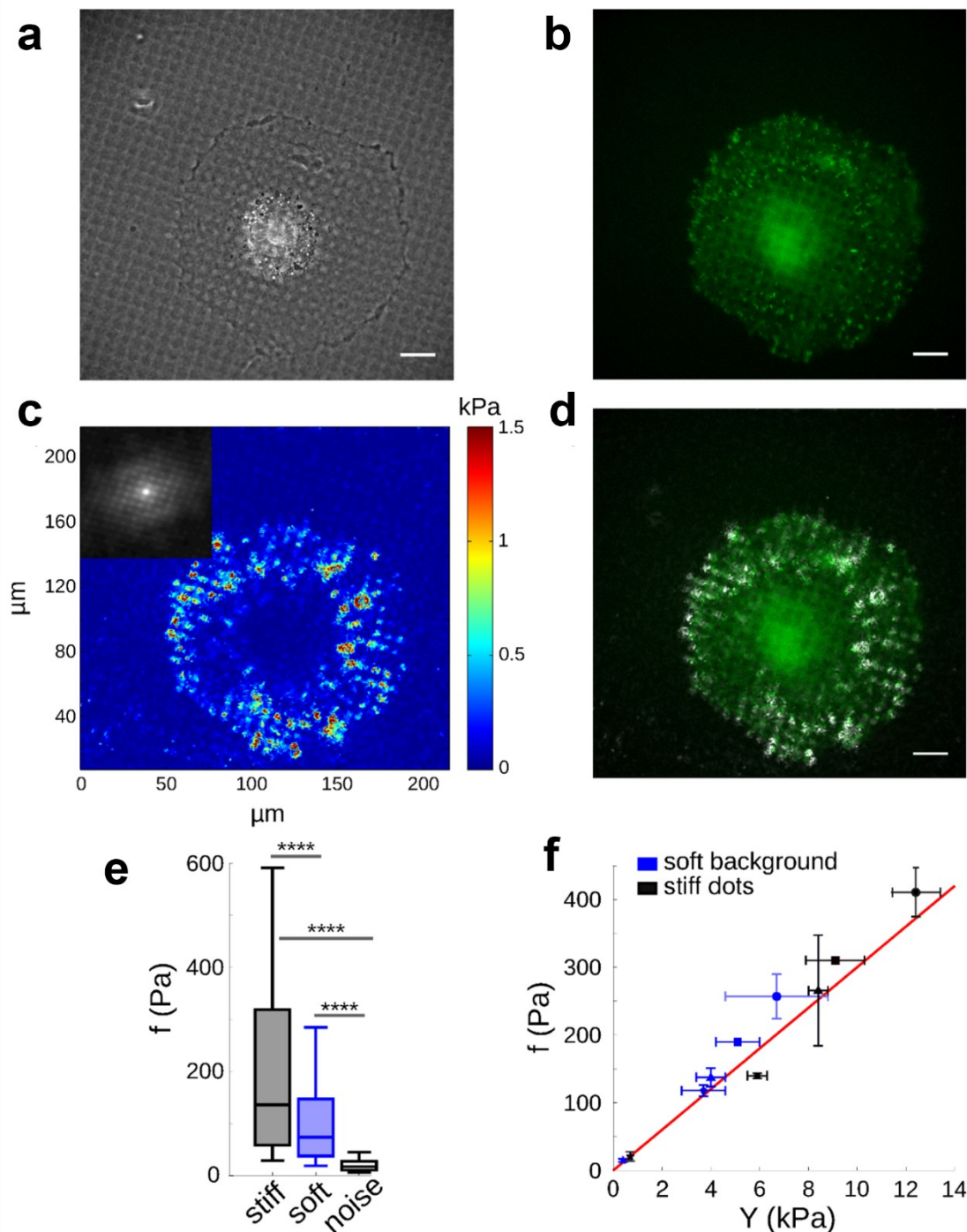


Figure 8.2 – (a) Phase contrast micrograph of a REF52 cell on a rigidity-patterned matrix. (b) Paxillin, a protein involved in focal adhesion and cell signaling, shows primary accumulation on the stiffer 'dots' of the matrix. (c) Mapping of the traction stresses generated by the cell. The periodic distribution of stress magnitudes, indicated by the autocorrelation function, aligns with the patterned rigidity of the matrix. (d) Overlay of stress magnitude (white) and paxillin staining (green), revealing a colocalization at regions of high stress and paxillin concentration. (e) A graphical representation of the stress amplitude across the cell. The stress is significantly larger on the stiffer dots as compared to the softer background, indicating an adaptive cellular response to substrate rigidity. (f) Scatter plot showing a linear correlation between average cell-generated traction stresses and the local Young's modulus of the hydrogel, indicating the mechanosensitive nature of cell-substrate interactions. Different pairs of rigidity are marked with unique symbols. Error bars represent the standard error of the mean. Image from [220].

As a result, it was measured that the cellular traction forces are larger on the stiff patterns than on the soft ones, the difference of amplitude being directly proportional to the Young's modulus of the substrate (Figure 8.2e).

However, the work by Yang et al. [227] has shown that a random stiffness texture could drastically change cell response, for example in terms of cell spreading or the localization of YAP (nuclear or cytoplasmic) and its sensitivity to the mean stiffness, meaning that cell adaptation to stiffness involves mechanisms at the cell level and does not limit to the molecular scale of integrins or of focal adhesions (Figure 8.3).

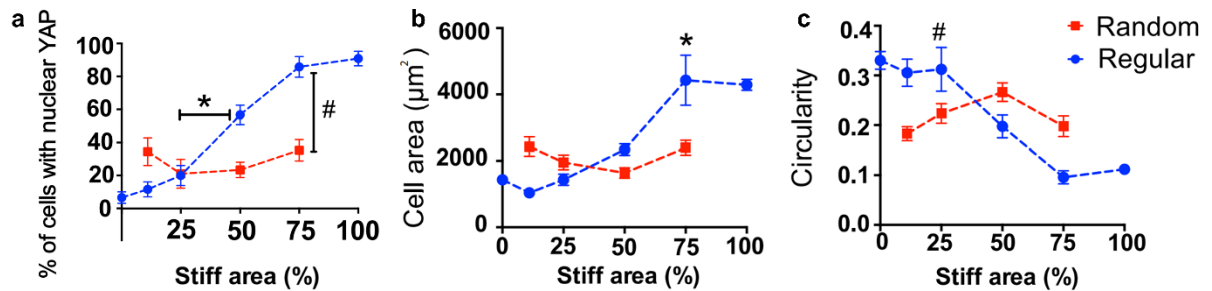


Figure 8.3 – (a) Quantification of intracellular YAP activation in hMSCs on regular and randomly patterned hydrogels. A sigmoidal increase in YAP activation occurs in regular patterns with a significant jump between 25% and 50% stiffness. This effect is absent on random patterns. (b) Cell spreading area on regularly and randomly patterned hydrogels. Consistent with YAP activation, spreading increases with stiffness on regular patterns, but is insensitive to stiffness changes on random patterns. (c) Cellular circularity decreases relative to stiffness on regular patterns, with no significant change observed on random patterns. Adapted from [227].

Thus, the technical developments achieved in this study now pave the way for a new study devoted to understanding the mechanisms underlying cellular sensitivity to stiffness at the cell level (Figure 8.4). These findings will be juxtaposed with biological markers from the CRCL studies and potentially contribute to understanding fundamental concepts related to mechanotransduction.

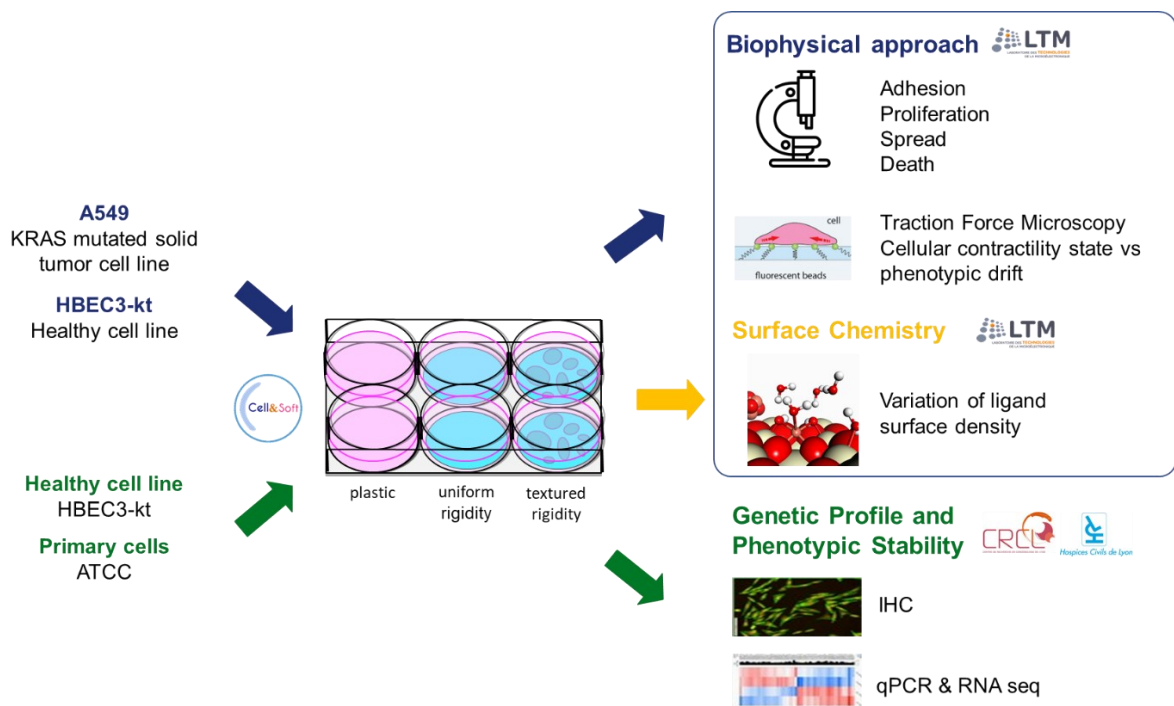


Figure 8.4 – Perspectives inputs and outputs scheme. Outputs inside the box. Genetic profile and phenotypic stability will be performed by CRCL and will serve as input to for data correlations.

Another pivotal aim is to broaden the scope of our research to other tissue types or disease specific tissues. This expansion will enable the characterization and production of tissue-specific stiffness textured hydrogels that closely mimic the tissue environment. The ultimate goal of these efforts is to provide substrates for 2D cell culture that bring cells closer to their physiological state, and thus accelerate the development of high-throughput drug screening processes.

Lastly, an important contribution of this thesis will be the practical application and industrial translation of the developed technological knowledge, such as design and mask fabrication processes, sample preparation and AFM characterization of soft human tissue. The expertise and methodologies generated throughout this research will be integrated by Cell&Soft for further commercial services. The aim is to leverage these research findings for practical industrial applications, potentially improving the efficiency and effectiveness of current processes or even pioneering new biotechnological methods and tools with the ultimate goal of bridging the gap between academic research and industry.

## BIBLIOGRAPHY

- [1] J. D. Humphrey, E. R. Dufresne, and M. A. Schwartz, “Mechanotransduction and extracellular matrix homeostasis,” *Nature Reviews Molecular Cell Biology*, vol. 15, no. 12. Nature Publishing Group, pp. 802–812, Dec. 11, 2014. doi: 10.1038/nrm3896.
- [2] N. M. E. Ayad, S. Kaushik, and V. M. Weaver, “Tissue mechanics, an important regulator of development and disease,” *Philosophical Transactions of the Royal Society B: Biological Sciences*, vol. 374, no. 1779, 2019, doi: 10.1098/rstb.2018.0215.
- [3] A. K. Harris, D. Stopak, and P. Wild, “Fibroblast traction as a mechanism for collagen morphogenesis,” *Nature*, vol. 290, no. 5803, pp. 249–251, Mar. 1981, doi: 10.1038/290249a0.
- [4] N. C. Gauthier and P. Roca-Cusachs, “Mechanosensing at integrin-mediated cell-matrix adhesions: from molecular to integrated mechanisms,” *Curr Opin Cell Biol*, vol. 50, pp. 20–26, 2018.
- [5] A. Elosegui-Artola, X. Trepac, and P. Roca-Cusachs, “Control of mechanotransduction by molecular clutch dynamics,” *Trends Cell Biol*, vol. 28, no. 5, pp. 356–367, 2018.
- [6] P. A. Janmey, D. A. Fletcher, and C. A. Reinhart-King, “Stiffness Sensing by Cells,” *Physiol Rev*, vol. 100, no. 2, pp. 695–724, Apr. 2020, doi: 10.1152/physrev.00013.2019.
- [7] S. R. Peyton and A. J. Putnam, “Extracellular matrix rigidity governs smooth muscle cell motility in a biphasic fashion,” *J Cell Physiol*, vol. 204, no. 1, pp. 198–209, Jul. 2005, doi: 10.1002/jcp.20274.
- [8] B. L. Bangasser *et al.*, “Shifting the optimal stiffness for cell migration,” *Nat Commun*, vol. 8, May 2017, doi: 10.1038/ncomms15313.
- [9] N. Zaari, P. Rajagopalan, S. K. Kim, A. J. Engler, and J. Y. Wong, “Photopolymerization in Microfluidic Gradient Generators: Microscale Control of Substrate Compliance to Manipulate Cell Response,” *Advanced Materials*, vol. 16, no. 23–24, pp. 2133–2137, Dec. 2004, doi: 10.1002/adma.200400883.
- [10] S. R. Caliarì and J. A. Burdick, “A practical guide to hydrogels for cell culture,” *Nature Methods*, vol. 13, no. 5. Nature Publishing Group, pp. 405–414, May 01, 2016. doi: 10.1038/nmeth.3839.
- [11] A. Isomursu *et al.*, “Negative durotaxis: cell movement toward softer environments,” 2020, doi: 10.1101/2020.10.27.357178.
- [12] C. Tomba, C. Migdal, D. Fuard, C. Villard, and A. Nicolas, “Poly-lysine/Laminin Surface Coating Reverses Glial Cell Mechanosensitivity on Stiffness-Patterned Hydrogels,” *ACS Appl Bio Mater*, vol. 5, no. 4, pp. 1552–1563, Apr. 2022, doi: 10.1021/acsabm.1c01295.
- [13] D. E. Discher, P. Janmey, and Y.-L. Wang, “Tissue Cells Feel and Respond to the Stiffness of Their Substrate,” 2005. [Online]. Available: <http://science.sciencemag.org/>
- [14] P. A. Janmey, R. G. Wells, R. K. Assoian, and C. A. McCulloch, “From tissue mechanics to transcription factors,” *Differentiation*, vol. 86, no. 3, pp. 112–120, Oct. 2013, doi: 10.1016/j.diff.2013.07.004.
- [15] C. Frantz, K. M. Stewart, and V. M. Weaver, “The extracellular matrix at a glance,” *J Cell Sci*, vol. 123, no. 24, pp. 4195–4200, Dec. 2010, doi: 10.1242/jcs.023820.
- [16] R. O. Hynes, “The Extracellular Matrix: Not Just Pretty Fibrils,” *Science (1979)*, vol. 326, no. 5957, pp. 1216–1219, Nov. 2009, doi: 10.1126/science.1176009.
- [17] N. Alam *et al.*, “The integrin—growth factor receptor duet,” *J Cell Physiol*, vol. 213, no. 3, pp. 649–653, Dec. 2007, doi: 10.1002/jcp.21278.
- [18] B. Trappmann *et al.*, “Extracellular-matrix tethering regulates stem-cell fate,” *Nat Mater*, vol. 11, no. 7, pp. 642–649, 2012, doi: 10.1038/nmat3339.
- [19] P. Müller and A. F. Schier, “Extracellular Movement of Signaling Molecules,” *Dev Cell*, vol. 21, no. 1, pp. 145–158, Jul. 2011, doi: 10.1016/j.devcel.2011.06.001.
- [20] Y. Zhu, A. Oganessian, D. R. Keene, and L. J. Sandell, “Type IIA Procollagen Containing the Cysteine-rich Amino Propeptide Is Deposited in the Extracellular Matrix of Prechondrogenic Tissue and Binds to TGF- $\beta$ 1 and BMP-2,” *J Cell Biol*, vol. 144, no. 5, pp. 1069–1080, Mar. 1999, doi: 10.1083/jcb.144.5.1069.
- [21] E. S. Wijelath *et al.*, “Heparin-II Domain of Fibronectin Is a Vascular Endothelial Growth Factor-Binding Domain,” *Circ Res*, vol. 99, no. 8, pp. 853–860, Oct. 2006, doi: 10.1161/01.RES.0000246849.17887.66.

- [22] R. O. Hynes, “The evolution of metazoan extracellular matrix,” *Journal of Cell Biology*, vol. 196, no. 6, pp. 671–679, Mar. 2012, doi: 10.1083/jcb.201109041.
- [23] D. R. Zimmermann and M. T. Dours-Zimmermann, “Extracellular matrix of the central nervous system: from neglect to challenge,” *Histochem Cell Biol*, vol. 130, no. 4, pp. 635–653, Oct. 2008, doi: 10.1007/s00418-008-0485-9.
- [24] A. Dityatev, M. Schachner, and P. Sonderegger, “The dual role of the extracellular matrix in synaptic plasticity and homeostasis,” *Nat Rev Neurosci*, vol. 11, no. 11, pp. 735–746, Nov. 2010, doi: 10.1038/nrn2898.
- [25] P. Lu, V. M. Weaver, and Z. Werb, “The extracellular matrix: A dynamic niche in cancer progression,” *Journal of Cell Biology*, vol. 196, no. 4, pp. 395–406, Feb. 2012, doi: 10.1083/jcb.201102147.
- [26] M. W. Pickup, J. K. Mouw, and V. M. Weaver, “The extracellular matrix modulates the hallmarks of cancer,” *EMBO Rep*, vol. 15, no. 12, pp. 1243–1253, Dec. 2014, doi: 10.15252/embr.201439246.
- [27] T. Wynn, “Cellular and molecular mechanisms of fibrosis,” *J Pathol*, vol. 214, no. 2, pp. 199–210, Jan. 2008, doi: 10.1002/path.2277.
- [28] S. Bin LIM, S. J. TAN, W.-T. LIM, and C. T. LIM, “An extracellular matrix-related prognostic and predictive indicator for early-stage non-small cell lung cancer,” *Nat Commun*, vol. 8, no. 1, p. 1734, Nov. 2017, doi: 10.1038/s41467-017-01430-6.
- [29] C. Storm, J. J. Pastore, F. C. MacKintosh, T. C. Lubensky, and P. A. Janmey, “Nonlinear elasticity in biological gels,” *Nature*, vol. 435, no. 7039, pp. 191–194, May 2005, doi: 10.1038/nature03521.
- [30] A. D. Theocharis, S. S. Skandalis, C. Gialeli, and N. K. Karamanos, “Extracellular matrix structure,” *Adv Drug Deliv Rev*, vol. 97, pp. 4–27, Feb. 2016, doi: 10.1016/j.addr.2015.11.001.
- [31] R. I. Litvinov, M. Pieters, Z. de Lange-Loots, and J. W. Weisel, “Fibrinogen and Fibrin,” 2021, pp. 471–501. doi: 10.1007/978-3-030-58971-4\_15.
- [32] L. Yang, K. O. van der Werf, P. J. Dijkstra, J. Feijen, and M. L. Bennink, “Micromechanical analysis of native and cross-linked collagen type I fibrils supports the existence of microfibrils,” *J Mech Behav Biomed Mater*, vol. 6, pp. 148–158, Feb. 2012, doi: 10.1016/j.jmbbm.2011.11.008.
- [33] J. W. Weisel, “The mechanical properties of fibrin for basic scientists and clinicians,” *Biophys Chem*, vol. 112, no. 2–3, pp. 267–276, Dec. 2004, doi: 10.1016/j.bpc.2004.07.029.
- [34] G. Burgstaller, B. Oehrle, M. Gerckens, E. S. White, H. B. Schiller, and O. Eickelberg, “The instructive extracellular matrix of the lung: Basic composition and alterations in chronic lung disease,” *European Respiratory Journal*, vol. 50, no. 1. European Respiratory Society, Jul. 01, 2017. doi: 10.1183/13993003.01805-2016.
- [35] M. Romero-López *et al.*, “Recapitulating the human tumor microenvironment: Colon tumor-derived extracellular matrix promotes angiogenesis and tumor cell growth,” *Biomaterials*, vol. 116, pp. 118–129, Feb. 2017, doi: 10.1016/j.biomaterials.2016.11.034.
- [36] W. W. Ahmed, É. Fodor, and T. Betz, “Active cell mechanics: Measurement and theory,” *Biochimica et Biophysica Acta (BBA) - Molecular Cell Research*, vol. 1853, no. 11, pp. 3083–3094, Nov. 2015, doi: 10.1016/j.bbamcr.2015.05.022.
- [37] N. Wang, J. D. Tytell, and D. E. Ingber, “Mechanotransduction at a distance: mechanically coupling the extracellular matrix with the nucleus,” *Nat Rev Mol Cell Biol*, vol. 10, no. 1, pp. 75–82, Jan. 2009, doi: 10.1038/nrm2594.
- [38] D. A. Fletcher and R. D. Mullins, “Cell mechanics and the cytoskeleton,” *Nature*, vol. 463, no. 7280, pp. 485–492, Jan. 2010, doi: 10.1038/nature08908.
- [39] F. Huber, A. Boire, M. P. López, and G. H. Koenderink, “Cytoskeletal crosstalk: when three different personalities team up,” *Curr Opin Cell Biol*, vol. 32, pp. 39–47, Feb. 2015, doi: 10.1016/j.ceb.2014.10.005.
- [40] S. Seetharaman and S. Etienne-Manneville, “Cytoskeletal Crosstalk in Cell Migration,” *Trends Cell Biol*, vol. 30, no. 9, pp. 720–735, Sep. 2020, doi: 10.1016/j.tcb.2020.06.004.
- [41] Q. Luo, D. Kuang, B. Zhang, and G. Song, “Cell stiffness determined by atomic force microscopy and its correlation with cell motility,” *Biochimica et Biophysica Acta (BBA) - General Subjects*, vol. 1860, no. 9, pp. 1953–1960, Sep. 2016, doi: 10.1016/j.bbagen.2016.06.010.



- [42] Y. Abidine *et al.*, “Mechanosensitivity of Cancer Cells in Contact with Soft Substrates Using AFM,” *Biophys J*, vol. 114, no. 5, pp. 1165–1175, Mar. 2018, doi: 10.1016/j.bpj.2018.01.005.
- [43] M. Nikolić, G. Scarcelli, and K. Tanner, “Multimodal microscale mechanical mapping of cancer cells in complex microenvironments,” *Biophys J*, vol. 121, no. 19, pp. 3586–3599, Oct. 2022, doi: 10.1016/j.bpj.2022.09.002.
- [44] Y. A. Ayala *et al.*, “Rheological properties of cells measured by optical tweezers,” *BMC Biophys*, vol. 9, no. 1, p. 5, Dec. 2016, doi: 10.1186/s13628-016-0031-4.
- [45] C. Aermes, A. Hayn, T. Fischer, and C. T. Mierke, “Environmentally controlled magnetic nano-tweezer for living cells and extracellular matrices,” *Sci Rep*, vol. 10, no. 1, p. 13453, Aug. 2020, doi: 10.1038/s41598-020-70428-w.
- [46] T. Mammoto and D. E. Ingber, “Mechanical control of tissue and organ development,” *Development*, vol. 137, no. 9, pp. 1407–1420, May 2010, doi: 10.1242/dev.024166.
- [47] R. Kalluri and M. Zeisberg, “Fibroblasts in cancer,” *Nat Rev Cancer*, vol. 6, no. 5, pp. 392–401, May 2006, doi: 10.1038/nrc1877.
- [48] P. A. Janmey, D. A. Fletcher, and C. A. Reinhart-King, “Stiffness Sensing by Cells,” *Physiol Rev*, vol. 100, no. 2, pp. 695–724, Apr. 2020, doi: 10.1152/physrev.00013.2019.
- [49] E. Takai, K. D. Costa, A. Shaheen, C. T. Hung, and X. E. Guo, “Osteoblast Elastic Modulus Measured by Atomic Force Microscopy Is Substrate Dependent,” *Ann Biomed Eng*, vol. 33, no. 7, pp. 963–971, Jul. 2005, doi: 10.1007/s10439-005-3555-3.
- [50] D. Docheva, D. Padula, M. Schieker, and H. Clausen-Schaumann, “Effect of collagen I and fibronectin on the adhesion, elasticity and cytoskeletal organization of prostate cancer cells,” *Biochem Biophys Res Commun*, vol. 402, no. 2, pp. 361–366, Nov. 2010, doi: 10.1016/j.bbrc.2010.10.034.
- [51] M. C. Lampi and C. A. Reinhart-King, “Targeting extracellular matrix stiffness to attenuate disease: From molecular mechanisms to clinical trials,” *Sci Transl Med*, vol. 10, no. 422, Jan. 2018, doi: 10.1126/scitranslmed.aao0475.
- [52] D. P. Jones, W. Hanna, G. M. Cramer, and J. P. Celli, “In situ measurement of ECM rheology and microheterogeneity in embedded and overlaid 3D pancreatic tumor stroma co-cultures via passive particle tracking,” *J Innov Opt Health Sci*, vol. 10, no. 06, p. 1742003, Nov. 2017, doi: 10.1142/S1793545817420032.
- [53] P. Lu, K. Takai, V. M. Weaver, and Z. Werb, “Extracellular Matrix Degradation and Remodeling in Development and Disease,” *Cold Spring Harb Perspect Biol*, vol. 3, no. 12, pp. a005058–a005058, Dec. 2011, doi: 10.1101/cshperspect.a005058.
- [54] N. Merchant *et al.*, “Matrix metalloproteinases: their functional role in lung cancer,” *Carcinogenesis*, vol. 38, no. 8, pp. 766–780, Aug. 2017, doi: 10.1093/carcin/bgx063.
- [55] M. S. Hall *et al.*, “Fibrous nonlinear elasticity enables positive mechanical feedback between cells and ECMs,” *Proceedings of the National Academy of Sciences*, vol. 113, no. 49, pp. 14043–14048, Dec. 2016, doi: 10.1073/pnas.1613058113.
- [56] M. Georgiadou *et al.*, “AMPK negatively regulates tensin-dependent integrin activity,” *Journal of Cell Biology*, vol. 216, no. 4, pp. 1107–1121, Apr. 2017, doi: 10.1083/jcb.201609066.
- [57] R. Baghban *et al.*, “Tumor microenvironment complexity and therapeutic implications at a glance,” *Cell Communication and Signaling*, vol. 18, no. 1, p. 59, Dec. 2020, doi: 10.1186/s12964-020-0530-4.
- [58] K. R. Levental *et al.*, “Matrix Crosslinking Forces Tumor Progression by Enhancing Integrin Signaling,” *Cell*, vol. 139, no. 5, pp. 891–906, 2009, doi: 10.1016/j.cell.2009.10.027.
- [59] F. J. Sulzmaier, C. Jean, and D. D. Schlaepfer, “FAK in cancer: mechanistic findings and clinical applications,” *Nat Rev Cancer*, vol. 14, no. 9, pp. 598–610, Sep. 2014, doi: 10.1038/nrc3792.
- [60] J. A. Dombroski, J. M. Hope, N. S. Sarna, and M. R. King, “Channeling the Force: Piezo1 Mechanotransduction in Cancer Metastasis,” *Cells*, vol. 10, no. 11, p. 2815, Oct. 2021, doi: 10.3390/cells10112815.
- [61] O. Maller *et al.*, “Tumour-associated macrophages drive stromal cell-dependent collagen crosslinking and stiffening to promote breast cancer aggression,” *Nat Mater*, vol. 20, no. 4, pp. 548–559, Apr. 2021, doi: 10.1038/s41563-020-00849-5.

- [62] D. E. Ingber, “Tensegrity I. Cell structure and hierarchical systems biology,” *J Cell Sci*, vol. 116, no. 7, pp. 1157–1173, Apr. 2003, doi: 10.1242/jcs.00359.
- [63] F. H. Silver, J. W. Freeman, and G. P. Seehra, “Collagen self-assembly and the development of tendon mechanical properties,” *J Biomech*, vol. 36, no. 10, pp. 1529–1553, Oct. 2003, doi: 10.1016/S0021-9290(03)00135-0.
- [64] P. A. Janmey and R. T. Miller, “Mechanisms of mechanical signaling in development and disease,” *J Cell Sci*, vol. 124, no. 1, pp. 9–18, Jan. 2011, doi: 10.1242/jcs.071001.
- [65] B. Depalle, Z. Qin, S. J. Shefelbine, and M. J. Buehler, “Influence of cross-link structure, density and mechanical properties in the mesoscale deformation mechanisms of collagen fibrils,” *J Mech Behav Biomed Mater*, vol. 52, pp. 1–13, Dec. 2015, doi: 10.1016/j.jmbbm.2014.07.008.
- [66] A. Nicolas-Boluda *et al.*, “Tumor stiffening reversion through collagen crosslinking inhibition improves T cell migration and anti-PD-1 treatment,” *Elife*, vol. 10, Jun. 2021, doi: 10.7554/eLife.58688.
- [67] W. Hiesinger *et al.*, “Myocardial tissue elastic properties determined by atomic force microscopy after stromal cell-derived factor 1 $\alpha$  angiogenic therapy for acute myocardial infarction in a murine model,” *J Thorac Cardiovasc Surg*, vol. 143, no. 4, pp. 962–966, Apr. 2012, doi: 10.1016/j.jtcvs.2011.12.028.
- [68] J. K. Mouw, G. Ou, and V. M. Weaver, “Extracellular matrix assembly: a multiscale deconstruction,” *Nat Rev Mol Cell Biol*, vol. 15, no. 12, pp. 771–785, Dec. 2014, doi: 10.1038/nrm3902.
- [69] C. F. Guimarães, L. Gasperini, A. P. Marques, and R. L. Reis, “The stiffness of living tissues and its implications for tissue engineering,” *Nature Reviews Materials*, vol. 5, no. 5. Nature Research, pp. 351–370, May 01, 2020. doi: 10.1038/s41578-019-0169-1.
- [70] N. Bouchonville, M. Meyer, C. Gaude, E. Gay, D. Ratel, and A. Nicolas, “AFM mapping of the elastic properties of brain tissue reveals kPa  $\mu\text{m}^{-1}$  gradients of rigidity,” *Soft Matter*, vol. 12, no. 29, pp. 6232–6239, 2016, doi: 10.1039/c6sm00582a.
- [71] A. F. Christ *et al.*, “Mechanical difference between white and gray matter in the rat cerebellum measured by scanning force microscopy,” *J Biomech*, vol. 43, no. 15, pp. 2986–2992, Nov. 2010, doi: 10.1016/j.jbiomech.2010.07.002.
- [72] S. Abuhattum *et al.*, “Adipose cells and tissues soften with lipid accumulation while in diabetes adipose tissue stiffens,” *Sci Rep*, vol. 12, no. 1, p. 10325, Jun. 2022, doi: 10.1038/s41598-022-13324-9.
- [73] M. Bontempi, F. Salamanna, R. Capozza, A. Visani, M. Fini, and A. Gambardella, “Nanomechanical Mapping of Hard Tissues by Atomic Force Microscopy: An Application to Cortical Bone,” *Materials*, vol. 15, no. 21, p. 7512, Oct. 2022, doi: 10.3390/ma15217512.
- [74] S. Ojha, J. Pribyl, S. Klimovic, D. Hadraba, M. Jirouskova, and M. Gregor, “Measurement of Liver Stiffness Using Atomic Force Microscopy Coupled with Polarization Microscopy,” *Journal of Visualized Experiments*, no. 185, Jul. 2022, doi: 10.3791/63974.
- [75] M. Kammoun *et al.*, “Development of a novel multiphysical approach for the characterization of mechanical properties of musculotendinous tissues,” *Sci Rep*, vol. 9, no. 1, p. 7733, May 2019, doi: 10.1038/s41598-019-44053-1.
- [76] H. K. Graham, J. C. McConnell, G. Limbert, and M. J. Sherratt, “How stiff is skin?,” *Exp Dermatol*, vol. 28, pp. 4–9, Feb. 2019, doi: 10.1111/exd.13826.
- [77] J. Crest, A. Diz-Muñoz, D.-Y. Chen, D. A. Fletcher, and D. Bilder, “Organ sculpting by patterned extracellular matrix stiffness,” *Elife*, vol. 6, Jun. 2017, doi: 10.7554/eLife.24958.
- [78] H. Sung *et al.*, “Global Cancer Statistics 2020: GLOBOCAN Estimates of Incidence and Mortality Worldwide for 36 Cancers in 185 Countries,” *CA Cancer J Clin*, vol. 71, no. 3, pp. 209–249, May 2021, doi: 10.3322/caac.21660.
- [79] F. Bray, J. Ferlay, I. Soerjomataram, R. L. Siegel, L. A. Torre, and A. Jemal, “Global cancer statistics 2018: GLOBOCAN estimates of incidence and mortality worldwide for 36 cancers in 185 countries,” *CA Cancer J Clin*, vol. 68, no. 6, pp. 394–424, Nov. 2018, doi: 10.3322/caac.21492.
- [80] R. Peto, A. D. Lopez, J. Boreham, and M. Thun, “MORTALITY FROM SMOKING IN DEVELOPED COUNTRIES 1950–2000 (2nd edition, revised June 2006: www.deathsfromsmoking.net),” 2006. [Online]. Available: www.deathsfromsmoking.net

- [81] A. Jemal *et al.*, “Annual report to the nation on the status of cancer, 1975-2005, featuring trends in lung cancer, tobacco use, and tobacco control,” *J Natl Cancer Inst*, vol. 100, no. 23, pp. 1672–1694, Dec. 2008, doi: 10.1093/jnci/djn389.
- [82] W. K. Lam, N. W. White, and M. M. Chan-Yeung, “Lung cancer epidemiology and risk factors in Asia and Africa,” 2004.
- [83] Y. Zhang *et al.*, “International trends in lung cancer incidence from 1973 to 2007,” *Cancer Med*, vol. 7, no. 4, pp. 1479–1489, Apr. 2018, doi: 10.1002/cam4.1359.
- [84] D. E. Midthun, “Early diagnosis of lung cancer,” *F1000Prime Rep*, vol. 5, Apr. 2013, doi: 10.12703/P5-12.
- [85] INCA Instituto Nacional de Cancer José Alencar Gomes da Silva, *ABC do câncer: abordagens básicas para o controle do câncer*. 2018. [Online]. Available: [www.inca.gov.br](http://www.inca.gov.br)
- [86] L. Jacob, M. Freyn, M. Kalder, K. Dinas, and K. Kostev, “Impact of tobacco smoking on the risk of developing 25 different cancers in the UK: a retrospective study of 422,010 patients followed for up to 30 years,” *Oncotarget*, vol. 9, no. 25, pp. 17420–17429, 2018, [Online]. Available: [www.oncotarget.com](http://www.oncotarget.com)
- [87] A. Agudo *et al.*, “Impact of cigarette smoking on cancer risk in the European prospective investigation into cancer and nutrition study,” *J Clin Oncol*, vol. 30, no. 36, pp. 4550–4557, Dec. 2012, doi: 10.1200/JCO.2011.41.0183.
- [88] M. J. Thun, S. J. Henley, D. Burns, A. Jemal, T. G. Shanks, and E. E. Calle, “Lung cancer death rates in lifelong nonsmokers,” *J Natl Cancer Inst*, vol. 98, no. 10, pp. 691–699, May 2006, doi: 10.1093/JNCI/DJJ187.
- [89] J. M. Samet *et al.*, “Lung Cancer In Never Smokers: Clinical Epidemiology And Environmental Risk Factors,” *Clin Cancer Res*, vol. 15, no. 18, p. 5626, Sep. 2009, doi: 10.1158/1078-0432.CCR-09-0376.
- [90] M. Zamboni, “Câncer do Pulmão e DPOC Lung Cancer in COPD,” 2013.
- [91] E. L. Leite, S. C. S. Pinto, and G. L. Pilatti, “Relação bidirecional entre doença periodontal e doença pulmonar obstrutiva crônica: revisão de literatura,” *Periodontia*, pp. 29–35, 2016.
- [92] T. Cascone, K. A. Gold, and B. S. Glisson, “Small Cell Carcinoma of the Lung,” in *The MD Anderson Manual of Medical Oncology*, Third. New York: McGraw-Hill Education, 2016, pp. 323–342.
- [93] G. D. Goss and J. N. Spaans, “Epidermal Growth Factor Receptor Inhibition in the Management of Squamous Cell Carcinoma of the Lung,” *Oncologist*, vol. 21, no. 2, pp. 205–213, Feb. 2016, doi: 10.1634/theoncologist.2015-0209.
- [94] R. Siegel, D. Naishadham, and A. Jemal, “Cancer statistics, 2012,” *CA Cancer J Clin*, vol. 62, no. 1, pp. 10–29, Jan. 2012, doi: 10.3322/caac.20138.
- [95] C. S. Dela Cruz, L. T. Tanoue, and R. A. Matthay, “Lung Cancer: Epidemiology, Etiology, and Prevention,” *Clinics in Chest Medicine*, vol. 32, no. 4, pp. 605–644, Dec. 2011. doi: 10.1016/j.ccm.2011.09.001.
- [96] C. Bica-Pop, R. Cojocneanu-Petric, L. Magdo, L. Raduly, D. Gulei, and I. Berindan-Neagoe, “Overview upon miR-21 in lung cancer: focus on NSCLC,” *Cellular and Molecular Life Sciences*, vol. 75, no. 19, pp. 3539–3551, Oct. 2018, doi: 10.1007/s00018-018-2877-x.
- [97] C.-Y. Huang, H.-Y. Huang, M. D. Forrest, Y.-R. Pan, W.-J. Wu, and H.-M. Chen, “Inhibition Effect of a Custom Peptide on Lung Tumors,” *PLoS One*, vol. 9, no. 10, p. e109174, Oct. 2014, doi: 10.1371/journal.pone.0109174.
- [98] World Cancer Research Fund International, “Diet, Nutrition, Physical Activity and Cancer: a Global Perspective - The Third Expert Report,” London, 2018.
- [99] B. Pesch *et al.*, “Cigarette smoking and lung cancer-relative risk estimates for the major histological types from a pooled analysis of case-control studies,” *Int J Cancer*, vol. 131, no. 5, pp. 1210–1219, Sep. 2012, doi: 10.1002/ijc.27339.
- [100] S. S. Devesa, F. Bray, A. P. Vizcaino, and D. M. Parkin, “International lung cancer trends by histologic type: Male:Female differences diminishing and adenocarcinoma rates rising,” *Int J Cancer*, vol. 117, no. 2, pp. 294–299, Nov. 2005, doi: 10.1002/ijc.21183.

- [101] J. Lortet-Tieulent, I. Soerjomataram, J. Ferlay, M. Rutherford, E. Weiderpass, and F. Bray, “International trends in lung cancer incidence by histological subtype: Adenocarcinoma stabilizing in men but still increasing in women,” *Lung Cancer*, vol. 84, no. 1, pp. 13–22, Apr. 2014, doi: 10.1016/j.lungcan.2014.01.009.
- [102] M. L. G. Janssen-Heijnen and J.-W. W. Coebergh, “Trends in incidence and prognosis of the histological subtypes of lung cancer in North America, Australia, New Zealand and Europe,” *Lung Cancer*, vol. 31, no. 2–3, pp. 123–137, Mar. 2001, doi: 10.1016/S0169-5002(00)00197-5.
- [103] P. Katira, M. H. Zaman, and R. T. Bonnecaze, “How changes in cell mechanical properties induce cancerous behavior,” *Phys Rev Lett*, vol. 108, no. 2, Jan. 2012, doi: 10.1103/PhysRevLett.108.028103.
- [104] J. E. Visvader, “Cells of origin in cancer,” *Nature*, vol. 469, no. 7330, pp. 314–322, Jan. 2011, doi: 10.1038/nature09781.
- [105] V. A. Bennett, E. A. Davies, R. H. Jack, V. Mak, and H. Møller, “Histological subtype of lung cancer in relation to socio-economic deprivation in South East England,” *BMC Cancer*, vol. 8, no. 1, p. 139, Dec. 2008, doi: 10.1186/1471-2407-8-139.
- [106] T. Yoshida, G. Zhang, and E. B. Haura, “Targeting epidermal growth factor receptor: Central signaling kinase in lung cancer,” *Biochem Pharmacol*, vol. 80, no. 5, pp. 613–623, Sep. 2010, doi: 10.1016/j.bcp.2010.05.014.
- [107] Z.-M. Yang, X.-P. Ding, L. Pen, L. Mei, and T. Liu, “Analysis of CEA Expression and EGFR Mutation Status in Non-small Cell Lung Cancers,” *Asian Pacific Journal of Cancer Prevention*, vol. 15, no. 8, pp. 3451–3455, Apr. 2014, doi: 10.7314/APJCP.2014.15.8.3451.
- [108] G. L. Lopes, E. F. de Q. Vattimo, and G. de Castro Junior, “Identifying activating mutations in the EGFR gene: prognostic and therapeutic implications in non-small cell lung cancer,” *Jornal Brasileiro de Pneumologia*, vol. 41, no. 4, pp. 365–375, Aug. 2015, doi: 10.1590/S1806-37132015000004531.
- [109] B. J. Solomon *et al.*, “First-Line Crizotinib versus Chemotherapy in *ALK* -Positive Lung Cancer,” *New England Journal of Medicine*, vol. 371, no. 23, pp. 2167–2177, Dec. 2014, doi: 10.1056/NEJMoa1408440.
- [110] J. Downward, “Targeting RAS signalling pathways in cancer therapy,” *Nat Rev Cancer*, vol. 3, no. 1, pp. 11–22, Jan. 2003, doi: 10.1038/nrc969.
- [111] B. Alberts, A. Johnson, and J. Lewis, *Molecular Biology of The Cell*, Sixth Edition. New York: Garland Science, 2015.
- [112] N. Karimi and S. J. Moghaddam, “KRAS-Mutant Lung Cancer: Targeting Molecular and Immunologic Pathways, Therapeutic Advantages and Restrictions,” *Cells*, vol. 12, no. 5, p. 749, Feb. 2023, doi: 10.3390/cells12050749.
- [113] P. J. Roberts and T. E. Stinchcombe, “KRAS mutation: Should we test for it, and does it matter,” *Journal of Clinical Oncology*, vol. 31, no. 8, pp. 1112–1121, Mar. 10, 2013. doi: 10.1200/JCO.2012.43.0454.
- [114] A. Daga, A. Ansari, S. Patel, S. Mirza, R. Rawal, and V. Umrana, “Current Drugs and Drug Targets in Non-Small Cell Lung Cancer: Limitations and Opportunities,” *Asian Pacific Journal of Cancer Prevention*, vol. 16, no. 10, pp. 4147–4156, Jun. 2015, doi: 10.7314/APJCP.2015.16.10.4147.
- [115] J. V. Aredo and S. K. Padda, “Management of KRAS-Mutant Non-Small Cell Lung Cancer in the Era of Precision Medicine,” *Current Treatment Options in Oncology*, vol. 19, no. 8. Springer New York LLC, Aug. 01, 2018. doi: 10.1007/s11864-018-0557-6.
- [116] J. M. Ostrem, U. Peters, M. L. Sos, J. A. Wells, and K. M. Shokat, “K-Ras(G12C) inhibitors allosterically control GTP affinity and effector interactions,” *Nature*, vol. 503, no. 7477, pp. 548–551, Nov. 2013, doi: 10.1038/nature12796.
- [117] G. Zimmermann *et al.*, “Small molecule inhibition of the KRAS–PDE $\delta$  interaction impairs oncogenic KRAS signalling,” *Nature*, vol. 497, no. 7451, pp. 638–642, May 2013, doi: 10.1038/nature12205.
- [118] A. Singh *et al.*, “De novo lipogenesis represents a therapeutic target in mutant Kras non-small cell lung cancer,” *The FASEB Journal*, vol. 32, no. 12, pp. 7018–7027, Sep. 2018, doi: 10.1096/fj.201800204.
- [119] Z.-Y. Dong *et al.*, “Potential Predictive Value of *TP53* and *KRAS* Mutation Status for Response to PD-1 Blockade Immunotherapy in Lung Adenocarcinoma,” *Clinical Cancer Research*, vol. 23, no. 12, pp. 3012–3024, Jun. 2017, doi: 10.1158/1078-0432.CCR-16-2554.

- [120] P. Liu, Y. Wang, and X. Li, “Targeting the untargetable KRAS in cancer therapy,” *Acta Pharm Sin B*, vol. 9, no. 5, pp. 871–879, Sep. 2019, doi: 10.1016/j.apsb.2019.03.002.
- [121] R. G. Wells, “The role of matrix stiffness in regulating cell behavior,” *Hepatology*, vol. 47, no. 4, pp. 1394–1400, Jan. 2008, doi: 10.1002/hep.22193.
- [122] A. Fritsch *et al.*, “Are biomechanical changes necessary for tumour progression?,” *Nat Phys*, vol. 6, no. 10, pp. 730–732, Oct. 2010, doi: 10.1038/nphys1800.
- [123] T. Hampton, “Lessening of Cell Stiffness Might Serve as New Biomarker for Malignancy,” *JAMA*, vol. 299, no. 3, Jan. 2008, doi: 10.1001/jama.299.3.276.
- [124] A. Torsvik *et al.*, “U-251 revisited: genetic drift and phenotypic consequences of long-term cultures of glioblastoma cells,” *Cancer Med*, vol. 3, no. 4, pp. 812–824, Aug. 2014, doi: 10.1002/cam4.219.
- [125] F. Mouriaux *et al.*, “Effects of Long-term Serial Passaging on the Characteristics and Properties of Cell Lines Derived From Uveal Melanoma Primary Tumors,” *Investigative Ophthalmology & Visual Science*, vol. 57, no. 13, p. 5288, Oct. 2016, doi: 10.1167/iovs.16-19317.
- [126] H. Liao *et al.*, “Effects of long-term serial cell passaging on cell spreading, migration, and cell-surface ultrastructures of cultured vascular endothelial cells,” *Cytotechnology*, vol. 66, no. 2, pp. 229–238, Mar. 2014, doi: 10.1007/s10616-013-9560-8.
- [127] K. Cheng *et al.*, “High Passage MIN6 Cells Have Impaired Insulin Secretion with Impaired Glucose and Lipid Oxidation,” *PLoS One*, vol. 7, no. 7, p. e40868, Jul. 2012, doi: 10.1371/journal.pone.0040868.
- [128] H. Gu, X.-Y. Wu, R.-T. Fan, X. Wang, Y.-Z. Guo, and R. Wang, “Side population cells from long-term passage non-small cell lung cancer cells display loss of cancer stem cell-like properties and chemoradioresistance,” *Oncol Lett*, vol. 12, no. 4, pp. 2886–2893, Oct. 2016, doi: 10.3892/ol.2016.4934.
- [129] P. Hughes, D. Marshall, Y. Reid, H. Parkes, and C. Gelber, “The costs of using unauthenticated, over-passaged cell lines: how much more data do we need?,” *Biotechniques*, vol. 43, no. 5, pp. 575–586, Nov. 2007, doi: 10.2144/000112598.
- [130] A. J. Engler, M. A. Griffin, S. Sen, C. G. Bönnemann, H. L. Sweeney, and D. E. Discher, “Myotubes differentiate optimally on substrates with tissue-like stiffness,” *Journal of Cell Biology*, vol. 166, no. 6, pp. 877–887, Sep. 2004, doi: 10.1083/jcb.200405004.
- [131] S. K. Kureel *et al.*, “Soft substrate maintains proliferative and adipogenic differentiation potential of human mesenchymal stem cells on long-term expansion by delaying senescence,” *Biol Open*, Jan. 2019, doi: 10.1242/bio.039453.
- [132] L. Zsákai *et al.*, “Targeted drug combination therapy design based on driver genes,” *Oncotarget*, vol. 10, no. 51, pp. 5255–5266, Sep. 2019, doi: 10.18632/oncotarget.26985.
- [133] D. T. Butcher, T. Alliston, and V. M. Weaver, “A tense situation: Forcing tumour progression,” *Nature Reviews Cancer*, vol. 9, no. 2, pp. 108–122, Feb. 2009, doi: 10.1038/nrc2544.
- [134] L. Martinez-Vidal *et al.*, “Causal contributors to tissue stiffness and clinical relevance in urology,” *Commun Biol*, vol. 4, no. 1, p. 1011, Aug. 2021, doi: 10.1038/s42003-021-02539-7.
- [135] E. Song, Y. Huang, N. Huang, Y. Mei, X. Yu, and J. A. Rogers, “Recent advances in microsystem approaches for mechanical characterization of soft biological tissues,” *Microsystems and Nanoengineering*, vol. 8, no. 1, Springer Nature, Dec. 01, 2022, doi: 10.1038/s41378-022-00412-z.
- [136] U. Schwarz, “Soft matters in cell adhesion: rigidity sensing on soft elastic substrates,” *Soft Matter*, vol. 3, no. 3, pp. 263–266, 2007, doi: 10.1039/B606409D.
- [137] G. Binnig, C. F. Quate, and Ch. Gerber, “Atomic Force Microscope,” *Phys Rev Lett*, vol. 56, no. 9, pp. 930–933, Mar. 1986, doi: 10.1103/PhysRevLett.56.930.
- [138] D. J. Müller *et al.*, “Atomic Force Microscopy-Based Force Spectroscopy and Multiparametric Imaging of Biomolecular and Cellular Systems,” *Chemical Reviews*, vol. 121, no. 19, American Chemical Society, pp. 11701–11725, Oct. 13, 2021, doi: 10.1021/acs.chemrev.0c00617.
- [139] J. M. Black *et al.*, “Fundamental aspects of electric double layer force-distance measurements at liquid-solid interfaces using atomic force microscopy,” *Sci Rep*, vol. 6, no. 1, p. 32389, Sep. 2016, doi: 10.1038/srep32389.

- [140] J. Peng, J. Guo, R. Ma, and Y. Jiang, “Water-solid interfaces probed by high-resolution atomic force microscopy,” *Surf Sci Rep*, vol. 77, no. 1, p. 100549, Mar. 2022, doi: 10.1016/j.surfrep.2021.100549.
- [141] D. Alsteens, H. E. Gaub, R. Newton, M. Pfreundschuh, C. Gerber, and D. J. Müller, “Atomic force microscopy-based characterization and design of biointerfaces,” *Nature Reviews Materials*, vol. 2, no. 5. Nature Publishing Group, Mar. 14, 2017. doi: 10.1038/natrevmats.2017.8.
- [142] M. Krieg *et al.*, “Atomic force microscopy-based mechanobiology,” *Nature Reviews Physics*, vol. 1, no. 1. Springer Nature, pp. 41–57, Jan. 01, 2019. doi: 10.1038/s42254-018-0001-7.
- [143] S. V. Kontomaris and A. Stylianou, “Atomic force microscopy for university students: Applications in biomaterials,” *European Journal of Physics*, vol. 38, no. 3. Institute of Physics Publishing, Feb. 22, 2017. doi: 10.1088/1361-6404/aa5cd6.
- [144] M. Lu, S. Huang, X. Yang, L. Yang, and R. Mao, “Semianalytical Solution for the Deformation of an Elastic Layer under an Axisymmetrically Distributed Power-Form Load: Application to Fluid-Jet-Induced Indentation of Biological Soft Tissues,” *Biomed Res Int*, vol. 2017, pp. 1–10, 2017, doi: 10.1155/2017/9842037.
- [145] N. Bouchonville and A. Nicolas, “Quantification of the elastic properties of soft and sticky materials using AFM,” in *Methods in Molecular Biology*, Humana Press Inc., 2019, pp. 281–290. doi: 10.1007/978-1-4939-8894-5\_16.
- [146] D. C. Lin, E. K. Dimitriadis, and F. Horkay, “Robust strategies for automated AFM force curve analysis - II: Adhesion-influenced indentation of soft, elastic materials,” *J Biomech Eng*, vol. 129, no. 6, pp. 904–912, Dec. 2007, doi: 10.1115/1.2800826.
- [147] K. L. Johnson, K. Kendall, and A. D. Roberts, “Surface energy and the contact of elastic solids,” *Proceedings of the Royal Society of London. A. Mathematical and Physical Sciences*, vol. 324, no. 1558, pp. 301–313, Sep. 1971, doi: 10.1098/rspa.1971.0141.
- [148] B. V. Derjaguin, V. M. Muller, and Yu. P. Toporov, “Effect of contact deformations on the adhesion of particles,” *J Colloid Interface Sci*, vol. 53, no. 2, pp. 314–326, Nov. 1975, doi: 10.1016/0021-9797(75)90018-1.
- [149] D. Tabor, “Surface forces and surface interactions,” *J Colloid Interface Sci*, vol. 58, no. 1, pp. 2–13, Jan. 1977, doi: 10.1016/0021-9797(77)90366-6.
- [150] V. M. Muller, V. S. Yushchenko, and B. V. Derjaguin, “On the Influence of Molecular Forces on the Deformation of an Elastic Sphere and Its Sticking to a Rigid Plane,” 1980.
- [151] J. A. Greenwood, “Adhesion of elastic spheres,” *Proceedings of the Royal Society of London. Series A: Mathematical, Physical and Engineering Sciences*, vol. 453, no. 1961, pp. 1277–1297, Jun. 1997, doi: 10.1098/rspa.1997.0070.
- [152] D. Maugis, “Adhesion of spheres: The JKR-DMT transition using a dugdale model,” *J Colloid Interface Sci*, vol. 150, no. 1, pp. 243–269, Apr. 1992, doi: 10.1016/0021-9797(92)90285-T.
- [153] R. W. Carpick, D. F. Ogletree, and M. Salmeron, “A General Equation for Fitting Contact Area and Friction vs Load Measurements,” *J Colloid Interface Sci*, vol. 211, no. 2, pp. 395–400, Mar. 1999, doi: 10.1006/jcis.1998.6027.
- [154] O. Piétremont and M. Troyon, “General equations describing elastic indentation depth and normal contact stiffness versus load,” *J Colloid Interface Sci*, vol. 226, no. 1, pp. 166–171, Jun. 2000, doi: 10.1006/jcis.2000.6808.
- [155] R. G. Horn, J. N. Israelachvili, and F. Pribac, “Measurement of the deformation and adhesion of solids in contact,” *J Colloid Interface Sci*, vol. 115, no. 2, pp. 480–492, Feb. 1987, doi: 10.1016/0021-9797(87)90065-8.
- [156] D. C. Lin, E. K. Dimitriadis, and F. Horkay, “Robust strategies for automated AFM force curve analysis - I. Non-adhesive indentation of soft, inhomogeneous materials,” *J Biomech Eng*, vol. 129, no. 3, pp. 430–440, Jun. 2007, doi: 10.1115/1.2720924.
- [157] M. Ciavarella, J. Joe, A. Papangelo, and J. R. Barber, “The role of adhesion in contact mechanics,” *J R Soc Interface*, vol. 16, no. 151, p. 20180738, Feb. 2019, doi: 10.1098/rsif.2018.0738.
- [158] L. H. Ling, S. M. Rogers, V. Tay, G. V. Limmon, Z. Dahai, and K. Rogers, “Comparison of Various Tissue-Preparation Techniques for Cryosectioning of Frozen Mouse Tissues,” *J Histotechnol*, vol. 32, no. 4, pp. 186–189, Dec. 2009, doi: 10.1179/his.2009.32.4.186.

- [159] G. Sridharan and A. Shankar, "Toluidine blue: A review of its chemistry and clinical utility," *Journal of Oral and Maxillofacial Pathology*, vol. 16, no. 2, p. 251, 2012, doi: 10.4103/0973-029X.99081.
- [160] J. P. Butler, M. Nakamura, H. Sasaki, T. Sasaki, and T. Takishima, "Poissons' Ratio of Lung Parenchyma and Parenchyma! Interaction with Bronchi," 1986.
- [161] J. L. Hutter and J. Bechhoefer, "Calibration of atomic-force microscope tips," *Review of Scientific Instruments*, vol. 64, no. 7, pp. 1868–1873, Jul. 1993, doi: 10.1063/1.1143970.
- [162] M. L. Oyen, "Nanoindentation of hydrated materials and tissues," *Curr Opin Solid State Mater Sci*, vol. 19, no. 6, pp. 317–323, Dec. 2015, doi: 10.1016/j.cossms.2015.03.001.
- [163] C. S. Chen, M. Mrksich, S. Huang, G. M. Whitesides, and D. E. Ingber, "Geometric control of cell life and death," *Science (1979)*, vol. 276, no. 5317, pp. 1425–1428, May 1997, doi: 10.1126/science.276.5317.1425.
- [164] T. Lecuit and P.-F. Lenne, "Cell surface mechanics and the control of cell shape, tissue patterns and morphogenesis," *Nat Rev Mol Cell Biol*, vol. 8, no. 8, pp. 633–644, Aug. 2007, doi: 10.1038/nrm2222.
- [165] K. H. Vining and D. J. Mooney, "Mechanical forces direct stem cell behaviour in development and regeneration," *Nat Rev Mol Cell Biol*, vol. 18, no. 12, pp. 728–742, Dec. 2017, doi: 10.1038/nrm.2017.108.
- [166] A. Pathak and S. Kumar, "Independent regulation of tumor cell migration by matrix stiffness and confinement," *Proceedings of the National Academy of Sciences*, vol. 109, no. 26, pp. 10334–10339, Jun. 2012, doi: 10.1073/pnas.1118073109.
- [167] B. Geiger, J. P. Spatz, and A. D. Bershadsky, "Environmental sensing through focal adhesions," *Nat Rev Mol Cell Biol*, vol. 10, no. 1, pp. 21–33, Jan. 2009, doi: 10.1038/nrm2593.
- [168] C. L. Essmann *et al.*, "Mechanical properties measured by atomic force microscopy define health biomarkers in ageing *C. elegans*," *Nat Commun*, vol. 11, no. 1, p. 1043, Feb. 2020, doi: 10.1038/s41467-020-14785-0.
- [169] A. J. Engler, S. Sen, H. L. Sweeney, and D. E. Discher, "Matrix Elasticity Directs Stem Cell Lineage Specification," *Cell*, vol. 126, no. 4, pp. 677–689, Aug. 2006, doi: 10.1016/j.cell.2006.06.044.
- [170] R. W. Tilghman *et al.*, "Matrix rigidity regulates cancer cell growth and cellular phenotype," *PLoS One*, vol. 5, no. 9, 2010, doi: 10.1371/journal.pone.0012905.
- [171] A. F. Pegoraro, P. Janmey, and D. A. Weitz, "Mechanical Properties of the Cytoskeleton and Cells," *Cold Spring Harb Perspect Biol*, vol. 9, no. 11, p. a022038, Nov. 2017, doi: 10.1101/cshperspect.a022038.
- [172] F.-S. Quan and K. S. Kim, "Medical applications of the intrinsic mechanical properties of single cells," *Acta Biochim Biophys Sin (Shanghai)*, vol. 48, no. 10, pp. 865–871, Oct. 2016, doi: 10.1093/abbs/gmw081.
- [173] D. Wirtz, K. Konstantopoulos, and P. C. Searson, "The physics of cancer: the role of physical interactions and mechanical forces in metastasis," *Nat Rev Cancer*, vol. 11, no. 7, pp. 512–522, Jul. 2011, doi: 10.1038/nrc3080.
- [174] M. Tian *et al.*, "The nanomechanical signature of liver cancer tissues and its molecular origin," *Nanoscale*, vol. 7, no. 30, pp. 12998–13010, Aug. 2015, doi: 10.1039/c5nr02192h.
- [175] V. Seewaldt, "ECM stiffness paves the way for tumor cells," *Nat Med*, vol. 20, no. 4, pp. 332–333, Apr. 2014, doi: 10.1038/nm.3523.
- [176] J. K. Mouw *et al.*, "Tissue mechanics modulate microRNA-dependent PTEN expression to regulate malignant progression," *Nat Med*, vol. 20, no. 4, pp. 360–367, 2014, doi: 10.1038/nm.3497.
- [177] H. Babahosseini, J. S. Strobl, and M. Agah, "Single cell metastatic phenotyping using pulsed nanomechanical indentations," *Nanotechnology*, vol. 26, no. 35, p. 354004, Sep. 2015, doi: 10.1088/0957-4484/26/35/354004.
- [178] S. E. Cross, Y. S. Jin, J. Rao, and J. K. Gimzewski, "Nanomechanical analysis of cells from cancer patients," *Nat Nanotechnol*, vol. 2, no. 12, pp. 780–783, 2007, doi: 10.1038/nnano.2007.388.
- [179] M. Plodinec *et al.*, "The nanomechanical signature of breast cancer," *Nat Nanotechnol*, vol. 7, no. 11, pp. 757–765, 2012, doi: 10.1038/nnano.2012.167.
- [180] G. N. Maksym and J. H. T. Bates, "A distributed nonlinear model of lung tissue elasticity," *J Appl Physiol*, vol. 82, no. 1, pp. 32–41, Jan. 1997, doi: 10.1152/jappl.1997.82.1.32.

- [181] B. Suki, S. Ito, D. Stamenović, K. R. Lutchen, and E. P. Ingenito, “Biomechanics of the lung parenchyma: critical roles of collagen and mechanical forces,” *J Appl Physiol*, vol. 98, no. 5, pp. 1892–1899, May 2005, doi: 10.1152/jappphysiol.01087.2004.
- [182] Z. Yuan *et al.*, “Extracellular matrix remodeling in tumor progression and immune escape: from mechanisms to treatments,” *Molecular Cancer*, vol. 22, no. 1. BioMed Central Ltd, Dec. 01, 2023. doi: 10.1186/s12943-023-01744-8.
- [183] A. L. Parker and T. R. Cox, “The Role of the ECM in Lung Cancer Dormancy and Outgrowth,” *Front Oncol*, vol. 10, Sep. 2020, doi: 10.3389/fonc.2020.01766.
- [184] V. Gkretsi, A. Stylianou, P. Papageorgis, C. Polydorou, and T. Stylianopoulos, “Remodeling Components of the Tumor Microenvironment to Enhance Cancer Therapy,” *Front Oncol*, vol. 5, Oct. 2015, doi: 10.3389/fonc.2015.00214.
- [185] S. Fang *et al.*, “Clinical significance and biological role of cancer-derived Type I collagen in lung and esophageal cancers,” *Thorac Cancer*, vol. 10, no. 2, pp. 277–288, Feb. 2019, doi: 10.1111/1759-7714.12947.
- [186] Y. Shen, T. Schmidt, and A. Diz-Muñoz, “Protocol on Tissue Preparation and Measurement of Tumor Stiffness in Primary and Metastatic Colorectal Cancer Samples with an Atomic Force Microscope,” *STAR Protoc*, vol. 1, no. 3, Dec. 2020, doi: 10.1016/j.xpro.2020.100167.
- [187] D. Sicard, A. J. Haak, K. M. Choi, A. R. Craig, L. E. Fredenburgh, and D. J. Tschumperlin, “Aging and anatomical variations in lung tissue stiffness,” *Am J Physiol Lung Cell Mol Physiol*, vol. 314, no. 6, pp. L946–L955, 2018, doi: 10.1152/ajplung.00415.2017.
- [188] S. R. Polio *et al.*, “Cross-platform mechanical characterization of lung tissue,” *PLoS One*, vol. 13, no. 10, pp. 1–17, 2018, doi: 10.1371/journal.pone.0204765.
- [189] F. Liu and D. J. Tschumperlin, “Micro-mechanical characterization of lung tissue using atomic force microscopy,” *J Vis Exp*, no. 54, 2011, doi: 10.3791/2911.
- [190] Z. I. Kalcioğlu, R. Mahmoodian, Y. Hu, Z. Suo, and K. J. Van Vliet, “From macro- to microscale poroelastic characterization of polymeric hydrogels via indentation,” *Soft Matter*, vol. 8, no. 12, pp. 3393–3398, Mar. 2012, doi: 10.1039/c2sm06825g.
- [191] E. Caló and V. V. Khutoryanskiy, “Biomedical applications of hydrogels: A review of patents and commercial products,” *European Polymer Journal*, vol. 65. Elsevier Ltd, pp. 252–267, 2015. doi: 10.1016/j.eurpolymj.2014.11.024.
- [192] F. M. Hecht, J. Rheinlaender, N. Schierbaum, W. H. Goldmann, B. Fabry, and T. E. Schäffer, “Imaging viscoelastic properties of live cells by AFM: power-law rheology on the nanoscale,” *Soft Matter*, vol. 11, no. 23, pp. 4584–4591, 2015, doi: 10.1039/C4SM02718C.
- [193] E. Moeendarbary *et al.*, “The cytoplasm of living cells behaves as a poroelastic material,” *Nat Mater*, vol. 12, no. 3, pp. 253–261, Mar. 2013, doi: 10.1038/nmat3517.
- [194] L. Deng *et al.*, “Fast and slow dynamics of the cytoskeleton,” *Nat Mater*, vol. 5, no. 8, pp. 636–640, Aug. 2006, doi: 10.1038/nmat1685.
- [195] S. P. Ramanathan, J. Helenius, M. P. Stewart, C. J. Cattin, A. A. Hyman, and D. J. Muller, “Cdk1-dependent mitotic enrichment of cortical myosin II promotes cell rounding against confinement,” *Nat Cell Biol*, vol. 17, no. 2, pp. 148–159, Feb. 2015, doi: 10.1038/ncb3098.
- [196] D. O. Asgeirsson, P. Oertle, M. Loparic, and M. Plodinec, “The Nanomechanical Signature of Tissues in Health and Disease,” in *Nanoscience and Nanotechnology for Human Health*, Weinheim, Germany: Wiley-VCH Verlag GmbH & Co. KGaA, 2016, pp. 209–240. doi: 10.1002/9783527692057.ch11.
- [197] B. Geiger, A. Bershadsky, R. Pankov, and K. M. Yamada, “Transmembrane crosstalk between the extracellular matrix and the cytoskeleton,” *Nat Rev Mol Cell Biol*, vol. 2, no. 11, pp. 793–805, Nov. 2001, doi: 10.1038/35099066.
- [198] A. Livne and B. Geiger, “The inner workings of stress fibers – from contractile machinery to focal adhesions and back,” *J Cell Sci*, vol. 129, no. 7, pp. 1293–1304, Apr. 2016, doi: 10.1242/jcs.180927.
- [199] F. Martino, A. R. Perestrelo, V. Vinarský, S. Pagliari, and G. Forte, “Cellular mechanotransduction: From tension to function,” *Frontiers in Physiology*, vol. 9, no. JUL. Frontiers Media S.A., Jul. 05, 2018. doi: 10.3389/fphys.2018.00824.



- [200] J. M. Goffin, P. Pittet, G. Csucs, J. W. Lussi, J.-J. Meister, and B. Hinz, “Focal adhesion size controls tension-dependent recruitment of  $\alpha$ -smooth muscle actin to stress fibers,” *Journal of Cell Biology*, vol. 172, no. 2, pp. 259–268, Jan. 2006, doi: 10.1083/jcb.200506179.
- [201] D. Sicard, L. E. Fredenburgh, and D. J. Tschumperlin, “Measured pulmonary arterial tissue stiffness is highly sensitive to AFM indenter dimensions,” *J Mech Behav Biomed Mater*, vol. 74, pp. 118–127, Oct. 2017, doi: 10.1016/j.jmbbm.2017.05.039.
- [202] E. A. Cavalcanti-Adam, A. Micoulet, J. Blümmel, J. Auernheimer, H. Kessler, and J. P. Spatz, “Lateral spacing of integrin ligands influences cell spreading and focal adhesion assembly,” *Eur J Cell Biol*, vol. 85, no. 3–4, pp. 219–224, Apr. 2006, doi: 10.1016/j.jcb.2005.09.011.
- [203] M. Meyer *et al.*, “The micro-mechanical signature of pituitary adenomas: new perspectives for the diagnosis and surgery,” 2020.
- [204] Y. Shen *et al.*, “Reduction of Liver Metastasis Stiffness Improves Response to Bevacizumab in Metastatic Colorectal Cancer,” *Cancer Cell*, vol. 37, no. 6, pp. 800–817.e7, Jun. 2020, doi: 10.1016/j.ccell.2020.05.005.
- [205] T. Fuhs *et al.*, “Rigid tumours contain soft cancer cells,” *Nat Phys*, vol. 18, no. 12, pp. 1510–1519, Dec. 2022, doi: 10.1038/s41567-022-01755-0.
- [206] A. S. Morr *et al.*, “Mechanical properties of murine hippocampal subregions investigated by atomic force microscopy and in vivo magnetic resonance elastography,” *Sci Rep*, vol. 12, no. 1, Dec. 2022, doi: 10.1038/s41598-022-21105-7.
- [207] M. Sonka, V. Hlavac, and R. Boyle, *Image Processing, Analysis and Machine Vision*. Boston, MA: Springer US, 1993. doi: 10.1007/978-1-4899-3216-7.
- [208] P. Singh, V. K. Gupta, and P. N. Hrisheekesha, “A Review on Shape based Descriptors for Image Retrieval,” *Int J Comput Appl*, vol. 125, no. 10, pp. 27–32, Sep. 2015, doi: 10.5120/ijca2015906043.
- [209] M. Peura and J. Iivarinen, “Efficiency of simple shape descriptors,” 1997.
- [210] Ming-Kuei Hu, “Visual pattern recognition by moment invariants,” *IEEE Trans Inf Theory*, vol. 8, no. 2, pp. 179–187, Feb. 1962, doi: 10.1109/TIT.1962.1057692.
- [211] V. Pence Delfino, T. Lettini, E. Vacca, F. Potente, P. Ragone, and R. Ricco, “Biological image analysis for microscopical diagnosis: The work-station S.A.M. (Shape Analytical Morphometry),” *Pathol Res Pract*, vol. 188, no. 4–5, pp. 587–592, Jun. 1992, doi: 10.1016/S0344-0338(11)80061-0.
- [212] D. C. Aziz and R. B. Barathur, “Quantitation and morphometric analysis of tumors by image analysis,” *J Cell Biochem Suppl*, 1994.
- [213] D. Zhang and G. Lu, “Review of shape representation and description techniques,” *Pattern Recognit*, vol. 37, no. 1, pp. 1–19, 2004, doi: 10.1016/j.patcog.2003.07.008.
- [214] A. Krizhevsky, I. Sutskever, and G. E. Hinton, “ImageNet Classification with Deep Convolutional Neural Networks,” 2012. [Online]. Available: <http://code.google.com/p/cuda-convnet/>
- [215] N. Otsu, “A Threshold Selection Method from Gray-Level Histograms,” *IEEE Trans Syst Man Cybern*, vol. 9, no. 1, pp. 62–66, Jan. 1979, doi: 10.1109/TSMC.1979.4310076.
- [216] M. A. Wirth, “Shape Analysis & Measurement,” 2004.
- [217] “Russ, John C - The Image processing handbook (2016, CRC Press LLC) - libgen.li”.
- [218] S. Sattari and M. Eskandari, “Characterizing the viscoelasticity of extra- and intra-parenchymal lung bronchi,” *J Mech Behav Biomed Mater*, vol. 110, p. 103824, Oct. 2020, doi: 10.1016/j.jmbbm.2020.103824.
- [219] G. Ciasca *et al.*, “Nano-mechanical signature of brain tumours,” *Nanoscale*, vol. 8, no. 47, pp. 19629–19643, Dec. 2016, doi: 10.1039/c6nr06840e.
- [220] A. Mgharbel *et al.*, “Cells on Hydrogels with Micron-Scaled Stiffness Patterns Demonstrate Local Stiffness Sensing,” *Nanomaterials*, vol. 12, no. 4, Feb. 2022, doi: 10.3390/nano12040648.
- [221] E. Limpert, W. A. Sthael, and Abbt Markus, “Log-normal Distributions across the Sciences: Keys and Clues,” *Bioscience*, vol. 51, no. 5, pp. 341–352, 2001, [Online]. Available: <http://stat.ethz.ch/vis/log-normal>

- [222] M. J. Paszek *et al.*, “Tensional homeostasis and the malignant phenotype,” *Cancer Cell*, vol. 8, no. 3, pp. 241–254, 2005, doi: 10.1016/j.ccr.2005.08.010.
- [223] I. Andreu *et al.*, “Heterogeneous micromechanical properties of the extracellular matrix in healthy and infarcted hearts,” *Acta Biomater*, vol. 10, no. 7, pp. 3235–3242, 2014, doi: 10.1016/j.actbio.2014.03.034.
- [224] J. Fenner, A. C. Stacer, F. Winterroth, T. D. Johnson, K. E. Luker, and G. D. Luker, “Macroscopic Stiffness of Breast Tumors Predicts Metastasis,” *Sci Rep*, vol. 4, no. 1, p. 5512, Jul. 2014, doi: 10.1038/srep05512.
- [225] B. M. Maccurtain, N. P. Quirke, S. D. Thorpe, and T. K. Gallagher, “Pancreatic ductal adenocarcinoma: Relating biomechanics and prognosis,” *Journal of Clinical Medicine*, vol. 10, no. 12. MDPI, Jun. 02, 2021. doi: 10.3390/jcm10122711.
- [226] S. Ishihara and H. Haga, “Matrix Stiffness Contributes to Cancer Progression by Regulating Transcription Factors,” *Cancers*, vol. 14, no. 4. MDPI, Feb. 01, 2022. doi: 10.3390/cancers14041049.
- [227] C. Yang *et al.*, “Spatially patterned matrix elasticity directs stem cell fate,” *Proc Natl Acad Sci U S A*, vol. 113, no. 31, pp. E4439–E4445, Aug. 2016, doi: 10.1073/pnas.1609731113.
- [228] J. A. Whitsett and T. Alenghat, “Respiratory epithelial cells orchestrate pulmonary innate immunity,” *Nat Immunol*, vol. 16, no. 1, pp. 27–35, Jan. 2015, doi: 10.1038/ni.3045.
- [229] L. M. Solis *et al.*, “Histologic patterns and molecular characteristics of lung adenocarcinoma associated with clinical outcome,” *Cancer*, vol. 118, no. 11, pp. 2889–2899, Jun. 2012, doi: 10.1002/cncr.26584.
- [230] R. Kalluri, “The biology and function of fibroblasts in cancer,” *Nat Rev Cancer*, vol. 16, no. 9, pp. 582–598, Sep. 2016, doi: 10.1038/nrc.2016.73.
- [231] R. Noy and J. W. Pollard, “Tumor-Associated Macrophages: From Mechanisms to Therapy,” *Immunity*, vol. 41, no. 1, pp. 49–61, Jul. 2014, doi: 10.1016/j.immuni.2014.06.010.
- [232] B. Suki, D. Stamenović, and R. Hubmayr, “Lung Parenchymal Mechanics,” in *Comprehensive Physiology*, Wiley, 2011, pp. 1317–1351. doi: 10.1002/cphy.c100033.
- [233] A. Stylianou, S. V. Kontomaris, C. Grant, and E. Alexandratou, “Atomic force microscopy on biological materials related to pathological conditions,” *Scanning*, vol. 2019, 2019, doi: 10.1155/2019/8452851.
- [234] T. Koorman *et al.*, “Spatial collagen stiffening promotes collective breast cancer cell invasion by reinforcing extracellular matrix alignment,” *Oncogene*, vol. 41, no. 17, pp. 2458–2469, Apr. 2022, doi: 10.1038/s41388-022-02258-1.
- [235] A. Stylianou, V. Gkretsi, M. Louca, L. C. Zacharia, and T. Stylianopoulos, “Collagen content and extracellular matrix cause cytoskeletal remodelling in pancreatic fibroblasts,” *J R Soc Interface*, vol. 16, no. 154, p. 20190226, May 2019, doi: 10.1098/rsif.2019.0226.
- [236] P. P. Provenzano, D. R. Inman, K. W. Eliceiri, H. E. Beggs, and P. J. Keely, “Mammary Epithelial-Specific Disruption of Focal Adhesion Kinase Retards Tumor Formation and Metastasis in a Transgenic Mouse Model of Human Breast Cancer,” *Am J Pathol*, vol. 173, no. 5, pp. 1551–1565, Nov. 2008, doi: 10.2353/ajpath.2008.080308.
- [237] T. R. Cox and J. T. Erler, “Remodeling and homeostasis of the extracellular matrix: implications for fibrotic diseases and cancer,” *Dis Model Mech*, vol. 4, no. 2, pp. 165–178, Mar. 2011, doi: 10.1242/dmm.004077.
- [238] J. T. Erler and V. M. Weaver, “Three-dimensional context regulation of metastasis,” *Clin Exp Metastasis*, vol. 26, no. 1, pp. 35–49, Jan. 2009, doi: 10.1007/s10585-008-9209-8.
- [239] M. Yamauchi, T. H. Barker, D. L. Gibbons, and J. M. Kurie, “The fibrotic tumor stroma,” *Journal of Clinical Investigation*, vol. 128, no. 1, pp. 16–25, Jan. 2018, doi: 10.1172/JCI93554.
- [240] S. Xu *et al.*, “The role of collagen in cancer: from bench to bedside,” *J Transl Med*, vol. 17, no. 1, p. 309, Dec. 2019, doi: 10.1186/s12967-019-2058-1.
- [241] F. Kai, A. P. Drain, and V. M. Weaver, “The Extracellular Matrix Modulates the Metastatic Journey,” *Dev Cell*, vol. 49, no. 3, pp. 332–346, May 2019, doi: 10.1016/j.devcel.2019.03.026.
- [242] J. J. Tomasek, G. Gabbiani, B. Hinz, C. Chaponnier, and R. A. Brown, “Myofibroblasts and mechano-regulation of connective tissue remodelling,” *Nat Rev Mol Cell Biol*, vol. 3, no. 5, pp. 349–363, May 2002, doi: 10.1038/nrm809.

- [243] Duffield Jeremy, M. Lupher, V. J. Thannickal, and T. A. Wynn, “Host responses in tissue repair and fibrosis,” *Annual Review of Pathology: Mechanisms of Disease*, vol. 8, pp. 241–276, 2013.
- [244] S. Holm Nielsen *et al.*, “Serological Assessment of Activated Fibroblasts by alpha-Smooth Muscle Actin ( $\alpha$ -SMA): A Noninvasive Biomarker of Activated Fibroblasts in Lung Disorders,” *Transl Oncol*, vol. 12, no. 2, pp. 368–374, Feb. 2019, doi: 10.1016/j.tranon.2018.11.004.
- [245] H. W. Lee *et al.*, “Alpha-Smooth Muscle Actin (ACTA2) Is Required for Metastatic Potential of Human Lung Adenocarcinoma,” *Clinical Cancer Research*, vol. 19, no. 21, pp. 5879–5889, Nov. 2013, doi: 10.1158/1078-0432.CCR-13-1181.
- [246] R. Surolia *et al.*, “Vimentin intermediate filament assembly regulates fibroblast invasion in fibrogenic lung injury,” *JCI Insight*, vol. 4, no. 7, Apr. 2019, doi: 10.1172/jci.insight.123253.
- [247] F. Danielsson, M. Peterson, H. Caldeira Araújo, F. Lautenschläger, and A. Gad, “Vimentin Diversity in Health and Disease,” *Cells*, vol. 7, no. 10, p. 147, Sep. 2018, doi: 10.3390/cells7100147.
- [248] R. Surolia and V. B. Antony, “Pathophysiological Role of Vimentin Intermediate Filaments in Lung Diseases,” *Front Cell Dev Biol*, vol. 10, Apr. 2022, doi: 10.3389/fcell.2022.872759.
- [249] B. Mehić, L. Duranović Rayan, N. Bilalović, D. Dohranović Tafro, and I. Pilav, “Lung adenocarcinoma mimicking pulmonary fibrosis—a case report,” *BMC Cancer*, vol. 16, no. 1, p. 729, Dec. 2016, doi: 10.1186/s12885-016-2763-6.
- [250] C. T. Mierke, D. Rösel, B. Fabry, and J. Brábek, “Contractile forces in tumor cell migration,” *Eur J Cell Biol*, vol. 87, no. 8–9, pp. 669–676, Sep. 2008, doi: 10.1016/j.ejcb.2008.01.002.
- [251] M. G. Mendez, D. Restle, and P. A. Janmey, “Vimentin Enhances Cell Elastic Behavior and Protects against Compressive Stress,” *Biophys J*, vol. 107, no. 2, pp. 314–323, Jul. 2014, doi: 10.1016/j.bpj.2014.04.050.
- [252] J. J. Northey, L. Przybyla, and V. M. Weaver, “Tissue Force Programs Cell Fate and Tumor Aggression,” *Cancer Discov*, vol. 7, no. 11, pp. 1224–1237, Nov. 2017, doi: 10.1158/2159-8290.CD-16-0733.
- [253] L.-S. Z. Rathje *et al.*, “Oncogenes induce a vimentin filament collapse mediated by HDAC6 that is linked to cell stiffness,” *Proceedings of the National Academy of Sciences*, vol. 111, no. 4, pp. 1515–1520, Jan. 2014, doi: 10.1073/pnas.1300238111.
- [254] C.-Y. Liu, H.-H. Lin, M.-J. Tang, and Y.-K. Wang, “Vimentin contributes to epithelial-mesenchymal transition cancer cell mechanics by mediating cytoskeletal organization and focal adhesion maturation,” *Oncotarget*, vol. 6, no. 18, pp. 15966–15983, Jun. 2015, doi: 10.18632/oncotarget.3862.
- [255] R. J. Petrie, H. Koo, and K. M. Yamada, “Generation of compartmentalized pressure by a nuclear piston governs cell motility in a 3D matrix,” *Science (1979)*, vol. 345, no. 6200, pp. 1062–1065, Aug. 2014, doi: 10.1126/science.1256965.
- [256] Y. Messica *et al.*, “The role of Vimentin in Regulating Cell Invasive Migration in Dense Cultures of Breast Carcinoma Cells,” *Nano Lett*, vol. 17, no. 11, pp. 6941–6948, Nov. 2017, doi: 10.1021/acs.nanolett.7b03358.
- [257] G. Burgstaller, M. Gregor, L. Winter, and G. Wiche, “Keeping the Vimentin Network under Control: Cell–Matrix Adhesion–associated Plectin 1f Affects Cell Shape and Polarity of Fibroblasts,” *Mol Biol Cell*, vol. 21, no. 19, pp. 3362–3375, Oct. 2010, doi: 10.1091/mbc.e10-02-0094.
- [258] K. Strouhalova, M. Přečková, A. Gandalovičová, J. Brábek, M. Gregor, and D. Rosel, “Vimentin Intermediate Filaments as Potential Target for Cancer Treatment,” *Cancers (Basel)*, vol. 12, no. 1, p. 184, Jan. 2020, doi: 10.3390/cancers12010184.
- [259] S. Mogre *et al.*, “Biomarker Potential of Vimentin in Oral Cancers,” *Life*, vol. 12, no. 2, p. 150, Jan. 2022, doi: 10.3390/life12020150.
- [260] M. Li *et al.*, “A novel function for vimentin: the potential biomarker for predicting melanoma hematogenous metastasis,” *Journal of Experimental & Clinical Cancer Research*, vol. 29, no. 1, p. 109, Dec. 2010, doi: 10.1186/1756-9966-29-109.
- [261] T. Wei *et al.*, “Vimentin-positive circulating tumor cells as a biomarker for diagnosis and treatment monitoring in patients with pancreatic cancer,” *Cancer Lett*, vol. 452, pp. 237–243, Jun. 2019, doi: 10.1016/j.canlet.2019.03.009.

- [262] J. R. van Beijnum *et al.*, “Extracellular vimentin mimics VEGF and is a target for anti-angiogenic immunotherapy,” *Nat Commun*, vol. 13, no. 1, p. 2842, May 2022, doi: 10.1038/s41467-022-30063-7.
- [263] M. Dauphin *et al.*, “Vimentin expression predicts the occurrence of metastases in non small cell lung carcinomas,” *Lung Cancer*, vol. 81, no. 1, pp. 117–122, Jul. 2013, doi: 10.1016/j.lungcan.2013.03.011.
- [264] D. E. Discher, L. Smith, S. Cho, M. Colasurdo, A. J. García, and S. Safran, “Matrix Mechanosensing: From Scaling Concepts in 'Omics Data to Mechanisms in the Nucleus, Regeneration, and Cancer,” *Annu Rev Biophys*, vol. 46, no. 1, pp. 295–315, May 2017, doi: 10.1146/annurev-biophys-062215-011206.
- [265] M. Yamauchi, T. H. Barker, D. L. Gibbons, and J. M. Kurie, “The fibrotic tumor stroma,” *Journal of Clinical Investigation*, vol. 128, no. 1, pp. 16–25, Jan. 2018, doi: 10.1172/JCI93554.
- [266] S. Xu *et al.*, “The role of collagen in cancer: from bench to bedside,” *J Transl Med*, vol. 17, no. 1, p. 309, Dec. 2019, doi: 10.1186/s12967-019-2058-1.
- [267] N. Mor-Vaknin, A. Punturieri, K. Sitwala, and D. M. Markovitz, “Vimentin is secreted by activated macrophages,” *Nat Cell Biol*, vol. 5, no. 1, pp. 59–63, Jan. 2003, doi: 10.1038/ncb898.
- [268] N. I. Nissen, M. Karsdal, and N. Willumsen, “Collagens and Cancer associated fibroblasts in the reactive stroma and its relation to Cancer biology,” *Journal of Experimental and Clinical Cancer Research*, vol. 38, no. 1. BioMed Central Ltd., Mar. 06, 2019. doi: 10.1186/s13046-019-1110-6.
- [269] A. V. Shinde, C. Humeres, and N. G. Frangogiannis, “The role of  $\alpha$ -smooth muscle actin in fibroblast-mediated matrix contraction and remodeling,” *Biochim Biophys Acta Mol Basis Dis*, vol. 1863, no. 1, pp. 298–309, Jan. 2017, doi: 10.1016/j.bbadis.2016.11.006.
- [270] O. Cordero-Llana *et al.*, “Clusterin secreted by astrocytes enhances neuronal differentiation from human neural precursor cells,” *Cell Death Differ*, vol. 18, no. 5, pp. 907–913, May 2011, doi: 10.1038/cdd.2010.169.
- [271] Syed. Rizvi, *Handbook of photomask manufacturing technology*. Taylor & Francis, 2005.
- [272] M. J. Madou, *Fundamentals of Microfabrication*. CRC Press, 2018. doi: 10.1201/9781482274004.
- [273] C. Vieu *et al.*, “Electron beam lithography: resolution limits and applications,” *Appl Surf Sci*, vol. 164, no. 1–4, pp. 111–117, Sep. 2000, doi: 10.1016/S0169-4332(00)00352-4.
- [274] K. Venkatakrisnan, B. K. A. Ngoi, P. Stanley, L. E. N. Lim, B. Tan, and N. R. Sivakumar, “Laser writing techniques for photomask fabrication using a femtosecond laser,” *Appl Phys A Mater Sci Process*, vol. 74, no. 4, pp. 493–496, Apr. 2002, doi: 10.1007/s003390101030.
- [275] R. Zaouk, B. Y. Park, and M. J. Madou, “Introduction to Microfabrication Techniques,” in *Microfluidic Techniques*, New Jersey: Humana Press, 2006, pp. 3–16. doi: 10.1385/1-59259-997-4:3.
- [276] S. Barcelo and Z. Li, “Nanoimprint lithography for nanodevice fabrication,” *Nano Converg*, vol. 3, no. 1, p. 21, Dec. 2016, doi: 10.1186/s40580-016-0081-y.
- [277] N. Fu, Y. Liu, X. Ma, and Z. Chen, “EUV Lithography: State-of-the-Art Review,” *Journal of Microelectronic Manufacturing*, vol. 2, no. 2, pp. 1–6, 2019, doi: 10.33079/jomm.19020202.
- [278] J. Loomis, D. Ratnayake, C. McKenna, and K. M. Walsh, “Grayscale lithography—automated mask generation for complex three-dimensional topography,” *Journal of Micro/Nanolithography, MEMS, and MOEMS*, vol. 15, no. 1, p. 013511, Mar. 2016, doi: 10.1117/1.JMM.15.1.013511.
- [279] S. I. Shah, G. H. Jaffari, E. Yassitepe, and B. Ali, “Evaporation,” in *Handbook of Deposition Technologies for Films and Coatings*, Elsevier, 2010, pp. 135–252. doi: 10.1016/B978-0-8155-2031-3.00004-1.
- [280] D. Depla, S. Mahieu, and J. E. Greene, “Sputter Deposition Processes,” in *Handbook of Deposition Technologies for Films and Coatings*, Elsevier, 2010, pp. 253–296. doi: 10.1016/B978-0-8155-2031-3.00005-3.
- [281] P. M. Martin, “Ion Plating,” in *Handbook of Deposition Technologies for Films and Coatings*, Elsevier, 2010, pp. 297–313. doi: 10.1016/B978-0-8155-2031-3.00006-5.
- [282] W. P. McCray, “MBE deserves a place in the history books,” *Nat Nanotechnol*, vol. 2, no. 5, pp. 259–261, May 2007, doi: 10.1038/nnano.2007.121.
- [283] K. Totsu and M. Esashi, “Gray-scale photolithography using maskless exposure system,” *Journal of Vacuum Science & Technology B: Microelectronics and Nanometer Structures*, vol. 23, no. 4, p. 1487, 2005, doi: 10.1116/1.1943438.

- [284] S. K. Bajpai, “Swelling Studies on Hydrogel Networks-A Review,” 2001.
- [285] S. Maji and H. Lee, “Engineering Hydrogels for the Development of Three-Dimensional In Vitro Models,” *Int J Mol Sci*, vol. 23, no. 5, Mar. 2022, doi: 10.3390/ijms23052662.
- [286] M. W. Tibbitt and K. S. Anseth, “Hydrogels as extracellular matrix mimics for 3D cell culture,” *Biotechnology and Bioengineering*, vol. 103, no. 4, pp. 655–663, Jul. 01, 2009. doi: 10.1002/bit.22361.
- [287] M. P. Lutolf *et al.*, “Synthetic matrix metalloproteinase-sensitive hydrogels for the conduction of tissue regeneration: Engineering cell-invasion characteristics,” *Proceedings of the National Academy of Sciences*, vol. 100, no. 9, pp. 5413–5418, Apr. 2003, doi: 10.1073/pnas.0737381100.
- [288] A. M. Kloxin, C. J. Kloxin, C. N. Bowman, and K. S. Anseth, “Mechanical properties of cellularly responsive hydrogels and their experimental determination,” *Advanced Materials*, vol. 22, no. 31, pp. 3484–3494, Aug. 2010, doi: 10.1002/adma.200904179.
- [289] N. A. Peppas, J. Z. Hilt, A. Khademhosseini, and R. Langer, “Hydrogels in biology and medicine: From molecular principles to bionanotechnology,” *Advanced Materials*, vol. 18, no. 11, pp. 1345–1360, Jun. 06, 2006. doi: 10.1002/adma.200501612.
- [290] A. T. Neffe, C. Löwenberg, and A. Lendlein, “Hydrogel networks by aliphatic dithiol Michael addition to glycidylmethacrylated gelatin,” *MRS Adv*, vol. 6, no. 33, pp. 796–800, Oct. 2021, doi: 10.1557/s43580-021-00136-8.
- [291] S. Yigit, R. Sanyal, and A. Sanyal, “Fabrication and Functionalization of Hydrogels through ‘Click’ Chemistry,” *Chem Asian J*, vol. 6, no. 10, pp. 2648–2659, Oct. 2011, doi: 10.1002/asia.201100440.
- [292] A. Kirillova *et al.*, “Fabrication of Biomedical Scaffolds Using Biodegradable Polymers,” *Chemical Reviews*, vol. 121, no. 18. American Chemical Society, pp. 11238–11304, Sep. 22, 2021. doi: 10.1021/acs.chemrev.0c01200.
- [293] K. Zhang, Q. Feng, Z. Fang, L. Gu, and L. Bian, “Structurally Dynamic Hydrogels for Biomedical Applications: Pursuing a Fine Balance between Macroscopic Stability and Microscopic Dynamics,” *Chemical Reviews*, vol. 121, no. 18. American Chemical Society, pp. 11149–11193, Sep. 22, 2021. doi: 10.1021/acs.chemrev.1c00071.
- [294] X. Xue, Y. Hu, S. Wang, X. Chen, Y. Jiang, and J. Su, “Fabrication of physical and chemical crosslinked hydrogels for bone tissue engineering,” *Bioactive Materials*, vol. 12. KeAi Communications Co., pp. 327–339, Jun. 01, 2022. doi: 10.1016/j.bioactmat.2021.10.029.
- [295] G. D. Nicodemus and S. J. Bryant, “Cell Encapsulation in Biodegradable Hydrogels for Tissue Engineering Applications,” *Tissue Eng Part B Rev*, vol. 14, no. 2, pp. 149–165, Jun. 2008, doi: 10.1089/ten.teb.2007.0332.
- [296] M. Tenje *et al.*, “A practical guide to microfabrication and patterning of hydrogels for biomimetic cell culture scaffolds,” *Organs-on-a-Chip*, vol. 2, p. 100003, Dec. 2020, doi: 10.1016/j.ooc.2020.100003.
- [297] J.-Y. Sun *et al.*, “Highly stretchable and tough hydrogels,” *Nature*, vol. 489, no. 7414, pp. 133–136, Sep. 2012, doi: 10.1038/nature11409.
- [298] C. E. Kadow, P. C. Georges, P. A. Janmey, and K. A. Beningo, “Polyacrylamide Hydrogels for Cell Mechanics: Steps Toward Optimization and Alternative Uses,” *Methods in Cell Biology*, vol. 83, pp. 29–46, 2007. doi: 10.1016/S0091-679X(07)83002-0.
- [299] E. E. Charrier, K. Pogoda, R. G. Wells, and P. A. Janmey, “Control of cell morphology and differentiation by substrates with independently tunable elasticity and viscous dissipation,” *Nat Commun*, vol. 9, no. 1, Dec. 2018, doi: 10.1038/s41467-018-02906-9.
- [300] J. Xia *et al.*, “Regulation of cell attachment, spreading, and migration by hydrogel substrates with independently tunable mesh size,” *Acta Biomater*, vol. 141, pp. 178–189, Mar. 2022, doi: 10.1016/j.actbio.2022.01.025.
- [301] M. Ermis, E. Antmen, and V. Hasirci, “Micro and Nanofabrication methods to control cell-substrate interactions and cell behavior: A review from the tissue engineering perspective,” *Bioactive Materials*, vol. 3, no. 3. KeAi Communications Co., pp. 355–369, Sep. 01, 2018. doi: 10.1016/j.bioactmat.2018.05.005.
- [302] Y. Yamanishi, T. Nakano, Y. Sawada, K. Itoga, T. Okano, and F. Arai, “Maskless gray scale lithography and its 3D microfluidic applications,” *Journal of Robotics and Mechatronics*, vol. 23, no. 3, pp. 426–433, 2011, doi: 10.20965/jrm.2011.p0426.

- [303] W. C. Mak and A. H. P. Ho, *Microfluidic biosensors*. 2023.
- [304] M. E. Wechsler, R. E. Stephenson, A. C. Murphy, H. F. Oldenkamp, A. Singh, and N. A. Peppas, “Engineered microscale hydrogels for drug delivery, cell therapy, and sequencing,” *Biomed Microdevices*, vol. 21, no. 2, p. 31, Jun. 2019, doi: 10.1007/s10544-019-0358-0.
- [305] B. Díaz-Bello *et al.*, “Method for the Direct Fabrication of Polyacrylamide Hydrogels with Controlled Stiffness in Polystyrene Multiwell Plates for Mechanobiology Assays,” *ACS Biomater Sci Eng*, vol. 5, no. 9, pp. 4219–4227, Sep. 2019, doi: 10.1021/acsbiomaterials.9b00988.
- [306] S. Paiva *et al.*, “Polyacrylamide Hydrogels with Rigidity-Independent Surface Chemistry Show Limited Long-Term Maintenance of Pluripotency of Human Induced Pluripotent Stem Cells on Soft Substrates,” *ACS Biomater Sci Eng*, vol. 6, no. 1, pp. 340–351, Jan. 2020, doi: 10.1021/acsbiomaterials.9b01189.
- [307] Z. Wei, S. Wang, J. Hirvonen, H. A. Santos, and W. Li, “Microfluidics Fabrication of Micrometer-Sized Hydrogels with Precisely Controlled Geometries for Biomedical Applications,” *Advanced Healthcare Materials*, vol. 11, no. 16. John Wiley and Sons Inc, Aug. 01, 2022. doi: 10.1002/adhm.202200846.
- [308] J. Huang, Q. Qin, and J. Wang, “A review of stereolithography: Processes and systems,” *Processes*, vol. 8, no. 9. MDPI, Sep. 01, 2020. doi: 10.3390/PR8091138.
- [309] K. C. Hribar, P. Soman, J. Warner, P. Chung, and S. Chen, “Light-assisted direct-write of 3D functional biomaterials,” *Lab Chip*, vol. 14, no. 2, pp. 268–275, 2014, doi: 10.1039/C3LC50634G.
- [310] S. Ghassemi, N. Biaias, K. Maniura, S. J. Wind, M. P. Sheetz, and J. Hone, “Fabrication of elastomer pillar arrays with modulated stiffness for cellular force measurements,” *Journal of Vacuum Science & Technology B: Microelectronics and Nanometer Structures Processing, Measurement, and Phenomena*, vol. 26, no. 6, pp. 2549–2553, Nov. 2008, doi: 10.1116/1.3013424.
- [311] J. R. Tse and A. J. Engler, “Stiffness Gradients Mimicking In Vivo Tissue Variation Regulate Mesenchymal Stem Cell Fate,” *PLoS One*, vol. 6, no. 1, p. e15978, Jan. 2011, doi: 10.1371/journal.pone.0015978.
- [312] X. Li *et al.*, “Accurate modulation of photoprinting under stiffness imaging feedback for engineering ECMs with high-fidelity mechanical properties,” *Microsyst Nanoeng*, vol. 8, no. 1, Dec. 2022, doi: 10.1038/s41378-022-00394-y.
- [313] Pierce Protein, “Pierce Protein,” *Pierce Protein*, vol. 12, no. 2, 2020.
- [314] S. Wong, W. Guo, I. Hoffecker, and Y. Wang, “Preparation of a Micropatterned Rigid-Soft Composite Substrate for Probing Cellular Rigidity Sensing,” 2014, pp. 3–15. doi: 10.1016/B978-0-12-800281-0.00001-4.
- [315] M. J. P. Biggs *et al.*, “The Functional Response of Mesenchymal Stem Cells to Electron-Beam Patterned Elastomeric Surfaces Presenting Micrometer to Nanoscale Heterogeneous Rigidity,” *Advanced Materials*, vol. 29, no. 39, p. 1702119, Oct. 2017, doi: 10.1002/adma.201702119.
- [316] A. S. Rowlands, P. A. George, and J. J. Cooper-White, “Directing osteogenic and myogenic differentiation of MSCs: interplay of stiffness and adhesive ligand presentation,” *Am J Physiol Cell Physiol*, vol. 295, pp. 1037–1044, 2008, doi: 10.1152/ajpcell.67.2008.-The.
- [317] wwwMicroChemicalscom, “Chapter 01 MicroChemicals ®-Fundamentals of Microstructuring WET-CHEMICAL ETCHING OF METALS Etching of Aluminium Properties and Application Areas of Aluminium.” [Online]. Available: [www.microchemicals.com/downloads/application\\_notes.html](http://www.microchemicals.com/downloads/application_notes.html)
- [318] S. Sheth, E. Jain, A. Karadaghy, S. Syed, H. Stevenson, and S. P. Zustiak, “UV Dose Governs UV-Polymerized Polyacrylamide Hydrogel Modulus,” *Int J Polym Sci*, vol. 2017, 2017, doi: 10.1155/2017/5147482.
- [319] C. Decker, “Polymérisation sous rayonnement UV,” *Techniques de l’ingénieur*, vol. AM3044 V1, 2000, Accessed: Jul. 20, 2023. [Online]. Available: <https://www.techniques-ingenieur.fr/base-documentaire/materiaux-th11/plastochimie-et-analyse-physico-chimique-42139210/polymerisation-sous-rayonnement-uv-am3044/>
- [320] S. A. Seabrook, P. Pascal, M. P. Tonge, and R. G. Gilbert, “Termination rate coefficients for acrylamide in the aqueous phase at low conversion,” *Polymer (Guildf)*, vol. 46, no. 23, pp. 9562–9573, Nov. 2005, doi: 10.1016/j.polymer.2005.08.062.
- [321] K. Mandal, I. Wang, E. Vitiello, L. A. C. Orellana, and M. Balland, “Cell dipole behaviour revealed by ECM sub-cellular geometry,” *Nat Commun*, vol. 5, no. 1, p. 5749, Dec. 2014, doi: 10.1038/ncomms6749.

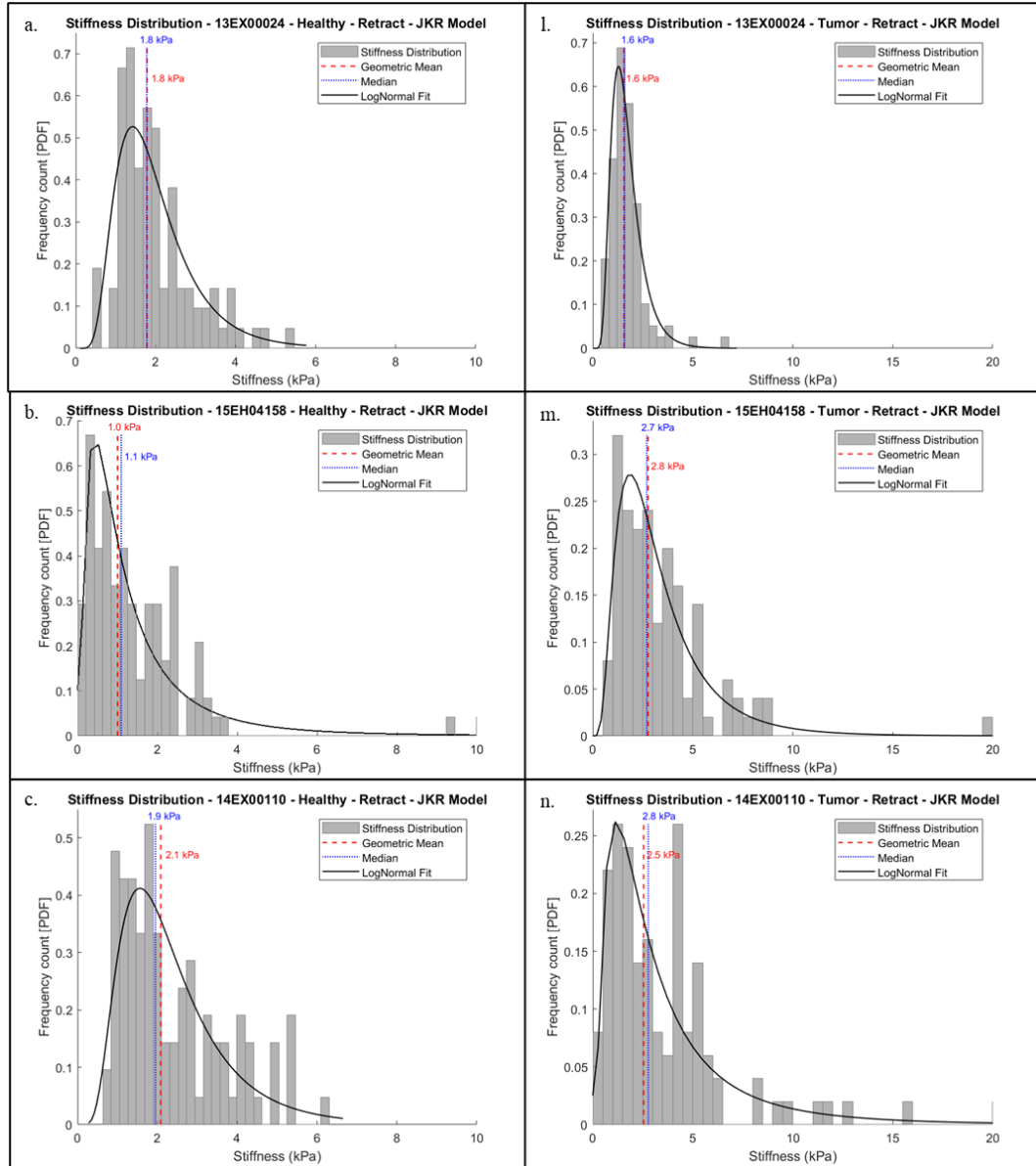
- [322] B. Ladoux and A. Nicolas, “Physically based principles of cell adhesion mechanosensitivity in tissues,” *Reports on Progress in Physics*, vol. 75, no. 11, Nov. 2012, doi: 10.1088/0034-4885/75/11/116601.
- [323] H. W. Ooi, S. Hafeez, C. A. Van Blitterswijk, L. Moroni, and M. B. Baker, “Hydrogels that listen to cells: A review of cell-responsive strategies in biomaterial design for tissue regeneration,” *Materials Horizons*, vol. 4, no. 6. Royal Society of Chemistry, pp. 1020–1040, Nov. 01, 2017. doi: 10.1039/c7mh00373k.
- [324] A. Vedadghavami *et al.*, “Manufacturing of hydrogel biomaterials with controlled mechanical properties for tissue engineering applications,” *Acta Biomater*, vol. 62, pp. 42–63, Oct. 2017, doi: 10.1016/j.actbio.2017.07.028.
- [325] M. Théry and M. Bornens, “Cell shape and cell division,” *Current Opinion in Cell Biology*, vol. 18, no. 6. pp. 648–657, Dec. 2006. doi: 10.1016/j.ceb.2006.10.001.
- [326] M. Théry, “Micropatterning as a tool to decipher cell morphogenesis and functions,” *Journal of Cell Science*, vol. 123, no. 24. pp. 4201–4213, Dec. 15, 2010. doi: 10.1242/jcs.075150.
- [327] P. Maiuri *et al.*, “The first World Cell Race,” *Current Biology*, vol. 22, no. 17, pp. R673–R675, Sep. 2012, doi: 10.1016/j.cub.2012.07.052.
- [328] K. A. Kilian, B. Bugarija, B. T. Lahn, and M. Mrksich, “Geometric cues for directing the differentiation of mesenchymal stem cells,” *Proc Natl Acad Sci U S A*, vol. 107, no. 11, pp. 4872–4877, Mar. 2010, doi: 10.1073/pnas.0903269107.
- [329] S. Dupont *et al.*, “Role of YAP/TAZ in mechanotransduction,” *Nature*, vol. 474, no. 7350, pp. 179–184, 2011, doi: 10.1038/nature10137.
- [330] J. Fu *et al.*, “Mechanical regulation of cell function with geometrically modulated elastomeric substrates,” *Nat Methods*, vol. 7, no. 9, pp. 733–736, Sep. 2010, doi: 10.1038/nmeth.1487.
- [331] J. d’Alessandro *et al.*, “Cell migration guided by long-lived spatial memory,” *Nat Commun*, vol. 12, no. 1, Dec. 2021, doi: 10.1038/s41467-021-24249-8.
- [332] W. J. Hadden *et al.*, “Stem cell migration and mechanotransduction on linear stiffness gradient hydrogels,” *Proc Natl Acad Sci U S A*, vol. 114, no. 22, pp. 5647–5652, May 2017, doi: 10.1073/pnas.1618239114.
- [333] A. K. Yip *et al.*, “Cellular response to substrate rigidity is governed by either stress or strain,” *Biophys J*, vol. 104, no. 1, pp. 19–29, Jan. 2013, doi: 10.1016/j.bpj.2012.11.3805.
- [334] S. Mattiassi, A. A. Conner, F. Feng, E. L. K. Goh, and E. K. F. Yim, “The Combined Effects of Topography and Stiffness on Neuronal Differentiation and Maturation Using a Hydrogel Platform,” *Cells*, vol. 12, no. 6, Mar. 2023, doi: 10.3390/cells12060934.
- [335] K. A. Gultian *et al.*, “Human induced mesenchymal stem cells display increased sensitivity to matrix stiffness,” *Sci Rep*, vol. 12, no. 1, Dec. 2022, doi: 10.1038/s41598-022-12143-2.
- [336] K. de Bruin *et al.*, “Cellular dynamics of EGF receptor-targeted synthetic viruses,” *Molecular Therapy*, vol. 15, no. 7, pp. 1297–1305, 2007, doi: 10.1038/sj.mt.6300176.
- [337] T. E. Angelini, E. Hannezo, X. Trepast, J. J. Fredberg, and D. A. Weitz, “Cell Migration Driven by Cooperative Substrate Deformation Patterns,” *Phys Rev Lett*, vol. 104, no. 16, p. 168104, Apr. 2010, doi: 10.1103/PhysRevLett.104.168104.
- [338] W. Thielicke and E. J. Stamhuis, “PIVlab – Towards User-friendly, Affordable and Accurate Digital Particle Image Velocimetry in MATLAB,” *J Open Res Softw*, vol. 2, Oct. 2014, doi: 10.5334/jors.bl.
- [339] S. Garcia, E. Hannezo, J. Elgeti, J. F. Joanny, P. Silberzan, and N. S. Gov, “Physics of active jamming during collective cellular motion in a monolayer,” *Proc Natl Acad Sci U S A*, vol. 112, no. 50, pp. 15314–15319, Dec. 2015, doi: 10.1073/pnas.1510973112.
- [340] L. Petitjean *et al.*, “Velocity fields in a collectively migrating epithelium,” *Biophys J*, vol. 98, no. 9, pp. 1790–1800, May 2010, doi: 10.1016/j.bpj.2010.01.030.
- [341] Q. Tseng *et al.*, “Spatial organization of the extracellular matrix regulates cell–cell junction positioning,” *Proceedings of the National Academy of Sciences*, vol. 109, no. 5, pp. 1506–1511, Jan. 2012, doi: 10.1073/pnas.1106377109.
- [342] M. Moussus *et al.*, “Intracellular stresses in patterned cell assemblies,” *Soft Matter*, vol. 10, no. 14, pp. 2414–2423, Apr. 2014, doi: 10.1039/c3sm52318g.

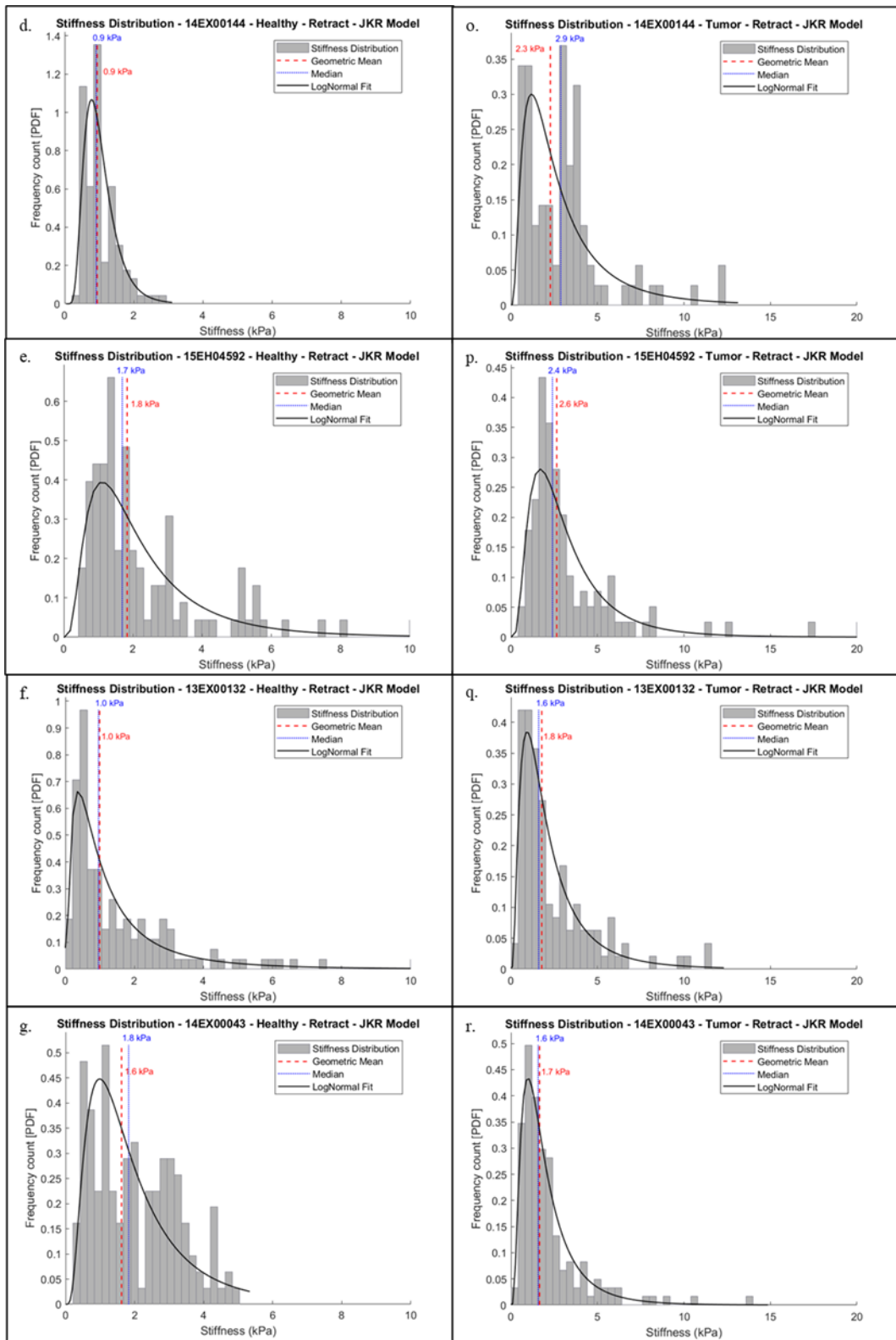
- [343] P. W. Oakes, S. Banerjee, M. C. Marchetti, and M. L. Gardel, “Geometry Regulates Traction Stresses in Adherent Cells,” *Biophys J*, vol. 107, no. 4, pp. 825–833, Aug. 2014, doi: 10.1016/j.bpj.2014.06.045.
- [344] A. Engler, L. Bacakova, C. Newman, A. Hategan, M. Griffin, and D. Discher, “Substrate Compliance versus Ligand Density in Cell on Gel Responses,” *Biophys J*, vol. 86, no. 1 I, pp. 617–628, 2004, doi: 10.1016/S0006-3495(04)74140-5.
- [345] O. Shebanova and D. A. Hammer, “Biochemical and mechanical extracellular matrix properties dictate mammary epithelial cell motility and assembly,” *Biotechnol J*, vol. 7, no. 3, pp. 397–408, Mar. 2012, doi: 10.1002/biot.201100188.
- [346] C.-M. Lo, H.-B. Wang, M. Dembo, and Y. Wang, “Cell Movement Is Guided by the Rigidity of the Substrate,” *Biophys J*, vol. 79, no. 1, pp. 144–152, Jul. 2000, doi: 10.1016/S0006-3495(00)76279-5.
- [347] A. Isomursu *et al.*, “Directed cell migration towards softer environments,” *Nat Mater*, vol. 21, no. 9, pp. 1081–1090, Sep. 2022, doi: 10.1038/s41563-022-01294-2.
- [348] K. Ohashi, S. Fujiwara, and K. Mizuno, “Roles of the cytoskeleton, cell adhesion and rho signalling in mechanosensing and mechanotransduction,” *J Biochem*, p. mvw082, Jan. 2017, doi: 10.1093/jb/mvw082.
- [349] K. Burridge, E. Monaghan-Benson, and D. M. Graham, “Mechanotransduction: From the cell surface to the nucleus via RhoA,” *Philosophical Transactions of the Royal Society B: Biological Sciences*, vol. 374, no. 1779. Royal Society Publishing, Aug. 19, 2019. doi: 10.1098/rstb.2018.0229.
- [350] D. Riveline *et al.*, “Focal Contacts as Mechanosensors,” *J Cell Biol*, vol. 153, no. 6, pp. 1175–1186, Jun. 2001, doi: 10.1083/jcb.153.6.1175.
- [351] L. Julian and M. F. Olson, “Rho-associated coiled-coil containing kinases (ROCK),” *Small GTPases*, vol. 5, no. 2, p. e29846, Apr. 2014, doi: 10.4161/sgtp.29846.
- [352] M. A. Wozniak and C. S. Chen, “Mechanotransduction in development: A growing role for contractility,” *Nature Reviews Molecular Cell Biology*, vol. 10, no. 1. pp. 34–43, Jan. 2009. doi: 10.1038/nrm2592.
- [353] A. Nukuda *et al.*, “Stiff substrates increase YAP-signaling-mediated matrix metalloproteinase-7 expression,” *Oncogenesis*, vol. 4, Sep. 2015, doi: 10.1038/oncsis.2015.24.
- [354] D. E. P. Pinto, M. M. T. da Gama, and N. A. M. Araújo, “Cell motility in confluent tissues induced by substrate disorder,” *Phys Rev Res*, vol. 4, no. 2, p. 023186, Jun. 2022, doi: 10.1103/PhysRevResearch.4.023186.
- [355] E. R. Banerjee and W. R. Henderson, “Characterization of lung stem cell niches in a mouse model of bleomycin-induced fibrosis,” *Stem Cell Res Ther*, vol. 3, no. 3, p. 21, Sep. 2012, doi: 10.1186/scrt112.
- [356] Y. Jia *et al.*, “Phenotypic Analysis of BrdU Label-Retaining Cells during the Maturation of Conducting Airway Epithelium in a Porcine Lung,” *Stem Cells Int*, vol. 2019, pp. 1–14, Feb. 2019, doi: 10.1155/2019/7043890.

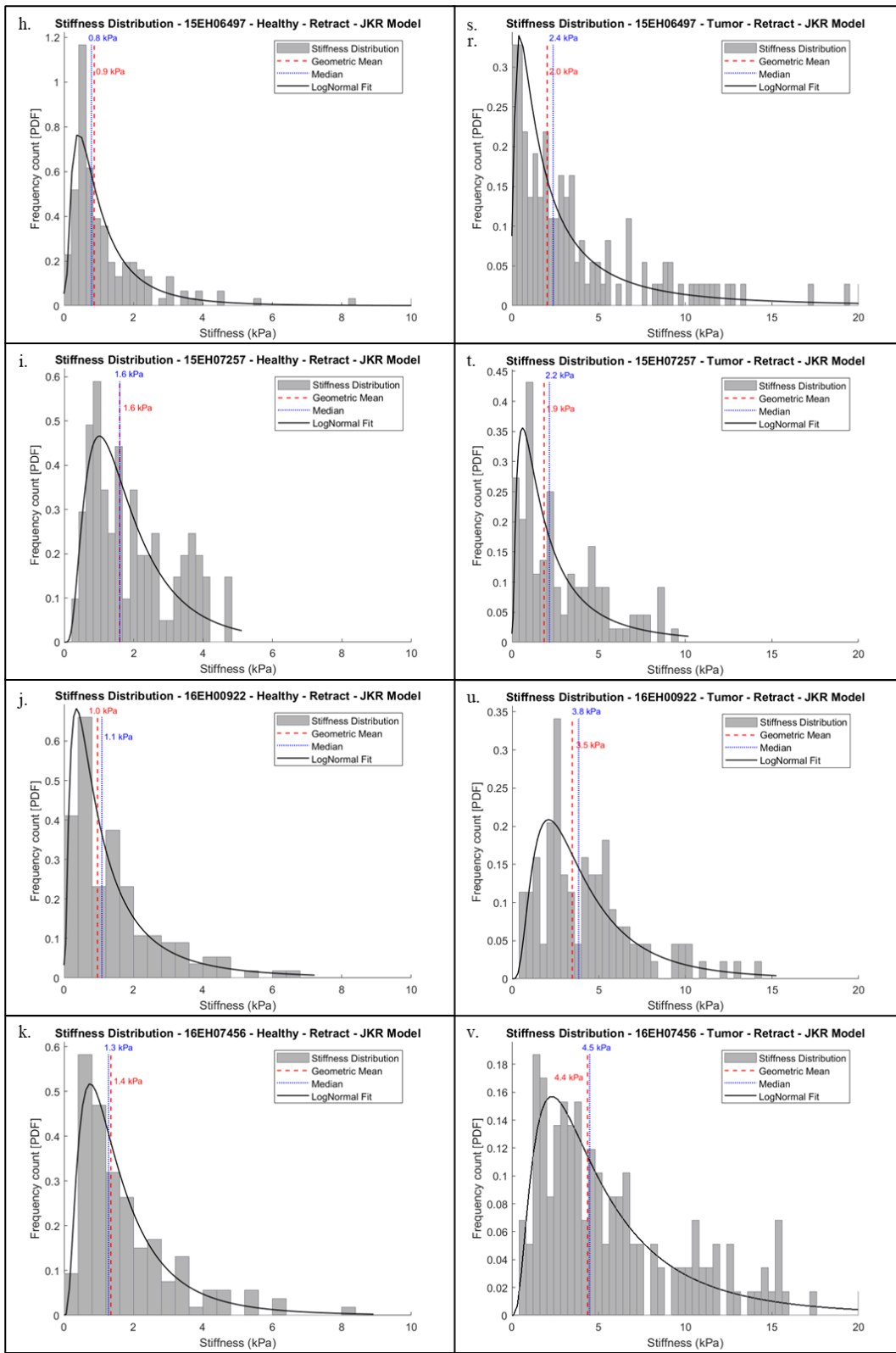


# APPENDIX A

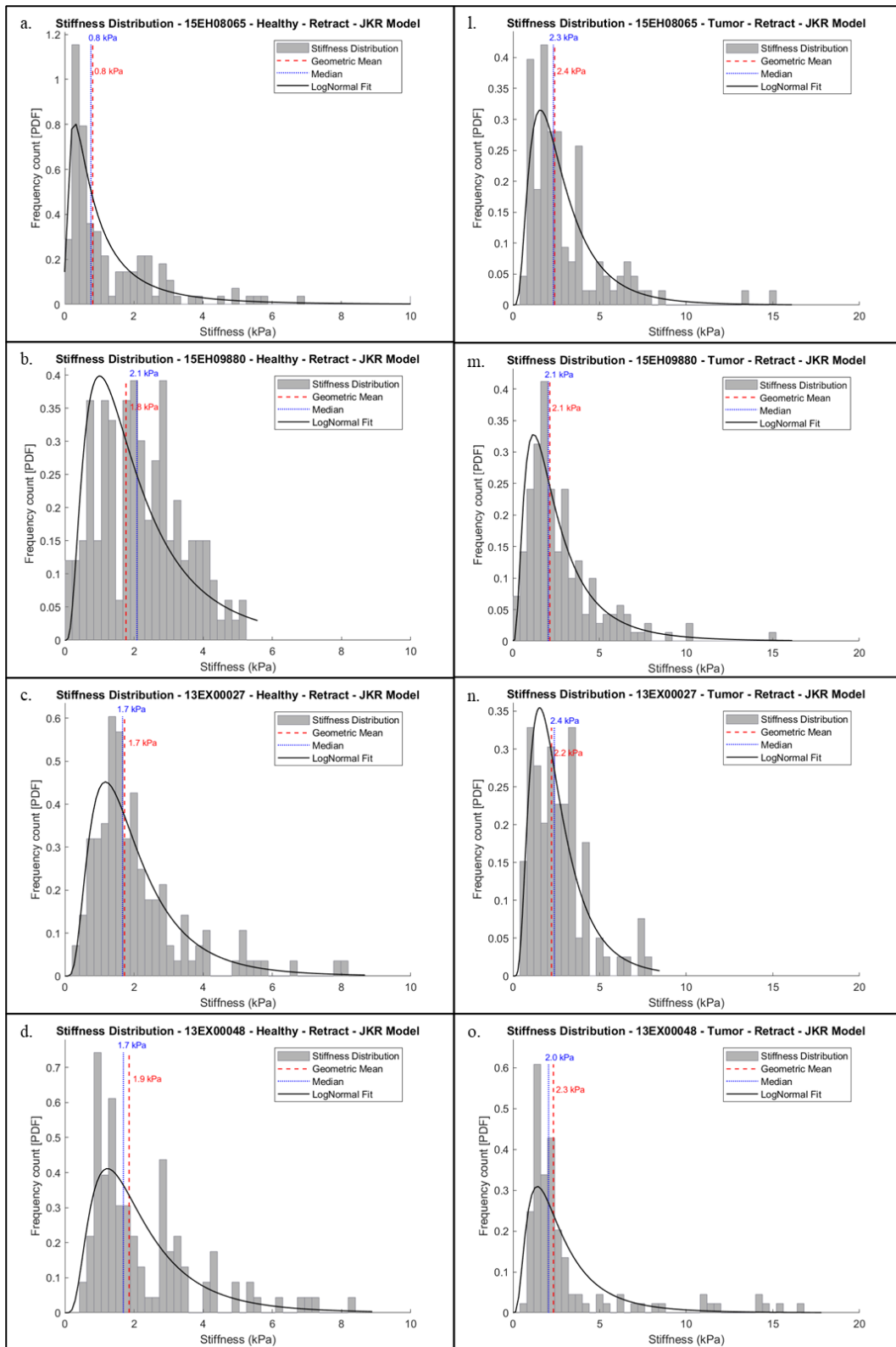
Frequency counts (probability density function) of the Young's moduli  $E$  of healthy (a-k) and tumor (l-v) human lung tissue, using JKR model to fit the indentation curves. Histograms are fitted for a log-normal distribution. The blue dotted lines represent the median and the red dashed lines the geometric mean of the distribution. .

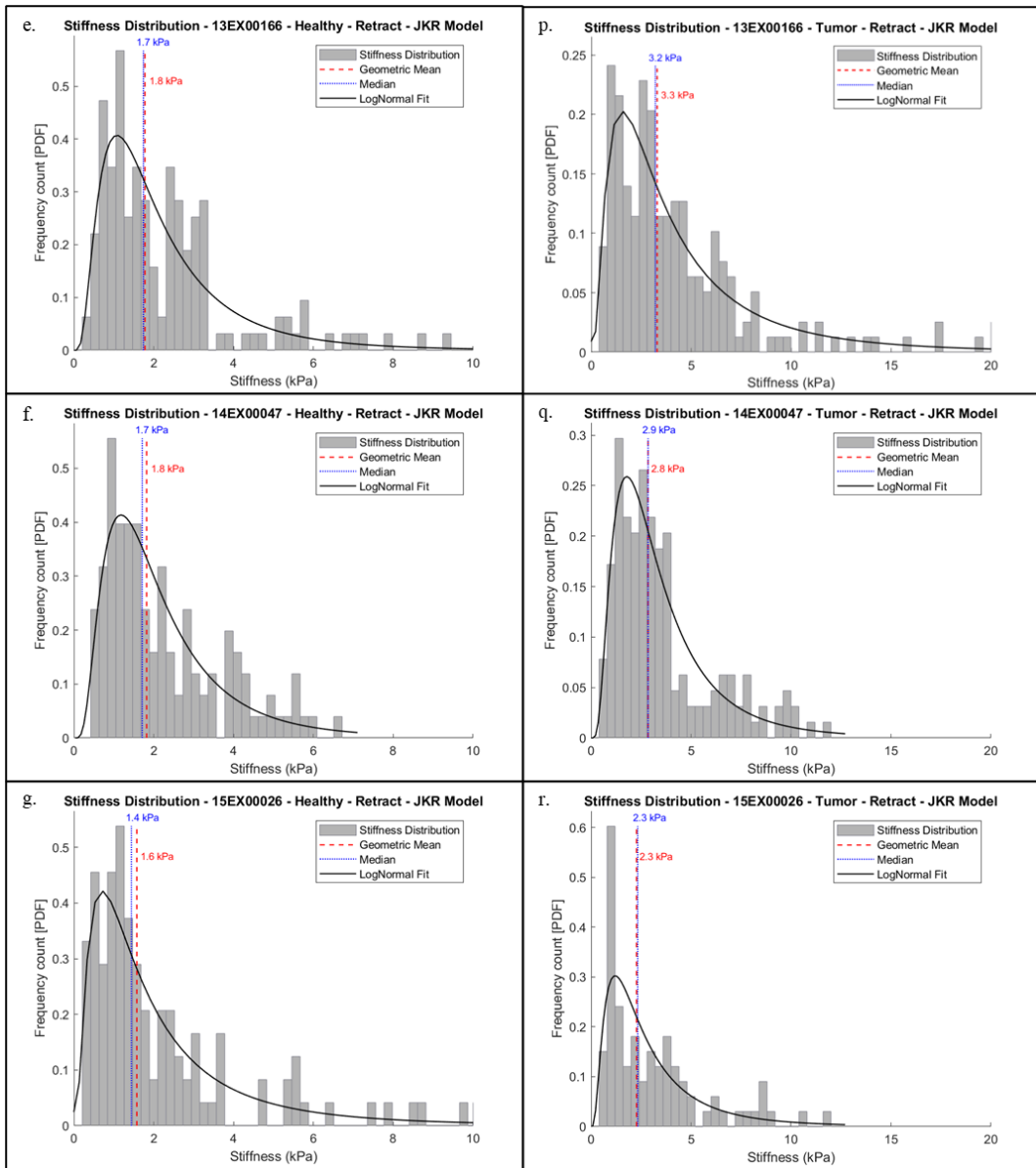






Healthy and acinar adenocarcinoma lung tissue stiffness distributions of biopsies a-l.13EX00024, b-m.15EH04158, c-n.14EX00110, f-q.14EX00144, g-r. 15EH04592, 13EX00132, 14EX00043, 15EH06497, 15EH07257, 16EH00922, 16EH07456.





Healthy (left) and solid adenocarcinoma (right) lung tissue stiffness distributions of biopsies a-l. 15EH08065, b-m. 15EH09880, c-n. 13EX00027, d-o.13EX00048, e-p. 13EX00166, f-q. 14EX00047 and g-r. 15EX00026.

---

## ANALYSE QUANTITATIVE DES PROPRIETES MECANIQUES DES TISSUS PULMONAIRES SAINS ET CANCEREUX POUR LA CONCEPTION DE SUBSTRATS DE CULTURE MECANO-MIMETIQUES

---

Les propriétés mécaniques des tissus sont de plus en plus reconnues comme étant cruciales dans la progression des maladies. Cette thèse examine les propriétés mécaniques des tissus pulmonaires normaux et tumoraux de 18 patients. Une méthodologie est développée en utilisant IT-AFM pour mesurer la rigidité des tissus à l'échelle microscopique et extraire des descripteurs de forme de la texture de rigidité. Une corrélation entre la composition du tissu et sa rigidité est aussi réalisée. En combinant ces paramètres avec la photolithographie, des hydrogels de polyacrylamide à texture de rigidité sont conçus, aboutissant à des substrats de culture qui imitent la distribution de la rigidité des tissus tumoraux. En cultivant des cellules A549 sur ces hydrogels, l'influence de la texture de rigidité du substrat sur le comportement cellulaire est évaluée. Le développement de cette plateforme mécano-mimétique promet de faire avancer le diagnostic, le traitement et la découverte de médicaments pour diverses maladies et révèle son applicabilité potentielle à d'autres tissus humains.

---

## QUANTITATIVE ANALYSIS OF THE MECHANICAL PROPERTIES OF HEALTHY AND CANCER LUNG TISSUE FOR THE DESIGN OF MECHANO-MIMETIC CULTURE SUBSTRATES

---

Mechanical properties of tissues are increasingly recognized as crucial in disease progression. This thesis investigates the mechanical properties of normal and adenocarcinoma lung tissues from 18 patients. A novel methodology is developed using IT-AFM to measure microscale tissue stiffness and extract shape descriptors of stiffness texture. Furthermore, a correlation between tissue composition and stiffness is performed. Combining these parameters with photolithography, stiffness-textured polyacrylamide hydrogels are engineered, resulting in culture substrates that mimic the tumor tissue's stiffness distribution. By culturing A549 cells on these hydrogels, the influence of substrate stiffness texture on cellular behavior is evaluated. The development of this versatile mechano-mimetic platform holds promise for advancing diagnosis, treatment, and drug discovery for various diseases and reveals its potential applicability to other human tissues.